Binary Neutron Star Mergers and Electromagnetic Counterparts

DISSERTATION

zur Erlangung des akademischen Grades
doctor rerum naturalium (Dr. rer. nat.)

seit 1558

vorgelegt dem Rat der

PHYSIKALISCH-ASTRONOMISCHEN FAKULTÄT

der

FRIEDRICH-SCHILLER-UNIVERSITÄT JENA

von

Vsevolod Nedora (M.Sc.)

geboren am 13.03.1993 in Wladiwostok

GUTACHER:

1.	PROF. DR. SEBASTIANO BERNUZZI	(FRIEDRICH-SCHILLER-UNIVERSITÄT JENA)
2.	PROF. DR. STEPHAN ROSSWOG	(STOCKHOLM UNIVERSITY)
3.	PROF. DR. GABRIEL MARTÍNEZ PINEDO	(TECHNISCHE UNIVERSITÄT DARMSTADT)

TAG DER DISPUTATION: 14.04.2022

Dissertation, Friedrich-Schiller-Universität Jena, [2022].

"*Devotion to the truth is the hallmark of morality; there is no greater, nobler, more heroic form of devotion than the act of a man who assumes the responsibility of thinking*"

Ayn Rand

"*In the midst of vastness of the Universe, and eternal time, I the human alone wander in wonder*"

Mahabishwe Mahakashe

Abstract

One of the fundamentally unknown areas in physics concerns the properties of matter at densities exceeding those present in nuclei. Such conditions are rare but can be found in remnants of dead stars such as neutron stars (NSs). Hidden within their cold interiors, they are difficult to study unless a certain event exposes them.

In August 2017, a merger of two neutron stars was detected for the first time via several carriers. Observed in gravitational waves (GWs), as well as in the electromagnetic (EM) spectrum, the GW170817 marked the dawn of multi-messenger (MM) astronomy for compact object mergers, and shed light on numerous astrophysical aspects of binary neutron star (BNS) mergers and on the properties of matter at supranuclear densities.

And yet many questions remain, starting with the outcome of the merger. Was it a massive NS temporarily supported against collapse, or a black hole (BH)? How important are BNS mergers in cosmic chemical evolution, *i.e.*, the evolution of spatial and temporal distributions of heavy elements in galaxies? It is known that they enrich their surroundings with very heavy elements, but are they the dominant source of these elements? Modeling these events on the computer, do we understand them correctly, *i.e.*, do our predictions regarding the properties of the ejected matter and its EM signatures agree with the newly gained data? And now, more than three years after the event, can further observations give us new insights into the processes that governed the merger?

This thesis is dedicated to addressing these questions by means of analyzing a large set of numerical simulations of BNS mergers, performed with state-of-the-art numerical tools, and targeted specifically to GW170817. Employing a suite of post-processing tools we study the matter dynamics. Special attention is given to matter, ejected from the system during and after merger, so-called ejecta. With the help of a parameterized nucleosynthesis model, we study the final abundances of heavy elements in ejecta, comparing them to solar abundances. Furthermore, we investigate EM emission, powered by the decay of newly synthesized heavy elements, comparing it to the observations of GW170817. Finally, we study the long-term emission of the ejected material as it propagates through the interstellar medium (ISM), via our new numerical tools, comparing the results with a recently detected change in the emission from GW170817.

Published content and contributions

V. Nedora, D. Radice, S. Bernuzzi, A. Perego, B. Daszuta, A. Endrizzi, A. Prakash, and F. Schianchi. Dynamical ejecta synchrotron emission as possible contributor to the rebrightening of GRB170817A. 4 2021. arXiv:2104.04537
I wrote 95% *of the text, performed all the postprocessing of numerical relativity simulations, and computed kilonova afterglow models. I created all the figures. I also wrote all of the* `PyBlastAfterglow` *code.*

V. Nedora, F. Schianchi, S. Bernuzzi, D. Radice, B. Daszuta, A. Endrizzi, A. Perego, A. Prakash, and F. Zappa. Mapping dynamical ejecta and disk masses from numerical relativity simulations of neutron star mergers. *Classical and Quantum Gravity*, 11 2021. arXiv:2011.11110
I wrote 95% *of the text, compiled the datasets available in the literature and performed the statistical analysis. I created all the figures.*

V. Nedora, S. Bernuzzi, D. Radice, B. Daszuta, A. Endrizzi, A. Perego, A. Prakash, M. Safarzadeh, F. Schianchi, and D. Logoteta. Numerical Relativity Simulations of the Neutron Star Merger GW170817: Long-Term Remnant Evolutions, Winds, Remnant Disks, and Nucleosynthesis. *Astrophys. J.*, 906(2):98, 2021. arXiv:2008.04333
I wrote 75% *of the text, performed all the postprocessing of numerical relativity simulations. I created all the figures.*

V. Nedora, S. Bernuzzi, D. Radice, A. Perego, A. Endrizzi, and N. Ortiz. Spiral-wave wind for the blue kilonova. *Astrophys. J.*, 886(2):L30, 2019. arXiv:1907.04872
I wrote 50% *of the text, performed all the postprocessing of numerical relativity simulations. I created all the figures.*

A. Prakash, D. Radice, D. Logoteta, A. Perego, **V. Nedora**, I. Bombaci, R. Kashyap, S. Bernuzzi, and A. Endrizzi. Signatures of deconfined quark phases in binary neutron star mergers. 6 2021. arXiv:2106.07885
I wrote the kilonova afterglow section (15% *of the paper text*) *and produced the related*

figures. I also helped with running some of the binary neutron star merger simulations used in this paper.

A. Hajela, R. Margutti, J. S. Bright, K. D. Alexander, B. D. Metzger, **V. Nedora**, A. Kathirgamaraju, B. Margalit, D. Radice, E. Berger, A. MacFadyen, D. Giannios, R. Chornock, I. Heywood, L. Sironi, O. Gottlieb, D. Coppejans, T. Laskar, Y. Cendes, R. Barniol Duran, T. Eftekhari, W. Fong, A. McDowell, M. Nicholl, X. Xie, J. Zrake, S. Bernuzzi, F. S. Broekgaarden, C. D. Kilpatrick, G. Terreran, V. A. Villar, P. K. Blanchard, S. Gomez, G. Hosseinzadeh, D. J. Matthews, and J. C. Rastinejad. The emergence of a new source of X-rays from the binary neutron star merger GW170817. Apr. 2021. `arXiv:2104.02070`
I wrote the section on the numerical relativity informed kilonova afterglow models, (5% *of the paper text), and produced the related figures.*

S. Bernuzzi, M. Breschi, B. Daszuta, A. Endrizzi, D. Logoteta, **V. Nedora**, A. Perego, D. Radice, F. Schianchi, F. Zappa, I. Bombaci, and N. Ortiz. Accretion-induced prompt black hole formation in asymmetric neutron star mergers, dynamical ejecta and kilonova signals. *Mon. Not. Roy. Astron. Soc.*, June 2020. `arXiv:2003.06015`
I helped with the postprocessing of numerical relativity simulations.

M. Breschi, A. Perego, S. Bernuzzi, W. Del Pozzo, **V. Nedora**, D. Radice, and D. Vescovi. AT2017gfo: Bayesian inference and model selection of multi-component kilonovae and constraints on the neutron star equation of state. 1 2021. `arXiv:2101.01201`
I helped with setting up the kilonova model selection runs.

Acknowledgements

First of all I would like to thank my parents, Sergey and Anna Nedora for their love and support, patience and wisdom. I would not have been able to carry on this journey without them.

I am deeply indebted to my advisor David Radice and my supervisor Sebastiano Bernuzzi for having guided me through my PhD studies. I was presented with an interesting project, and I was given a lot of freedom in how to approach it and how to explore areas of MM astrophysics beyond its scope. This creative and research freedom facilitated my desire to continue the research.

It is my pleasure to thank all the people with whom I worked most closely during my PhD: Albino Perego, Andrea Endrizzi, Nestor Ortiz, Francesco Zappa, Matteo Breschi.

I am also grateful to Aprajita Hajela for inviting me into an exciting project regarding the analysis and interpretation of newly detected change in GRB170817A afterglow. This was very inspiring experience.

It is my pleasure to thank Charles Bishop for proofreading the thesis and pointing out typos and incorrect articles, and Ssohrab Borhanian for helping me with the German abstract of this thesis.

Contents

Acknowledgements **ix**

1 Introduction **1**

1.1 Theoretical picture of BNS mergers 3

1.1.1 Inspiral 3

1.1.2 Merger and post-merger 4

1.1.3 Ejecta 8

1.1.4 *R*-process nucleosynthesis 9

1.1.5 Kilonova 11

1.1.6 Non-thermal afterglows 14

1.2 Aims and organization of this thesis 16

2 Methods of BNS merger simulations **19**

2.1 The $3 + 1$ formulation of General Relativity 19

2.2 General relativistic hydrodynamics 22

2.3 The neutron star equation of state 24

2.3.1 Finite temperature treatment 24

2.3.2 EOSs in cold configurations of neutron stars 25

2.4 Neutrino Radiation Transport 26

2.4.1 Neutrino leakage scheme 27

2.4.2 Neutrino M0 scheme 30

2.5 Magnetic field induced turbulence 30

2.6 Simulations and postprocessing 32

2.6.1 Disk & Remnant 33

2.6.2 Density modes 34

2.6.3 Angular momentum 34

2.6.4 Ejecta 35

The Geodesic criterion 35

The Bernoulli criterion 35

3 Binary Neutron Star merger simulations 37
3.1 Overview of the remnant-disk interactions 37
3.1.1 Final disk structure 44
3.1.2 Mass and angular momentum loss 45
3.2 Mass ejection in BNS merger simulations 50
3.2.1 Dynamical Ejecta 50
3.2.2 Fast tail of dynamical ejecta 56
3.2.3 Spiral-wave wind 59
3.2.4 Neutrino-driven wind 62

4 Nucleosynthesis 65
4.1 Modeling the nucleosynthesis 65
4.1.1 Basics of a nuclear reaction network 66
4.1.2 Parameterized nucleosynthesis 67
4.2 Nucleosynthetic yields in BNS ejecta 70

5 Kilonova 73
5.1 Overview of kilonova modeling 73
5.2 Semi-analytic kilonova model 74
5.3 Numerical relativity informed kilonova models 76
5.4 Fit-informed kilonova models 77
5.5 Summary of ejecta kilonova signatures 80

6 Non-thermal emission from BNS mergers 83
6.1 Overview of afterglow modeling methods 83
6.1.1 The dynamical evolution of a blast wave 83
6.1.2 Electron distribution 85
6.1.3 Synchrotron emission 86
6.1.4 Relativistic effects 86
6.2 `PyBlastAfterglow` 87
6.2.1 Method validation 89
6.3 Kilonova afterglow and changes in GRB170817A 91

7 Discussion and Conclusions 95

A BNS ejecta and disk mass statistics 101
A.1 Method 101

A.2 Analysis of dynamical ejecta . . . 103
  A.2.1 Dynamical ejecta mass . . . 103
  A.2.2 Mass-averaged velocity . . . 107
  A.2.3 Electron fraction . . . 109
  A.2.4 Root mean square half-opening angle . . . 110
A.3 Remnant disk . . . 111
A.4 Tables with fitting coefficients . . . 115

Bibliography **121**

Abbreviations and Notation

We employ the geometric units, $c = G = \mathrm{M}_{\odot} = 1$, unless specified otherwise. In several cases we write c, and $\mathrm{M}_{\odot}$ explicitly for clarity.

The following abbreviations are used (they are also introduced in the text at their first appearance):

ADM	Arnowitt, Deser and Misner
AGN	active galactic nucleus
BH	black hole
BNS	binary neutron star
CBM	circumburst medium
CCSN	core-collapse supernova
DE	dynamical ejecta
EATS	equal time arrival surface
EFE	Einstein's field equations
EM	electromagnetic
EOS	equation of state
EOB	effective-one-body
FIR	far infrared
GR	general relativity
GRB	gamma-ray burst
GRHD	general-relativistic hydrodynamics
GRLES	general-relativistic large-eddy simulation
GRMHD	general-relativistic magnetohydrodynamics
GW	gravitational wave
HD	hydrodynamics
HMNS	hyper-massive neutron star
IR	infrared
ISM	interstellar medium
IVP	initial value problem
JWST	James Webb Space Telescope
kN	kilonova
LC	light curve

LES	large-eddy simulation
LF	Lorentz factor
LIGO	Laser Interferometer Gravitational-Wave Observatory
LOS	line of sight
LTE	local thermodynamic equilibrium
MHD	magnetohydrodynamics
MF	magentic field
MM	multi-messenger
MNS	massive neutron star
MP	metal-poor
MRI	magnetorotational instability
NIR	near-infrared
NR	numerical relativity
NRN	nuclear reaction network
NS	neutron star
NSBH	neutron star-black hole
NSE	nuclear statistical equilibrium
ODE	ordinary differential equation
PC	prompt collapse
PDE	partial differential equation
PN	post-Newtonian
RHS	right hand side
RMF	relativistic mean-field
RMS	root mean square
RR	reaction rate
SGRB	short gamma-ray burst
SMNS	supra-massive neutron star
SN	supernova
SWW	spiral-wave winds
TOV	Tolman-Oppenheimer-Volkoff

I dedicate this work to my parents, Sergey and Anna Nedora,
whose love and support have never abandoned me

Chapter 1

Introduction

At the end of their evolution, pairs of massive stars undergo supernovae (SNe) explosions, leaving a pair of compact objects orbiting each other, if the progenitors were sufficiently massive. Of particular interest is a pair of neutron stars (NSs), compact, heavy objects sustained against gravitational collapse by the neutron degeneracy pressure. The theory of general relativity (GR) predicts that the orbit of these NSs shrinks as the system loses energy and angular momentum to gravitational waves (GWs). The stars inspiral until they merge at the last orbit.

The high compactness of NSs leads to an energetic, explosive merger, where a small fraction of NS matter is ejected from the system at mildly relativistic velocities. Additionally, the massive post-merger remnant and gravitationally bound matter surrounding it are subjected to complex dynamical interactions, weak processes and magnetically induced turbulence, that might cause further matter outflows. This makes binary neutron star (BNS) mergers strong contributors to the cosmic chemical evolution. The matter ejected at/after mergers, *i.e.*, ejecta, has unique properties rarely found in other astrophysical sites. Specifically, the abundance of free neutrons allows for the so-called rapid neutron capture process (r-process). The r-process is responsible for the production of the heaviest elements in the Universe: lanthanides and actinides.

The wide range of possible types and properties of ejecta leads to a similarly broad range of possible electromagnetic (EM) counterparts to BNS mergers. For instance, heavy elements produced via r-process nucleosynthesis eventually decay, powering the quasi-thermal EM counterpart, kilonova (kN), that can be observed from days to weeks after the merger. Additionally, BNS mergers are expected to produce powerful jets that can be observed as short gamma-ray bursts (SGRBs), whose afterglow lasts for hundreds of days. Furthermore, expanding into the interstellar medium (ISM), mildly relativistic ejecta is expected to generate non-thermal afterglow emission that can be observed years after a merger. Together with GW emission, these signals allow us to study the processes occurring at mergers in great detail. Studies of BNS mergers are crucial for investigating the origin of SGRBs and cosmic chemical evolution. Perhaps most importantly, they provide unique constraints on the theory of gravity and properties of matter at densities many times that of the nuclear saturation.

In August 2017, the first BNS merger was observed as a source of GWs by Laser Interferometer Gravitational-Wave Observatory (LIGO)/Virgo, GW170817. The unprecedented EM follow-up campaign, spanning hundreds of observatories across the world, led to the identification of the merger EM counterparts: kN, AT2017gfo and SGRB, GRB170817A (Abbott et al., 2017a; Abbott et al., 2017c; Abbott et al., 2019b). Notably, the observations continue to this day (Hajela et al., 2021).

Studies of GWs from GW170817 together with its EM counterparts (so-called multi-messenger (MM) studies) allowed to put constraints on the properties of matter at densities several times that of the nuclear matter, and investigate astrophysical implications of BNS mergers (Abbott et al., 2017b; Villar et al., 2017a; Hajela et al., 2019; Radice et al., 2019).

The complexity, non-linearity, non-stationarity and multidimensionality of physical processes operating at BNS mergers on a wide range of scales of length and time imply that self-consistent, quantitative studies are only possible with numerical simulations (Sekiguchi et al., 2011; Wanajo et al., 2014; Palenzuela et al., 2015; Foucart et al., 2016b; Radice, 2017; Fujibayashi et al., 2018; Radice et al., 2018a). These simulations, performed with numerical relativity (NR) codes that took years or even decades to develop and test, are very computationally expensive, rare, and require detailed post-processing and analysis. Moreover, the self-consistent modeling of a BNS merger and its EM counterparts is still beyond the reach of modern methods. Generally, the short-term (hundreds of milliseconds) evolution of the merger itself is handled with NR codes while the nucleosynthesis and EM emission are computed after, in postprocessing.

The main goal of this thesis is to strengthen the link between the ab-inito numerical relativity simulations of BNS mergers and their EM signatures, and in doing so, provide better constraints on the properties of GW170817 and ultimately, the NS equation of state (EOS). We expand upon this at the end of this Chapter, after we introduce the necessary concepts and discuss the current state of the field.

1.1 Theoretical picture of BNS mergers

In this section we provide a brief summary of the current picture of BNS mergers, which has been largely derived from NR simulations. We also overview their impact on the galactic chemical evolution, and their EM counterparts. The section is largely based on the recent reviews from different leading groups working on BNS merger simulations (Shibata et al., 2019; Bernuzzi, 2020; Radice et al., 2020) and their EM signatures (Kumar et al., 2014; Fernández et al., 2016; Metzger, 2020). For the sake of brevity we omit most of the technical details, and we refer the interested reader to the aforementioned reviews and references therein.

1.1.1 Inspiral

The inspiral phase of a BNS system is primarily governed by the emission of GWs. Several approximations exists to describe this phase. When stars are sufficiently far apart, the post-Newtonian (PN) approximation to GR (the expansion in υ/c, with $\upsilon/c \ll 1$, υ being the speed of matter) can be used. Another approximation of the two-body dynamics in GR is the effective-one-body (EOB) formalism, which is a Hamiltonian formalism, applicable to all stages of the binary evolution. The latter has the advantage of taking into account the finite size of NSs, *i.e.*, how the gravitational field of one star affects another. These are the so-called tidal effects. Their description involves the stars' dimensionless relativistic Love numbers (Binnington et al., 2009; Damour et al., 2009b) which, if the stars are sufficiently far apart, can be computed by considering stationary perturbations of a spherical relativistic star, *i.e.*, solving the stellar structure, Tolman-Oppenheimer-Volkoff (TOV) equations in GR. These Love numbers carry the imprint of NS EOS on the BNS dynamics. The inclusion of tidal effects manifests as a faster inspiral and merger at higher frequencies of GWs (Damour et al., 2010). The effects of tides appear in GW waveform calculations as radiation reaction complimenting the conservative dynamics of the binary (Damour et al., 2009a).

Discussing the tidal effects, it is convenient to introduce the reduced tidal parameter (Favata, 2014) as,

$$\tilde{\Lambda} = \frac{16}{13}\frac{(M_A + 12M_B)M_A^4\Lambda_A}{M^5} + (A \leftrightarrow B)\,, \tag{1.1}$$

where $\Lambda_i \equiv 2/3\, C_i^{-5} k_i^{(2)}$ are the quadrupolar tidal parameters, $k_i^{(2)}$ are the dimensionless gravitoelectric Love numbers (Damour et al., 2009b), $C_i \equiv GM_A/(c^2 R_A)$ are the

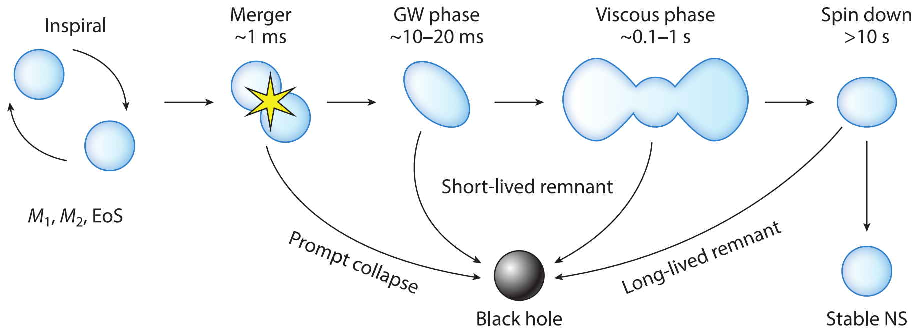

FIGURE 1.1: Schematic picture of a BNS merger with relative timescales. After the inspiral NSs merger forming a massive object, the early evolution of which is governed primarily by hydrodynamics and by GW emission. If a black hole (BH) does not form after $\sim 10-20\,\mathrm{ms}$, GW emission subsides and other physical processes start affecting the evolution. These processes include angular momentum redistribution (due to viscous effects) and neutrino emission. This phase proceeds on a timescale of seconds, but can be interacted at any point by a BH formation. On even longer timescale the postmerger remnant continues to spin down due to magnetohydrodynamics (MHD) effects. (Adapted from Radice et al. (2020)).

compactness parameters, and $i = A, B$. Here A, B subscripts are used to label individual stars with individual gravitational masses M_A and M_B, baryonic masses as $M_{b\ A}$ and $M_{b\ B}$. The total mass is $M = M_A + M_B$, and the mass ratio $q = M_A/M_B \geq 1$. Masses and velocities are given in units of $\mathrm{M}_\odot$ and c, respectively.

From the analysis of GWs, GW170817 was interpreted as a BNS merger with total mass of $\simeq 2.7\,\mathrm{M}_\odot$, chirp mass $\mathcal{M} = ((M_A M_B)^{3/5}/(M_A + M_B)^{1/5}) = 1.186(1)\,\mathrm{M}_\odot$, mass ratio $q \in [1, 1.34]$ and $\tilde{\Lambda} \simeq 300$ (with an upper bound of ~ 800) (Abbott et al., 2017c; Abbott et al., 2019a,b).

1.1.2 Merger and post-merger

At the end of the inspiral, NSs merge. The system's subsequent evolution can take one of the possible trajectories depicted in Fig. 1.1. Overall, the early post-merger phase is charaterized by strong GW emission and hydrodynamic effects. On a longer timescale, MHD stresses contribute to angular momentum redistribution, while neutrino emission alters the matter composition and cools it. If a BH does not form, the MHD torques and residual GW emission spin down the NS remnant.

More specifically, the dynamics of the system at merger is governed by the star's orbital motion, and more compact stars (with lower $\tilde{\Lambda}$), experience more violent mergers. At collision, the NSs cores plunge into the lower density matter of the companion, squeezing past each other and inducing the first wave of gravity-driven compression.

The maximum values of temperatures and densities are reached at this point (Perego et al., 2019). As nuclear and centrifugal forces start to dominate, the cores bounce back until gravity takes over once again. This is referred to as core bounce (*e.g.* Radice et al., 2018a).

While shocks do form at the remnant NS surface, inside the remnant the speed of sound is too high for shock formation. There, matter remains cold throughout the merger with the exception of the interface between two merged cores, where compression and shear dissipation raises the temperature to $\mathcal{O}(100\,\mathrm{MeV})$.

The newly born NS remnant is not hydrodynamically stable. Its dynamics are characterized by $m = 2$ bar- and $m = 1$ one-armed- deformations (*e.g.* Radice et al., 2016b). Notably, the former leads to the strong GW emission in $\sim 10 - 20$ ms post-merger. The backreaction from the energy and angular momentum loss dumps the $m = 2$ mode efficiently and GW emission subsides. This phase of evolution is sometimes referred to as the GW-dominated post-merger phase.

After the emission of GWs subsides, the NS remnant may still have an excess in angular momentum and gravitational mass with respect to a cold, rigidly rotating equilibrium with the same baryonic mass (Radice et al., 2018c). In other words, such an object is supported against collapse artificially, *e.g.*, by differential rotation. Its subsequent evolution proceeds towards a more axisymmetric configuration close to the limit that a rigidly rotating NS can have. However, it can be interrupted at any moment by a BH formation as shown in Fig. 1.1. Depending on the lifetime of post-merger remnants, *i.e.*, whether the collapse occurred during the GW-dominated phase or not, we distinguish *short-lived* and *long-lived* ones respectively.

The matter outside the bouncing cores, lifted by tidal torques and squeezed out at the collisional interface, forms a disk (or a torus). This is gravitationally bound matter that can be distinguished from the remnant by a sharp change in hydrodynamic quantities. The evolution of the disk as it interacts with the NS remnant consists of a quasi-adiabatic expansion of its outer layers and a cooling of the inner regions. Additionally, the dynamical instabilities in the remnant inject energy and angular momentum into the disk, – a process that manifests itself in the form of spiral waves, propagating through the disk.

Within the conditions of the post-merger, weak processes take place. Together with spiral density waves they cool and periodically shock the fluid, bringing the disk to a configuration with an overall smooth temperature profile and quasi-Keplerian orbit. Notably, if a BH does form, the densest part of the disk is accreted on a dynamical timescale, shrinking the disk and reducing its total mass by half (Perego et al., 2019).

Whether ordered, large-scale magnetic fields (MFs) can form in a post-merger environment via dynamo processes is presently unknown. They are important in producing polar collimated outflows, jets (Bucciantini et al., 2012; Ruiz et al., 2016) and mildly relativistic outflows (Metzger et al., 2018a; Fernández et al., 2019). Random magnetic fields are also relevant for the post-merger evolution, as they generate stresses, enhancing angular momentum transport. Presently, these processes are not well understood, as seed MHD instabilities operate on small scales (centimeters) and cannot be resolved in global MHD BNS merger simulations.

The primary cooling mechanism in the post-GW-dominated phase is the emission of neutrinos produced in hot, dense areas of the disk and remnant, and that are able to escape (Eichler et al., 1989; Rosswog et al., 2003b; Sekiguchi et al., 2011). The neutrinos are radiated on the diffusion timescale (Perego et al., 2014). Within the remnant NS, neutrinos are in a weak and thermal equilibrium with matter. There, the production of electron neutrinos, ν_e, is suppressed by degeneracy, and electron antineutrinos, $\bar{\nu}_e$, dominate. Within the optically thick environment of the remnant, the effect of these neutrinos on the remnant evolution was found to be comparatively weak (Foucart et al., 2016b; Perego et al., 2019). Within the disk, however, the optical depth for neutrinos is $\simeq$1, allowing neutrinos to diffuse out on a timescale of milliseconds, lowering the disk temperature (Beloborodov, 2008).

During the early post-merger, the luminosity of the electron antineutrinos exceeds that of the electron neutrinos, as the free neutrons are abundant in the disk and the absorption opacity for ν_e exceeds that of $\bar{\nu}_e$. The maximum values of fluid temperature in the disk are reached within the spiral waves. During the post-merger evolution, the disk expands and cools via neutrino emission. High temperatures lead to electron-positron pair creation, facilitating positron capture by free neutrons in the disk. The average energy of a particle is large, close to the mass difference between a neutron and a proton (Perego et al., 2019). In combination with the high ν_e and $\bar{\nu}_e$ luminosities, the large number of available positrons leads to an increase in the average charge per baryon, *i.e.*, electron fraction Y_e[1], of the fluid in relation to the initially neutron-rich material (Qian et al., 1996). This process is called deleptonization.

Additionally, a NS remnant itself is a major emitter of neutrinos. The neutrino irradiation of the surrounding area alters its composition, as neutrons and protons absorb the neutrinos, $n + \nu_e \rightarrow p + e^-$ and $p + \bar{\nu}_e \rightarrow n + e^+$. This drives the neutron and proton fraction towards an equilibrium, raising the Y_e. If a NS remnant collapses to a BH, the main source of neutrinos shuts down.

---

[1] $Y_e = 1/(1 + N_n/N_p)$, where N_n and N_p are the total proper number density of neutrons and protons respectively

The post-merger dynamics and, ultimately, the remnant's fate, depend strongly on the NS EOS, and especially on its high density part. The NS EOS is currently not well constrained. For instance, it is unknown whether during the merger new particle species can form, changing the EOS (*e.g.* Vidana et al., 2011; Fore et al., 2020). The EOS effects on the system's dynamics can be quantified with $\tilde{\Lambda}$, and it is common to discuss the EOS in this context as being *softer* or *stiffer* if the $\tilde{\Lambda}$ is larger or smaller (we discuss this more in Sec. 2.3). Another quantity describing the EOS is the maximum supported mass of a non-rotating NS, $M_{\rm max}^{\rm TOV}$ (Shibata, 2016). Thus, the remnant fate depends on the binary parameters, $\tilde{\Lambda}$, $M_{\rm max}^{\rm TOV}$, and finite temperature and non-equilibrium[2] composition effects.

BH formation directly at merger is usually referred to as prompt collapse (PC). The conditions for it are not well understood. Simulations show that in equal mass binaries, PC occurs if the total mass exceeds a certain fraction, $1.3-1.7$, of the $M_{\rm max}^{\rm TOV}$ (Shibata et al., 2005, 2006; Hotokezaka et al., 2011; Bauswein et al., 2013a).

A remnant that does not undergo PC is a massive NS, temporarily supported against collapse by fast rotation (Baumgarte et al., 2000; Rosswog et al., 2003a; Shibata et al., 2006; Bernuzzi et al., 2016). Its lifetime depends on the EOS, finite temperature effects and viscosity, and is currently very uncertain. A commonly adopted classification based on the properties of equilibrium models (neglecting the dynamical, finite temperature, and magnetic effects), *i.e.*, considering only $M_{\rm max}^{\rm TOV}$ and $M_{\rm max}^{\rm RNS}$[3], distinguishes between (i) hyper-massive neutron star (HMNS) if $M > M_{\rm max}^{\rm RNS}$, (ii) supra-massive neutron star (SMNS) if $M_{\rm max}^{\rm TOV} < M < M_{\rm max}^{\rm RNS}$, and (iii) stable massive neutron star (MNS) if $M < M_{\rm max}^{\rm TOV}$ (*e.g.* Baumgarte et al., 2000). A HMNS is supported by differential rotation that viscosity reduces with time, and it is expected to collapse to a BH. A SMNS can avoid the collapse even after reaching rigidly rotating configuration. The lifetimes of a HMNS and a SMNS depend on the efficiency of mass and angular momentum loss due to, *e.g.*, GWs and massive winds (Radice et al., 2018c).

---

[2] Beta-equilibrium is the condition when $\mu_n = \mu_p + \mu_e$, where μ_n, μ_p, and μ_e are the chemical potentials of neutrons, protons and electrons respectively.

[3] $M_{\rm max}^{\rm RNS}$ is the maximum mass of a rigidly rotating NS (no differential rotation) supported by zero-temperature (cold) EOS. Also sometimes referred as mass-shedding limit.

1.1.3 Ejecta

Tidal interactions and shocks exerted upon NSs at merger trigger the ejection of material on a dynamical timescale. This is called dynamical ejecta (DE) (*e.g.* Bauswein et al., 2013b; Hotokezaka et al., 2013a; Radice et al., 2016a, 2018a), composed of a tidal and shocked components as follows. Shortly before and during a merger, the outer parts of the NSs, opposite to the collisional interface, are stripped away by tidal torques and centrifugal forces, forming the tidal component of DE. This is more massive in binaries with a larger mass ratio and is maximum in those that experience tidal disruption (*e.g.* Radice et al., 2018a; Bernuzzi et al., 2020). Overall, the tidal ejecta component is mostly equatorial and its velocity is related to the NSs' velocity at merger. NR simulations suggest that the ejecta mass and velocity lie in $(10^{-4} - 10^{-2})\,\mathrm{M}_{\odot}$ and $(0.1 - 0.3)\,c$ respectively (Bauswein et al., 2013b; Hotokezaka et al., 2013a; Sekiguchi et al., 2016; Radice et al., 2018a). When NSs' cores collide and bounce, shocks propagate outwards, inducing matter ejection. Additionally, a small amount of material at the NSs' collisional interface is shock-heated and launched into the polar direction. This comprises the shocked component of DE (Bauswein et al., 2013b; Radice et al., 2018a). It is more massive and faster if NSs are more compact and they collide at higher velocities (*e.g.* Radice et al., 2018a).

DE has a broad distribution in terms of composition, velocity and mass, that is dependent on the parameters of the binary and NS EOS. However, due to large numerical and systematic uncertanties, the relation between the binary parameters and ejecta properties is still largely unconstrained (Dietrich et al., 2017b; Krüger et al., 2020).

NR simulations show that within the velocity distribution of DE, there is $\sim(10^{-6} - 10^{-5})\,\mathrm{M}_{\odot}$ of matter ejected at $\sim 0.8\,c$ (Metzger et al., 2015; Hotokezaka et al., 2018; Radice et al., 2018a,d), due to shocks launched at core bounces (Radice et al., 2018a). This sometimes referred to as the fast tail of DE.

As the disk expands and cools, the recombination of nucleons into alpha particles starts to take place. The energy released in recombination might be sufficient for the outermost layers to become unbound, leading to a massive outflow (Beloborodov, 2008; Lee et al., 2009; Fernández et al., 2013). Furthermore, strong neutrino irradiation can drive low-mass outflows, so-called neutrino-driven winds (ν-driven winds; Dessart et al. (2009), Perego et al. (2014), and Just et al. (2015)). Winds and outflows occurring on a secular timescale sometimes referred to as secular ejecta.

The presence of the remnant modifies properties of the ejected material by means of neutrino irradiation (Fernández et al., 2016), providing a possibility to infer the nature of the remnant from EM observations. Modeling this process, however, requires very long-term 3D ab-initio BNS merger simulations with complete physics, that are currently unavailable. Overall, analytical estimates and simulations with various approximations show that up to $\sim$40% of the disk can be ejected via viscous processes with a typical velocity $\lesssim$0.1 c (Radice et al., 2018c; Fernández et al., 2019). The ejecta is expected to be relatively slow and neutron-rich.

1.1.4 *R*-process nucleosynthesis

Nuclides with atomic number $A \geq 56$ cannot be synthesized via nuclear burning due to their large Coulomb barriers. They are produced via neutron capture processes (Burbidge et al., 1957). The maximum A of a nuclide is limited by its binding energy, Q_n, as at $Q_n \simeq 1\,\mathrm{MeV}$ photodisintegration starts breaking nuclides apart. The place in the parameter space of temperature and density where this occurs is called *neutron drip line* (Rolfs et al., 1988).

Nuclides produced via neutron capture are generally unstable to β-decay, and depending on whether the timescale for the decay is slower or faster than the timescale of neutron capture, one can distinguish between rapid and slow processes respectively, where the former is called r-process and the latter is called s-process. The s-process moves along the valley of stability[4], while the r-process moves along the neutron drip line.

When a nuclide reaches a closed neutron shell configuration, the cross-section for the subsequent neutron capture shrinks, and capture processes suspend until several β-decays take place. This results in an overproduction of nuclides that are located at the intersection between the neutron drip line and the closed neutron shell for the r-process. This manifests as "peaks" in the final abundance pattern at A corresponding to these configurations. Closed shell nuclides are located at $N = 50,\ 82,\ 126$ and corresponding abundance peaks $A = 80,\ 130,\ 194$ for r-process (see *e.g.*, Arnould et al. (2007)).

The outcome of the r-process nucleosynthesis depends strongly on the hydrodynamic properties of matter and its composition. A particularly important quantity is the ratio between the number of free neutrons and the number of seed nuclides: the neutron-to-seed ratio. At high entropy, where the neutron-to-seed ratio is high, even if seed nuclei are light, *full* (or *main*) r-process can occur, producing elements at abundance peaks at $A = 130$ and 195. At low entropy, the r-process is jugged as there are not many free neutrons available, but the presence of very heavy seed nuclei still allows for the nucleosynthesis to proceed. At high Y_e, where ejecta is less neutron rich, the full r-process no longer occurs as there are not enough neutrons per seed nucleus to reach the third peak. The nucleosynthesis that results in the production of only the lightest r-process nuclei, up to $A \sim 125$, is generally referred as *weak* r-process. However, at high entropy and low Y_e the 3rd peak elements can be synthesized because, while there are few seed nuclei, the neutron-to-seed ratio is high. It was pointed out that the main quantity defining the final abundances is electron fraction, Y_e (Lippuner et al., 2015).

---

[4] The valley of stability is the region in nuclides chart where nuclides are stable to radioactive decay based on their binding energy.

Conditions for the r-process can be achieved in different astrophysical sites, *e.g.*, certain types of SNe and BNS mergers where very neutron rich (*i.e.*, low Y_e fraction) conditions can be reached (Mathews et al., 1990; Thielemann et al., 2011; Lippuner et al., 2015; Siegel, 2019).

The r-process is expected to take place in different types of ejecta from BNS mergers. In ν-driven winds the neutrino irradiation can significantly increase the electron fraction, which, depending on the ejecta velocity, can reach $\leq$0.45 (Qian et al., 1996). At this point the equilibrium sets in between the ejecta and neutrinos. High electron fraction implies that only light elements will be produced. The numerical studies indeed support this picture (Dessart et al., 2009; Perego et al., 2014; Just et al., 2015; Martin et al., 2015; Foucart et al., 2016a).

The bulk of the ejecta from BNS mergers is expected to come in the form of viscous- and recombination-driven winds. Studies have shown that these ejecta have a broad distribution of Y_e, and the r-process nucleosynthesis within it produces light as well as heavy elements (*e.g.* Just et al., 2015; Wu et al., 2016; Fernández et al., 2019). The production of very heavy r-process elements, however, might be supressed in these ejecta if a long-lived NS remnant is present (Metzger et al., 2014; Lippuner et al., 2017a).

Regarding the SNe, winds driven by strong neutrino fluxes from the hot, deleptonized core (Qian et al., 1996) were suggested as a promising site of r-process nucleosynthesis (Woosley et al., 2002; Wanajo, 2006). However, high Y_e found in such winds does not allow for the full r-process and only “light” heavy nuclide, up to $A \sim 130$, can be synthesized (*e.g.* Qian et al., 1996; Martinez-Pinedo et al., 2012; Wanajo, 2013) A full r-process can be achieved in so-called magnetorotationally driven core-collapse supernova (CCSN), a rare type of CCSN with a rapidly spinning strongly magnetized core, initiated by magnetorotational instability (MRI) and accompanied by the formation of a collimated bipolar jet (Wheeler et al., 2000; Shizuka et al., 2003; Burrows et al., 2007; Mösta et al., 2014; Mösta et al., 2015; Siegel, 2019). Conditions within such a jet were found to be suffient for full r-process nucleosynthesis (Winteler et al., 2012; Nishimura et al., 2015).

Under very neutron-rich conditions, nuclides beyond $A = 300$ can be produced. Being unstable to fission, they decay into seed nuclides shortly after formation. However, before they reach the valley of stability, neutron capture occurs again, and the cycle repeats. This is so-called *fission cycling*. It is maintained as long as there are free neutrons, after which nuclides decay for the last time, forming a remarkably robust abundance pattern independent from the number of cycles (and thus from the exact matter conditions) (see Figure 4 in Korobkin et al. (2012)).

There is no consensus yet on what is the main source of r-process material in the Universe. Observed r-process abundances in metal-poor (MP) stars, formed early in the Galactic history, point towards a source that was active in the early Universe, which is in tension with the long, $10^6 - 10^9$ years, delay time required for compact object inspiral (De Donder et al., 2004; Dominik et al., 2012). This estimate, however, depends strongly on the uncertain common envelop evolution phase of the massive binary (progenitors) (*e.g.* Dominik et al., 2012). Observations of certain ultra-faint dwarf galaxies (UFGs) suggest that stars there have been enriched by rare, high-yield events (*e.g.*, UFG Reticulum II showed abundances similar to solar, while other UFG galaxies show $2 - 3$ times lower abundances) (Ji et al., 2016). Earth crust and meteorites ^{244}Pu studies also point towards rare, high-yield events (Wallner et al., 2015; Tsujimoto et al., 2017). This estimation has been confirmed with models of galactic mixing (Hotokezaka et al., 2015b). It is, however, difficult to explain the observed uniform distribution of r-process elements in the Galaxy with such events (Argast et al., 2004). Population synthesis models have indicated that with a contribution from magnetorotationally driven CCSNe, the compact object mergers can account for the observed distribution (Cescutti et al., 2015; Ishimaru et al., 2015; Voort et al., 2015; Wehmeyer et al., 2015).

1.1.5 Kilonova

Li et al. (1998) suggested that radioactive decay of material enriched with r-process elements, ejected in BNS or neutron star-black hole (NSBH) mergers, can power an

EM transient. The authors showed that, contrary to the normal SNe, the ejecta would quickly become transparent to its own emission, which would reach its peak on a timescale of around a few days. The main difficulty in this pioneering work was the lack of nucleosynthesis models to estimate the radioactive heating in ejecta.

The first self-consistent estimation of heating rates based on nuclear reaction network (NRN) calculations of the r-process in ejecta, were carried out by Metzger et al. (2010). The authors showed that based only on DE, the EM transient is $\sim 10^3$ times brighter than Novae – hence, the term kilonova was coined.

The main components of the kN modeling include: (i) ejecta geometry and properties, (ii) composition of the expanding ejecta and its optical opacity, (iii) dominant sources of energy within ejecta and how efficiently this energy thermalizes.

Regarding opacity, there are several sources of opacity that affect photons with different energies. These include: (i) free-free transitions, (ii) bound-bound transitions, (iii) certain optically thick lines, (iv) ejecta clumping, (v) ejecta re-ionisation by *e.g.*, high energy photons from the central engine. An additional complication in opacity calculations arises from the fact that the ejecta is rapidly expanding, which implies that the matter "sees" incoming radiation as Doppler shifted. When considering frequency-integrated intensities, frequency independent, gray opacities are employed. For example, Plank mean opacity is used when computing integrated thermal emission for an optically thin plasma. The calculation of mean opacities, however, still requires complex atomic models. Another approach to account for the matter dynamics is to consider line expansion opacity, often estimated under the Sobolev approximation (Pinto et al., 2000). This method was applied to kNe modeling by Barnes et al. (2013) and Tanaka et al. (2013). However, it becomes increasingly inaccurate, as lines broaden *i.e.*, if the line spacing of strong lines becomes comparable to the intrinsic thermal line width (Kasen et al., 2013; Fontes et al., 2015; Fontes et al., 2017).

Generally speaking, calculations of kN emission are complicated by the lack of experimental data and numerical models of the optical opacity of matter enriched with singly and doubly ionized heavy r-process elements. Iron-group gray opacities were initially considered (Roberts et al., 2011), but were later found to severely underestimate those of lanthanides and actinides with their complex atomic structures (Kasen et al., 2013; Tanaka et al., 2013). Higher opacities shift light curve peak time by $\sim$1 week (Barnes et al., 2013) and shift the spectral peak from optical/ultraviolet (UV) to near-infrared (NIR).

The heating in ejecta occurs through a combination of β- and α-decays, and fission

(Metzger et al., 2010; Barnes et al., 2016; Hotokezaka et al., 2017). Decay products then thermalize with a certain efficiency that depends on interactions between them and the thermal plasma. Notably, neutrinos escape the ejecta freely. Very high energy photons (gamma rays), are also free after about ∼1 day as the Klein-Nishina opacity decreases (Barnes et al., 2016; Hotokezaka et al., 2017). The α and β particles, however, interact efficiently with the matter via ionization (Barnes et al., 2016) and Coulumb scattering (Metzger et al., 2010). For a fixed energy, α-particles thermalize more efficiently than β-particles. For charged particles, the thermalization processes depend on the magnetic field strength and its configuration (Barnes et al., 2016). Additionally, if actinides are synthesized in the r-process, their decay products, *e.g.*, α-particles, thermalize with high efficiency.

The properties of the kN emission have strong dependency on the properties and geometry of BNS merger ejecta (Metzger, 2020). Describing the complex kN signature, it is common to generalize it into two main components, "blue" and "red", depending on whether the fraction of lanthanides and actinides is low or high. The former corresponds to the high Y_e material that produces emission that peaks in UV/optical bands on a timescale of hours-days, while the latter is related to low-Y_e material that generates the emission peaking on a significantly longer timescale, tens of days, in infrared (IR) and NIR bands (Barnes et al., 2013; Grossman et al., 2014; Lippuner et al., 2015).

Notably, BNS mergers that experience PC are not expected to eject large amounts of material and are generally thought of as being EM-quiet (Bauswein et al., 2017; Margalit et al., 2017). From EM observations of a merger, the fate of the remnant can be inferred, albeit in a model-dependent way.

To model the kN emission robustly, time- and energy-dependent photon radiation transport models are required (Kasen et al., 2017; Tanaka et al., 2017; Bulla, 2019; Miller et al., 2019a). Meanwhile, semi-analytic one- or multi-component spherical kN models are often employed due to their simplicity and high computation speed. Notably, systematic uncertainties in nuclear physics (*e.g.*, mass models, fission fragments and β-decay rates) and atomic physics (*e.g.*, detailed wavelength dependent opacities for r-process elements) enter all the current kN models (Eichler et al., 2015; Rosswog et al., 2017; Gaigalas et al., 2019).

Our understanding of kN has significantly improved after the detection of AT2017gfo (*e.g.* Metzger, 2020). Both "blue kN" and "red kN" were observed, confirming the qualitative picture and implying a diverse composition of the ejected material (*e.g.* Villar et al., 2017a). The presence of EM counterparts strongly disfavors PC in the case of GW170817 (Bauswein et al., 2017; Margalit et al., 2017; Radice et al., 2018b). However, the question of whether it was HMNS or SMNS remains open (Margalit et al., 2017; Ai et al., 2018).

The outflow properties inferred for AT2017gfo using multi-component semi-analytic and 2D radiation transport kN models, including ejecta anisotropy and cross-component irradiation, are broadly compatible with the results from merger simulations (*e.g.* Kawaguchi et al., 2018). However, certain disagreements remain. For instance, the required amount of low-Y_e, material (which is somewhat lower if sophisticated radiation transport kN models are considered), is in tension with NR BNS merger simulations (Sekiguchi et al., 2016; Perego et al., 2017; Kawaguchi et al., 2018; Siegel, 2019). Moreover, it is difficult to reproduce the early blue emission that requires low opacity and massive ejecta, that is not generally found in NR simulations (Fahlman et al., 2018). Notably, the early blue component can be explained by the emission arising from the interaction between a relativistic jet and the ejecta (Lazzati et al., 2017; Piro et al., 2017; Bromberg et al., 2018). However, simulations show that successful jets do not deposit a sufficient amount of thermal energy in ejecta for this mechanism to work (Duffell et al., 2018). Other possibilities include the presence of highly magnetized winds (Metzger et al., 2018b; Fernández et al., 2019), or the presence of the so-called viscous dynamical ejecta (Radice et al., 2018d). These explanations, however, require the development of large-scale strong magnetic fields.

Prior to AT2017gfo, there were other kN candidates based on the detection of SGRBs, with infrared excess *e.g.*, GRB130603B, (Berger et al., 2013; Tanvir et al., 2013), GRB060614 (Jin et al., 2015; Yang et al., 2015), GRB050709 (Jin et al., 2016). However the exact nature of observed signals was not well constrained.

1.1.6 Non-thermal afterglows

Observed since 1967, gamma-ray bursts (GRBs) are irregular pulses of gamma-ray radiation with broken power-law (non-thermal) spectrum, peaking at KeV-MeV (Meegan et al., 1992; Band et al., 1993; Kouveliotou et al., 1993). With respect to the duration, GRBs are split into two categories: SGRBs that last $\leq 2\,\mathrm{s}$, and long GRBs that last $\gtrsim 2\,\mathrm{s}$. It is generally accepted that the latter are the result of the collapse of massive $\geq 15\,M_{\odot}$ stars, while the former, at least in part, are attributed to mergers of compact objects. However, the exact physical origin of different duration GRBs is not fully understood.

GRBs are distant events, most of which were localized to outside the Local Group (*e.g.* Mao et al., 1992; Piran, 1992; Fenimore et al., 1993). Particularly useful for distance estimations are the observations of GRB afterglows (fading X-ray, optical and radio emission), that allow the estimation of redshift (*e.g.* Costa et al., 1997; Frontera et al., 1998).

Analysis of the multi-wavelength afterglow data of GRBs (*e.g.* Panaitescu et al., 2003) suggested that the mechanism behind the afterglow emission is non-thermal. Specifically, the afterglow is attributed to the synchrotron emission coming from the external forward-shock, which forms when GRB-ejecta sweeps-up the ISM medium[5] (Rees et al., 1992; Meszaros et al., 1993; Paczynski et al., 1993; Meszaros et al., 1997).

The origin of SGRBs was first linked to elliptical galaxies with dominant older stellar population (*e.g.* Gehrels et al., 2005; Nakar, 2007), and thus with BNS mergers. A more direct evidence came with the detection of SGRB, GRB170817A, (Alexander et al., 2017; Troja et al., 2017; Hajela et al., 2019), detected by the space observatories Fermi (Ajello et al., 2016) and INTEGRAL (Winkler et al., 2011), one of the counterparts of GW170817 (Abbott et al., 2017c). However, while the GRB170817A has confirmed that BNS mergers are responsible for at least some SGRBs, it was dimmer than any other event of its class. The unusual signature of GRB170817A is now commonly attributed to the fact that it was a structured jet[6], which was also observed off-axis (*e.g.* Ghirlanda et al., 2019). The GRB170817A late emission, the afterglow, provided information on the energetics of the event and on the properties of the ISM (*e.g.* Hajela et al., 2019).

In addition to the GRB beamed emission, more isotropic non-thermal emission is expected to arise from mildly relativistic ejecta expanding into the ISM (Nakar et al., 2011). Called kN afterglow, it is expected to peak in radio band and continue to be observable on a time scale of years after a merger, providing a source of information that is largely free from uncertainties in the nuclear and atomic physics of kN models. Notably, all ejecta components contribute to the emission, but depending on the ejecta velocities and kinetic energy, the brightness in different frequencies varies. The mechanism behind this emission is phenomenologically similar to the one responsible for the GRB afterglow. Specifically, as various ejecta components interact with each other and with the ISM, a long-lived blast wave is generated. The formed shock, propagating upstream, amplifies random magnetic fields and accelerates electrons that subsequently emit synchrotron radiation (Kumar et al., 2014).

---

[5] The specific indications for the non-thermal origin of the emission are the power law decay of light curves, and the power-law spectrum.

[6] A structured jet, contrary to a top-hat jet, has an angular dependency of the matter energy and Lorentz factor. Such structure is believed to appear when a jet drills its way through the merger ejecta (Lamb et al., 2017).

As NR simulations showed the presence of mildly relativistic ejecta, *e.g.*, from core bounces, such emission was studied in previous works (*e.g.* Piran et al., 2013; Hotokezaka et al., 2015a, 2018; Radice et al., 2018a) and was expected in the case of GW170817 (*e.g.* Kathirgamaraju et al., 2019).

Since $\sim$160 days after the merger the non-thermal emission from GW170817 has been consistent with SGRB afterglow (Hajela et al., 2019; Troja et al., 2020). However, $\simeq$1243 days after the merger, a change in spectral and temporal behaviour of the afterglow was observed. A change that is not compatible with the afterglow from a structured jet. While the exact nature of this change remains at present unclear, one of the possible explanations is the emergence of the kN afterglow[7] (Hajela et al., 2021).

1.2 Aims and organization of this thesis

BNS mergers are at the center of a variety of physical processes in astrophysics. And while significant work has been done to advance our understanding of these events, many fundamental questions remain. The foundation of BNS merger research are NR simulations. However, most BNS NR simulations available in the literature are either short, typically $\lesssim$10 ms post-merger, but with advanced physics (*e.g.* Vincent et al., 2020), or neglect important physics, *e.g.*, neutrino reabsorption and effects of the MF-induced turbulence (*e.g.* Lehner et al., 2016b).

In this thesis we postprocess and analyze a large sample of new NR simulations performed using `WhiskyTHC` NR code. Our simulations include GR, microphysical EOSs with finite-temperature effects, neutrino emission and reabsorption, and effects of MFs on the angular momentum transport. Some of our simulations have been continued till $\gtrsim$100 ms post-merger. All our simulations have chirp-mass, equal to that inferred for GW170817. Postprocessing and analyzing these simulations, computing r-process nucleosynthetic yields, and thermal and non-thermal EM counterparts to mergers, we aim to investigate the following questions:

- What is the evolutionary trajectory of a NS remnant born with an excess in mass and angular momentum with respect to the mass-shedding limit, *i.e.*, HMNS? Does it collapse to a BH?

---

[7] See, however, Troja et al. (2021) for an alternative explanation

- Based on the abundance pattern in ejecta, can BNS mergers be considered the prime source of r-process elements in the Universe?
- How do the statistical properties of DE of our simulations differ with respect to other published models? What is the up-to-date relation between binary parameters and ejecta properties?
- Can the kN produced by ejecta from our long simulations provide better explanations to AT2017gfo?
- Is the kN afterglow from our models consistent with the changing behaviour of GRB170817A afterglow?

Ultimately, we aim to find a possibility for further constraining the properties of GW170817 and NS EOS.

The thesis is organized as follows. In Chapter 2 we provide a brief overview of the methods used to model BNS mergers and implemented in `WhiskyTHC`, and techniques we used to postprocess these simulations. In Chapter 3 we present the results of simulation postprocessing and discuss the post-merger dynamics and ejecta. In Chapter 4 we overview a method to compute r-process nucleosynthesis final abundances in ejecta, and compare these abundances in ejecta from our simulations with solar ones. In Chapter 5 we overview a method to compute kN emission. Then, we apply a previously developed model to ejecta from our simulations and compare the result with observations of AT2017gfo. In Chapter 6 we overview a method to compute synchrotron radiation from ejecta, focusing on particular techniques that we implement numerically. Then we apply our new tool to the ejecta from our simulations and compare the result with the GRB170817A afterglow. Finally, in Chapter 7 we conclude our work and provide an outlook.

Chapter 2

Methods of BNS merger simulations

In this chapter we briefly overview the methods and techniques used to simulate BNS mergers. The chapter is based on the NR monographs by Alcubierre (2008), Baumgarte et al. (2010), and Rezzolla et al. (2013), augmented with more specialized literature on the methods implemented in the NR code `WhiskyTHC`, (Radice et al., 2012, 2016a; Radice, 2017; Radice et al., 2018a; Radice, 2020). As we neither develop nor implement any of these methods, we restrict ourselves to a very general overview. We refer to the aforementioned sources for a more detailed description.

2.1 The $3+1$ formulation of General Relativity

Einstein's field equations (EFE) are a cornerstone of modern cosmology, the physics of NSs and BHs, the emission of gravitational radiation, and many other cosmic phenomena where strong gravity effects are present.

EFE in a covariant form, neglecting the cosmological constant, read

$$G_{\mu\nu} = R_{\mu\nu} - \frac{1}{2} R g_{\mu\nu} = 8\pi T_{\mu\nu} \,, \tag{2.1}$$

where $G_{\mu\nu}$ is the Einstein tensor, $R_{\mu\nu}$ is the Ricci curvature tensor with its trace, $R^{\nu}_{\nu} = R$, $g_{\mu\nu}$ is the metric tensor and $T_{\mu\nu}$ is the stress-energy tensor.

For numerical applications it is desirable to represent Eq. (2.1) as an initial value problem (IVP) where once the initial data is specified at time zero, the evolution can be computed. This is a highly non-trivial task because of the complexity of objects entering Eq. (2.1). One of the common approaches is to perform $3+1$ *decomposition*, where the 4D manifold, representing space-time, is split into a foliation of 3D spacelike hypersurfaces (Gourgoulhon, 2007; Alcubierre, 2008; Baumgarte et al., 2010; Rezzolla et al., 2013).

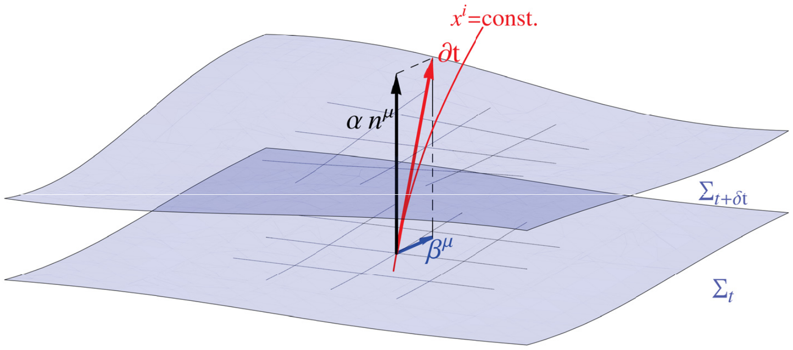

FIGURE 2.1: Visual representation of the 4D manifold $\mathcal{M}$ by 3D hypersurfaces Σ_t. The lapse function α and shift vector β^μ describe the coordinate change between hypersurfaces. (Adapted from Dietrich (2016)).

Eq. (2.1) represents a set of 10 non-linear partial differential equations (PDEs) that can be defined on a whole manifold $\mathcal{M}$ or a domain $\Omega \subset \mathcal{M}$ with the boundary $\partial\Omega$. The initial data is defined on a null hypersurface $\Sigma \subset \mathcal{M}$. The subsequent evolution requires that the foliation $\mathcal{M} = \Sigma \times \mathbb{R}$, depicted in Fig. 2.1, is allowed, or in other words, that the spacetime is strongly hyperbolic.

The transition between the two hypersurfaces, Σ_t and Σ_{t+dt}, where t is a smooth scalar function on $\mathcal{M}$, can be decomposed into a part tangent to the hypersurface Σ_{t+dt} and expressed as a vector, $\vec{\beta}$, and a part normal to the hypersurface Σ_t in the direction of Σ_{t+dt}, $\vec{n}$, as $\alpha\vec{n}$. Then, the vector $\vec{t}$ can be written as $\vec{t} = \alpha\vec{n} + \vec{\beta}$, where α is called *lapse function* and $\vec{\beta}$ – *shift vector*.

In order to describe how the normal to the hypersurface Σ_t changes from point to point, the extrinsic curvature, $\boldsymbol{K}$, is introduced and can be interpreted as the "speed of the $\vec{n}$ during the parallel transport along the hypersurface Σ_t".

To choose a foliation, gauge conditions must be set, *i.e.*, the lapse function and shift vector. The correct choice is crucial for stable evolution (Alcubierre et al., 2003) alongside the well-posedness of the system of PDEs[1].

The choice of the lapse function is referred to as the slicing condition, while the choice of the shift vector is referred to as the spatial gauge condition. In our simulations, so-called "1+log" slicing is used. The name stems from the fact that if $\beta^i = 0$, the integral form of the condition reads as $\alpha = 1 + \log\gamma$, where γ is the trace of the metric on Σ. The condition has the advantages of being singularity avoiding, formulated in the form of hyperbolic equations, and not very expensive numerically (Alcubierre et al., 2003).

---

[1] Well-posedness means that (i) a solution exists, (ii) the solution is unique, (iii) the solution's behaviour changes continuously with the initial conditions.

For the spatial gauge condition our simulations employ the Gamma-driver (Alcubierre et al., 2003; Meter et al., 2006). The requirements for the spatial gauge are similar to those for the slicing condition, namely, hyperbolicity and the minimization of numerical distortions for more stable evolution. It is preferred that a gauge condition tries to decrease the coordinate stretching that occurs in the vicinity of a singularity. The combination of the "1+log" slicing and Gamma-driver is usually referred to as *moving puncture* gauge. Together with the Z4c formulation of EFE (discussed below) it forms a strongly hyperbolic system of equations that can be solved numerically.

The dynamics of the gravitational field is embedded into EFE. Casting EFE, Eq. (2.1), into the 3+1 form results in a system of *evolution* and a system of *constraint* equations. As such, the right hand side (RHS) of Eq. (2.1), the energy-momentum tensor, $T_{\mu\nu}$, in $3 + 1$ form can be written using the spatial projection operator, that decomposes $T_{\mu\nu}$ into its spatial part, $S_{\mu\nu}$, momentum density, S_μ, and the energy density, $E = n^\mu n^\nu T_{\mu\nu}$, measured by an Eulerian observer with the four-velocity n^ν.

The set of constraint equations is derived by utilizing two relations. Gauss (Gauss-Codazzi) equations connect the 3D Riemann tensor on a hypersurface, the 4D Riemann tensor on the manifold, and the extrinsic curvature. Codazzi (Codazzi-Mainardi) equations relate the 4D Ricci tensor to the extrinsic curvature. The derived system of two constraint equations, called *Hamiltonian* and *momentum constraints*, represent a set of elliptic equations that must be satisfied on every hypersurface Σ_i of the foliation. It is, however, possible to show that EFE preserve the constraints, meaning that if they are satisfied at the initial slice Σ_0 they will be satisfied at any time in the future. Constraint equations allow one to construct initial data.

Evolution equations can be derived by expanding the definition of the extrinsic curvature. Together with the constraint equations they form the IVP for EFE and are known as Arnowitt, Deser and Misner (ADM) system of equations (*e.g.* Arnowitt et al., 2008).

It has been shown that the ADM system of equations in its original form is only weekly hyperbolic (Baumgarte et al., 2003). Specifically, it was shown that the numerical errors tend to couple with zero-velocity modes (Alcubierre et al., 2000). In order to address this problem, other formulations of EFE as IVP were proposed.

Our simulations are performed with the Z4c formulation of EFE that was developed in a series of works by Bernuzzi et al. (2010), Ruiz et al. (2011), Cao et al. (2012), Weyhausen et al. (2012), and Hilditch et al. (2013). It is summarized in Hilditch et al. (2013). The idea behind the Z4c formulation is to derive a set of evolution equations that is free from the zero-speed modes of the original ADM and thus strongly-hyperbolic, and which also inherits the constraint violation dampening properties of the original Z4 formulation, as well as retaining the possibility of choosing a gauge.

2.2 General relativistic hydrodynamics

In Newtonian physics, a fluid is an “entity” whose dynamics are described by flows of quantities such as energy density, mass, and momentum density. However, in general and special relativity, these quantities are not well defined and depend on the observer. In other words, different observers perceive the same fluid as being in different thermodynamic states. Hence, a description of the fluid dynamics in relativity requires a formulation in which a fluid is not represented by the scalar and vector fields that are observer-dependent, but is implicitly represented by a "flow" in spacetime. These are flux-conservative formulations of hydrodynamics (HD).

Consider classical density, scalar ρ, usually defined as the total number of particles N of rest-mass m in the volume V. Then, the total mass is given by the spatial integral of $\rho \mathrm{d}^3x = m \int_V n \mathrm{d}^3x = mN$. However, while the number of particles N would be the same regardless of the observer, the d^3x would be measured differently by observers moving in relation to each other. Hence, the n would differ. One of the solutions is to consider a frame of reference that is comoving with the fluid. However, this would hinder the ability to generalize the formulation to other reference frames. A better solution is to construct a covariant description in terms of invariant quantities.

The foundation of HD is fluid kinematics, described by its stress-energy tensor. The latter can be obtained by considering the conservation of the number of particles, flux, and the rest-mass density four-vector, written in a form of a mixed tensor $\boldsymbol{T}$. We have already mentioned $\boldsymbol{T}$, when we described the RHS of EFE. There, if EFE are satisfied, the Bianchi identities dictate that covariant derivative, ∇_μ, of $\boldsymbol{T}$ must vanish *i.e.*,

$$\nabla_\mu T^{\mu\nu} = 0 \,. \tag{2.2}$$

In our BNS merger simulations, the NS matter is modeled as a perfect fluid, meaning that in the co-moving frame there is no heat conduction and no viscosity. The former criterion implies that the fluid is in local thermodynamic equilibrium (LTE).

The latter is more complex, as there is still no consensus on the correct mathematical formulation (especially with respect to the numerical applications) of the viscous and/or thermally conducting fluids in GR (*e.g.* Andersson et al., 2007).

The stress-energy tensor of a perfect fluid in the comoving frame reads

$$T^{\mu\nu} = \rho h u^{\mu} n^{\nu} + p g^{\mu\nu} \, , \tag{2.3}$$

where u^{μ} is the four-velocity, ρ is the rest-mass density, the scalar p is pressure, $h = 1 + \epsilon = p/\rho$ is the specific enthalpy, ϵ is the specific internal energy, and $g^{\mu\nu}$ is the metric.

The description of the fluid dynamics, *i.e.*, the relativistic Euler equation, can be obtained from Eq. (2.2) by considering the general relativistic Boltzmann equation and Liuville theorem. The description then reads

$$\rho h n^{\nu} \nabla_{\nu} u^{\mu} = -(g^{\mu\nu} + u^{\mu} u^{\mu}) \nabla_{\nu} p \, . \tag{2.4}$$

From the rest-mass conservation, the continuity equation reads

$$\nabla_{\nu}(\rho u^{\nu}) = 0 \, . \tag{2.5}$$

For numerical reasons it is essential to cast these equations into the conservative formulation. In `WhiskyTHC`, the "Valencia formulation" of general-relativistic hydrodynamics (GRHD) (Banyuls et al., 1997) was implemented (Radice, 2013). The formulation introduces *primitive variables* and *conserved variables*. The former include the proper rest-mass density of the fluid, ρ, velocity υ_i, and energy density ϵ, as seen by a Lagrangian observer. The latter includes the conserved rest-mass, D, momentum, S_i, and internal energy E densities, as seen by the Eulerian observer. It is convenient to combine them into state vectors $\boldsymbol{w} = (\rho, \upsilon_i, \epsilon)$ and $\boldsymbol{q} = (D, S_i, E)$. The expressions for the conserved quantities, associated fluxes, $\boldsymbol{F}^i$, and sources, $\boldsymbol{S}$, form the first-order, hyperbolic, flux-conservative system

$$\frac{1}{\sqrt{-g}} \left[\frac{\partial(\sqrt{\gamma} \boldsymbol{q})}{\partial x^0} + \frac{\partial(\sqrt{-g} \boldsymbol{F}^i)}{\partial x^i} \right] = \boldsymbol{S} \, . \tag{2.6}$$

The "Valencia formulation" allows us to study ultra-relativistic flows and resolve shocks without spurious oscillations and without the need for artificial viscosity (a numerical technique used to tackle the problem of excessive oscillations arising at shocks (*e.g.*

Font, 2008)).

2.3 The neutron star equation of state

In order to close the system of hyperbolic equations that include GRHD equations and gauge, a relation between the pressure, internal energy, and density is required, *i.e.*, the EOS. There are several possible options when it comes to modeling the NS EOS. Specifically, (i) polytropic EOSs, $P(\rho) = \kappa\rho^{\Gamma}$, (ii) ideal gas EOSs, $P(\rho, \epsilon) = (\Gamma - 1)\rho\epsilon$, (iii) piecewise polytropic EOSs $P(\rho, \epsilon) = \kappa_i\rho^{\Gamma}$, with $\rho \in (\rho_i, \rho_{i+1})$, (iv) piecewise-polytropic EOSs with thermal contribution $P(\rho, \epsilon) = \kappa_i\rho^{\Gamma_i} + (\Gamma_{th} - 1)\rho\epsilon_{th}$ with $\rho \in (\rho_i, \rho_{i+1})$, and $\epsilon_{th} = \epsilon - \epsilon_{cold}$ (where the latter is computed from polytropic EOSs), (v) microphysical EOSs.

In our BNS merger simulations, 5 finite-temperature, composition-dependent EOSs were used, namely HS(DD2) (hereafter DD2) (Hempel et al., 2010; Typel et al., 2010), BLh (Bombaci et al., 2018; Logoteta et al., 2021), LS220 (Lattimer et al., 1991), HS(SFHo) (hereafter SFHo) (Steiner et al., 2013), and SLy4-SOR EOS (hereafter SLy4) (Schneider et al., 2017). All EOSs include neutrinos (n), protons (p), nuclei, electrons, positrons and photons as important thermodynamic degrees of freedom. The radii and maximum masses of NSs composed of the cold, neutrino-less β-equilibrium matter from these EOSs fall in line with current astrophysical constraints, *e.g.*, LIGO/Virgo constraints from GW170817 (Abbott et al., 2017c; Abbott et al., 2018; De et al., 2018; Abbott et al., 2019b).

2.3.1 Finite temperature treatment

Finite temperature effects are important for the thermal evolution of NS matter.

In the EOSs that are based on Skyrme effective nuclear interactions, *e.g.*, LS220 and SLy4 EOSs, the thermal effects are added in a form of the temperature dependency of the nuclear effective interaction. The single particle potentials are computed via the variation of the internal energy with respect to neutron and proton densities. Thus, the smaller the effective masses, the larger are kinetic energies and hence, higher matter temperature, assuming the entropy remains constant. Thus, the finite temperature behavior of these EOSs is largely set by the nucleon effective mass.

For the SFHo and DD2 EOSs, the thermal effects for various species are introduced via Fermi-Dirac distributions at finite temperatures. Then, self-consistent solution of

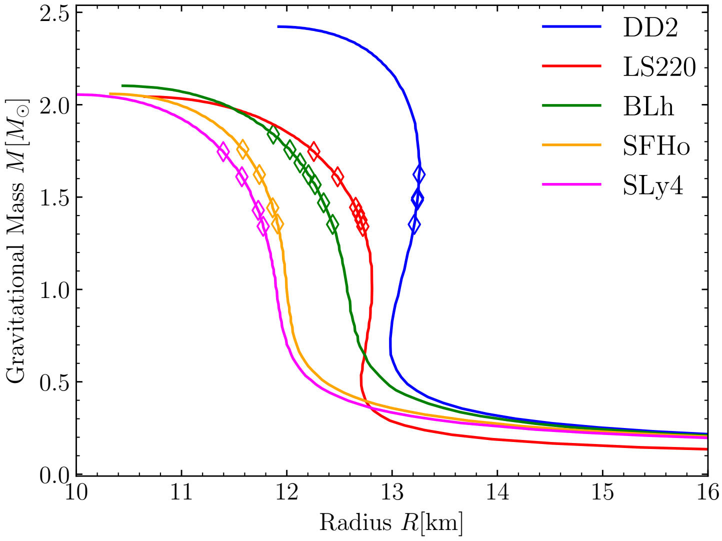

FIGURE 2.2: Mass-radius relations for the EOSs used in this work. Markers along the sequences indicate the NSs analyzed in this thesis.

the mean filed equation introduces the temperature dependence for other thermodynamic quantities.

The BLh EOS employs a different approach to incorporate temperature effects. The method is based on evaluating the free energy in the Brueckner-Hartree-Fock formalism, which in turn requires the effective in-medium nuclear interactions to be defined. Then, the nucleon single particle potentials are evaluated. The potentials represent the mean field that a nucleon with a certain momentum experiences, surrounded by other nucleons. From nucleon single particle potentials, the free energy is then evaluated, and subsequently other thermodynamic quantities. A notable difference with other EOSs discussed here is that the many-body correlations extend beyond the mean field approximation.

2.3.2 EOSs in cold configurations of neutron stars

To characterize the EOSs that employ very different microphyscis and finite temperature properties we consider cold, non-rotating NSs by solving the TOV equations. The results are shown in Fig 2.2, where we also place the primary star of our BNS merger simulations. The maximum TOV mass supported by these EOSs span $M_{\rm max}^{\rm TOV} \sim 2.06 - 2.10\,{\rm M}_\odot$, while the predicted radii of a $1.4\,{\rm M}_\odot$ NS lay in the range $R_{1.4} \sim 11.78 - 12.74$ km. More specifically, LS220, SFHo, SLy4, BLh and DD2 EOSs have $M_{\rm max}^{\rm TOV}$ of 2.04, 2.06, 2.06, 2.10 and 2.42 $\rm M_{\odot}$, and $R_{1.4}$ of 12.8, 12.0, 11.9, 12.5 and 13.2 km respectively. These values are compatible, albeit in general lower, than those inferred from the recent detection of an extremely massive millisecond pulsar (Cromartie et al., 2019), and with results obtained by the NICER collaboration (Miller et al., 2019b; Riley et al., 2019). Notably, EOSs that allow $R_{1.4} \gg 13$ km are currently disfavored by both GW170817 analysis and X-ray pulsar observations (Abbott et al., 2019b; Miller et al., 2019b; Riley et al., 2019).

$M_{\rm max}^{\rm TOV}$ and $R_{1.4}$ are related to pressure at half saturation density (Lattimer, 2012). This motivates the naming convention that we have already introduced for EOSs, *i.e.*, those that lead to NSs with smaller radii are called "softer" and those that lead to NSs with larger radii – "stiffer".

Finite temperature effects provide complimentary pressure support which is not sufficient to raise the maximum TOV mass (Kaplan et al., 2014); but it can increase the radii of hot NSs. Specifically, comparing the cold and hot ($s = 2\ k_{\rm B}$ baryon^{-1}) configurations, the thermal effects were shown to raise the $R_{1.4}$ by 15.6% for the LS220 EOS and 36.4% for the SLy4 EOS, while for the BLh and the SFHo EOS the variation is $\sim 21 - 22\%$. Both NS radius and maximum mass are increased if a NS is rotating. For instance, at the Keplerian limit, the maximum NS mass is increased by $\sim 20\%$ for all EOS models and the radius is increased by $\sim 40\%$ (Bernuzzi et al., 2020). In addition, fast rotation can decrease the central density. These observations highlight the importance of using EOSs with finite-temperature effects.

2.4 Neutrino Radiation Transport

At high densities and temperatures reaching several MeV, weak interactions become increasingly important, moving the material away from the original chemical equilibrium with respect to the β-processes. At this point, the emission of numerous neutrinos with neutrino luminosity reaching $\sim 10^{53}\,$erg s^{-1} commences. Neutrino transport is of primary importance for recovering the composition of matter ejected at mergers (Wanajo et al., 2014; Foucart et al., 2015; Sekiguchi et al., 2015; Foucart et al., 2016b), affecting the nucleosynthesis in ejecta (Wanajo et al., 2014; Goriely et al., 2015) (See also Ch. 4), and ultimately EM counterparts (Metzger et al., 2014; Lippuner et al., 2015) (See also Ch. 5 & Ch. 6).

Neutrino interactions depend on matter composition, density and temperature, and neutrino energies. For instance, at rest-mass density 10^{12}g cm^{-3} and temperature

~ 10 MeV, the neutrino scattering on matter becomes so efficient that neutrinos fall into thermal equilibrium with it. Their mean free path becomes in the order of $\sim 50\,\mathrm{m}$. These neutrinos are considered *trapped*. At densities below $10^{11}\,\mathrm{g\,cm^{-3}}$, neutrinos with energy lower than $10\,\mathrm{MeV}$ are no longer coupled to matter and their mean free path can reach tens of kilometers. Such neutrinos are considered *free-streaming*. If there is a sharp density gradient, *e.g.*, a NS surface where density falls by several orders of magnitude, then neutrinos can be effectively divided into trapped and free-streaming. The transition region, however, is more difficult to treat.

Radiation-transport equations are complex and expensive to solve numerically. Radiation carriers are described by their location in space, *i.e.*, 3D space, momenta (which requires 2 additional components for the angular direction), and finally one component for the energy of carriers. Thus, with the addition of time there are $(6+1)$ dimensions for the problem. Moreover, radiation transport depends strongly on the optical depth of matter, *i.e.*, how effectively the matter traps neutrinos, reducing their mean-free path.

Most commonly used approaches to simplify radiation transport rely on reducing the dimensionality of the problem. In particular, reducing the number of spatial dimensions by assuming certain symmetries. Another possibility is to simplify the momentum space. Notably, the main source of complexity in the radiation transport stems from the scattering integral over all 4π steradian. By dividing the solid angle into a number of discrete angular intervals (rays), the integral can be replaced with a finite sum, converting the integrodifferential equation into a linear system of equations.

2.4.1 Neutrino leakage scheme

It is numerically advantageous to treat neutrinos in the optically thick regime, where radiation and matter are coupled via the so-called "leakage scheme" (Ruffert et al., 1996; Rosswog et al., 2003b; O'Connor et al., 2010; Sekiguchi, 2010; Galeazzi et al., 2013). The method approximates the radiation transport by considering the instantaneous energy loss via neutrino emission, and the evolution of the composition of the nuclear matter. The particular advantage of this method is its computational efficiency and its ability to account for non-trivial geometries of emitting regions. It was first proposed by Riper et al. (1981) to study neutrino cooling through weak interactions in CCSNe. The leakage scheme is a popular choice for modelling neutrino effects in CCSNe and compact object mergers. A modified version of Galeazzi et al. (2013) scheme is implemented in the NR code `WhiskyTHC` (Radice et al., 2016a, 2018a).

TABLE 2.1: Weak reactions employed in our simulations and references for their implementation. The left column describes each reaction, where ν_i are the neutrinos, $\bar{\nu}_i$ are the antineutrinos, n, p are the neutrinos and protons respectively, and A are the nuclei. The central column describes the role, with "P" standing for production, "A" for absorption and "S" for scattering. When two roles are included, the second refers to the inverse ($\leftarrow$) reaction. (The Table is taken from Radice et al. (2018a)).

Reaction	Role	Ref.
$p + e^- \leftrightarrow \nu_e + n$	P,A	(Bruenn, 1985)
$n + e^+ \leftrightarrow \bar{\nu}_e + p$	P,A	(Bruenn, 1985)
$e^+ + e^- \rightarrow \nu + \bar{\nu}$	P	(Ruffert et al., 1996)
$\gamma + \gamma \rightarrow \nu + \bar{\nu}$	P	(Ruffert et al., 1996)
$N + N \rightarrow \nu + \bar{\nu} + N + N$	P	(Burrows et al., 2006)
$\nu + N \rightarrow \nu + N$	S	(Ruffert et al., 1996)
$\nu + A \rightarrow \nu + A$	S	(Shapiro et al., 1983)

The goal of the scheme is to describe the series of effective emissivities, R_ν^{eff} and Q_ν^{eff} for electron neutrinos, ν_e, anti-electron neutrinos, $\bar{\nu}_e$, and heavy-lepton neutrinos, which are collectively labeled as ν_x. Here, R_ν^{eff} describes the number of neutrinos emitted per second and per baryon, and Q_ν^{eff} describes the energy emitted via neutrinos per second and per baryon. Then, the optical depth is evaluated and used to reduce the intrinsic emissivites, mimicking the effect of the diffusion of radiation from the optically thick regions. Neutrinos are assumed to be massless and in thermal equilibrium with the surrounding matter. The effective emissivites can be evaluated from various weak-interaction processes that are present in the hot and dense post-merger environment. The reactions implemented in `WhiskyTHC` and used in our models are listed in Tab. 2.1.

It is possible to evaluate the emission rates corresponding to these processes using only the quantities provided by EOS tables. For instance, consider the strong neutrino emitting process (the direct Urca process), that consists of the β-decay, $e^+ + n \rightarrow p + \bar{\nu}_e$, and the electron capture on free nucleons (n), $e^- + p \rightarrow n + \nu_e$ (the first two reactions in Tab. 2.1). This process moves matter into the β-equilibrium, in which the rates of both reactions are the same, and the chemical potentials $\mu_{\nu_e,\bar{\nu}_e} = 0$. For both β-decay (labeled, pc), and electron capture, (ec), the emissivities have strong temperature, T, dependence (Galeazzi et al., 2013),

$$Q_{pc}(\bar{\nu}_e), Q_{ec}(\nu_e) \propto T^6, \quad R_{pc}(\bar{\nu}_e), R_{ec}(\nu_e) \propto T^5. \tag{2.7}$$

This dependency couples the EOS finite temperature effects and emerging neutrino fluxes, highlighting the importance of both.

In addition to the emission of neutrinos, the leakage scheme considers neutrino absorption and scattering, (see "A" and "S" entries in Tab. 2.1). Of particular importance are the neutrino scattering on heavy nuclei and on free nucleons, as well as electron-flavor neutrino absorption on free nucleons. For mathematical formulations of these opacities see Galeazzi et al. (2013) and their Appendix A. The neutrino scattering on nuclei becomes the dominant source of opacity at sufficiently low temperatures, $< 15\,\mathrm{MeV}$, and at densities below the saturation, when such nuclei become abundant (Rosswog et al., 2003b).

Considering scattering and absorption processes, the local mean free-path for each neutrino species can be computed. From it, the energy-independent mean free path can be derived, which in turn depends only on local thermodynamic conditions. This allows the evaluation of energy-independent part of the optical depth and diffusion rates. The optical depth, in turn, allows one to assess the extent of the optically thick region (that is neutrino-species dependent), and compute the time needed for neutrinos to diffuse out of the dense matter *i.e.*, the diffusion timescale.

In `WhiskyTHC`, both absorption, "a", and scattering, "s", opacities are split into two types: density weighted opacities, $\kappa^0_{\nu;a}$ and $\kappa^0_{\nu;s}$, and energy density weighted opacities, $\kappa^1_{\nu;a}$ and $\kappa^1_{\nu;s}$. The former are related to the rate at which neutrinos escape the material, while the latter set the rate at which energy escapes the material (Ruffert et al., 1996). The optical depth, τ^{α}_{ν}, is computed taking into account total neutrino opacities, $\kappa^j_{\nu;a} + \kappa^j_{\nu;s}$, (Neilsen et al., 2014). Optical depth is then used to estimate the effective emission rates (Ruffert et al., 1996) as

$$R^{\mathrm{eff}}_{\nu} = \frac{R_{\nu}}{1 + t^0_{\mathrm{diff}}(t^0_{\mathrm{loss}})^{-1}}\,, \tag{2.8}$$

where t_{diff} and t_{loss} are the neutrino diffusion time and emission timescales (Radice et al., 2018a). Similarly, the effective energy emission rate Q^{eff}_{ν} is computed using τ^1_{ν}, $\kappa^1_{\nu;a}$ and $\kappa^1_{\nu;s}$.

The neutrinos that escape according to the effective rate, R^{eff}_{ν}, comprise the free streaming neutrinos with number density n^{fs}_{ν}. These neutrinos are treated afterwards according to the M0 scheme in the optically thin region (Radice et al., 2016a).

2.4.2 Neutrino M0 scheme

Computation of the free-streaming neutrino number density and energy evolution is done considering the zeroth momentum (M0) of the free-streaming neutrino distribution function on a set of individual radial rays, with the closure adapted to the post-merger geometry (Radice et al., 2016a, 2018a).

The scheme approximates the Boltzmann equation that describes neutrino transport (Thorne, 1981),

$$\frac{DF}{Dl} = \mathbb{C}[F]\,,$$

where l parameterizes the neutrino's worldline, F is the distribution function for a given neutrino species, and $\mathbb{C}$ is the "collisional operator" that describes the interactions.

Sources of neutrinos are taken from the effective emissivities computed with the leakage scheme. The collisional term is approximated in such a way that it only includes neutrino absorption and emission. Scattering is neglected. For the evaluation of the absorption opacities, LTE is assumed. The closure is achieved by considering neutrinos propagating only radially with the speed of light, (Radice et al., 2016a, 2018a).

Both leakage and M0 schemes were included in all BNS merger simulations discussed in this thesis.

2.5 Magnetic field induced turbulence

Magnetic field induced turbulence is important for self-consistent treatment of the angular momentum transport in BNS mergers (Duez et al., 2006; Kiuchi et al., 2014; Guilet et al., 2017; Kiuchi et al., 2018). Such effects are studied with high-resolution general-relativistic magnetohydrodynamics (GRMHD) simulations. However, despite rapid progress in these methods (*e.g.* Rezzolla et al., 2011; Kiuchi et al., 2014; Ruiz et al., 2016), the degree to which the magnetoturbulence affects the structure and the lifetime of the post-merger NS remnant before collapse is still poorly constrained. Specifically, while MRI are believed to be present within the remnant and are responsible for the redistribution of angular momentum affecting the remnant's lifetime (*e.g.* Duez et al., 2006; Siegel et al., 2013), the fastest growing modes of MRI remain beyond the reach of even very high resolution simulations (*e.g.* Kiuchi et al., 2014).

In `WhiskyTHC` an effective method, based on the large-eddy simulation (LES) model, is employed to account for the MF induced turbulence (Radice, 2017, 2020). The

Table 2.2: Summary table of all the simulations and dynamical ejecta properties. The columns contain the following information, starting from the left. Equation of state, mass-ratio, available resolutions, inclusion of subgrid turbulence, time of the simulation end, time of the BH formation for LR, SR, HR resolutions separately, time of last output, time the disk mass is extracted, disk mass, mass of the dynamical ejecta, mass-averaged electron fracton, terminal velocity and RMS angle (from the binary plane) for dynamical ejecta. For all data except t_{BH}, $t_{\rm end}$ and $t_{\rm disk}$, the value that is given is a mean value across resolutions, with an error estimated as one standard diviaion from the mean. In case where only one resolution is present, the error is assumed to be 20% of the value. Adopted from Nedora et al. (2021b).

EOS	q	$\tilde{\Lambda}$	Resolution	GRLES	$t_{\rm end}$ [ms]	$t_{\rm BH}$ [ms]	$t_{\rm disk}$ [ms]	$M_{\rm disk}^{\rm last}$	$M_{\rm ej}^{\rm d}$ $[10^{-2}M_{\odot}]$	$\langle Y_e^{\rm d}\rangle$	$\langle v_{\infty}^{\rm d}\rangle$ $[c]$	$\langle \theta_{\rm ej}^{\rm d}\rangle$
BLh	1.00	541	`LR SR HR`	✓	43.3 91.8 23.1	> 43.3 > 91.8 > 23.1	23.1	$0.166^{+0.052}_{-0.052}$	$0.14^{+0.02}_{-0.02}$	$0.27^{+0.01}_{-0.01}$	$0.17^{+0.01}_{-0.01}$	$39.65^{+0.35}_{-0.35}$
BLh	1.00	541	`LR SR`	✗	15.9 103.2	> 15.9 > 103.2	15.6	$0.261^{+0.008}_{-0.008}$	$0.12^{+0.01}_{-0.01}$	$0.27^{+0.01}_{-0.01}$	$0.16^{+0.01}_{-0.01}$	$38.80^{+0.44}_{-0.44}$
BLh	1.18	539	`LR`	✓	69.4	> 69.4	69.0	$0.202^{+0.101}_{-0.101}$	$0.30^{+0.06}_{-0.06}$	$0.18^{+0.04}_{-0.04}$	$0.19^{+0.04}_{-0.04}$	$33.65^{+6.73}_{-6.73}$
BLh	1.18	539	`LR`	✗	16.4	> 16.4	15.9	$0.229^{+0.115}_{-0.115}$	$0.25^{+0.05}_{-0.05}$	$0.16^{+0.03}_{-0.03}$	$0.20^{+0.04}_{-0.04}$	$30.86^{+6.17}_{-6.17}$
BLh	1.34	539	`LR SR`	✓	63.4 9.8	> 63.4 > 9.8	9.8	$0.192^{+0.004}_{-0.004}$	$0.25^{+0.05}_{-0.05}$	$0.14^{+0.04}_{-0.04}$	$0.17^{+0.00}_{-0.00}$	$28.79^{+5.00}_{-5.00}$
BLh	1.34	539	`LR`	✗	18.0	> 18.0	18.0	$0.211^{+0.106}_{-0.106}$	$0.19^{+0.04}_{-0.04}$	$0.17^{+0.03}_{-0.03}$	$0.17^{+0.03}_{-0.03}$	$33.39^{+6.68}_{-6.68}$
BLh	1.43	540	`LR SR`	✓	35.1 59.6	> 35.1 > 59.6	33.8	$0.265^{+0.001}_{-0.001}$	$0.27^{+0.08}_{-0.08}$	$0.19^{+0.03}_{-0.03}$	$0.16^{+0.00}_{-0.00}$	$34.49^{+3.59}_{-3.59}$
BLh	1.54	543	`LR`	✓	45.8	> 45.8	53.8	$0.324^{+0.162}_{-0.162}$	$0.20^{+0.04}_{-0.04}$	$0.17^{+0.03}_{-0.03}$	$0.13^{+0.03}_{-0.03}$	$31.21^{+6.24}_{-6.24}$
BLh	1.54	543	`LR`	✗	17.4	> 17.4	30.1	$0.287^{+0.144}_{-0.144}$	$0.22^{+0.04}_{-0.04}$	$0.21^{+0.04}_{-0.04}$	$0.16^{+0.03}_{-0.03}$	$35.05^{+7.01}_{-7.01}$
BLh	1.66	538	`LR SR`	✓	64.6 20.1	> 64.6 1.8	19.2	$0.289^{+0.005}_{-0.005}$	$0.42^{+0.05}_{-0.05}$	$0.11^{+0.01}_{-0.01}$	$0.12^{+0.01}_{-0.01}$	$24.08^{+0.29}_{-0.29}$
BLh	1.82	532	`LR SR HR`	✓	12.0 17.5 9.6	1.4 1.4 1.5	5.9	$0.170^{+0.001}_{-0.001}$	$0.81^{+0.04}_{-0.04}$	$0.03^{+0.01}_{-0.01}$	$0.11^{+0.00}_{-0.00}$	$6.53^{+0.65}_{-0.65}$
BLh	1.82	532	`LR SR HR`	✗	53.8 26.3 45.2	1.7 1.3 1.0	43.2	$0.098^{+0.049}_{-0.049}$	$1.07^{+0.07}_{-0.07}$	$0.03^{+0.01}_{-0.01}$	$0.12^{+0.00}_{-0.00}$	$6.27^{+0.53}_{-0.53}$
DD2	1.00	853	`LR SR`	✗	92.0 110.2	> 92.0 > 110.2	9.4	$0.154^{+0.052}_{-0.052}$	$0.11^{+0.01}_{-0.01}$	$0.25^{+0.00}_{-0.00}$	$0.18^{+0.01}_{-0.01}$	$38.07^{+0.52}_{-0.52}$
DD2	1.00	853	`LR SR HR`	✓	123.0 113.0 74.4	> 123.0 > 113.0 > 74.4	8.2	$0.111^{+0.040}_{-0.040}$	$0.12^{+0.03}_{-0.03}$	$0.27^{+0.01}_{-0.01}$	$0.16^{+0.00}_{-0.00}$	$40.03^{+0.71}_{-0.71}$
DD2	1.20	847	`LR SR HR`	✗	37.3 91.0 55.2	> 37.3 > 91.0 > 55.2	36.6	$0.261^{+0.028}_{-0.028}$	$0.21^{+0.08}_{-0.08}$	$0.18^{+0.03}_{-0.03}$	$0.17^{+0.01}_{-0.01}$	$29.07^{+3.75}_{-3.75}$
DD2	1.22	847	`LR SR HR`	✓	42.7 107.3 19.8	> 42.7 > 107.3 > 19.8	8.7	$0.209^{+0.033}_{-0.033}$	$0.25^{+0.02}_{-0.02}$	$0.19^{+0.01}_{-0.01}$	$0.17^{+0.01}_{-0.01}$	$30.74^{+0.89}_{-0.89}$
DD2	1.43	820	`LR SR`	✓	37.7 62.0	> 37.7 > 62.0	36.7	$0.304^{+0.051}_{-0.051}$	$0.70^{+0.64}_{-0.64}$	$0.14^{+0.05}_{-0.05}$	$0.14^{+0.01}_{-0.01}$	$25.51^{+9.58}_{-9.58}$
LS220	1.00	715	`LR SR`	✓	27.0 27.1	13.7 13.7	16.1	$0.073^{+0.032}_{-0.032}$	$0.16^{+0.02}_{-0.02}$	$0.25^{+0.02}_{-0.02}$	$0.16^{+0.01}_{-0.01}$	$35.70^{+0.78}_{-0.78}$
LS220	1.00	715	`LR SR HR`	✗	35.9 37.2 27.1	33.4 16.1 15.4	34.6	$0.072^{+0.006}_{-0.006}$	$0.16^{+0.06}_{-0.06}$	$0.22^{+0.00}_{-0.00}$	$0.16^{+0.01}_{-0.01}$	$34.99^{+1.68}_{-1.68}$
LS220	1.05	715	`SR HR`	✗	23.3 24.1	17.3 13.9	22.3	$0.107^{+0.054}_{-0.054}$	$0.16^{+0.02}_{-0.02}$	$0.21^{+0.01}_{-0.01}$	$0.16^{+0.01}_{-0.01}$	$33.28^{+2.37}_{-2.37}$
LS220	1.11	717	`SR HR`	✗	25.1 24.4	17.0 > 24.4	24.2	$0.140^{+0.071}_{-0.071}$	$0.22^{+0.03}_{-0.03}$	$0.19^{+0.02}_{-0.02}$	$0.18^{+0.02}_{-0.02}$	$30.25^{+4.43}_{-4.43}$
LS220	1.16	714	`SR HR`	✓	95.8 11.3	68.9 > 11.3	95.5	$0.306^{+0.153}_{-0.153}$	$0.34^{+0.00}_{-0.00}$	$0.22^{+0.00}_{-0.00}$	$0.16^{+0.00}_{-0.00}$	$34.08^{+1.00}_{-1.00}$
LS220	1.16	714	`LR SR HR`	✗	29.5 36.1 28.8	> 29.5 > 36.1 24.1	-	-	$0.33^{+0.05}_{-0.05}$	$0.17^{+0.01}_{-0.01}$	$0.17^{+0.01}_{-0.01}$	$30.01^{+0.64}_{-0.64}$
LS220	1.43	710	`LR SR`	✓	19.8 28.5	15.7 12.3	19.6	$0.178^{+0.072}_{-0.072}$	$0.73^{+0.03}_{-0.03}$	$0.16^{+0.02}_{-0.02}$	$0.17^{+0.01}_{-0.01}$	$26.77^{+3.50}_{-3.50}$
LS220	1.66	707	`LR SR`	✓	6.8 8.0	1.4 2.1	2.0	$0.068^{+0.008}_{-0.008}$	$1.11^{+0.38}_{-0.38}$	$0.07^{+0.01}_{-0.01}$	$0.14^{+0.01}_{-0.01}$	$13.18^{+1.33}_{-1.33}$
SFHo	1.00	413	`SR HR`	✓	25.3 11.6	6.0 4.0	50.0	$0.023^{+0.012}_{-0.012}$	$0.40^{+0.07}_{-0.07}$	$0.21^{+0.00}_{-0.00}$	$0.19^{+0.01}_{-0.01}$	$32.48^{+1.79}_{-1.79}$
SFHo	1.00	413	`LR SR HR`	✗	3.2 7.7 9.0	> 3.2 4.1 3.8	7.2	$0.019^{+0.007}_{-0.007}$	$0.28^{+0.07}_{-0.07}$	$0.23^{+0.01}_{-0.01}$	$0.21^{+0.01}_{-0.01}$	$31.66^{+1.80}_{-1.80}$
SFHo	1.13	412	`SR HR`	✓	14.2 14.3	6.3 > 14.3	-	-	$0.44^{+0.12}_{-0.12}$	$0.18^{+0.01}_{-0.01}$	$0.23^{+0.01}_{-0.01}$	$33.20^{+0.78}_{-0.78}$
SFHo	1.13	412	`LR SR HR`	✗	16.5 19.3 15.2	5.5 11.6 3.9	15.1	$0.046^{+0.041}_{-0.041}$	$0.42^{+0.03}_{-0.03}$	$0.17^{+0.03}_{-0.03}$	$0.22^{+0.01}_{-0.01}$	$29.63^{+4.39}_{-4.39}$
SFHo	1.43	414	`LR`	✓	19.6	4.8	18.9	$0.201^{+0.101}_{-0.101}$	$0.38^{+0.08}_{-0.08}$	$0.14^{+0.03}_{-0.03}$	$0.20^{+0.04}_{-0.04}$	$29.20^{+5.84}_{-5.84}$
SFHo	1.43	414	`SR`	✓	46.5	> 46.5	50.8	$0.241^{+0.121}_{-0.121}$	$0.24^{+0.05}_{-0.05}$	$0.19^{+0.04}_{-0.04}$	$0.14^{+0.03}_{-0.03}$	$32.86^{+6.57}_{-6.57}$
SFHo	1.66	408	`LR SR`	✓	11.2 16.8	1.3 1.3	11.6	$0.177^{+0.153}_{-0.153}$	$0.15^{+0.00}_{-0.00}$	$0.07^{+0.00}_{-0.00}$	$0.12^{+0.01}_{-0.01}$	$10.39^{+1.14}_{-1.14}$
SLy4	1.00	402	`LR SR`	✓	10.5 13.1	2.8 2.8	-	-	$0.09^{+0.02}_{-0.02}$	$0.23^{+0.02}_{-0.02}$	$0.27^{+0.02}_{-0.02}$	$30.81^{+2.81}_{-2.81}$
SLy4	1.00	402	`LR SR`	✗	12.7 22.0	2.7 13.8	12.5	$0.071^{+0.175}_{-0.175}$	$0.31^{+0.20}_{-0.20}$	$0.23^{+0.03}_{-0.03}$	$0.22^{+0.01}_{-0.01}$	$32.23^{+4.84}_{-4.84}$
SLy4	1.13	402	`LR SR`	✗	8.4 20.3	> 8.4 13.0	8.0	$0.164^{+0.023}_{-0.023}$	$0.59^{+0.07}_{-0.07}$	$0.16^{+0.00}_{-0.00}$	$0.24^{+0.01}_{-0.01}$	$29.67^{+1.97}_{-1.97}$
SLy4	1.43	399	`SR`	✓	40.3	> 40.3	45.2	$0.200^{+0.100}_{-0.100}$	$0.20^{+0.04}_{-0.04}$	$0.21^{+0.04}_{-0.04}$	$0.15^{+0.03}_{-0.03}$	$34.03^{+6.81}_{-6.81}$
SLy4	1.66	397	`SR`	✓	7.2	1.2	3.9	$0.138^{+0.069}_{-0.069}$	$0.28^{+0.06}_{-0.06}$	$0.05^{+0.01}_{-0.01}$	$0.12^{+0.02}_{-0.02}$	$8.43^{+1.69}_{-1.69}$

approach considers GRHD equations in the conservative form without neutrino source terms, which are closed with a given EOS and Euler equations for the conservation of baryon and lepton numbers. Importantly, while modes of all scales are present in these equations, only "resolved" modes are evolved in numerical simulations.

In accordance with the LES model, a linear filtering operator is introduced that discards modes or features below a given scale. Numerically, this requires a cell-averaging operator to perform filtering. The averaging procedure yields a system of non-linear equations. The required closure is then achieved by introducing the so-called subgrid-scale turbulence tensor (Radice, 2017).

The turbulence tensor can, in turn, be expressed as a function of turbulent viscosity, $\nu_T = l_{\text{mix}} c_s$, where l_{mix} is the mixing length, which is a characteristic length scale of turbulence, and c_s is the sound speed. The mixing length parameter, l_{mix}, is related to the length over which effects of turbulence are present. With respect to MRI, it is natural to set $l_{\text{mix}} \sim \lambda_{\text{MRI}}$, where $\lambda_{\text{MRI}} \sim \Omega^{-1} B$ with Ω being the angular velocity of the fluid and B is the magnetic field strength (Duez et al., 2006).

Viscous flows in accretion disks are often described in terms of a dimensionless constant α (the so-called α-viscosity model (Shakura et al., 1973)) which is related to the mixing length as $l_{\text{mix}} = \alpha c_s \Omega^{-1}$. The value of α can be constrained by very high resolution GRMHD simulations, with the seed magnetic field strong enough that MRI within the remnant NS are resolved. This was done in Radice (2020) (see their Fig. 71) using a GRMHD simulation of Kiuchi et al. (2018).

A subset of our BNS merger simulations was computed with the above described method. We refer to them as simulations with viscosity or subgrid turbulence.

2.6 Simulations and postprocessing

With the NR code `WhiskyTHC` that incorporates methods discussed in previous sections, a large set of BNS merger simulations was performed. Some of them have been analyzed and presented before (Perego et al., 2019), but most of these simulations are new. We summarize their properties in Tab. 2.2. Each simulation was performed with at least two resolutions to assess the finite-grid-size effects. We distinguish high, standard and low resolutions, denoted as `HR`, `SR` and `LR` respectively. In total 76 BNS merger simulations were analyzed, out of which 37 unique simulations are presented in Tab. 2.2. Several binaries that resulted in the formation of a NS remnant that does not collapse to a BH were evolved up to ∼100 ms post-merger. Most simulations include the effects of subgrid turbulence. Those that are not are marked with "*" next to the EOS name. The naming convention for simulations is the following: the EOS name, the mass ratio, and the resolution, *e.g.*, " BLh* $q = 1.00$ (`SR`) " would refer to the simulation of an equal mass binary performed with BLh EOS, without subgrid turbulence, and at a standard resolution. If resolution is not mentioned, `SR` is assumed.

The novelty of our set of simulations with respect to the previous study by Radice et al. (2018a) where the same code, similar numerical setup and same EOSs (except BLh EOS) were used, is that all our simulations include neutrino heating via the M0 scheme in addition to the neutrino cooling, and for most models the effects of subgrid turbulence are included. Additionally, all our models are targeted to GW170817 with chirp mass, $\mathcal{M}_c = 1.188\,\mathrm{M}_\odot$. The total gravitational mass covers the range $M \in [2.73, 2.88]\,\mathrm{M}_\odot$, while the mass ratio $q = [1, 1.8]$. We show the masses and radii of computed models as markers in Fig. 2.2.

In order to analyze the output of `WhiskyTHC` and compute additional physical quantities, we employ the following postprocessing methods.

Describing a certain property of matter, f, we discretize its mass distribution and make use of mass-averaging defined as

$$\langle f \rangle = \frac{\sum_i f(m_i) m_i}{\sum_i m_i}\,, \tag{2.9}$$

where m_i is the mass contained in the i-th element.

2.6.1 Disk & Remnant

While a disk around a BH can be defined as matter outside the apparent horizon, a disk around a NS remnant is more difficult to define. Commonly, the threshold $\rho \sim 10^{13}\,\mathrm{g\ cm^{-3}}$ is assumed. This choice is motivated by studies that showed that the angular velocity profiles become approximately Keplerian at this point (*e.g.* Shibata et al., 2005, 2006; Hanauske et al., 2017; Kastaun et al., 2017). This convention was adopted in several recent works (Radice et al., 2018a; Kiuchi et al., 2019; Vincent et al., 2020).

We compute the disk baryonic mass evaluating the volume integral of the conserved rest-mass density, D, as

$$M_{\text{disk}} = \int \sqrt{\gamma}\, W \rho \mathrm{d}^3 x = \int D \mathrm{d}^3 x \tag{2.10}$$

from 3D snapshots of our simulations in postprocessing. Here γ is the trace of the metric, and W is the Lorentz factor.

2.6.2 Density modes

We monitor the hydrodynamic instabilities in a newly formed NS remnant by decomposing the Eulerian rest-mass density on the equatorial plane in Fourier modes, $e^{-im\phi}$ (see Eq. (1) in Radice et al., 2016b). We focus on the development and evolution of $m = 2$ and $m = 1$ modes. For data availability reasons we consider only $\rho(x, y, z = 0, t)$, *i.e.* restricting our analysis to the equatorial plane, $z = 0$, and compute

$$C_m(t) = \int \rho(x, y, z = 0, t) e^{-im\phi(x,y)} \mathrm{d}x\mathrm{d}y \, . \tag{2.11}$$

We note that the above quantity is gauge dependent.

2.6.3 Angular momentum

The calculation of the fluid's angular momentum is done assuming axisymmetry. That is, we assume $\phi^\mu = (\partial_\phi)^\mu$ is a Killing vector. Accordingly, the conservation law, Eq. (2.2), in $3 + 1$ decomposition formalism reads

$$\partial_t (T^{\mu\nu} \phi_\nu n_\nu \sqrt{\gamma}) - \partial_i (\alpha T^{i\nu} \phi_\nu \sqrt{\gamma}) = 0 \ , \tag{2.12}$$

where n^μ is the normal vector to the spacelike hypersurfaces. The equation implies a conservation of the angular momentum, defined as

$$J = - \int T_{\mu\nu} n^\mu \phi^\nu \sqrt{\gamma} \, \mathrm{d}^3 x \ . \tag{2.13}$$

In cylindrical coordinates, $x^i = (r, \phi, z)$, adapted to the symmetry, the angular momentum density is

$$j = \rho h W^2 v_\phi \ , \tag{2.14}$$

and the angular momentum flux is

$$\alpha \sqrt{\gamma} T^r_\nu \phi^\nu = \alpha \sqrt{\gamma} \rho h W^2 (v^r v_\phi) \, . \tag{2.15}$$

We evaluate these quantities from the 3D snapshots of our simulations.

2.6.4 Ejecta

The matter expelled at high velocities during BNS mergers may ultimately become unbound from the system's central gravitational potential. There are two indicators commonly adopted to mark the unbound matter.

The Geodesic criterion

Assuming that the spacetime is stationary (∂_t is the Killing vector), the four-velocity, u_t, is a constant of motion for geodesics. Additionally, we assume that the space is asymptotically flat ($u_t = -W$ at spatial infinity, where W is the fluid element Lorentz factor) Under these assumptions, if a fluid element has $u_t < -1$, it may be considered unbound as it will retain a non-zero positive velocity at infinity. The fluid asymptotic velocity reads

$$v_\infty \simeq \sqrt{2E_\infty}, \tag{2.16}$$

where $E_\infty = -u_t - 1$. This criterion can be thought of as assuming that the fluid is made of isolated particles that follow geodesics in a static spacetime. Indeed, the effects of an EOS (*i.e.*, fluid's pressure gradient, internal energy and heating) are neglected which might lead to an underestimation in the ejecta mass. Strictly speaking, none of the assumptions made here are fulfilled in a BNS post-merger environment. However, due to its simplicity and versatility, this criterion is widely used in the literature (*e.g.* Radice et al., 2018a; Vincent et al., 2020).

The Bernoulli criterion

From the relativistic Bernoulli equation (Rezzolla et al., 2013), it follows that for a stationary relativistic flow, the hu_t is constant along the fluid worldlines. Here h is the (relativistic) enthalpy. Since h is defined up to a constant factor which can be set such that $h \leftarrow 1$ at spatial infinity, the condition $hu_t < -1$ would mark the unbound matter. The associated asymptotic velocity is calculated as

$$v_\infty \simeq \sqrt{2(h(E_\infty + 1) - 1)}. \tag{2.17}$$

The criterion can be regarded as assuming that all the internal energy of the fluid gets added to the fluid kinetic energy as fluid decompresses from the post-merger environment. This criterion has been reported to estimate the amount of unbound material more accurately (Foucart et al., 2016b). The difference was found to reach a factor of two in terms of ejecta mass, estimated with these two criteria applied to matter within a given volume (Kastaun et al., 2015).

We adopt the geodesic criterion to study the “burst-like ” short outflows, such as DE, where the pressure gradient is not expected to make a significant contribution. For steady-state outflows, like post-merger winds, we adopt the Bernoulli criterion. The term ejecta would refer to the material gravitationally unbound according to either of the criteria. All ejecta properties are evaluated at $R \simeq 294$ from the center of the simulation domain unless stated otherwise.

Chapter 3

Binary Neutron Star merger simulations

In this chapter we present the results of the postprocessing of our BNS merger simulations. We begin by discussing the dynamics of post-merger remnants and their interactions with the surrounding disks in Sec. 3.1. We focus on the disk evolution and its final state. Additionally, we assess possible evolution trajectories beyond what was simulated. Next, in Sec. 3.2 we analyze the properties of ejecta. Regarding DE we focus on statistics, connecting ejecta properties to the binary parameters. We also take a closer look at the fast tail of DE. Regarding post-merger winds, we discuss the mechanism behind these winds and their properties.

The results presented in this and subsequent Chapters are published in Nedora et al. (2019), Bernuzzi et al. (2020), and Nedora et al. (2020, 2021a,b).

3.1 Overview of the remnant-disk interactions

We begin by analyzing the dynamics of post-merger NS remnants. Hydrodynamic instabilities are monitored by a decomposition in Fourier modes, $e^{-im\phi}$, of the Eulerian rest-mass density on the equatorial plane (see Sec. 2.6.2 for more details). We consider two representative simulations, LS220 $q = 1.00$ (`SR`) and DD2 $q = 1.00$ (`SR`), that produce short- and long-lived remnants respectively.

As we mentioned in Sec. 1.1.2, newly born NS remnants are not axisymmetric, displaying characteristic spiral arms in their density profile that extend outwards from the shock interface of collided cores. Specifically, the $m = 2$ instability, characterized by the bar-shaped geometry, dominates the early post-merger, while the $m = 1$ instability, characterized by one-armed geometry, starts to dominate in the late evolution (*e.g.* Bernuzzi et al., 2014; Kastaun et al., 2015; East et al., 2016b; Radice et al.,

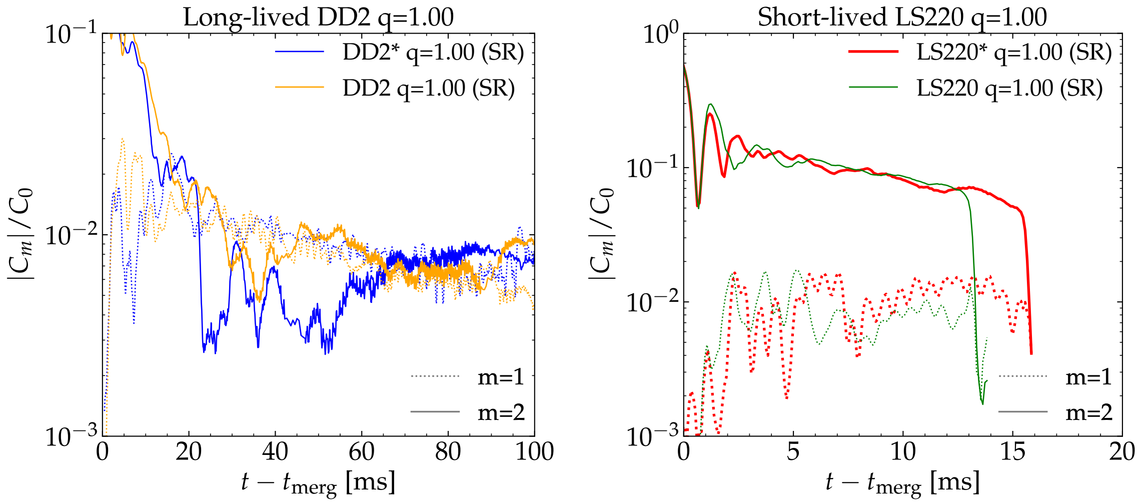

FIGURE 3.1: The evolution of $m = 1$ and $m = 2$ modes in two representative equal mass simulations with DD2 and LS220 EOSs on the *left panel* and the *right panel* respectively. The mode amplitudes are computed via Eq. (2.11). The plot shows that in the case of a long-lived remnant, the $m = 2$ mode is dumped, *i.e.*, decays quickly after the merger, and on a timescale of $\gtrsim 20$ ms it becomes comaprable to $m = 1$ mode. In case of a short-lived remnant, $m = 2$ remains the dominant mode until the remnant collapses to a BH. (Adopted from Nedora et al., 2021b).

2016b). Fig. 3.1 corroborates this picture. Indeed, the $m = 2$ mode remains the dominant one until $\sim 15 - 20$ ms post-merger. After that, the LS220 $q = 1.00$ model forms a BH. In the DD2 $q = 1.00$ model, however, the amplitude the of the $m = 1$ mode becomes comparable with that of the $m = 2$, and both modes persist throughout the remainder of the evolution, after the GW-dominated phase ends (Bernuzzi et al., 2016; Radice et al., 2016b).

We find that the magnitude of the $m = 1$ mode increases with the binary mass ratio. For instance, the largest $C_{m=1}$ are found in models with BLh and LS220 EOSs and mass ratios $q = 1.43$ and $q = 1.22$ respectively. The dependency of the $C_{m=2}$ on mass ratio, however, is not very clear. Overall, our results are in agreement with what was reported by Lehner et al. (2016a).

The formation of spiral arms is a generic hydrodynamic effect that was identified in NR simulations with polytropic EOSs (Bernuzzi et al., 2014; Radice et al., 2016b). However, the evolution of these arms and the quantitative behaviour of hydrodynamic modes depend on the physics input of simulations, and are not well understood. We observe that turbulent viscosity, for instance, leads to faster suppression of $m = 2$. By contrast, the $m = 1$ mode is not significantly affected by viscosity, as shown in Fig. 3.1. If a remnant is short-lived, as is the case for LS220 $q = 1.00$ model, the effect

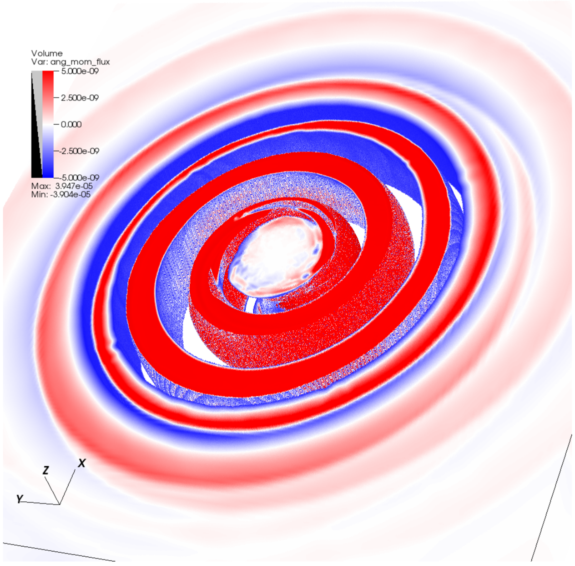

FIGURE 3.2: Volume rendering of the angular momentum flux, J_r, distribution in $3D$ for DD2 $q = 1.00$ `SR` model. The snapshot is taken at ∼43.5 ms after merger. J_r is shown on a central region of $(89 \times 89 \times 60)$ km^3 covering the remnant NS and disk, and it is given in units where $c = G = \mathrm{M}_\odot = 1$. (Adapted from Nedora et al. (2019)).

of subgrid turbulence is not apparent because the dynamical evolution is interrupted by the collapse.

We compute the angular momentum and its flux from the energy-momentum tensor, Eq. (2.3), in cylindrical coordinates, (r, ϕ, z), under the additional assumption of axisymmetry (see Sec. 2.6.3 for more details). The disk is assumed to be comprised of matter with $\rho \leq 10^{13}\,\mathrm{g\ cm}^{-3}$ (see also Sec. 2.6.1).

We find that for a long-lived NS remnant on a timescale of ∼20 ms, about half of the total angular momentum of the remnant is transferred into the disk. This is a consequence of the fact that the remnant NS is strongly deformed after merger and exerts gravitational torques on the surrounding matter, allowing for a rapid angular momentum transport.

Following the disk and remnant mass evolution we observe that the spiral density modes inject $\sim 0.1 - 0.4\,\mathrm{M}_\odot$ of baryon mass into the disk during the first ∼20 ms. The mass injection appears to be stronger in models with stiffer EOSs. With respect to the mass ratio, we find that higher q binaries form more massive disks *e.g.*, the BLh* $q = 1.82$ model (that undergoes PC) and the LS220* $q = 1.43$ model.

Fig. 3.2 shows that the angular momentum is transported via spiral waves, induced by the $m = 1$ and $m = 2$ hydrodynamic modes, discussed above. We find the characteristic spiral wave structure in all our simulations. It smears out only if a BH is

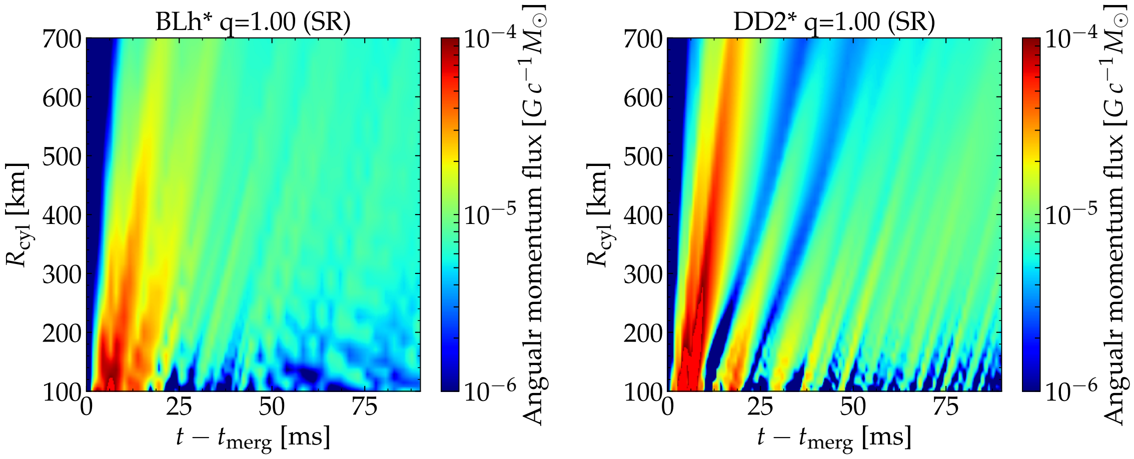

FIGURE 3.3: The evolution of the angular momentum flux through consecutive cylindrical surfaces (for cylindrical radii from $R_{\rm cyl} = 100$ to $R_{\rm cyl} = 500$). The angular momentum transport through the disk is depicted for two equal mass BNS post-merger remnants without viscosity. (Adapted from Nedora et al. (2021b)).

formed. In Fig. 3.3 we show how the angular momentum is being transported from the NS remnant into the disk in two models with long-lived NS remnants: DD2* $q = 1.00$ and BLh* $q = 1.00$. Notably, in the model with a more stiff DD2 EOS, the first wave is considerably stronger.

The subgrid turbulence enhances the angular momentum transport. However, more simulations of long-lived NS remnants are needed to assess the effects of the subgrid turbulence systematically.

We find that in BNS merger simulations with high mass ratio, $q \gtrsim 1.67$, the companion star (the less massive one) undergoes tidal disruption before merger as tidal forces overcome the star's binding energy, creating a disk around the primary. The disk accretion brings the remaining NS mass above the maximum mass supported by its EOS, which leads to a PC of the remaining star. These BNS models are characterized by a monotonic increase in their central density during the merger. We also observe that at formation, the disk is massive, $\sim 0.15\,\mathrm{M}_\odot$, in comparison with disks formed in PC of equal mass binaries (*e.g.* Radice et al., 2018a), and is also very neutron-rich, $Y_e \sim 0.1$.

Binaries with a small mass ratio, $q \lesssim 1.4$, produce either a short- or a long-lived remnant depending on the post-merger configuration and properties. Most binaries that produce short-lived remnants have relatively soft EOSs and small mass ratios, *e.g.*, models LS220 $q = 1.1$, $q = 1.2$, SFHo $q = 1.1$, $q = 1.4$, and SLy $q = 1.1$, $q = 1.4$. They collapse within ∼20 ms post-merger. The exact time of the collapse, however,

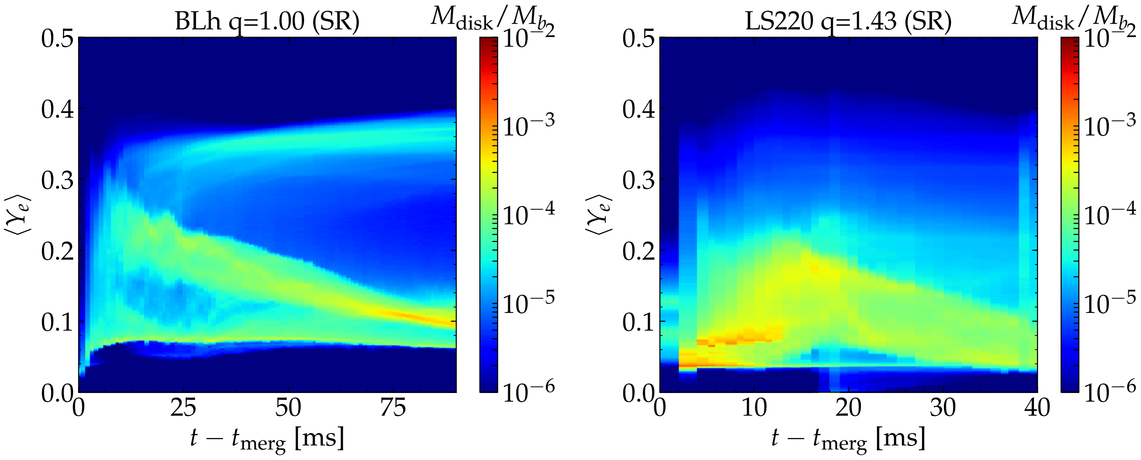

FIGURE 3.4: Evolution of the mass-averaged electron fraction in the disk of two models, BLh $q = 1.00$ and LS220 $q = 1.43$ shown on the *left panel* and *right panel* respectively, that produce long- and short-lived remnants respectively. The plot shows that during the post-merger evolution, neutrino cooling lowers the Y_e of the bulk of the disk matter. A small fraction of the disk, however, reaches higher Y_e, while being irradiated by neutrinos and processed by shocks (Adapted from Nedora et al. (2021b)).

depends on the simulation resolution and on the inclusion of subgrid turbulence as was previously noted by Radice (2017).

As we discussed in Sec. 1.1.2, the strong neutrino fluxes emanating from the remnant and the hot disk matter raise the fluid electron fraction. If a NS remnant collapses to a BH, the main source of neutrinos shuts down, the inner part of the disk accretes rapidly, and the disk itself moves to a quasi-steady state with axisymmetric and approximately Keplerian profile. Indeed, in our models we find that the inner part of the post-merger disk, at densities $\rho \sim 10^{13}$ g cm^{-3}, is relatively hot, $T \sim 10\,$MeV, but neutron-rich $Y_e \sim 0.1$, as it is shielded from the neutrino irradiation. The matter gets progressively colder and proton-rich outwards, with Y_e reaching 0.4 at the disk edges.

We examine this behaviour in two representative models, BLh $q = 1.00$ and LS220 $q = 1.43$, where the former model was evolved till ∼90 ms post-merger. The evolution of the mass-weighted electron fraction in these models is shown in Fig. 3.4. We observe that, during the disk formation, shocks and spiral waves raise the disk electron fraction to $Y_e \sim 0.25$. As the disk evolves, the bulk of its mass, shielded from neutrinos, returns to neutron-rich conditions with $Y_e \lesssim 0.1$. The outer part of the disk, however, is subjected to strong neutrino irradiation and reaches $Y_e \sim 0.4$ on a timescale of

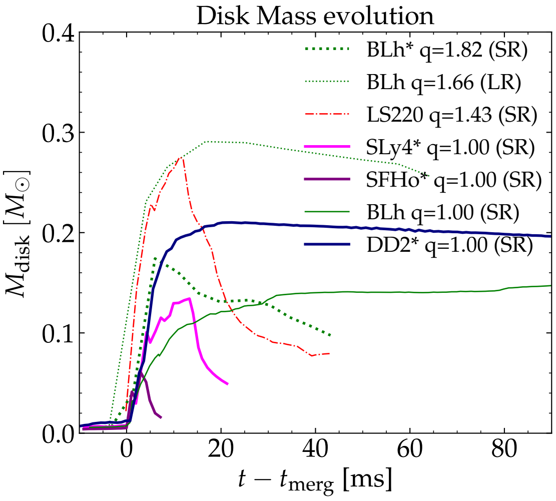

FIGURE 3.5: Time evolution of the mass of the disk for a representative list of simulations, that includes those that produce long-lived remnants, *e.g.*, DD2* $q = 1.00$, short-lived remnants, *e.g.*, SLy4* $q = 1.00$, and a simulation that undergoes PC, BLh* $q = 1.82$. The plot shows that the post-merger evolution of disk mass depends strongly on the remnant. If the remnant is a NS, the disk is accreted slowly and its mass remains almost unchanged by the end of our simulations, while if BH forms, the disk is accreted rapidly (if mass ratio is not large). (Adapted from Nedora et al. (2021b)).

$\sim$40 ms[1]. In case of the LS220 $q = 1.43$ models that produces a short-lived NS remnant, the average electron fraction is lower, as the main source of neutrinos collapses shortly after merger.

The disk mass at formation shows dependency on the NS EOS. Specifically, binaries with stiffer EOSs (larger NS radii) produce more massive disks. The disk mass also shows dependency on mass ratio. For instance, the most massive disks are formed in LS220 $q = 1.43$ and BLh $q = 1.82$ models. The disk accretion onto a BH removes up to 50% of its mass on a timescale of tens of milliseconds. If the NS remnant is long-lived, the disk has time to complete its formation, and thus it is more massive and extended (Perego et al., 2019). The final mass is higher for models with larger mass ratios and stiffer EOSs. For instance, in the BLh $q = 1.00$ model the disk mass reaches $\lesssim$0.15 $M_\odot$, while in the DD2 $q = 1.00$ model it exceeds $\sim$0.2 $M_\odot$. For models with BLh EOSs, the disk mass increases between $q = 1.00$ and $q \sim 1.4 - 1.5$ by 100%.

The long-term evolution of a disk is driven by its interaction with the post-merger remnant, and by cooling. In Fig. 3.5 disk mass as a function of time for a set of

---

[1] The apparent gap in the Y_e distribution in Fig. 3.4 at $\langle Y_e \rangle \simeq 0.15$ might not be of physical origin, but an artifact from the neutrino M0 scheme that assumes neutrinos propagate along the radial directions (see Sec. 2.4).

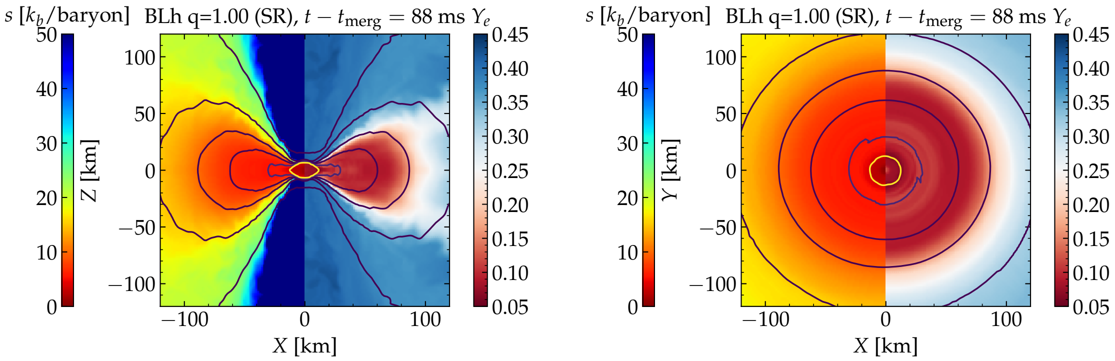

FIGURE 3.6: Snapshots of disk properties on (x, z) *left panel* and (x, y) *right panel* for the BLh $q = 1.00$ model, taken 88 ms post-merger. On each panel, the entropy per baryon is shown on the left side of the panel, and the electron fraction on the right. Solid contours mark the rest mass density values, which read $[10^{13}, 10^{12}, 10^{11}, 10^{10}, 10^{9}]$ g cm^{-3} from the innermost yellow contour encompassing the remnant. (Adapted from Nedora et al. (2021b)).

models is shown. If a BH forms, the only possible interaction is disk accretion onto a BH, which leads to the depletion of the disk. However, if a remnant is a massive NS, the picture is more complex. Neutrino cooling and gravitational pull from the remnant facilitate accretion. Simultaneously, spiral density waves inject energy and angular momentum into the disk, as well as centrifugally supported material, raising its temperature and geometrical extent. This is the case for the DD2* $q = 1.00$ and BLh $q = 1.00$ models where the quasi-steady state disk accretion and mass-shedding maintain the disk mass almost constant until the end of the simulation. The strong mass-shedding in the BLh $q = 1.00$ model can be attributed to the very high average temperatures of the remnant and the disk. This is a direct consequence of the thermal effects included in the BLh EOS (see Sec. 2.3), and the softness of this EOS, which leads to strong oscillations of the remnant after merger. Higher temperatures lead to lower rotational frequency at which mass shedding occurs (Kaplan et al., 2014).

When the subgrid turbulence is included, the mass distribution of the disk's properties appears smeared. The distributions of electron fraction, entropy per baryon and temperature appears broader. A more detailed quantitative analysis would require more simulations performed at several resolutions to disentangle the effects caused by the subgrid turbulence and by the finite grid (Bernuzzi et al., 2020; Radice, 2020).

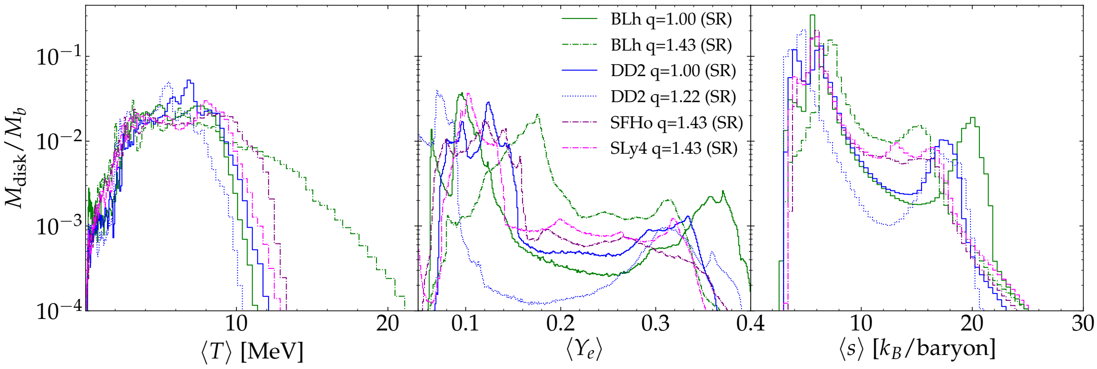

FIGURE 3.7: Disk properties in the form of mass histograms at the end of evolution for a set of simulations. From left to right, panels depict the temperature, T, fraction Y_e and entropy s. (Adapted from Nedora et al. (2021b)).

3.1.1 Final disk structure

From the density contours in Fig. 3.6, we observe that even at ~88 ms after merger the disk of the BLh $q = 1.00$ model remains geometrically thick. Comparing with other models, we note that the root mean square (RMS) half-opening angle of the disk appears to be independent of the EOS and mass ratio, and is $\langle\theta\rangle_{\rm rms} \sim 60°$. The radial extent of the disk, however, increases with the EOS softness and q. Similarly, the final disk mass is larger for the unequal mass binaries, ranging overall between ~$0.1\,{\rm M}_\odot$ and ~$0.4\,{\rm M}_\odot$ (see Tab. 2.2), and is larger in models that produce long-lived remnants.

We examine disk mass dependencies on binary parameters in Appendix A, Sec. A.3, where we combine our data with the data available in the literature (see Sec. 3.2) and show that the aforementioned dependencies on q and $\tilde{\Lambda}$ can be captured by a simple two parameter, second order polynomial in these quantities. We find that in comparison with other fitting formulae available in the literate the polynomial performs better. The systematics in data, however, are large. More BNS merger simulations with advanced physics and a consistent method of disk mass extraction are required for constraining the polynomial, especially at the known boundaries of the parameter space, *e.g.*, $\tilde{\Lambda} \to 0$.

The mass-averaged temperature, electron fraction and entropy per baryon for several models are presented in Fig. 3.7. The plot shows that the mass-weighted distribution of entropy and the electron fraction have a bimodal structure, which is more pronounced in the case of equal mass binaries. The low entropy, $s \sim 5-10\,k_B$/baryon, peak corresponds to the bulk, mildly shocked material, while the higher entropy peak,

$s \sim 15 - 22\,k_B$/baryon, marks the strongly shocked material. Notably, the low entropy peak is largely independent of the EOS and mass ratio, while the high entropy peak is more pronounced in models with softer EOSs. Similarly, the low Y_e peak, $Y_e \sim 0.1$, corresponds to the neutrino-shielded part of the disk, while the high Y_e peak, $Y_e \sim 0.3 - 0.4$, marks the outer parts of the disk, where fluid is subjected to strong neutrino irradiation.

Comparing the disk properties with the 2D snapshots of the electron fraction and density within the disk, shown in Fig. 3.6, we observe that indeed, the two peaks in the mass-weighted distribution of s and Y_e correspond to different regions within the disk. Similarly, we observe that the innermost parts of the disk are hotter than the outermost ones. The bulk of the disk has $T \sim 1 - 10\,$MeV. The disk temperature distribution appears to be largely independent of the EOS and mass ratio.

3.1.2 Mass and angular momentum loss

Quantitative understanding of the long-term post-merger dynamics requires ab-initio NR simulations in (3+1)D with complete physics. Here we assess a possible long-term evolution via an indirect method, focusing on the BLh $q = 1.00$ (`SR`) model, one of the longest runs performed.

In this simulation, after the merger, a NS remnant is born with an excess in baryon mass with respect to the beta-equilibrium NS configurations. In Fig. 3.8 we show the evolution of the total baryonic mass, M_b, and total angular momentum, J (the solid black line), evaluated in cylindrical coordinates assuming axisymmetry and accounting for matter in the remnant and in the disk. At early post-merger, before any substantial mass-loss could occur, the evolution is governed by the emission of GWs. The remnant loses angular momentum but retains constant baryonic mass. In order to evaluate the total amount of angular momentum lost to GWs we perform the frequency-domain integration of the GW strain with the extraction sphere of $R = 400\,\mathrm{M}_{\odot}$ using the `strain.py` module of the public library `scidata`[2]. The method is discussed in Bernuzzi et al. (2012), Damour et al. (2012), and Bernuzzi et al. (2015).

Subtracting the angular momentum lost to GWs from the initial data, we obtain the value that is left to the system after the GW phase (the yellow marker in Fig. 3.8[3]). We observe that at this stage the remnant still has an excess in angular momentum

---

[2] https://bitbucket.org/dradice/scidata

[3] Due to different assumptions in its calculation the agreement with J from the volume integrals is not expected.

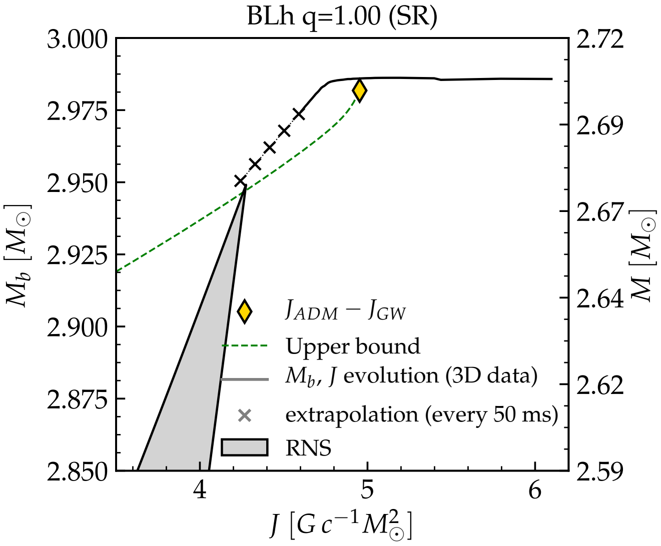

FIGURE 3.8: Evolution of the BLh $q = 1.00$ post-merger remnant J-M_b space, where J is the total angular momentum and M_b is the baryonic mass, depicted by the solid black line. The evolution begins in the upper right corner and proceeds towards the lower left one, as the remnant loses first angular momentum to GW emission, then both J and M_b to massive winds. The point where the GW-phase ends is marked with yellow marker. The end of the solid black line indicates the end of our simulation. We linearly extrapolate the evolution trajectory, and plot it with black crosses. The green dashed line is a conservative estimate of the mass ejection and a possible trajectory for the viscous evolution as estimated in Radice et al. (2018c). The gray shaded region is the region of stability of rigidly rotating NS equilibria. (Adapted from Nedora et al. (2021b)).

in comparison with the rigidly rotating NS configurations with the same baryon mass (the gray triangular region in Fig. 3.8). The equilibria configurations were computed using the `RNS` public code [4]. We observe the same situation in all our models.

Notably, the baryonic mass of the post-merger remnant also exceeds the maximum mass that a rigidly rotating equilibria could have. As we mentioned in Sec. 1.1.2, such a remnant is generally referred to as a HMNS (Baumgarte et al., 2000) and is expected to collapse to a BH shortly after formation. However, as Fig. 3.8 shows, a remnant that efficiently loses mass sets on a trajectory towards the rigidly rotating, stable configuration. The extrapolation of the final trend of the mass and angular momentum loss suggests that if $\approx$0.05 $M_\odot$ ($\approx$40% of the final disk at the end of the simulation) is ejected, a NS remnant would approach the rigidly rotating equilibria region at the mass-shedding limit. For the BLh $q = 1.00$ model, if the ejecta mass flux does not change, the equilibrium would be reached within ∼350 ms post-merger. Thus, in principle, a HMNS remnant could avoid collapse. This calls for a more detailed investigation with long-term NR BNS merger simulations that employ advanced physics.

---

[4] `RNS` is a code written by Nikolaos Stergioulas which constructs models of rapidly rotating, relativistic, compact stars using tabulated EOS `http://www.gravity.phys.uwm.edu/rns/`.

The massive outflow that starts to dominate the post-merger dynamics after the GW-phase, is driven by the interaction between the non-axisymmetric remnant, subjected to $m = 1$ and $m = 2$ instabilities, and the disk. We call this ejecta spiral-wave winds (SWW). The properties of SWW are discussed in the next section.

Additionally, we estimate a conservative upper bound evolution of the long-lived remnant based on the following considerations (Radice et al., 2018c). The recombination of nucleons into nuclei and the subsequent liberation of nuclear binding energy can be a driving force behind massive outflows (see Sec. 1.1.3). Matter becomes unbound gravitationally once it reaches cylindrical radius r^*, at which point the nuclear recombination energy becomes equal to the gravitational binding energy (*e.g.* Fernández et al., 2013),

$$GMm_b/r^* \simeq 8.8\,\mathrm{MeV},$$

where M is the central object mass and m_b is the average baryon mass. Thus, a ring of material located at $r < r^*$ would, once it becomes unbound, remove the angular momentum required to reach to r^*, in addition to its specific angular momentum $j(r)$. If the disk is Keplerian, the angular momentum carried away by the ring initially at r, is $j^*(r) = j(r)(r^*/r)^{1/2}$, where $r^* = 300G/c^2M$ is the fiducial value, corresponding to assumed total mass $M \approxeq 2.5M_\odot$ (Radice et al., 2018c). The expected trajectory is shown as the green line in Fig. 3.8. This analysis further suggests that sufficiently massive outflows can bring post-merger HMNS remnants to stability.

Our other simulations also produce NS remnants with similar evolutionary paths. Models with the DD2 EOS, however, are born with an excess in angular momentum but not in baryonic mass. They also evolve towards the rigidly rotating equilibria, but more slowly. Models with $q > 1.00$ produce remnants that generally have larger excess in angular momentum and mass. They have to shed a larger amount of mass to reach an equilibrium configuration. Overall, we estimate that models with $q = 1.00$ need to shed $\sim 0.05\,\mathrm{M}_\odot$ while models with $q \approxeq 1.4$ need to remove $0.2\,\mathrm{M}_\odot$ to reach such a configuration.

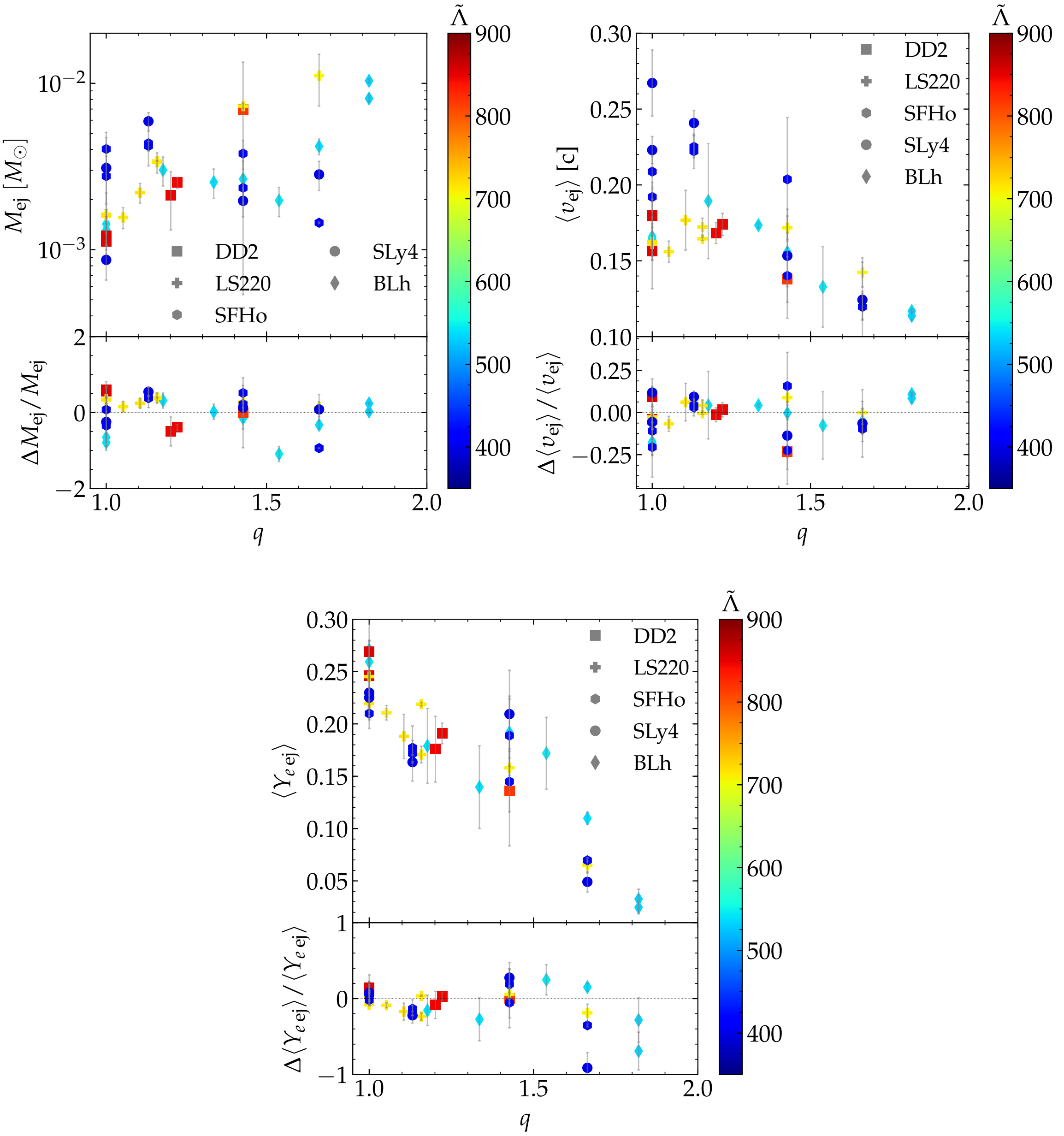

FIGURE 3.9: DE properties from our simulations as functions of binary parameters q and $\tilde{\Lambda}$. The *first*, *second* and *third panels* show the mass, mass-averaged velocity and electron fraction respectively. In each panel, the lower suplot shows the relative difference between the data and values inferred from the polynomial fitting formula (see the text). (Adapted from Nedora et al. (2021b))

TABLE 3.1: Characteristics of the collected sets of BNS models. The first column contains the sources from which the data was taken, and the last column lists the names of the datasets that we define based on the physics setup of simulations, specifically, neutrino treatment, that is listed in the 3rd column. The second contains the information on the EOS which is either microphysical or piecewise polytropic (PWP). Other columns state the availability of a certain binary and ejecta parameter. The black crosses indicate that the data is not available, and thus, the corresponding models were not used in the related analysis. (Adapted from Nedora et al. (2020))

Ref.	EOS	Neutrinos	M	M_b	$\tilde{\Lambda}$	$M_{\rm ej}$	$\upsilon_{\rm ej}$	Y_e	$M_{\rm disk}$	Dataset
(Perego et al., 2019)	Micro	Leak+M0	✓	✓	✓	✓	✓	✓	✓	`M0RefSet` & `M0/M1Set`
(Nedora et al., 2019)	Micro	Leak+M0	✓	✓	✓	✓	✓	✓	✓	`M0RefSet` & `M0/M1Set`
(Bernuzzi et al., 2020)	Micro	Leak+M0	✓	✓	✓	✓	✓	✓	✓	`M0RefSet` & `M0/M1Set`
(Nedora et al., 2021b)	Micro	Leak+M0	✓	✓	✓	✓	✓	✓	✓	`M0RefSet` & `M0/M1Set`
(Vincent et al., 2020)	Micro	M1	✓	✓	✓	✓	✓	✓	✗	`M0/M1Set`
(Sekiguchi et al., 2015)	Micro	Leak+M1	✓	✗	✗	✓	✗	✓	✗	`M0/M1Set`
(Sekiguchi et al., 2016)	Micro	Leak+M1	✓	✗	✗	✓	✓	✓	✓	`M0/M1Set`
(Radice et al., 2018a) (M0)	Micro	Leak+M0	✓	✓	✓	✓	✓	✓	✓	`M0/M1Set`
(Lehner et al., 2016b)	Micro	Leak	✓	✓	✗	✓	✓	✗	✗	`LeakSet`
(Radice et al., 2018a) (LK)	Micro	Leak	✓	✓	✓	✓	✓	✓	✓	`LeakSet`
(Kiuchi et al., 2019)	PWP	-	✓	✓	✓	✓	✗	✗	✓	`NoNusSet`
(Dietrich et al., 2017a)	PWP	-	✓	✓	✓	✓	✓	✗	✓	`NoNusSet`
(Dietrich et al., 2017a)	PWP	-	✓	✓	✓	✓	✓	✗	✓	`NoNusSet`
(Hotokezaka et al., 2013b)	PWP	-	✓	✗	✗	✓	✓	✗	✗	`NoNusSet`
(Bauswein et al., 2013b)	Micro	-	✓	✗	✗	✓	✓	✗	✗	`NoNusSet`

3.2 Mass ejection in BNS merger simulations

3.2.1 Dynamical Ejecta

We discussed the mechanisms behind DE in Sec. 1.1.3. Here we assess the properties of DE in our simulations. These properties are final, as the ejecta mass flux saturates $\lesssim$20 ms after merger, and all our simulations are longer than that. We extract them at $R = 294\,\mathrm{km}$ from the remnant (unless specified otherwise), using the geodesic criterion (See Sec. 2.6.4).

Comparing ejecta properties between simulations with and without subgrid turbulence (See Tab. 2.2) we observe that its effect on DE properties is rather weak and comparable to the effects of finite grid discretization (Bernuzzi et al., 2020; Radice, 2020).

In Fig. 3.9 we show the ejecta mass, velocity and electron fraction as a function of binary parameters: mass ratio, q, and tidal deformability parameter, $\tilde{\Lambda}$, for our models. The plot shows that while there is a large degree of scatter, certain overall trends can be deduced, and a relation between the ejecta and binary parameters can be constructed. In order to examine these relations in more detail, we enlarge the sample of simulations by collecting the published sets of BNS merger models.

The datasets used for the analysis are summarized in Tab. 3.1. We group them with respect to the employed neutrino treatment:

- `M0/M1Set` comprises a set of models with neutrino emission and absorption and microphysical EOSs. It includes 8 models with leakage+M0 scheme of Radice et al. (2018a) and models of Sekiguchi et al. (2015, 2016) and Vincent et al. (2020), in which leakage+M1 scheme or gray M1 scheme are employed for the neutrino transport. Models reported in these studies span $q \in [1, 1.30]$, $\tilde{\Lambda} \in [340, 1437]$, $M_{\mathrm{tot}} \in [2.52, 2.88]$, and $M_{\mathrm{chirp}} \in [1.10, 1.25]$.

- `M0RefSet` harbors our models. Because they are uniform in terms of numerical setup, code and physics, and have fixed chirp mass, we group them into a separate, reference dataset. The models of this set span $q \in [1, 1.82]$, $\tilde{\Lambda} \in [400, 850]$, $M_{\mathrm{tot}} \in [2.73, 2.88]$ with the chirp mass $M_{\mathrm{chirp}} = 1.19$.

- `LeakSet` comprises models with leakage scheme as neutrino treatment and microphysical EOSs. The dataset includes a subset of models from Radice et al. (2018a) and the set of models from Lehner et al. (2016b). The models

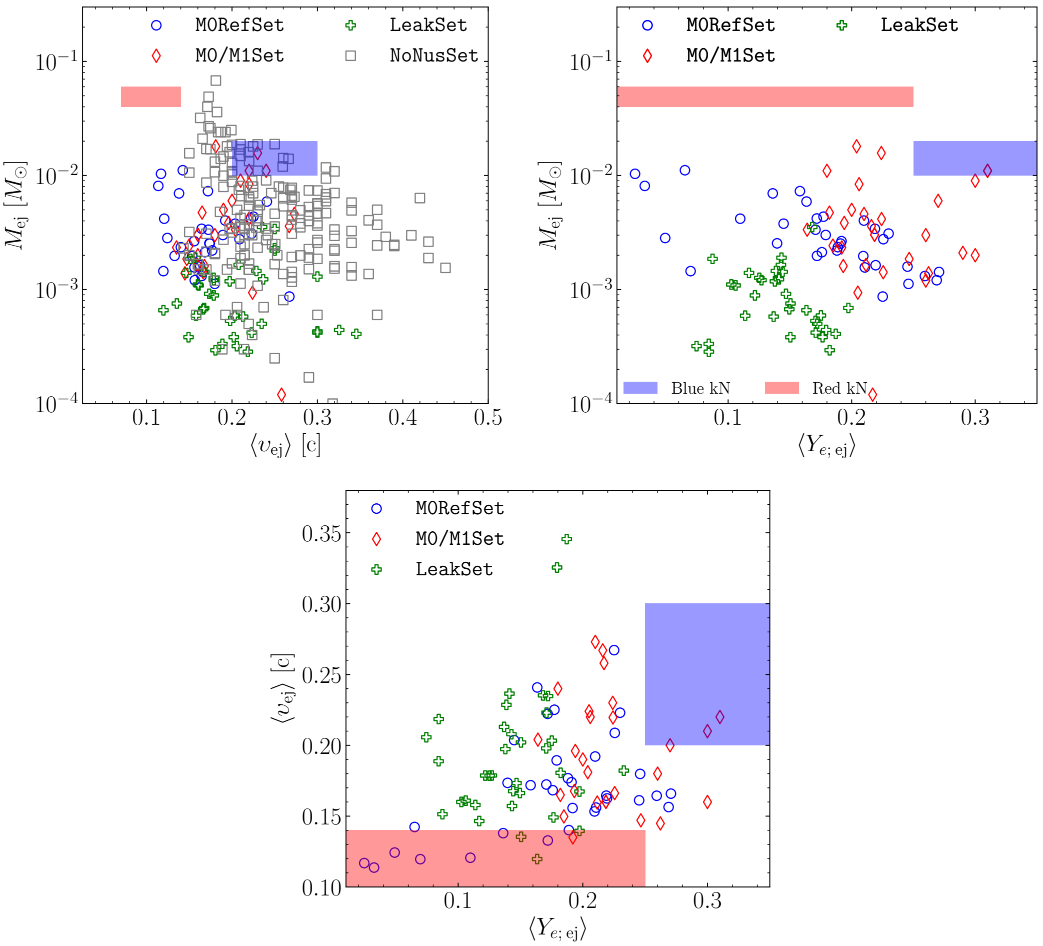

FIGURE 3.10: Properties of DE for all datasets (Tab. 3.1), including total ejecta mass, $M_{\rm ej}$, mass-averaged electron fraction, $\langle Y_{\rm e;ej}$, and velocity $\lambda \upsilon_{\rm ej}\rangle$. The colored patches represent ranges inferred from AT2017gfo kN models (Villar et al., 2017a; Siegel, 2019) (see Ch. 5 for the kN discussion). (Adapted from Nedora et al. (2020)).

in this dataset span $q \in [1, 1.31]$, $\tilde{\Lambda} \in [116, 1688]$, $M_{\rm tot} \in [2.40, 3.42]$, and $M_{\rm chirp} \in [1.04, 1.49]$.

- `NoNusSet` is composed of models with piecewise-polytropic EOSs of Bauswein et al. (2013b), Hotokezaka et al. (2013b), Dietrich et al. (2015, 2017a), and Kiuchi et al. (2019), in which temperature effects are approximated by a gamma-law pressure contribution, while composition and weak effects are neglected. The models in this dataset span $q \in [1, 2.06]$, $\tilde{\Lambda} \in [50, 3196]$, $M_{\rm tot} \in [2.4, 4.0]$, and $M_{\rm chirp} \in [1.04, 1.74]$.

In total 324 NR models are collected. In cases where $\tilde{\Lambda}$ is not available, we compute it by solving TOV equations[5] for the corresponding gravitational masses and EOSs. For a subset of models with polytropic EOSs of Bauswein et al. (2013a) and Kiuchi et al. (2019), however, the EOS data are not available and the $\tilde{\Lambda}$ cannot be estimated. We exclude these models from the statistical analysis. Overall, out of 324, we consider 271 models for which the required binary data are available/computed. For all 271 models the ejecta mass, $M_{\rm ej}^{\rm d}$, is present. The average velocity, $\langle v_{\infty}^{\rm d} \rangle$, is available for only 246 models, as a subset of models from Kiuchi et al. (2019) does not contain this information. The electron fraction is found for 99 models, as we exclude the subset of models of Lehner et al. (2016b) with leakage scheme for which these data are not given.

The collected data are shown in Fig. 3.10. We note that the overall properties of DE are similar between the `M0RefSet` and `M0/M1Set`. This is expected, as these datasets include similar, albeit not the same, physics, regarding EOS and neutrino treatment. The important exceptions are the high mass ratio models of `M0RefSet`, that undergo PC. DE ejecta from these models is of tidal origin only.

Comparing the properties of datasets with and without neutrino reabsorption, we observed that the the inclusion of this effect leads to an increase in DE mass, in addition to the expected increase in average electron fraction. This is especially noticeable when comparing models of `M0RefSet` and a subset of Radice et al. (2018a) with leakage scheme only.

In Appendix A.4 we report detailed statistical analysis, where we examine the change in mean values of ejecta properties between different datasets and fit the data with different fitting formulae found in the literature, as well as applying simple polynomials of q and $\tilde{\Lambda}$ of second order, $P_2^1(\tilde{\Lambda})$ and $P_2^2(q, \tilde{\Lambda})$, respectively. The results of this analysis are the following.

For the ejecta mass we observe that the inclusion of mass ratio into a fitting formula is required to capture the leading trends in data and the simple polynomial, $P_2^2(q, \tilde{\Lambda})$, shows a comparatively good statistical performance. The statistical analysis also suggests that the $M_{\rm ej}^{\rm d}$ depends sensibly on the physics input of the simulations: the neutrino scheme and EOS treatment. The magnitude of systematic uncertainties in the data, however, reduces the ability of any fitting formula to identify and quantitatively capture leading trends.

---

[5] The code for solving TOV equations for a NS with a tabulated EOS was developed by Sebastiano Bernuzzi, a simplified version of which is available at `http://sbernuzzi.gitpages.tpi.uni-jena.de/gr/`.

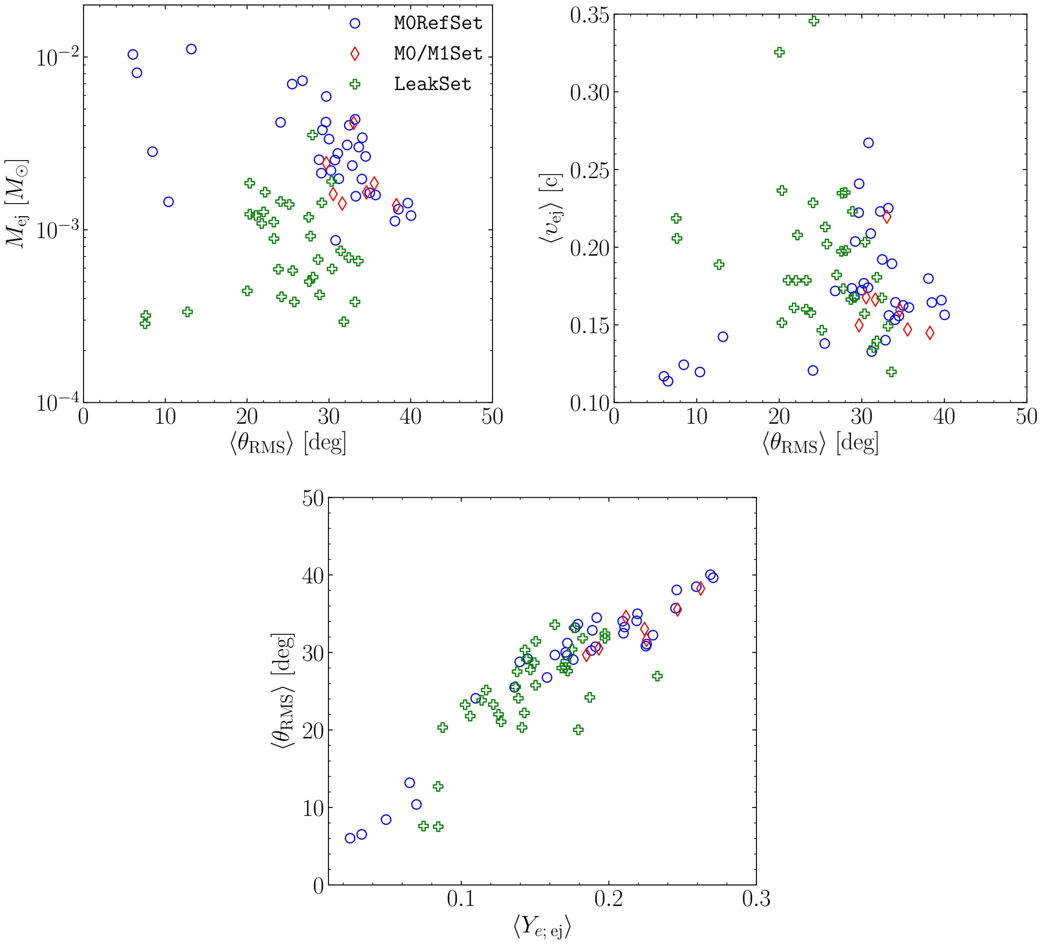

FIGURE 3.11: Same as Fig. 3.10, but including also the mass-averaged RMS half-opening angle about the orbital plane of the DE distribution, $\langle\theta_{\rm RMS}\rangle$. The plotted data is limited to datasets in which this quantity is available. (Adapted from Nedora et al. (2020)).

Considering the mass-averaged ejecta velocity, $\langle v_\infty^{\rm d}\rangle$, of the `M0RefSet` we find that it is in overall agreement with the dataset with neutrino leackage scheme of Radice et al. (2018a), and ranges from $0.11\,c$ to $0.27\,c$. However, while in that study there was no apparent correlation observed between the velocity and binary parameters, upon visual inspection we find that in models of `M0RefSet` the $\langle v_\infty^{\rm d}\rangle$ is correlated with $\tilde\Lambda$, as shown in Fig 3.9. This might be attributed to the fact that the `M0RefSet` encompass models with fixed chirp mass. The best fitting formula to the $\langle v_\infty^{\rm d}\rangle$, among those considered, is $P_2^2(q,\tilde\Lambda)$, which appears to be able to capture the leading trends in the data. The ejecta velocity shows a strong dependency on the neutrino treatment and binary parameters, specifically, mass ratio.

Considering the average value of the mass-averaged electron fraction, $\langle Y_e^{\rm d}\rangle$, we find that when only models of `M0RefSet` are considered, $\langle Y_e^{\rm d} \rangle$ varies between 0.03, found in very high mass ratio binaries, that produce cold, low-Y_e, tidal ejecta, and 0.27 in $q \sim 1$ binaries, where the contribution from the shocked component is significant (see also Fig. 3.9). Naturally, datasets that include the effects of neutrino absorption display on average higher $\langle Y_e^{\rm d} \rangle$. Here we only consider the polynomials as fitting formulae. The analysis suggests that $P_2^2(q, \tilde{\Lambda})$ is the best fitting one, as it is able to reproduce both the low-Y_e and high-Y_e models of `M0/M1Set` and `M0RefSet`.

The ejecta geometry has been shown to be very important for modeling EM counterparts to mergers (see Chapter 5 and Chapter 6). However, its statistical analysis is very non-trivial. Because of the limited data, and for the sake of simplicity, we consider the mass-averaged RMS half-opening angle of the ejecta about the plane of the binary, $\langle \theta_{\rm RMS} \rangle$. We introduce the $\langle \theta_{\rm RMS} \rangle$ in accordance with Radice et al. (2018a), assuming the axial symmetry and computing:

$$\langle \theta_{\rm RMS} \rangle = \frac{180}{\pi} \left(\frac{\sum m_i \theta_i^2}{\sum m_i} \right)^{1/2}, \tag{3.1}$$

where θ_i and m_i are the angle (from the binary plane), and the mass of an element of DE, respectively. Unfortunately, this quantity is available only for the `M0RefSet` and for a subset of models of Radice et al. (2018a). Hence, the statistical analysis is limited to a small sample of models.

The dependency of the $\langle \theta_{\rm RMS} \rangle$ on other ejecta properties discussed above is shown in Fig. 3.11. With respect to the models of Radice et al. (2018a), we observe that the models of `M0RefSet` have overall larger $\langle \theta_{\rm RMS} \rangle$. This suggests that the inclusion of neutrino reabsorption leads to a more spherically distributed ejecta. The third panel of Fig. 3.11 shows a clear linear relation between the $\langle \theta_{\rm RMS} \rangle$ and $\langle Y_e^{\rm d} \rangle$ that can be attributed to the mass ratio dependency of DE properties observed above, which we extend as follows. Binaries with large mass ratios have ejecta of mostly tidal origin that is confined to the binary plane and characterized by a low electron fraction. Meanwhile, binaries with $q \sim 1$ have ejecta of both tidal and shocked origin that are both more spread out and more processed by shocks and neutrino irradiation having, thus, higher $\langle Y_e^{\rm d} \rangle$. Similar to the case of $\langle Y_e^{\rm d} \rangle$, we find that the $P_2^2(q, \tilde{\Lambda})$ provides the best fit to the data. All coefficients to all fitting formulae are reported in Appendix A.

Overall, we observe that the properties of DE depend on mass ratio and EOS softness that can be parameterized with $\tilde{\Lambda}$, and a simple polynomial in these two

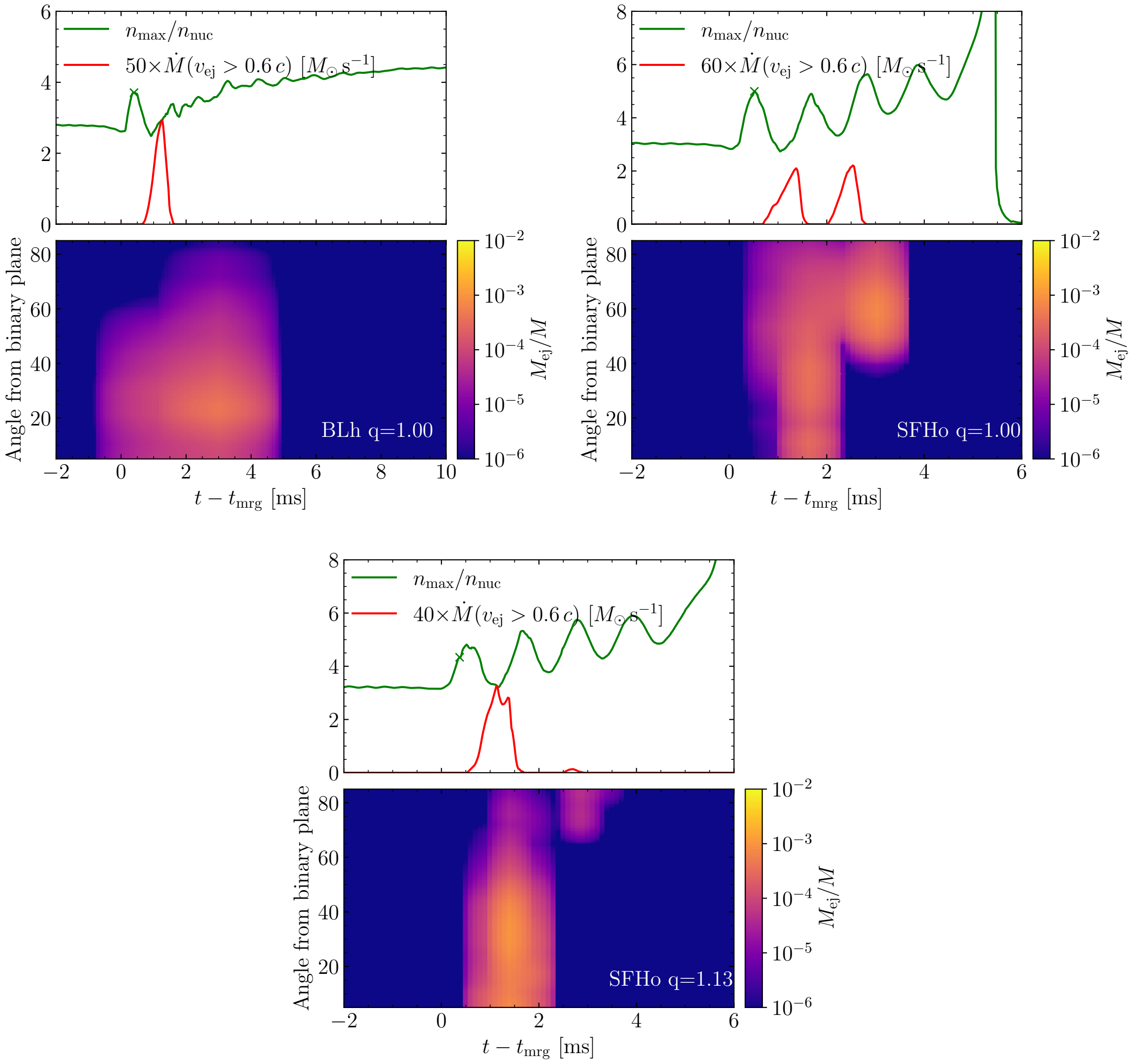

FIGURE 3.12: Time evolution of the fast tail of DE, $\dot{M}(\upsilon_{\rm ej} > 0.6\,c)$, alongside the time evolution of normalized central density $n_{\rm max}/n_{\rm nuc}$ for three simulations, BLh $q = 1.00$, SFHo $q = 1.00$ and SFHo $q = 1.13$, one per panel. The lower subpanel on each panel depicts the time evolution of the fast tail of DE angular distribution. In both panels the outflow rate and histograms are computed at a radius of $R = 443$ km and shifted in time by $R\langle\upsilon_{\rm fast}\rangle^{-1}$, $\langle\upsilon_{\rm fast}\rangle$ being the mass averaged velocity of the fast tail at the radius R. (Adapted from Nedora et al. (2021a)).

quantities show a comparable or better performance with resepct to other fitting formulae available in the literature. However, a larger sample of ab-initio NR simulations with complete physics and publicly available data is required to refine these relations.

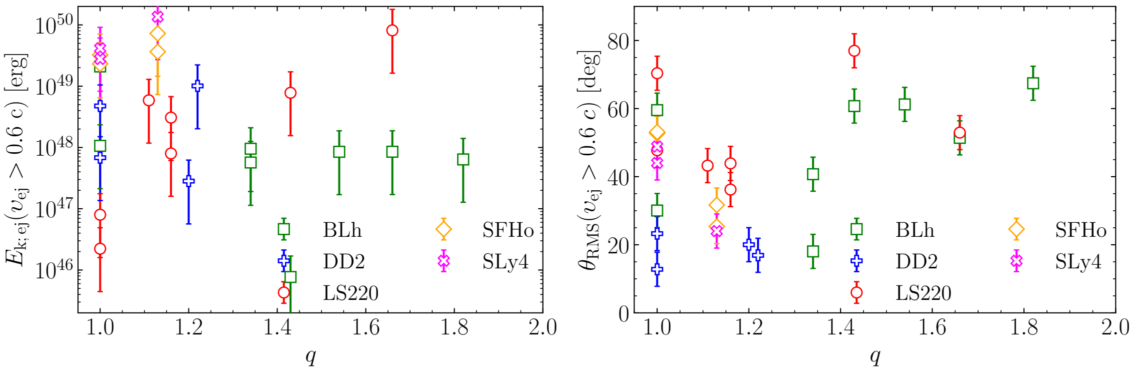

FIGURE 3.13: Total kinetic energy (*left panel*) and RMS half-opening angle (*right panel*) as a function of binary mass ratio, q, for the of the fast tail of DE. (Adapted from Nedora et al. (2021a)).

3.2.2 Fast tail of dynamical ejecta

In order to analyze the low mass, very fast component of DE, we choose the furthest extraction sphere from the remnant, at $R = 443\,\mathrm{km}$. This ensures that the ejecta had the longest evolution within the simulation domain. In addition, this allows for a consistent comparison with the results of Radice et al. (2018a). Following the authors, we define the fast ejecta component (tail) as the ejecta with $v_\infty \geq 0.6\,c$.

We find a non-negligible amount of fast ejecta in all our simulations except for those with very stiff EOSs and high mass ratios. The DE velocity distribution from these models shows a sharp cut-off at $\lesssim 0.5\,c$ that can be attributed to the fact that in these simulations, DE are primarily of tidal origin and display on average lower velocities, that, in turn, are set mainly by NSs velocities at the last orbit and the system escape velocity.

We show the mechanism that is responsible for producing most of the fast ejecta in Fig. 3.12. We find that the ejection of mass with velocity $v > 0.6\,c$ coincides with core bounces. This was previously noted by Radice et al. (2018a). Most of the fast ejecta originate at the first core bounce in models with moderately soft EOSs or large mass ratios, *e.g.*, the BLh $q = 1.00$ model. Similar behaviour is observed in models with higher mass ratios and softer EOSs. We also observe that in models with very soft EOSs (and small mass ratios), *e.g.*, the SLy4* $q = 1.00$ model, a strong influx of fast ejecta occurs during the second core bounce. Notably, while the first-bounce component is generally equatorial, the second-bounce component is more polar. A possible explanation for this might include the increase in baryon pollution of the low latitude region around the post-merger remnant.

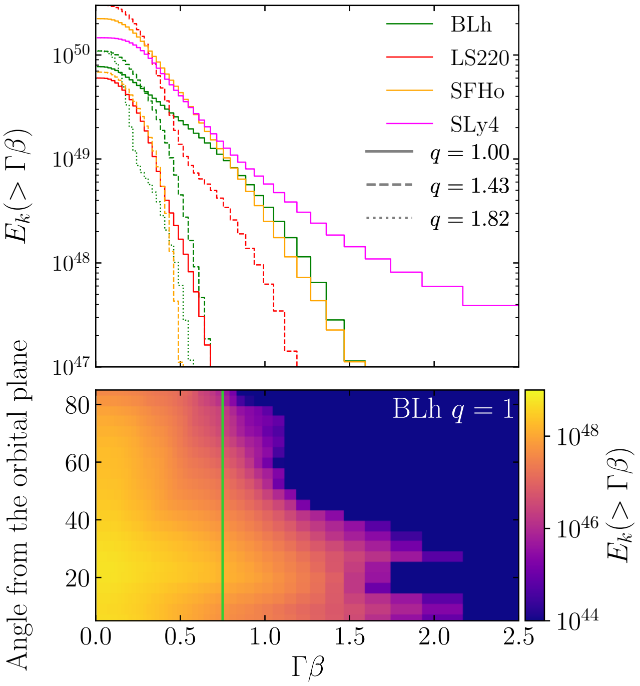

FIGURE 3.14: Cumulative kinetic energy distribution (*top panel*) for a set of representative model and its angular dependence for the BLh $q = 1.00$ model (*bottom panel*). The green line corresponds to $\upsilon_{\rm ej} = 0.6$. (Adapted from Nedora et al. (2021a)).

In our sample of simulations, the resolution does not affect whether there is a fast tail of DE or not, but it does affect its mass, and we find that it changes by a factor of a few between `SR` and `HR` simulations. A larger sample of simulations performed at high resolution is required to assess this uncertainty more quantitatively.

Mass-averaged properties of the fast ejecta tail, such as velocity, electron fraction and angular distribution appear to be robust with resolution, similar to what was observed for DE overall (see Tab. 2.2). We find that the mass-averaged velocity is close to $0.6\,c$, increasing with the softness of the EOS. The mass-averaged electron is generally above 0.25, indicating that these ejecta were shock-heated and reprocessed by neutrinos. The high average electron fraction implies that only weak r-process nucleosynthesis would occur, producing elements up to the 2nd r-process peak (Lippuner et al., 2015) (see Sec. 1.1.4 and Chapter 4).

The total kinetic energy of the fast tail, $E_{\rm k}(\upsilon > 0.6\,c)$, is shown in Fig. 3.13, first panel. Considering the resolution dependency of the ejecta properties discussed above, we set a conservative error bar of ∼1 order of magnitude. The figure shows that

TABLE 3.2: Summary table of the spiral-wave winds properties of long-lived remnants. The columns contain the following information, starting from the left. Equation of state, mass-ratio, available resolutions, inclusion of subgrid turbulence, time of the simulation end, mass of the spiral-wave winds, mass-loss rate via spiral-wave winds, mass-averaged electron fracton, terminal velocity and, finally, RMS angle for spiral-wave winds. For these four quantities we give the mean value among the resolutions and one-sigma deviations. For binaries for which only one resolution is present, the error is assumed to be 20% of the value. (Adapted from Nedora et al., 2021b).

EOS	q	Resolution	GRLES	$t_{\rm end}$ [ms]	$M_{\rm ej}^{\rm w}$ [$10^{-2}M_{\odot}$]	$M_{\rm ej}^{\rm w}/\Delta t$ [$M_{\odot}/s$]	$\langle Y_e^{\rm w}\rangle$	$\langle v_{\infty}^{\rm w}\rangle$ [c]	$\langle\theta_{\rm ej}^{\rm w}\rangle$
BLh	1.00	`SR HR LR`	✓	43.3 91.8 23.1	$0.39^{+0.07}_{-0.07}$	$0.70^{+0.32}_{-0.32}$	$0.31^{+0.01}_{-0.01}$	$0.12^{+0.01}_{-0.01}$	$27.06^{+2.61}_{-2.61}$
BLh	1.00	`SR`	✗	103.2	$1.12^{+0.57}_{-0.57}$	$1.07^{+0.21}_{-0.21}$	$0.34^{+0.01}_{-0.01}$	$0.12^{+0.02}_{-0.02}$	$15.72^{+2.00}_{-2.00}$
BLh	1.18	`LR`	✓	69.4	$1.28^{+0.64}_{-0.64}$	$1.23^{+0.25}_{-0.25}$	$0.33^{+0.01}_{-0.01}$	$0.11^{+0.02}_{-0.02}$	$14.98^{+2.00}_{-2.00}$
BLh	1.43	`LR SR`	✓	35.1 59.6	$0.75^{+0.18}_{-0.18}$	$1.06^{+0.67}_{-0.67}$	$0.27^{+0.01}_{-0.01}$	$0.09^{+0.01}_{-0.01}$	$19.43^{+2.22}_{-2.22}$
BLh	1.54	`LR`	✓	45.8	$0.63^{+0.32}_{-0.32}$	$0.44^{+0.09}_{-0.09}$	$0.32^{+0.01}_{-0.01}$	$0.10^{+0.02}_{-0.02}$	$21.46^{+2.00}_{-2.00}$
BLh	1.66	`LR SR`	✓	64.6 20.1	$0.12^{+0.09}_{-0.09}$	$0.37^{+0.34}_{-0.34}$	$0.33^{+0.05}_{-0.05}$	$0.13^{+0.01}_{-0.01}$	$52.08^{+20.89}_{-20.89}$
DD2	1.00	`LR SR HR`	✓	123.0 113.0 74.4	$1.25^{+0.14}_{-0.14}$	$1.30^{+0.19}_{-0.19}$	$0.30^{+0.01}_{-0.01}$	$0.17^{+0.00}_{-0.00}$	$14.88^{+0.87}_{-0.87}$
DD2	1.20	`LR SR HR`	✗	37.3 91.0 55.2	$0.48^{+0.09}_{-0.09}$	$0.74^{+0.24}_{-0.24}$	$0.26^{+0.01}_{-0.01}$	$0.15^{+0.00}_{-0.00}$	$24.54^{+2.23}_{-2.23}$
DD2	1.43	`LR SR`	✓	37.7 62.0	$0.60^{+0.02}_{-0.02}$	$0.51^{+0.06}_{-0.06}$	$0.23^{+0.12}_{-0.12}$	$0.16^{+0.00}_{-0.00}$	$21.74^{+0.03}_{-0.03}$
SFHo	1.43	`SR`	✓	46.5	$0.58^{+0.30}_{-0.30}$	$0.43^{+0.09}_{-0.09}$	$0.31^{+0.01}_{-0.01}$	$0.17^{+0.02}_{-0.02}$	$22.67^{+2.00}_{-2.00}$
SLy4	1.43	`SR`	✓	40.3	$0.53^{+0.27}_{-0.27}$	$0.38^{+0.08}_{-0.08}$	$0.29^{+0.01}_{-0.01}$	$0.18^{+0.02}_{-0.02}$	$23.52^{+2.00}_{-2.00}$

the $E_{\mathrm{k}}(\upsilon > 0.6\,c)$ ranges between $\sim 10^{46}$ erg, and $\geq 10^{50}$ erg, without clear dependency on the EOS, even though models with very soft EOSs (*e.g.*, SLy4 and SFHo) tend to display larger energies. The dependency on the mass ratio is more noticeable, especially for SLy4, SFHo and LS220 EOSs, where for the latter, the $E_{\mathrm{k}}(\upsilon > 0.6\,c)$ increases by ~ 3 orders of magnitude between $q = 1$ and $q = 1.7$.

Considering the RMS half-opening angle of the fast ejecta around the orbital plane (Fig. 3.13, second panel) we set the conservative error of 5 degrees based on the comparison with higher resolution simulations. We observe that in models with stiff EOSs, *e.g.*, DD2 EOS, where the first core-bounce ejection mechanism dominates, the fast ejecta tail is generally equatorial. Meanwhile, in simulations with soft EOSs and high mass ratios, the fast ejecta show a more uniform angular distribution set by a combination of the core dynamics and finite temperature effects.

Next we examine the distribution of the cumulative kinetic energy of DE, defined as the total kinetic energy of DE with velocity exceeding a certain value, and denoted as $E_k(>\Gamma\beta)$. Here β is the ejecta velocity expressed in units of c and $\Gamma = 1/\sqrt{1-\beta^2}$ is the Lorentz factor. The result is shown in Fig. 3.14. We observe that for all models the bulk of the kinetic energy is confined to the low $\Gamma\beta$ matter. However, models with soft EOSs, (*e.g.*, SLy4) and small mass ratios show an extended high $\Gamma\beta$ tail.

The bottom panel of Fig. 3.14 illustrates the cumulative kinetic energy distribution in terms of $\Gamma\beta$ and angle from the plane of the binary for the BLh $q = 1.00$ model. The plot shows that the distribution is not uniform with respect to the angle. High velocity matter is confined more to the plane of the binary, while a large fraction of very energetic matter is channeled into the polar region.

3.2.3 Spiral-wave wind

As we discussed in the previous section, the interaction between the NS remnant and the disk generates density waves that propagate outwards through the disk and induce massive outflows, SWW (see Sec. 3.1). We track SWW as the matter unbound according to the Bernoulli criterion (see Sec. 2.6.4), starting after DE mass flux has saturated (*e.g.*, $\gtrsim$10 ms post-merger), and using the extraction sphere located at $R = 294$ km.

In Tab. 3.2 we report the overall properties of SWW for all models with long-lived NS remnants that were also evolved for a sufficiently long time. Notably, in all simulations, SWW persist until the time these simulations were terminated without saturation. This is the manifestation of the mechanism driving the outflow: the angular

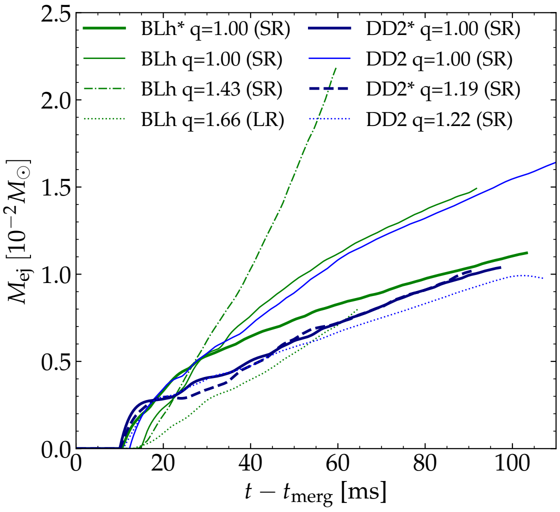

FIGURE 3.15: Time evolution of the cumulative SWW mass for a set of simulations with long-lived remnants. Here t_0 indicates the moment of merger. The wind calculation starts when DE saturates $\gtrsim$10 ms post-merger. Adapted from Nedora et al. (2019).

momentum and mass transport induced by the dynamical instabilities in the remnant, the $m = 1, 2$ modes. And, as the $m = 1$ modes are not efficiently damped (Paschalidis et al., 2015; East et al., 2016a; Lehner et al., 2016a; Radice et al., 2016b), SWW could theoretically continue until the system collapses to a BH or reaches an equilibrium.

The time evolution of the cumulative mass of SWW is shown in Fig. 3.15. The strongest SWW are found in binaries with $q > 1$, such as the BLh $q = 1.43$ (`SR`) model. With the mass-loss rate $\sim$0.5 $M_{\odot}$/s these models can eject $\sim$0.02 $M_{\odot}$ within $\sim$50 ms of the post-merger evolution. Meanwhile, models with softer EOSs reach similarly high mass flux at lower mass ratios. For instance, the mass flux of the BLh* $q = 1.66$ model is achieved by the LS220* $q = 1.22$ model. A possible explanation for this is that the softer the EOS is, the stronger are the $m = 1$ modes in the remnant (see Sec. 3.1).

We observe that the inclusion of turbulent viscosity enhances the SWW mass by $\sim$25% in the case of the DD2 $q = 1.00$ model, exceeding the finite resolution effects which are $\sim$15% and $\sim$8% for the SWW mass when the resolution increases from `SR` to `HR`. The resolution effects on other wind properties, *e.g.*, velocity and Y_e, are found to be within 4%.

When a NS remnant collapses to a BH and the mechanism that injects angular momentum into the disk shuts down, the SWW mass flux subsides. Thus, the total ejected mass via SWW is directly related to the lifetime of the NS remnant, in addition to the binary parameters and the EOS.

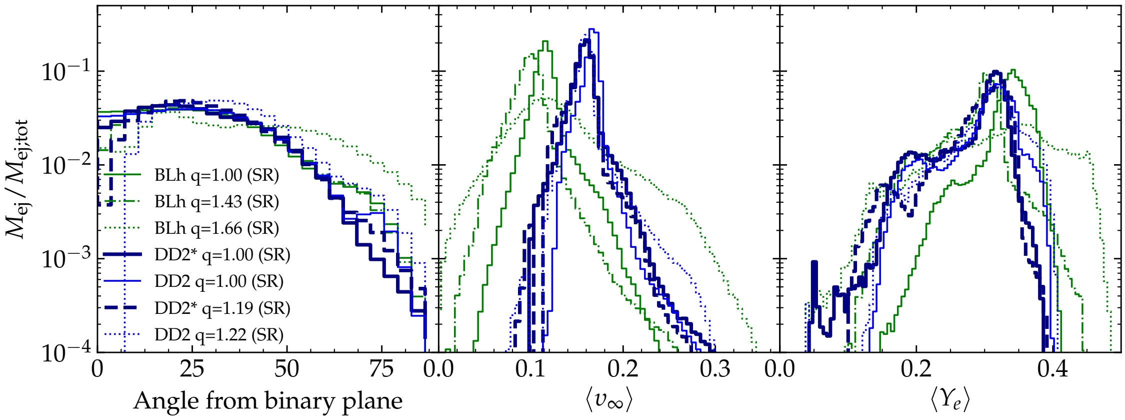

FIGURE 3.16: Properties of the SWW from the set of simulations with long-lived remnants. From left to right, the angular, velocity and electron fraction distributions are shown in a form of mass-histograms. (Adapted from Nedora et al. (2021b)).

The SWW mass flux depends on the disk configuration, as more extended disks have outer layers that are less gravitationally bound. In turn, the disk configuration is dependent on thermal effects. Higher temperatures lead to a stronger thermal pressure that increases the disk size. However, the dependency of the SWW mass flux on the stiffness of an EOS appears to be stronger, as stiffer EOSs lead to more massive disks, as discussed in Sec. 3.1. More simulations with longer post-merger evolution are needed to make a quantitative assessment.

We find that contrary to the mass flux, other properties of SWW depend only weakly on the binary parameters and the EOS. Mass-histograms of the wind angular distribution, velocity and electron fraction are displayed in Fig. 3.16 for several representative models. The angular distribution of SWW is similar to that of DE, displaying a broad distribution around the binary plane.

SWW have a high average electron fraction. Its overall broad distribution, $0.1 \lesssim \langle Y_e^{\rm w} \rangle \lesssim 0.4$, peaks at $\simeq$0.35. The low electron fraction material originates primarily during early times, when the material does not have enough time to be processed by neutrinos and before the outflow reaches quasi-steady state. The SWW average velocity is higher in models with stiffer EOSs, with the peak of the distribution lying between $\sim$0.1 c and $\sim$0.2 c. However, more simulations of the post-merger remnant long-term evolution are required to confirm and quantitatively investigate these trends.

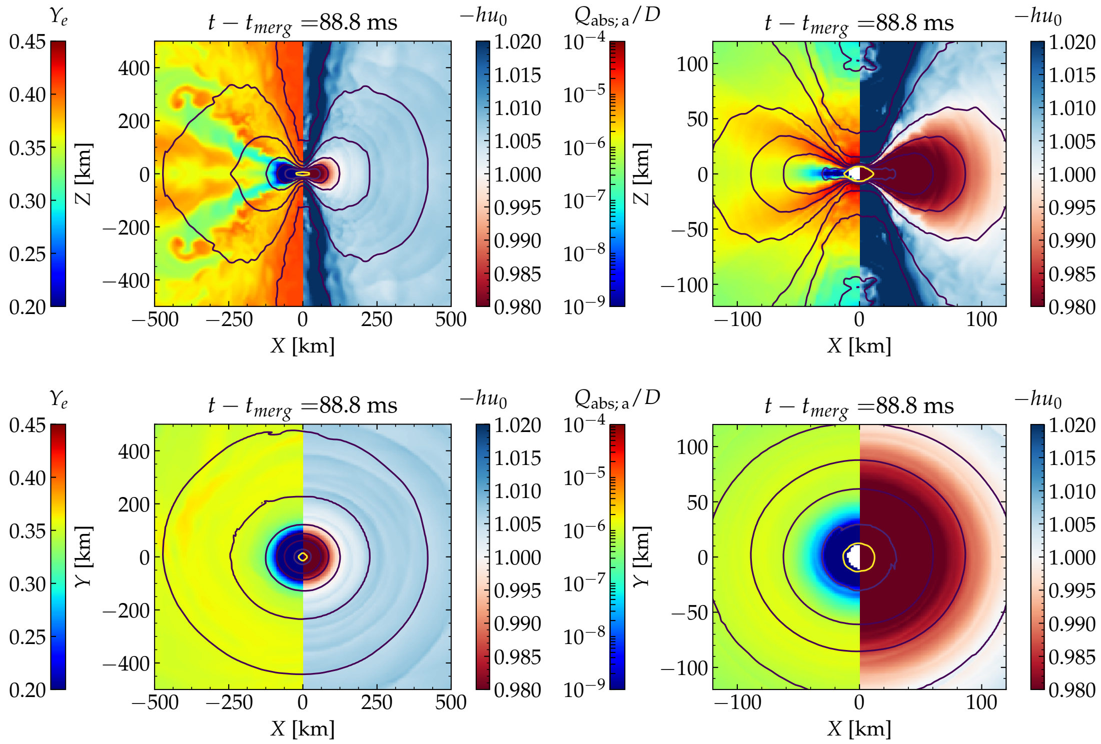

FIGURE 3.17: Snapshots of the BLh $q = 1.00$ model taken 88 ms post-merger, showing the distribution of electron fraction, Y_e, Bernoulli parameter, $-hu_t$, and electron anti-neutron absorption energy rate, $Q_{\mathrm{abs};\,\bar{\nu}_e}$ normalized to the fluid density D in units of $c^5/(GM_\odot)$. *Top row of panels* displays these properties in (x, z) plane, while the *bottom row* shows (x, y) slices. (Adapted from Nedora et al. (2021b)).

3.2.4 Neutrino-driven wind

In Sec. 1.1.3 we discussed that, the presence of strong neutrino fluxes may drive the emergence of baryonic winds. Since the strongest source of neutrinos is a NS remnant, such ν-driven winds are expected to be polar and characterized by elevated electron fraction (*e.g.* Perego et al., 2014). Having neutrino absorption included in our simulation setup (See Sec. 2.4), we assess whether there are ν-driven winds in our simulations. Naturally, we expect them to be a part of SWW, but polar and with high Y_e. For this analysis, for the sake of brevity, we focus on one simulation, BLh $q = 1.00$ (`SR`).

In the left column of plots in Fig. 3.17 we compare the Bernoulli parameter, $-hu_t$, and the fluid electron fraction. In the right column of the plots in Fig. 3.17 we compare the Bernoulli parameter with the heating energy rate due to electron anti-neutrino absorption, $Q_{\mathrm{abs};\,\bar{\nu}_e}$, computed by the M0 scheme (see Sec. 2.4) and normalized with the fluid's conserved rest-mass density. We observe that the electron fraction in the polar region ($\theta > 60°$, where θ is the angle from the binary plane) reaches $Y_e \sim 0.35$ due to the absorption of electron-type anti-neutrinos. The strongest neutrino heating occurs in the vicinity of the remnant, at densities $\rho \sim 10^{11}$ g cm^{-3}, roughly corresponding to the location of the neutrinosphere (Endrizzi et al., 2020), the region where neutrinos decouple from matter. Additionally, we found that if the neutrino absorption is not included into a simulation, *e.g.*, using the leakage scheme only, ν-driven winds are significantly suppressed.

Notably, there is no clear distinction between ν-driven winds and SWW, especially at intermediate latitudes ($\theta \sim 45°$), where both strong neutrino fluxes and spiral density waves are present. In order to compute the mass flux of ν-driven winds we impose additional criteria. We consider two physically motivated options, the geometrical, flagging the part of SWW as ν-driven winds if they are polar, *i.e.*, $\theta > 60°$, and the composition criterion, *i.e.*, if $Y_e > 0.35$.

We find that ν-driven winds are not steady state outflows, contrary to the bulk of SWW. After the initial strong rise, the mass flux rapidly decays in time, and for most models, stops before the simulation is terminated. This behaviour is independent of the criterion we use. We attribute this to the rise of the baryon loading above the remnant as the material gets lifted by the thermal pressure from the disk.

The total mass of ν-driven winds is $\sim 10^{-3} - 10^{-4} M_{\odot}$. Its properties resemble those reported in *e.g.*, Dessart et al. (2009), Perego et al. (2014), and Fujibayashi et al. (2020b). Notably, in some of the works, ν-driven winds were found to require longer timescales to develop. This can be attributed to the strict criteria to isolate the ν-driven winds and by the absence of SWW in other works. Additionally, our simulations might not be sufficiently long to achieve the conditions required for the development of the quasi-steady state ν-driven winds.

Chapter 4

Nucleosynthesis

In Sec. 1.1.4 we discussed the conditions for, and sites of, r-process nucleosynthesis, and its contribution to the Universe's chemical evolution. In this chapter we expand upon this discussion by computing the nucleosynthetic yields in ejecta from our BNS merger models and comparing the result with solar abundances. In Sec. 4.1 we briefly overview methods for computing r-process nucleosynthesis in merger ejecta, focusing on a recently developed nuclear reaction network `SkyNet` (Lippuner et al., 2017b; Lippuner, 2018) and how the final nucleosynthetic yields can be parameterized for quick estimation of final abundances in BNS merger ejecta. In Sec. 4.2 we present our results.

4.1 Modeling the nucleosynthesis

To study nucleosynthesis in different physical environments, it is necessary to model nuclear reactions, computing the total energy generation (*e.g.* Weaver et al., 1978; Mueller, 1986; Timmes et al., 1999) and tracking the evolution of the whole ensemble of nuclear species. A mathematical and/or numerical model that describes entangled nuclear reactions, tracking the evolution of abundances of various species, coupled by non-linear reaction rates (RRs), is called a nuclear reaction network (NRN).

The complexity of a network, *i.e.*, the number of species and reactions evolved, varies depending on the intended implementation. The most challenging are the neutron capture processes that produce unstable nuclides that decay via complex chains of reactions involving hundreds or even thousands of steps. Thus, a NRN has to be adequately complex for modeling the s-process (*e.g.* Prantzos et al., 1990; Käppeler et al., 2011; Nishimura et al., 2017) and even more so to model the r-process. Targets for such studies include neutrino driven winds from CCSNe (*e.g.* Woosley et al., 1992; Arcones et al., 2010; Wanajo, 2013), outflows from magnetorotational CCSNe (*e.g.* Winteler et al., 2012; Nishimura et al., 2015), and outflows from compact object mergers. In the latter case, several sites with different physical conditions require modeling. (See Lippuner (2018) for an overview).

Several NRNs are available in the literature. In particular: a set of networks by Timmes et al. (1999)[1], `XNet` by Hix et al. (1999)[2], `NucNet` by Meyer et al. (2007)[3] and `SkyNet` by Lippuner et al. (2015)[4]. The latter is a popular choice to study nucleosynthesis in neutron rich environments (*e.g.* Lippuner et al., 2015; Radice et al., 2016a, 2018a).

4.1.1 Basics of a nuclear reaction network

The key part of a NRN is modeling the interaction between two or more nuclides. These interactions are characterized by RRs as well as single particle reactions such as β-decay. Charged particle reactions require the Coulomb barrier to be overcome, and in general, RRs depend strongly on the particle energy as well as on resonances in compound nuclear systems (see *e.g.*, §4 in Clayton (1968)). Generally, only a subset of particles is evolved by a NRN, while for others the conditions are assumed to be unchanged. For instance, photons are assumed to be in equilibrium at all times, while electron and positron densities are set by the charge neutrality.

When describing particle interactions and nuclide transmutations it is common to introduce entrance and exit channels representing reactants and products. Then, a RR is defined as a speed at which a reaction proceeds per particle in the entrance channel. For example, if there is no change between particles in the entrance and exit channels, the RR is zero. A particularly useful quantity is *abundance*, Y_i, defined as

$$Y_i = \frac{n_i}{n_B} = \frac{N_i/V}{N_B/V} = \frac{N_i}{N_B}, \tag{4.1}$$

where V is the volume of the fluid element, N_i and N_B are the total numbers of particles of species i and baryons respectively. It is usually abundances that are evolved by a NRN rather than particle number densities, n_i, as the latter depend on a volume that is often not constant. The abundance evolution equation reads

---

[1] http://cococubed.asu.edu/code_pages/burn.shtml
[2] http://eagle.phys.utk.edu/xnet/trac
[3] https://sourceforge.net/projects/nucnet-tools
[4] https://bitbucket.org/jlippuner/skynet

$$\frac{\mathrm{d}Y_i}{\mathrm{d}t} = \sum \lambda_\alpha (-R_i^\alpha + P_i^\alpha) N_i^\alpha \prod_{m \in \mathcal{R}_\alpha} Y_m^{N_m^\alpha} \tag{4.2}$$

where λ_α are the RRs of the forward processes, R_i^α and P_i^α are the reactants and the products respectively, N_i^α is the number of particles of the species i, and $Y_m^{N_m^\alpha}$ are the abundances of the particles of species i (see *e.g.*, Hix et al. (1999)).

`SkyNet` solves the system of coupled, first-order, non-linear ordinary differential equations (ODEs), Eq. (4.1), for a given set of reaction rates. Eq. (4.1) can be understood as follows. The time derivative of the abundances (of species i) is given by the sum over all reactions in which the species in question participate. Each reaction contribution consists of multipliers: a RR; a factor describing creation or destruction of particles (of species i); and abundances of reactants.

As RRs can span many orders of magnitude, the system of ODEs is very stiff (Timmes et al., 1999; Hix et al., 2006), and implicit ODE solvers are more suitable for it (Timmes et al., 1999; Winteler et al., 2012; Longland et al., 2014). `SkyNet` relies on the first-order implicit backward Euler method (Hix et al., 1999). Thus, for a given temperature and density, which are functions of time, the network evolves a composition vector, $Y(t)$, via the implicit backward Euler method, obtaining the abundances at the end of a timestep as well as the time derivative of the abundances, $\dot{Y}(Y, T, \rho)$, from known abundances at the beginning of it.

4.1.2 Parameterized nucleosynthesis

A way to evaluate the nucleosynthetic yields in BNS merger ejecta in postprocessing, is to run a NRN coupled with a hydrodynamical evolution model on ejecta, or on Lagrangian tracer particles evolved by the NR code itself (*e.g.* Goriely et al., 2011; Korobkin et al., 2012; Grossman et al., 2014; Wanajo et al., 2014; Just et al., 2015; Martin et al., 2015). This is, however, numerically expensive when the number of BNS merger models is large. Another approach is to construct a parameterized nucleosynthesis model, computed for a grid of parameters that describe the ejecta, then map the NR ejecta properties onto this grid to estimate the final abundances (Lippuner et al., 2015). This method was successfully applied in Radice et al. (2016a, 2018a). In Radice et al. (2018a) the result was compared to the direct nucleosynthesis calculations on tracer particles. It was shown that within a factor of two, both methods yield similar results. However, several caveats were pointed out, including the errors arising in ignoring the actual density history ($\simeq$25%). Moreover, it was noted that due to the approximation of Eulerian flow with Lagrangian flow, an error of $\sim$40% in final abundances can be expected.

The method can be summarized as follows. The r-process in a given fluid element depends on how fast it decompresses from the merger environment, and on ejecta parameters, *e.g.*, mass, velocity and composition (Lippuner et al., 2015). Thus, the final abundances can be pre-computed for a grid of these parameters. The grid that we use is the following:

- The electron fraction, Y_e, is sampled uniformly between 0.01 and 0.5 ($Y_e > 0.5$ is not favorable for the r-process).
- The specific entropy, s, is sampled logarithmically between 1 and 100 k_B/baryon.
- The expansion timescale, τ, is sampled between 0.1 ms and 500 ms.
- The density profile is that of a homologously (self-similar) expanding fluid, *i.e.*, velocity is proportional to the radius, $\upsilon(r) \propto r$.

The fixed choice of the density profile,

$$\rho(t) = \rho(s, Y_e, T = 6\mathrm{GK})\left(\frac{3\tau}{2.72t}\right)^3, \tag{4.3}$$

gives the control over the dynamical timescale for r-process calculations while also matching the expected density profile, as ejecta reaching the extraction sphere has already significantly decompressed, and its density has decreased by $\sim$3 orders of magnitude. This profile was shown to be in agreement with NR simulations (Foucart et al., 2014; Lippuner et al., 2015). The value of the initial density, $\rho_0 = \rho(s, Y_e, T = 6\mathrm{GK})$, is computed from nuclear statistical equilibrium (NSE) for a given value of entropy and temperature. The ρ_0 spans the range $(10^5 - 10^{12})\,\mathrm{g\ cm^{-3}}$.

Under the assumption that ejecta from BNS mergers expand homologously, its density profile reads

$$\rho(t) = \rho_E\left(\frac{\upsilon_E t}{r_E}\right)^{-3} = \rho_E\left(\frac{\upsilon_E t}{r_E}t\right)^{-3}, \tag{4.4}$$

where ρ_E, υ_E, and r_E are the density, velocity and radius of ejecta. Solving Eq. (4.4) and Eq. (4.3) together, the expansion timescale, τ, can be obtained.

In order to compute the nucleosynthetic yields, we discretize ejecta from our BNS merger models in the parameter space of (s, Y_e, τ), compute the yields in each bin, and sum all the contributions.

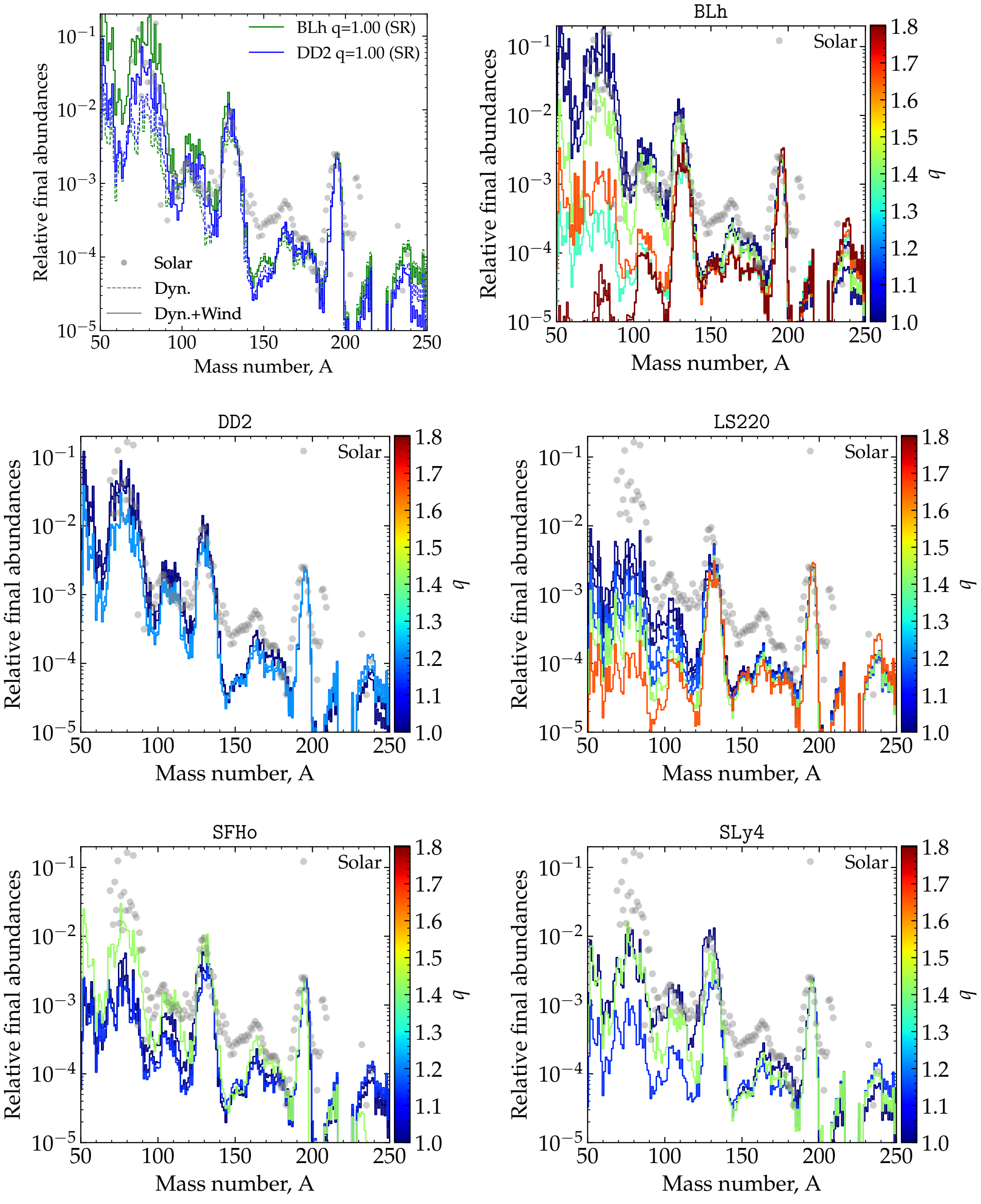

FIGURE 4.1: *The first panel* shows nucleosynthesis yields as a function of atomic number, A, from DE only (dashed lines) and DE plus SWW (solid lines). *The other five panels* show the total nucleosynthetic yields from the total ejecta from all simulations (one EOS per panel). The binary mass ratio is color-coded. In all panels, the gray markers indicate solar abundances, and model abundances are normalized to solar at $A = 195$. (Adapted from Nedora et al. (2021b))

4.2 Nucleosynthetic yields in BNS ejecta

With the procedure outlined above we compute the isotopic abundances of the r-process elements 32 years after merger.

A particular novelty of our analysis with respect to the previous works by Radice et al. (2016a, 2018a) (in addition to the novelties of our simulation set discussed in Sec. 2.6), is the presence of an additional, massive ejecta component, SWW (see Sec. 3.2).

We compare the model abundances with the recently updated solar residual r-process abundances from Prantzos et al. (2020), multiplying the model abundances by a constant factor that brings the abundances at $A = 195$ to the solar ones. This normalization allows us to quantitatively assess relative abundances in different models.

Total ejecta from models with long-lived NS remnants is dominated by SWW, (see Sec. 3.2). In the first panel of Fig. 4.1 we compare the final abundances in DE and in the total ejecta (including SWW). We focus on two models, BLh $q = 1.00$ and DD2 $q = 1.00$. The electron fraction of SWW is higher than that of DE, and thus the r-process nucleosynthesis in SWW produces primarily light elements around the first r-process peak, $A < 95$. We emphasize that we compare only relative abundances, as all the results have been rescaled by normalization. The plot shows that the r-process in ejecta from the BLh $q = 1.00$ model produces a larger amount of light elements than in ejecta from DD2 $q = 1.00$. This can be attributed to the higher electron fraction in SWW from the former. In both cases, however, the abundances of light elements are very close to solar.

In other panels of Fig. 4.1 we show nucleosynthesis yields from all ejecta components for all our simulations. For models with short-lived post-merger remnants, the total ejecta is comprised of DE only, while for models with long-lived ones, the total ejeta consists of DE and SWW.

Fig. 4.1 shows that, when we consider models with moderately soft EOSs that form long-lived remnants (*e.g.*, DD2 and BLh EOSs), the final r-process abundances in ejecta are in a good agreement with solar across all three r-process peaks. This is because DE are a robust source of heavy elements, having a low electron fraction that leads to fission cycling (see Sec. 1.1.4), and thus, a consistent reproduction of 2nd and 3rd r-process elements. Meanwhile, a moderatly high electron fraction of SWW makes them a robust source of lighter, 1st and 2nd peak elements.

Considering models with short-lived remnants, the final r-process abundances at solar 1st and 2nd r-process peaks show strong dependency on mass ratio. For instance, as models with high q have DE which is mostly of tidal origin, and thus have a low electron fraction, final r-process abundances in such ejecta are characterized by the underproduction of light elements. The final abundances in ejecta from equal mass binaries, however, display the presence of light r-process elements. This is the result of the higher electron fraction in DE from these models which include the shocked, neutrino processed material (Wanajo et al., 2014; Radice et al., 2018a).

Further, we observe that the final abundances in ejecta from all our models show the presence of actinides (elements with $A \sim 230$). The relative abundances of actinides, however, depend strongly on the ejecta electron fraction, and thus on the binary mass ratio. Notably, only for binaries with the highest mass ratio, $q \sim 1.8$, does the r-process in DE result in both 3rd peak and actinide (at ^{232}Th) abundances close to solar values. This suggests that high mass ratio mergers or NSBH mergers might be an important contributor to the cosmic chemical evolution.

Chapter 5

Kilonova

In Sec. 1.1.5 we discussed the thermal EM counterpart to BNS mergers, powered by the decay of newly synthesized heavy elements, kilonova (kN). In this Chapter we expand upon this discussion by computing kN models for ejecta from our BNS merger simulations, and comparing synthetic light curves (LCs) to observations. First, in Sec. 5.1 we overview the basic concepts behind modeling kN emission. Then, in Sec. 5.2 we describe a particular model developed by Perego et al., 2017 that was used in our analysis to produce synthetic light curves. Finally, in Sec. 5.3 and Sec. 5.4 we report the results of our analysis, and in Sec. 5.5 we summarize the kN signatures from different types of ejecta and compare them with AT2017gfo.

5.1 Overview of kilonova modeling

In general, ejecta from BNS mergers is stratified and non-axisymmetric. A way to compute EM emission from such ejecta is to perform multi-dimensional, multi-group radiative transfer simulations coupled to a HD (or MHD) simulation of ejecta itself. It is, however, possible to compute bolometric[1] properties considering only the total amount of energy released and emitted by radioactive decay within the ejecta.

Let the radioactive decay of a newly synthesized heavy isotope, i, release $\dot{Q}_i \propto \exp(-t/\tau_i)$ energy, with τ_i being its half-life. Then, assuming equal distribution of τ_i per logarithmic time, the heating rate of ejecta at time t is $\dot{Q}_{LP} = fMc^2/t$, where f is a free parameter and M is the ejecta mass[2] (Metzger, 2020).

Then, for a single shell of hot and optically thick matter (in which the thermal energy is not immediately radiated away), and expanding with constant velocity, the energy release can be described as follows. For a shell of mass $\mathrm{d}M_v$ and velocity v that has a fraction of r-process elements $X_{r,v}$, the energy release is given by the specific heating, $\dot{e}_r(t)$, and can be approximated as

---

[1] Related to the total emitted radiation at all wavelengths.

[2] In general, heating is time-dependent as thermodynamic histories of the expanding ejecta (from NR simulations) showed (Metzger et al., 2010; Roberts et al., 2011; Korobkin et al., 2012). See also Hotokezaka et al. (2017) for the discussion on physical principles behind the decay.

$$\dot{Q}_{r,v} = \mathrm{d}M_v X_{r,v} \dot{e}_r(t). \tag{5.1}$$

The optical depth τ, and the radiation diffusion timescale t_{diff}, are

$$\tau = \rho\kappa R = \frac{3}{4}\frac{\mathrm{d}M\kappa}{\pi R^2}, \qquad t_{\mathrm{diff}} \approx \frac{R}{c}\tau = \frac{3}{4}\frac{\mathrm{d}M\kappa}{\pi c R} = \frac{3}{4}\frac{\mathrm{d}M\kappa}{\pi c v t}, \tag{5.2}$$

where κ is the opacity (cross section per unit mass), and ρ is the mean density, *i.e.*, $\rho = 3\mathrm{d}M/(4\pi R^3)$. As ejecta expands and cools (via adiabatic losses), its opacity decreases, and so does the diffusion timescale. When t_{diff} reaches t, the radiation can escape the ejecta (Arnett, 1982). Hence, the characteristic timescale of the peak of the emitted radiation is

$$t_{\mathrm{peak}} = \left(\frac{3}{4\pi}\frac{1}{\beta}\frac{\mathrm{d}M\kappa}{vc}\right)^{1/2}, \tag{5.3}$$

where the constant β depends on the exact ejecta density profile. The t_{peak} is of order of days for lanthanides-free and weeks for lanthanides-rich ejecta. The peak luminosity is set by the total heating rate, $\dot{Q}(t)$, within the ejecta, as described by *Arnett's Law* (Arnett, 1982).

5.2 Semi-analytic kilonova model

We compute the kN light curves using a semi-analytic, multi-component, asnisotropic code `MKN` (Perego et al., 2017; Barbieri et al., 2019; Breschi et al., 2021). The method can be summarized as follows.

Each ejecta component (*e.g.*, DE, SWW) is described through the angular distribution of its mass, $M_{\mathrm{ej}}(\theta)$, velocity, $v_{\mathrm{ej}}(\theta)$, and opacity, $\kappa_{\mathrm{ej}}(\theta)$. The polar angle, θ, measured from the rotational axis of the post-merger remnant, is discretized in $N_\theta = 30$ angular bins evenly spaced in $\cos(\theta)$. Additionally, within each ray, the matter has a fixed velocity distribution, $\xi(v) \propto (1-(v/v_{\mathrm{max}})^2)^3$, where $\xi(v)\mathrm{d}v$ is the matter contained in an infinitesimal layer of speed $[v, v+\mathrm{d}v]$, and $v_{\mathrm{max}} = v_{\mathrm{max}}(v_{\mathrm{RMS}})$ is the maximum velocity at the outermost edge of the ejecta component.

The emitted luminosity from every bin is evaluated according to the following model. The model assumes that the thermal radiation is emitted at the photosphere, located at $R_{\rm ph}$, with effective emission temperature, $T_{\rm eff}$, and is evaluated with the Stefan-Boltzmann law, *i.e.*, assuming black-body radiation. This assumption is justified for modeling the early emission when ejecta is hot and opaque.

Time-dependent nuclear heating rates, $\epsilon_{\rm nuc}$, are approximated via an analytic fitting formula, derived from detailed nucleosynthesis calculations (Korobkin et al., 2012)

$$\epsilon_{\rm nuc}(t) = \epsilon_0 \, \frac{\epsilon_{\rm th}(t)}{0.5} \, \epsilon_{\rm nr}(t) \, \left[\frac{1}{2} - \frac{1}{\pi} \arctan \left(\frac{t - t_0}{\sigma} \right) \right]^{\alpha} , \tag{5.4}$$

where $\sigma = 0.11\,{\rm s}$, $t_0 = 1.3\,{\rm s}$, $\alpha = 1.3$, ϵ_0 is the constant and $\epsilon_{\rm th}(t)$ is the thermalization efficiency, tabulated according to Barnes et al. (2016). For a neutron-rich ejecta, $Y_e \leq 0.2$, the heating rate is dominated by a large statistical ensemble of nuclei, however, at higher $Y_e \gtrsim 0.2$, corrections are required. These corrections are introduced in a form of time-dependent heating factor, $\epsilon_{\rm nr}(t)$, adjusted roughly to the regime of mildly neutron-rich matter (Perego et al., 2017).

The mean plank opacities for the hot ejecta are adopted from the recent systematic study by Tanaka et al. (2020). Notably, when ejecta temperature drops and atoms become neutral, the photon opacity sharply decreases. This was shown to have a strong effect on LCs in high-frequency bands (Villar et al., 2017b). In order to account for the drop in opacity when the temperature falls below a certain value, corresponding to the full recombination, the $T_{\rm floor}$ is introduced as a minimum value that $T_{\rm eff}$ can have (Kasen et al., 2017, 2018). Because BNS merger ejecta composition can include a significant amount of lanthinides, `MKN` employs two floor temperatures depending on the composition: the $T_{\rm floot}^{\rm Ni}$ and $T_{\rm floot}^{\rm La}$ for lanthanides free and rich ejecta, respectively.

The emission coming from different angular bins is combined to obtain the spectral flux at the observer location as,

$$F_{\nu}(\mathbf{n}, t) = \int_{\mathbf{n}_{\Omega} \cdot \mathbf{n} > 0} \left(\frac{R_{\rm ph}(\Omega, t)}{D_L} \right)^2 B_{\nu}(T_{\rm eff}(\Omega, t)) \; \mathbf{n} \cdot {\rm d}\boldsymbol{\Omega} \, , \tag{5.5}$$

where $\mathbf{n}$ is the unitary vector along the line of sight, $\mathbf{n}_{\Omega}$ is the unitary vector spanning the solid angle Ω, D_L is the luminosity distance, $R_{\rm ph}$ is the local radial coordinate of the photospheric surface, and $B_{\nu}(T_{\rm eff})$ is the spectral radiance at frequency ν for a surface with temperature $T_{\rm eff}$. We also make use of the apparent AB magnitude, ${\rm mag}_b$, in a given photometric band, b, defined as:

$${\rm mag}_b(\mathbf{n}, t) = -2.5 \log_{10} \left(F_{\nu_b}(\mathbf{n}, t) \right) - 48.6 \, , \tag{5.6}$$

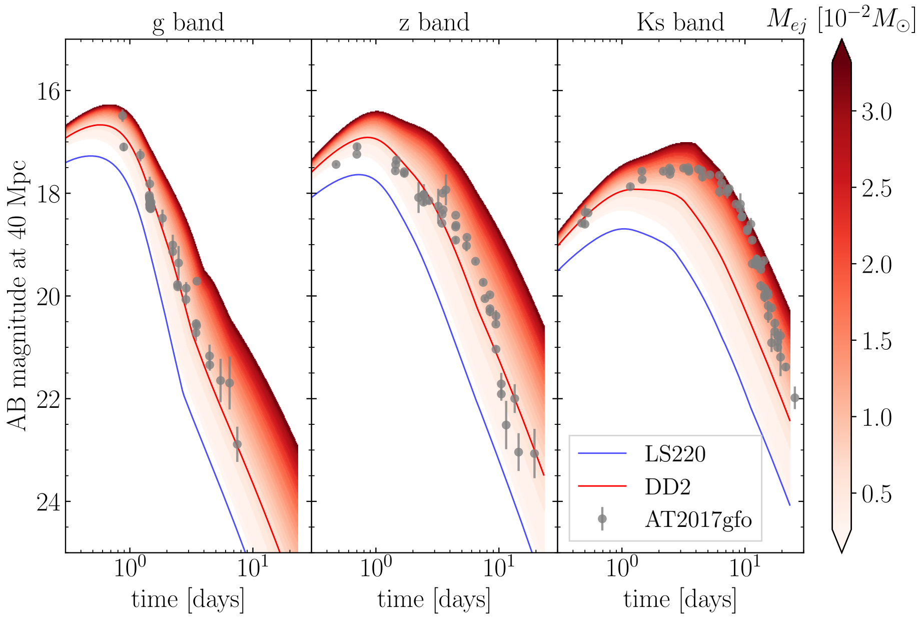

FIGURE 5.1: Bolometric LCs in three photometric bands (one per panel) for ejecta from two BNS merger models, DD2 $q = 1.00$ and LS220 $q = 1.00$. LCs corresponding to DE only are shown with solid lines, while the red color gradient represents a range of possible LCs for DE plus SWW, depending on the total mass of the latter (color-coded). The SWW mass flux for DD2 $q = 1.00$ is linearly extrapolated after the end of the simulation until 250 ms post-merger.

where ν_b is the effective central frequency of the band b.

We consider DE ejecta and SWW geometries directly imported from our BNS merger simulations in a form of angular profiles (assuming axisymmetry). We refer to such kN models as NR-informed. In several cases we also use analytical ejecta profiles, with either smooth or step-like dependency on the polar angle. The viewing angle, $\theta_{\rm obs}$, is measured as the angle between the polar axis and the line of sight (LOS) of the observer.

5.3 Numerical relativity informed kilonova models

We begin by considering two equal mass BNS merger models with LS220 and DD2 EOSs, that produce short and long-lived post-merger remnants respectively (see Chapter 3). Using the `MKN` code, discussed above, we compute NR-informed LCs for both DE only, and the combination of DE and SWW[3]. The result is shown in Fig. 5.1.

---

[3] The `MKN` code does not include the effects of ejecta component iteration. We leave this to future works.

We observe that when only DE is considered, the kN emission is significantly dimmer in the case of the LS220 $q = 1.00$ model. And while the amount of mass ejected by both models is rather similar, DE from the DD2 $q = 1.00$ model is faster and less neutron-rich, and hence have lower photon opacities.

However, DE alone do not produce emission bright enough to match AT2017gfo, especially at early times in g band and at late times in K_s band. The latter can be attributed to the absence of low-Y_e secular ejecta in our simulations. The former, however, suggests the need of a low-Y_e, massive ejecta component. It is natural to consider whether SWW can account for this early blue emission. Since the total mass of SWW depends on the lifetime of a remnant, $t_{\rm coll}$, (see Sec. 3.2.3) and the remnant of the DD2 $q = 1.00$ model does not collapse until the end of the simulation ($\sim$100 ms post-merger), we extrapolate the SWW mass, considering a range of $t_{\rm coll}$ up to 250 ms post-merger. The range of associated kN LCs is shown in Fig. 5.1 as red color gradient. The analysis suggests that sufficiently massive SWW can indeed account for the early blue emission of AT2017gfo. However, the emission in other bands, *e.g.*, z band, becomes significantly brighter than what was observed.

Our results, however, have uncertainties related to our simplified calculation of kN LCs which is expected to be less accurate at late times when absorption features and deviations from LTE become more relevant (see *e.g.* Smartt et al., 2017). A more detailed analysis of kNe produced by DE and SWW, that considers various ejecta profiles and cross-ejecta interactions, dynamical as well as radiative, is required to draw a more solid conclusion.

5.4 Fit-informed kilonova models

In Ch. 3 Sec. 3.2, we pointed out that a simple second order polynomial in mass ratio and $\tilde{\Lambda}$ provides a reasonable fit to ejecta properties of BNS mergers. Here we compare the kN LCs informed by these fitting formulae against NR-informed kN models. We employ one- and two-component kNe models. When one component kN is considered, only DE ejecta properties are used, such as mass, velocity, and RMS half-opening angle separating the low opacity polar outflow and the high opacity equatorial one. When two component kN is considered, in addition to DE we include the secular outflow from the disk, assuming that a fixed fraction, 40%, of it would become unbound. The angular distributions of mass, velocity and opacity are assumed to be uniform.

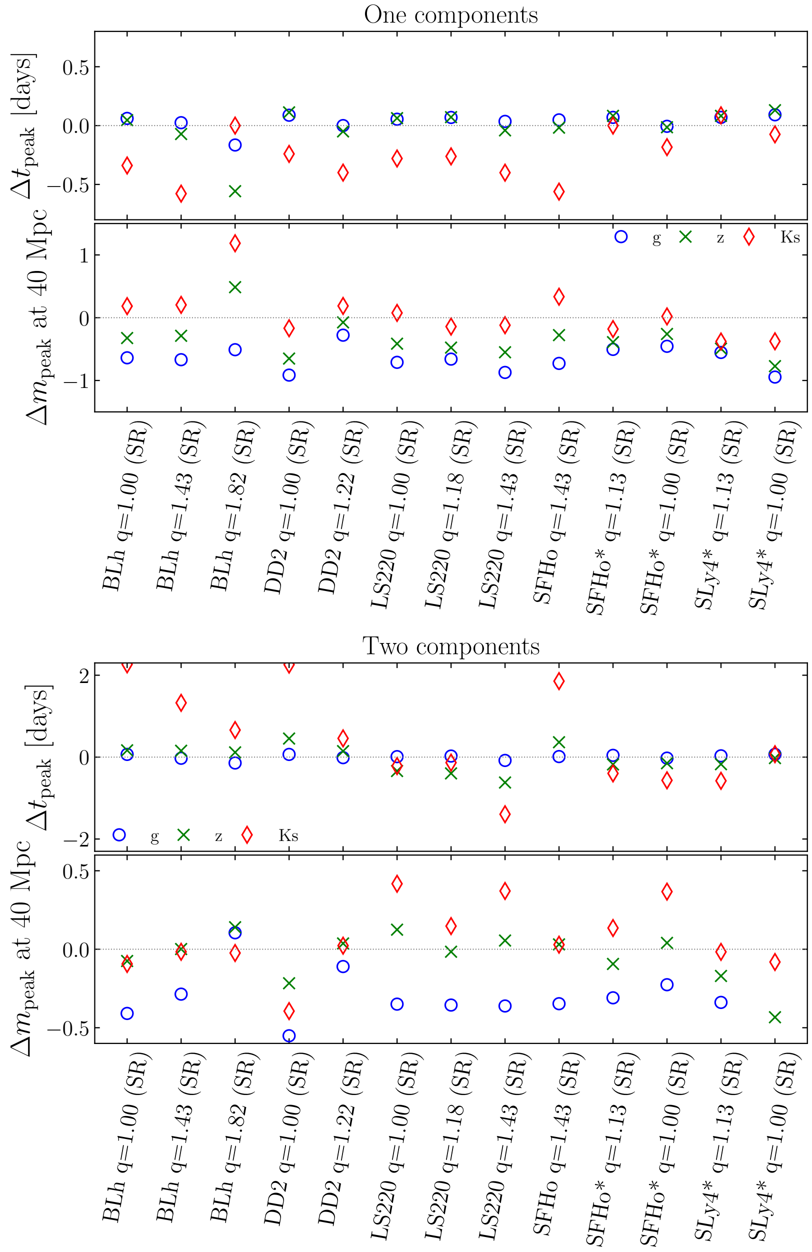

FIGURE 5.2: Differences in peak time (*top subpanel*) and peak magnitude *(bottom subpanel)* between fit-informed kN model LCs, and LCs computed using the actual ejecta profile from a simulation. The *top panel* shows this comparison for a single component kN model (only considering DE), while the *bottom panel* is for two-component model, where DE and secular winds are considered. The comparison is shown for three different bands indicated with different markers. The best result is when all three markers of all three colors are at 0 for a given simulation.

Comparing the properties of NR-informed and fit-informed kN LCs, we maintain all other parameters fixed.

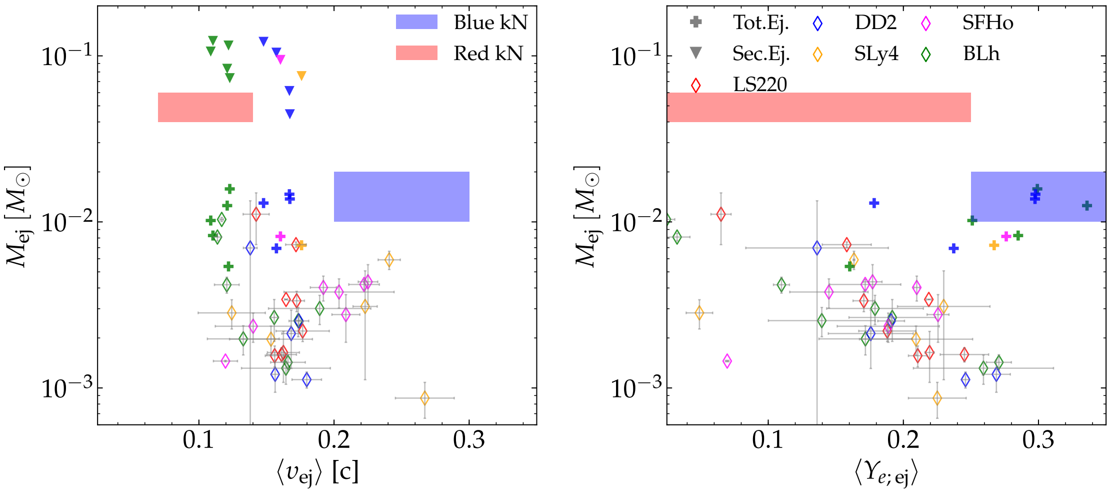

FIGURE 5.3: Properties of various types of ejecta (indicated with different markers) for all our simulations, alongside the regions inferred for AT2017gfo (colored patches) based on Siegel (2019). Ejecta types shown: DE (diamond markers with error bars), DE plus SWW (solid cross markers), estimated secular ejecta assuming 40% of the disk mass is unbounded on secular timescales with the velocity of SWW (down triangle markers). (Adapted from Nedora et al. (2021b)).

In Fig. 5.2 we show the result of our analysis. For clarity we show the differences, $\Delta t_{\rm peak} = t_{\rm peak;NR} - t_{\rm peak;fit}$, and $\Delta m_{\rm peak} = m_{\rm peak;NR} - m_{\rm peak;fit}$, for peak times, t_p, and magnitudes, $m_{\rm AB}$, respectively. The comparison is shown for 3 different photometric bands, g, z, and K_s (indicated by different markers) and for a set of representative BNS merger simulations.

Considering one-component kN LCs, (top panel), we observe that the t_p is recovered with an error margin of ~0.2 days in g and z bands, and within a 0.5 day margin in K_s band. Notably, fit-informed LCs systematically underestimate t_p in the K_s band. The largest deviation is found for the model with $q = 1.8$ and BLh EOS. This highlights a limitation of our fitting formula, insofar as it is not able to reproduce PC model properties well.

Comparing peak magnitudes, $m_{\rm AB}$, we observe that differences between NR- and fit-informed LCs are on average ~0.5 mag. In g band, however, the deviations are ~1 mag. Considering two-component kN models, we observe that the t_p in K_s band differ between the fit- and NR-informed LCs by ~2 days. The $m_{\rm AB}$ is reproduced within ±0.5 mag on average in z and K_s bands. The larger differences in $m_{\rm AB}$ for one component kN LCs can be attributed to the influence of the ejecta geometry that is not fully accounted for by the single parameter, $\langle\theta_{\rm RMS}\rangle$, that we use to separate low and high opacity material.

Overall we observe that, while there are considerable deviations between fit- and NR-informed LCs which can be attributed to the limitations of our fitting formula as well as the specifics of the kN model used for the analysis, certain kN properties, *e.g.*, peak time in high-frequency bands, appear to be captured robustly.

5.5 Summary of ejecta kilonova signatures

Observed data for AT2017gfo has been extensively studied, and many kN models, most of which were spherical, two-component kN models, were employed to infer the properties of ejecta that produced the observed emission (*e.g.* Villar et al., 2017a). Due to differences in physics input and modeling techniques, these methods gave broad ranges of expected values for ejecta mass, velocity and composition that read (Siegel, 2019): $M_{\rm ej}^{\rm red} \in (4,6) \times 10^{-2}\,{\rm M}_{\odot}$ and $\upsilon_{\rm ej}^{\rm red} \in (0.07, 0.14)\,c$ for the red component, and $M_{\rm ej}^{\rm blue} \in (1,2) \times 10^{-2}\,{\rm M}_{\odot}$ and $\upsilon_{\rm ej}^{\rm blue} \in (0.2, 0.3)\,c$ for the blue component. We show these ranges in Fig. 5.3, alongside the ejecta properties from our models.

With respect to the red component, we observe that DE from our models have too high average velocities and not nearly enough mass. This result suggests that an additional, low Y_e ejecta component is required in order to explain the AT2017gfo red component (*e.g.* Perego et al., 2017; Kawaguchi et al., 2018).

As we showed in Chapter 3, Sec 3.2.1, DE properties can be mapped onto binary parameters, *e.g.*, mass ratio, q, and tidal deformability, $\tilde{\Lambda}$, via a simple 2nd order polynomial, $P_2^2(q, \tilde{\Lambda})$. The ranges in q and $\tilde{\Lambda}$ inferred for GW170817 from GW analysis (Abbott et al., 2017c; Abbott et al., 2018; De et al., 2018; Abbott et al., 2019b), *i.e.*, 90% credible intervals, are $\tilde{\Lambda} = 300^{+500}_{-190}$ and $q \in [1., 1.37]$. Mapping them onto ejecta parameters via $P_2^2(q, \tilde{\Lambda})$, we obtain $M_{\rm ej}^{\rm d} \in [0.72, 7.52] \times 10^{-3}\,{\rm M}_{\odot}$ and $\langle \upsilon_{\infty}^{\rm d} \rangle \in [0.16, 0.39]\,c$ and $\langle Y_e^{\rm d} \rangle \in [0.11, 0.23]$. Predictably, we observe that the obtained ranges do not agree with those inferred for AT2017gfo. This is partially due to the simplified ejecta geometry considered in many kN models, but also because other ejecta types besides DE contributed to the observed emission.

As we showed in Sec. 5.3, SWW could be a significant contributor to AT2017gfo, assuming that the post-merger remnant of GW170817 survived for $\mathcal{O}(100)$ ms. Specifically, we showed that SWW properties are in line with those required to explain the early blue emission of AT2017gfo. Indeed, as we show in Fig. 5.3 (left panel), the total ejecta (DE+SWW) mass from several of our models, *e.g.*, BLh $q = 1.18$, BLh $q = 1.42$ and DD2 $q = 1.00$ is sufficiently massive and proton-rich to account for the blue kN of AT2017gfo. Meanwhile, the left panel of Fig. 5.3 shows that the total ejecta is slower than what is required. Notably, ejecta properties inferred from AT2017gfo change when sophisticated radiation transport models, which take into account ejecta geometry and cross-ejecta interactions, are considered. Furthermore, other proton-rich ejecta components are expected on timescales larger than our simulations permit (*e.g.* Fujibayashi et al., 2018; Radice et al., 2018c; Fernández et al., 2019).

Nuclear recombination and viscous processes are expected to unbind $\sim$40% of a disk in a form of outflows with typical velocity $\lesssim 0.1\,c$ on a secular timescale (*e.g.* Siegel et al., 2017; Fujibayashi et al., 2018; Radice et al., 2018c; Fernández et al., 2019; Fujibayashi et al., 2020b). Considering disk masses of our BNS merger simulations and adapting the fix fraction of 40% of the $M_{\rm disk}$, we estimate that about $\sim 0.05\,{\rm M}_{\odot}$ would be ejected in the form of secular winds. Plotting the expected masses of secular ejecta from our models with long-lived remnants (lower triangles in Fig. 5.3), we observe that they would be sufficient to explain the red component of AT2017gfo.

A more quantitative analysis requires ab-initio BNS merger simulations, that are sufficiently long and have sufficiently advanced physics input, to capture all the aforementioned ejection mechanisms.

Chapter 6

Non-thermal emission from BNS mergers

In Sec. 1.1.6 we discussed the origin of the non-thermal emission from BNS mergers, focusing on GRB and kN afterglows. In this chapter we expand upon this discussion. First, in Sec. 6.1, we recall the basic methods for computing synchrotron emission from a relativistic blast wave expanding into the ISM. Then, in Sec. 6.2, we describe specific methods that we implemented numerically in the `PyBlastAfterglow` code, and verify the code performance by comparing our results with published results. Finally, in Sec. 6.3, we present kN afterglow LCs from ejecta from our BNS merger simulations and compare them with observations.

6.1 Overview of afterglow modeling methods

The theory of relativist shocks with applications to active galactic nuclei (AGNs) jets was developed by Blandford et al. (1976) and further expanded by, *e.g.*, Eerten et al. (2012), Pe'er (2012), and Nava et al. (2013). The theory was successfully applied to GRB afterglows (*e.g.* Costa et al., 1997; Paradijs et al., 1997; Lamb et al., 2017) (see Kumar et al. (2014) for a review) and kN afterglows (*e.g.* Nakar et al., 2011; Hotokezaka et al., 2015a, 2018). The key components of afterglow modeling are: (i) blast wave dynamics; (ii) electron energy distribution; and (iii) EM emission.

6.1.1 The dynamical evolution of a blast wave

A universal part of the afterglow theory is the dynamics of a blast wave propagating through the ISM, which is also called a "fireball".

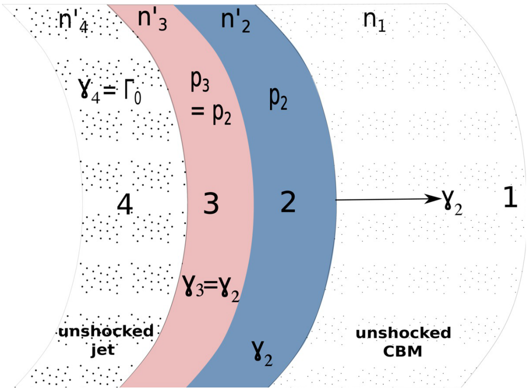

FIGURE 6.1: Schematic sketch of a pair of shocks produced when a relativistic jet from a GRB collides with the ISM, as viewed from the rest frame of the unshocked ISM. Regions 2 & 3 represent the shocked ISM and shocked GRB ejecta respectively. They move together with the same Lorentz factor (LF) (γ_2, as viewed by a stationary observer in the unshocked ISM), and have the same pressure but different densities. (Adapted from Kumar et al. (2014), Fig. 8)

Analytical studies and numerical simulations showed that a blast wave expanding into the ISM generates a pair of shocks: a forward shock, that propagates through the upstream ISM, and a reverse shock that moves back, through ejecta (*e.g.* Blandford et al., 1976; Ayache et al., 2021). In Fig. 6.1, this pair of shocks is schematically depicted as boundaries between regions $1-2$ and $3-4$ respectively. Overall, there are four distinct regions: unshocked and shocked ISM (regions 1 and 2), and shocked and unshocked GRB or kN ejecta (regions 3 and 4). The comoving- and observer-frame quantities are marked with and without superscript prime ($'$) respectively.

The evolution of the physical properties of a shock are governed by three conservation laws: baryon number, and energy and momentum fluxes across the shock front. The latter two are embedded into the fluid energy momentum tensor, Eq. (2.3).

If the internal structure of a blast wave can be neglected, then it is possible to express these conservation laws as follows (Blandford et al., 1976; Rezzolla et al., 2013):

$$\frac{e'_2}{n'_2} = (\gamma_{21} - 1) m_p c^2, \qquad \frac{n'_2}{n'_1} = \frac{\hat{\gamma}\gamma_{21} + 1}{\hat{\gamma} - 1}, \qquad \gamma_{1s}^2 = \frac{(\gamma_{21} + 1)[\hat{\gamma}(\gamma_{21} - 1) + 1]^2}{\hat{\gamma}(2 - \hat{\gamma})(\gamma_{21} - 1) + 2}, \tag{6.1}$$

where subscripts 2 and 1 stand for the downstream and upstream respectively, shown in Fig. 6.1, e' is the internal energy density, n' is the proton number density, γ_{21} is the relative LF of a fluid in region 2 with respect to region 1, γ_{1s} is the relative LF of a fluid in region 1 with respect to the shock front, and $\hat{\gamma}$ is the adiabatic index of a fluid, which is $\hat{\gamma} = 4/3$ for the ideal relativistic fluid and $\hat{\gamma} = 5/3$ for a subrelativisitc fluid.

Solving the system of equations, Eq. (6.1), for the forward and reverse shocks gives the full evolution of quantities describing the blast wave.

A shock propagating through the ISM compresses the fluid. For a relativistic case with $\hat{\gamma} = 4/3$, the compression ratio in a downstream fluid is $n_2'/n_1' = 3((4/3)\gamma_{21}+1) = 4\gamma_{21}+3 \approx 4\gamma_{21}$. Additionally, a shock front randomizes the velocity vectors of particle, raising their thermal energy, while their LF remains unchanged.

6.1.2 Electron distribution

As the shock compresses the fluid and amplifies random magnetic fields, it accelerates the inbound particles into a power-law distribution in energy space (*e.g.* Kumar et al., 2014). The continuity equation for electrons in this space reads

$$\frac{\partial}{\partial t}\frac{dn_e}{d\gamma_e} + \frac{\partial}{\partial \gamma_e}\left[\dot{\gamma}_e \frac{dn_e}{d\gamma_e}\right] = S(\gamma_e)\,, \tag{6.2}$$

where $dn/d\gamma_e$ is the electron distribution function, $\dot{\gamma}_e = -\sigma_T B'^2 \gamma_e^2/(6\pi m_e c)$ is the rate at which the electron LF changes due to energy losses, and $S(\gamma_e)$ is the injection rate of electrons into the system.

Consider a characteristic LC, γ_c. Electrons with LFs $\gamma_e > \gamma_c$ can efficiently lose their energy to synchrotron radiation. Then, after a certain characteristic time, t_0, their γ_e drops below γ_c, which can be expressed as

$$c^2\frac{dm_e}{dt}\gamma_e = -\frac{\sigma_T}{6\pi}B^2\gamma_e^2 c\,, \qquad \gamma_c \sim \frac{6\pi m_e c}{\sigma_T B^2 t_0}. \tag{6.3}$$

where $\sigma_T = 8\pi q^4/(3m_e^2c^4)$ is the Thompson cross section.

Assuming that the injection of electrons is constant (steady-state solution, $\partial_t = 0$), and has a minimum, γ_m, such that, $S(\gamma_e) = 0$ for $\gamma_e < \gamma_m$, the solution to Eq. (6.2) reads

$$\frac{dn_e}{d\gamma_e} \propto \begin{cases} \gamma_e^{-2} & \text{if } \gamma_c < \gamma_e < \gamma_m, \\ \gamma_e^{-p-1} & \text{if } \gamma_e > \gamma_c > \gamma_m. \end{cases} \tag{6.4}$$

The $\gamma_c < \gamma_e < \gamma_m$ regime is usually referred as *slow cooling* and $\gamma_e > \gamma_c > \gamma_m$ as *fast cooling* (Sari et al., 1998).

6.1.3 Synchrotron emission

The power of the synchrotron radiation, P'_{syn}, emitted by an electron moving with the speed, υ_e, corresponding to the LF, γ_e, in the magnetic field, B', perpendicular to the field lines is given by Larmor's formula. Within a magnetic field, an electron is following a spiral trajectory. The characteristic frequency of the synchtrontron radiation, ν'_{syn}, is therefore given by the angular speed of the electron (*e.g.*, its Larmor frequency) The power per unit frequency at the peak, $P'_{syn}(\nu_{syn})$, can be computed as follows (Rybicki et al., 1986):

$$P'_{syn} = \frac{\sigma_T B'^2 \gamma_e^2 \upsilon_e^2}{4\pi c}, \quad \nu'_{syn} \sim \frac{q B' \gamma_e^2}{2\pi m_e c}, \quad P'_{syn}(\nu'_{syn}) \sim \frac{\sigma_T B' m_e c^2}{2q}. \tag{6.5}$$

The synchrotron radiation spectrum, emitted by an ensemble of electrons that have a distribution function $dn_e/d\gamma_e$, is given by convolving the distribution function with the power spectrum of a single electron, $P_{syn}(\nu)$, as

$$f'(\nu') = \int_{\gamma_m}^{\gamma_M} d\gamma_e \frac{dn_e}{d\gamma_e} P'_{syn}(\nu'), \tag{6.6}$$

where γ_m and γ_M are the minimum and maximum LFs within which electrons contribute to the specific flux.

6.1.4 Relativistic effects

Consider a spherical coordinate system, (r, θ, ϕ), where r is the distance to the coordinate center, and θ and ϕ are the latitudinal and azimuthal angles respectively. The BNS merger remnant is located at $r = 0$. Its axis coincides with $\theta = 0$. The observer lies on the $\phi = \pi/2$, and the $\theta_{\rm obs}$ is the angle between LOS and remnant axis.

For a fluid element moving with velocity, υ (and LF, Γ), and emitting photons at angle, θ, from the LOS, the time between two consecutive emissions in the observer frame, $\delta t_{\rm obs}$, and in the comoving frame, $\delta t'$, are related via the Lorentz transformation as

$$\delta t_{\rm obs} = \frac{\delta t'}{\mathcal{D}}, \quad \mathcal{D} = \frac{1}{\Gamma(1 - \beta \cos(\theta))}, \quad \nu = \frac{\nu'}{\Gamma(1 - \upsilon \cos(\theta)/c)} = \frac{\nu'}{\mathcal{D}}, \tag{6.7}$$

where $\mathcal{D}$ is the Doppler factor, and $\nu = \nu'/\mathcal{D}$ is the classical Doppler shift formula for the frequency of the radiation.

For a thin spherical shell, radiation emitted at $(r = \upsilon t, \theta, \phi)$ arrives at the observer with a time delay of

$$t_{\rm obs} = t - \frac{r\cos(\theta)}{c} = t\Big(1 - \frac{\upsilon\cos(\theta)}{c}\Big) = \frac{t}{\Gamma\mathcal{D}}\,. \tag{6.8}$$

Then, the total emission at a given Doppler shifted frequency, from the entire shell at the observer frame, is obtained by integrating over all elements with the same $t_{\rm obs}$.

Finally, the observed flux at a frequency $\nu_{\rm obs}$ from a spherical thin shell in our coordinate system can be obtained by integrating Eq. (6.6) over the equal time arrival surface (EATS)

$$F_{\nu_{\rm obs}} = \frac{1+z}{4\pi D_L^2}\int_{\rm (EATS)}\mathcal{D}^3 f'(\nu')d\Omega \tag{6.9}$$

where $d\Omega = \sin\theta d\theta d\phi$ is the solid angle, z is the red-shift, and D_L is the luminosity distance.

6.2 `PyBlastAfterglow`

We design a code, `PyBlastAfterglow`, to numerically compute the synchrotron emission from an arbitrarily structured blast wave, employing the following methods.

Considering the spherical coordinates we introduced in the previous section, we discretize it into $[N_\theta, N_\phi]$ elements. Extracted from BNS merger simulations (Chapter 3), DE angular profiles are then mapped onto this grid to provide the initial conditions for the evolution. Each element of this structured blast wave is evolved independently as follows.

We adopt the blast wave dynamics formalism developed by Nava et al. (2013) that casts Eqs. (6.1) into a set of ODEs for the blast wave LF, energy and swept-up mass that read

$$\frac{d\Gamma}{dr} = -\frac{(\Gamma_{\rm eff}+1)(\Gamma-1)c^2\frac{dm}{dr} + \Gamma_{\rm eff}\frac{dE'_{\rm ad}}{dr}}{(m_0+m)c^2 + E'_{\rm int}\frac{d\Gamma_{\rm eff}}{d\Gamma}}\,, \tag{6.10a}$$

$$\frac{dE'_{\rm int}}{dr} = \frac{dE_{\rm sh}}{dr} + \frac{dE'_{\rm ad}}{dr} + \frac{dE'_{\rm rad}}{dr}\,, \tag{6.10b}$$

$$\frac{dm}{dr} = 2\pi\rho(1-\cos(\theta))r^2\,, \tag{6.10c}$$

where Γ is the blast wave LF, r is its radius, $\Gamma_{\rm eff} = (\hat{\gamma})\Gamma^2 - \hat{\gamma} + 1/\Gamma$ is the effective LF (see Nava et al. (2013)) with $\hat{\gamma}$ being the fluid adiabatic index, $E'_{\rm tot}$ and $E'_{\rm int}$ are the total and internal energies respectively, $dE'_{\rm ad}$ and $dE'_{\rm rad}$ denote the adiabatic and radiative losses respectively, m_0 is the initial mass, θ is the opening angle of the blast wave, and ρ is the ISM density. Eqs. 6.10 are solved via the explicit Runge-Kutta method of order $8(5,3)$ (with stepsize control) (Dormand et al., 1980). The effects of radiation losses, discussed in Nava et al. (2013), and the lateral spreading of the blast wave (*e.g.* Granot et al., 2012), are turned off, *i.e.*, $dE'_{\rm rad}/dr = d\theta/dr = 0$. The adiabatic index, $\hat{\gamma}$, is computed from the approximation to the numerical study of the trans-relativistic fluid (Service, 1986)

$$\begin{aligned}\hat{\gamma} \approx (5 - 1.21937z + 0.18203z^2 - 0.96583z^3 + \\ 2.32513z^4 - 2.39332z5 + 1.07136z^6)/3.\end{aligned} \tag{6.11}$$

where $z \approx T/(0.24 + T)$ with T being the normalization temperature (Pe'er, 2012). The approximation smoothly connects the $\hat{\gamma} = 4/3$ and $\hat{\gamma} = 5/3$ regimes.

We adopt a common assumption that fixed fractions of the shock energy, ε_e and ε_B, are deposited into electrons and magnetic fields respectively (*e.g.* Dermer et al., 1998). We adopt the power-law electron distribution, Eq. (6.4), with p, the spectral index, being a free parameter. We compute the characteristic LFs, γ_c and γ_m, using the standard prescriptions (*e.g.* Dermer et al., 2008)

$$\gamma_{min} = \frac{p-2}{p-1}\varepsilon_e(\Gamma - 1), \qquad \gamma_c = \frac{6\pi m_e c}{\sigma_T \Gamma B'^2 t_{\rm obs}} \tag{6.12}$$

where $t_{obs} = \int dr/(\beta c)$ is the time in the observer frame and B' is the magnetic field strength.

The synchrotron emission in the comoving frame, Eq. (6.6), for the slow and fast cooling regimes, is approximated with a smooth broken power-law (Johannesson et al., 2006)

$$\begin{aligned}
P'(\nu') &= P'_{\rm max;\,f}\left[\left(\frac{\nu'}{\nu'_c}\right)^{-\kappa_1/3} + \left(\frac{\nu'}{\nu'_c}\right)^{\kappa_1/2}\right]^{-1/\kappa_2}\left[1 + \left(\frac{\nu'}{\nu'_m}\right)^{(p-1)\kappa_2/2}\right]^{-1/\kappa_2}, \\
P'(\nu') &= P'_{\rm max;\,s}\left[\left(\frac{\nu'}{\nu'_m}\right)^{-\kappa_1/3} + \left(\frac{\nu'}{\nu'_m}\right)^{\kappa_3(p-1)/2}\right]^{-1/\kappa_3}\left[1 + \left(\frac{\nu'}{\nu'_c}\right)^{((1-p)/2+p/2)\kappa_4}\right]^{-1/\kappa_4},
\end{aligned} \tag{6.13}$$

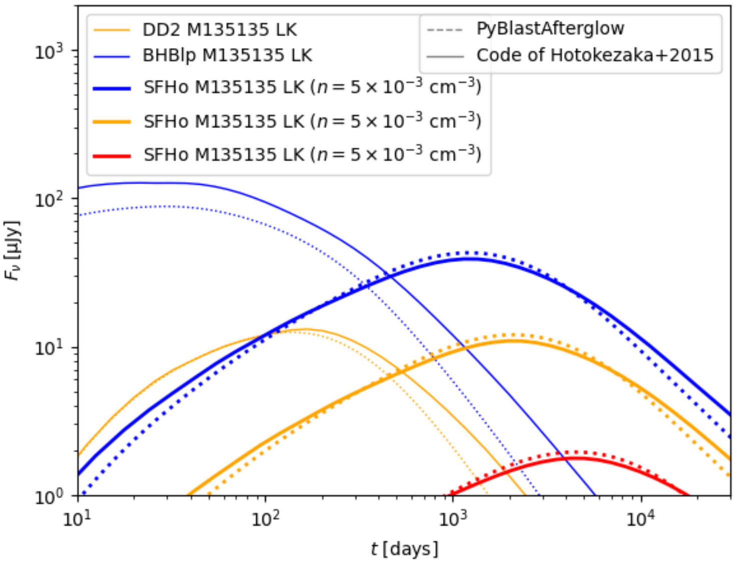

FIGURE 6.2: Comparison between kN afterglow LCs computed with `PyBlastAfterglow` and the code of Hotokezaka et al. (2015a) for DE from a set of BNS merger models of Radice et al. (2018a).

where $\nu'_i = \chi_p \gamma_i^2 (3B'/4\pi m_e c)$ are characteristic frequencies, and the $P'_{\mathrm{max;\,i}}$ are the maximum values of the power density,

$$P'_{\mathrm{max;\,f}} = 2.234 \phi_p \frac{q_e^3 n' B'}{m_e c^2}, \tag{6.14}$$

$$P'_{\mathrm{max;\,s}} = 11.17 \phi_p \frac{p-1}{3p-1} \frac{e^3 n' B'}{m_e c^2}, \tag{6.15}$$

where, ϕ_p, χ_p, and κ_i are polynomials that describe the p-dependence (Johannesson et al., 2006).

The flux density in the observer frame at a given time is obtained by integrating over the EATS, Eq. (6.9).

6.2.1 Method validation

We verify the performance of `PyBlastAfterglow` by comparing synthetic LCs to those available in the literature. Specifically, we consider the kN afterglow LCs presented in Radice et al. (2018a) (see their Fig. 30 and Fig. 31) computed for DE from a set of BNS merger models. As we aim to conduct a similar study, and our BNS merger simulations were computed with the same NR code, they are a natural point of comparison.

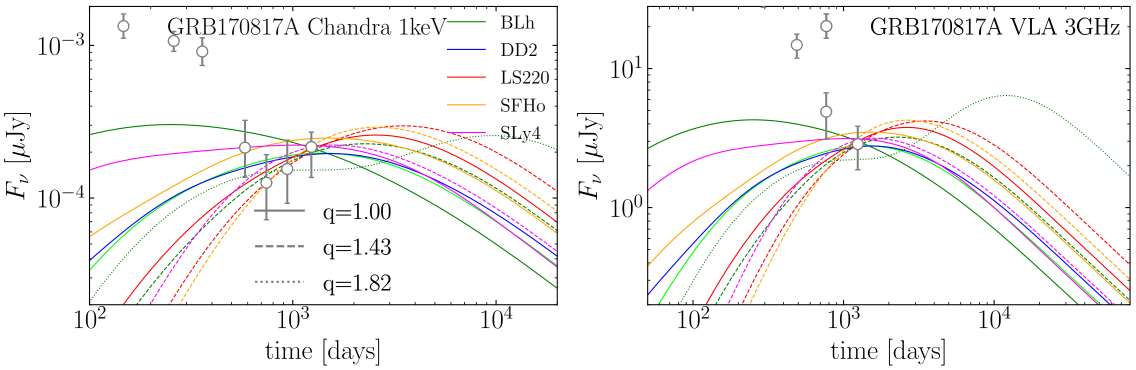

FIGURE 6.3: NR-informed kN afterglow LCs in X-ray (*left panel*) and radio (*right panel*) for a set of BNS merger models. Different colors represent different EOSs, while various line styles indicate three mass ratios. The LCs are computed with microphysical parameters reported in Tab. 6.1. The observational data (depicted with gray circles) are obtained from Balasubramanian et al. (2021) and Hajela et al. (2021). (Adapted from Nedora et al. (2021a)).

TABLE 6.1: Microphysical parameters and the ISM density used in kN afterglow calculations for BNS merger models depicted in Fig 6.3 and Fig. 6.5, where the data for the latter is shown in the bottom row. (Adapted from Nedora et al. (2021a))

Fig 6.3	p	ϵ_e	ϵ_b	$n_{\rm ISM}$
BLh q=1.00	2.05	0.1	0.002	0.005
BLh q=1.43	2.05	0.1	0.003	0.005
BLh q=1.82	2.05	0.1	0.01	0.01
DD2 q=1.00	2.05	0.1	0.005	0.005
LS220 q=1.00	2.05	0.1	0.01	0.005
LS220 q=1.43	2.05	0.1	0.001	0.005
SFHo q=1.00	2.05	0.1	0.001	0.004
SFHo q=1.43	2.05	0.1	0.01	0.005
SLy4 q=1.00	2.05	0.1	0.001	0.004
SLy4 q=1.43	2.05	0.1	0.004	0.005
Fig. 6.5	2.15	0.2	0.005	0.005

The result is shown in Fig. 6.2. Overall, in most cases we observe a good agreement between our results and those shown in Radice et al. (2018a). We find the level of agreement sufficient, considering the very different treatments of the blast wave dynamics and synchrotron emission. Furthermore, these discrepancies are considerably smaller than those introduced by uncertain microphysics parameters and ejecta properties (discussed below).

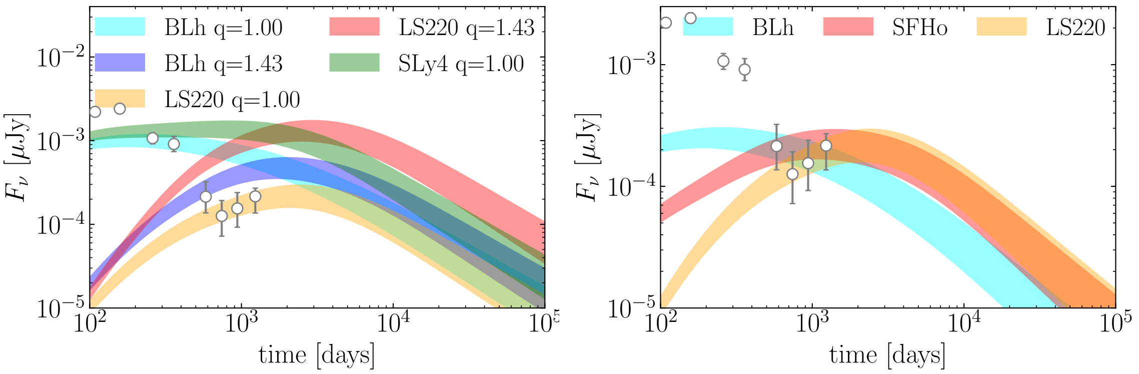

FIGURE 6.4: The effect of changing p from 2.15 (lower boundary of colored bands) to 2.05 (upper boundary of colored bands), shown for a set of kN afterglow X-ray LCs for DE from a sample of NR BNS merger simulations. In the *first panel* the models with different mass ratio are shown and the $n_{\rm ISM} = 6 \times 10^{-3}$ cm^{-3}, and microphysical parameters, $\varepsilon_{\rm e} = 10^{-1}$, $\varepsilon_{\rm B} = 10^{-2}$. In the *second panel* the models with $q = 1$ are shown and the afterglow parameters are adjusted to fit observations, with $\varepsilon_{\rm e} = 0.1$ fixed and $n_{\rm ISM} \sim 6\times10^{-3}, 5\times10^{-3}, 5\times10^{-3}\,{\rm cm}^{-3}$ $\varepsilon_{\rm B} \sim 10^{-2}, 2\times10^{-3}, 10^{-3}$ for models with LS220, BLh and SFHo EOSs respectively. (Adapted from Hajela et al. (2021)).

6.3 Kilonova afterglow and changes in GRB170817A

In order to compute kN afterglow LCs, several free parameters of the model need to be set. Ideally, these parameters should be obtained by fitting synthetic LCs to observational data via *e.g.*, Bayesian methods. Instead we opt to consider the parameters inferred for GRB170817A afterglow by prior studies, and investigate whether within their ranges of uncertainty they can lead to LCs compatible with observations, leaving the more rigorous analysis to future works.

Specifically, we consider the ISM density to be uniform with $n_{\rm ISM} \in (10^{-3}, 10^{-2})$ cm^{-3} (Hajela et al., 2019). The observational angle, is set to $\theta_{\rm obs} = 30\,{\rm deg}$ (Abbott et al., 2017c). The luminosity distance of NGC 4993, the host galaxy of GW170817, is $41.3 \times 10^{6}\,{\rm pc}$ with the redshift $z = 0.0099$ (Hjorth et al., 2017). The index of the electron energy distribution, p, and microphysical parameters are chosen based on the recent observations of GRB170817A, where the spectral evolution was detected (Hajela et al., 2021). We consider $\varepsilon_e \in (0.1, 0.2)$, $\varepsilon_B \in (10^{-3}, 10^{-2})$, and $p \in [2.05, 2.15]$.

In Chapter 3, Sec. 3.2, we discussed the properties of DE. Here we examine how these properties translate to kN afterglow signatures. Fig. 6.3 shows synthetic LCs in X-ray and radio bands for several representative BNS merger models, together with the latest GRB170817A data. We observe that ejecta velocity and angular distribution primarily define the shape of afterglow LCs. Specifically, the broad velocity distribution found in equal mass BNS models with soft EOSs (*e.g.*, the SLy4 $q = 1.00$ model, shown in Fig. 3.14) translates into wide LCs with an early rise time, compatible with that of the early GRB170817A afterglow. This behaviour is governed by the deceleration of the fastest ejecta shells, as the emission coming from these shells reaches its peak early. If the velocity distribution is rather narrow, with most of the material moving at $\leq 0.2\,c$ (*e.g.*, the LS220 $q = 1.43$ model), the LC rise is steeper and occurs later ($\sim 10^2$ days after merger).

Fig. 6.3 also shows that kN afterglow LCs computed for most of our BNS merger models are in good agreement with the changing behaviour of GRB170817A within the uncertainties introduced by microphsical parameters and ISM density. Specifically, this agreement is particularly good for models with moderately stiff EOSs and $1.00 < q < 1.82$, considering the LC peak time.

Spectral analysis of the changing behaviour of GRB170817A indicated a possible change in the electron distribution index (Hajela et al., 2021). Specifically, while previous GRB170817A analysis suggested $p = 2.15$ with high degree of confidence (*e.g.* Hajela et al., 2019), the latest observations suggest a lower value, $p \leq 2.05$ (Hajela et al., 2021). The effect of the decrease in p is shown in Fig. 6.4. Notably, the parameters p, ε_e. ε_b and $n_{\rm ISM}$ are very degenerate, meaning that the change in one can be offset by the change in another within these parameters' ranges of credibility inferred for GRB170817A.

If we fix the ISM density and microphysical parameters to $n_{\rm ISM} = 5 \times 10^{-3}$ g cm^{-3}, $\varepsilon_e = 0.1$ and $\varepsilon_b = 5 \times 10^{-3}$, we observe that the LC peak flux, $F_{\nu;p}$, is the highest for models with soft EOSs such as SLy4. In general, however, we do not find a strong dependency between EOSs and $F_{\nu;p}$. With respect to the mass ratio we find that for models with stiff EOSs, the larger the mass ratio, the smaller the $F_{\nu;p}$. This behaviour can be attributed to the overall dependency of the ejecta mass-averaged velocity on the mass ratio (see Sec. 3.2, Fig. 3.9). As the mass-averaged velocity decreases when mass ratio increases, the kinetic energy budget of the fast ejecta of these models decreases. Slower, more massive ejecta produces afterglow with lower peak flux. Notably, for models with stiffer EOSs, the dependency on mass ratio is not clear.

We find that the LC shape and peak time do not depend strongly on the uncertain microphysical parameters and ISM density. With respect to the latter, the peak time changes by a factor of a few when $n_{\rm ISM}$ varies between 10^{-3} cm^{-3} and 10^{-2} cm^{-3}. Finite resolution effects that are present in ejecta properties do affect the afterglow

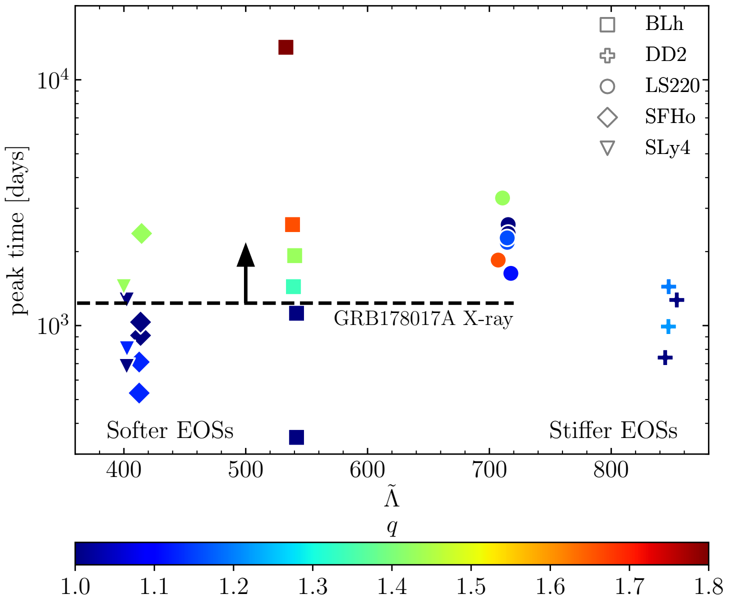

FIGURE 6.5: The time of kN afterglow LC peak for a set of BNS merger simulations as a function of binary parameters of these simulations, tidal deformability $\tilde{\Lambda}$ and mass ratio, q (color-coded). The microphysical parameters and ISM density are fixed for all models (See Tab. 6.1). The time of the latest GRB170817A observation is shown as a black dashed line. The black arrow indicates that, at the time of the observation, the flux appears to be rising, *i.e.*, the peak has not yet been reached. (Adapted from Nedora et al. (2021a))

LCs. Specifically, the t_p changes by a factor of ≤ 2, and $F_{\nu;p}$ changes within a factor of ≤ 4. However, our analysis shows that the uncertainty in $n_{\rm ISM}$, ε_e, ε_b and p have a stronger effect on the LC properties.

Comparing the GRB170817A observations and synthetic LCs, we observe that the changing afterglow at 1243 days after merger has the following implications: the kN afterglow peak should be (i) later and (ii) brighter than what is currently observed. Condition (ii) is weak as the LC peak flux is not well constrained due to uncertain microphysical parameters. The condition (i), however, is more robust from that point of view and allows us to assess which model's afterglow is in better agreement with observations.

We show the peak time of afterglow LCs of our BNS merger models in Fig. 6.5. There, the microphysical parameters and $n_{\rm ISM}$ are fixed and listed in Tab. 6.1 (last row). Here we consider all models, including those that do not have fast ejecta tail (see Sec. 3.2.2) as their ejecta is still energetic enough to produce bright afterglow. The LC peak times are $\sim 10^3$ days for all models that do not undergo PC. The latter, (BLh $q = 1.82$ model) produces massive and slow ejecta that is characterized by late afterglow with a LC peak of $\sim 10^4$ days. Otherwise, we find $t_p < 10^3$ days for models with $q \sim 1$, and $t_p > 10^3$ days for models with larger mass ratio. This relation appears more prominent for models with soft EOSs, as ejecta in these models has a strong contribution from the shocked, fast component of DE (when mass ratio is small), and the kinetic energy of the ejecta fast tail increases with a growing contribution from the shocked component (see Fig. 3.13). The afterglow of faster, less massive ejecta peaks earlier (*e.g.* Hotokezaka et al., 2015a). Indeed, the time of the LC peak depends primarily on the ejecta dynamics, the so-called deceleration time (*e.g.* Piran et al., 2013).

In Fig. 6.5 we also show the time of the latest observation of the rising flux in GRB170817A (the horizontal line). This provides the lower limit on t_p in accordance with (ii). We observe that synthetic LCs of models with a moderate amount of fast ejecta, *e.g.*, models with EOSs of mild stiffness and mass ratio, lie above the limit, while models with very energetic fast tails, found in $q = 1$ models with very stiff EOSs, peak earlier. This provides a new avenue to constrain binary parameters and perform MM analysis.

Chapter 7

Discussion and Conclusions

The scope of this thesis is to advance our understanding of BNS mergers and fundamental physics by using state-of-the-art NR simulations with advanced physics and EM models in tandem with multi-messenger observations of GW170817.

Considering the post-merger evolution of BNS merger remnants, we find an overall strong dependency on the system mass ratio and the EOS, and on the finite temperature effects in the latter. One of the key affected parameters is the remnant lifetime. We find that models with soft EOSs or/and large mass ratios produce short-lived NS remnants that collapse within a few $\sim$10 ms after merger. More symmetric models with stiffer EOSs produce long-lived, possibly stable remnants. The lifetime of the NS remnant appears to be correlated with the disk mass for the $q \sim 1$ models, in agreement with previous findings (Radice et al., 2018a,b). Binaries with larger mass ratios tend to have more massive disks and more massive tidal components of DE.

The long-term evolution of post-merger NS remnants is governed by the accretion, induced by neutrino cooling and viscous stresses, and mass shedding that originates in gravitational and hydrodynamical torques and neutrino reabsorption (heating). Notably, a newly formed NS remnant with mass exceeding the maximum of the uniformly rotating configuration, HMNS, does not necessarily collapse to a BH. Instead, massive winds, such as SWW, can efficiently remove the excess in mass (alongside the angular momentum), bringing the NS remnant to a rigidly rotating configuration.

Considering the matter ejected during and after mergers, we find two distinct types: DE and post-merger SWW. With respect to the former we augment the analysis of our own models by considering all available BNS merger models in the literature with various physics inputs. The statistical analysis of DE properties highlights the strong dependency of these properties on neutrino reabsorption. Its inclusion raises the ejecta mass and velocity. Meanwhile, the composition of DE from our models, computed with an approximated M0 neutrino scheme, is similar to that found in simulations with more sophisticated neutrino treatment methods (Sekiguchi et al., 2016; Vincent et al., 2020). Taking the largest-to-date set of BNS simulations, we link the DE properties back to the binary parameters considering a variety of fitting formulae. We update these relations that are very important for MM astronomy. We also find that a simple two parameter polynomial, $P_2^2(q, \tilde{\Lambda})$, shows a comparable or better statistical performance than other fitting formulae.

In cases where the post-merger remnant is long-lived, we identify a new ejecta component, SWW. These winds are driven by energy and angular momentum injected into the disk by a remnant which is subjected to bar-mode and one-armed dynamical instabilities. We find that within the simulation time, up to ~100 ms, SWW do not saturate unless the NS remnant collapses to a BH. SWW have a broad distribution in electron fraction that is on average higher than that of DE. SWW have narrow distribution in velocity and can unbind $\sim 0.1 - 0.5\,\mathrm{M}_{\odot}$ within a second.

A part of SWW, channeled along the polar axis and exhibiting the highest electron fraction, we identify as ν-driven winds. Contrary to other studies of neutrino-driven outflows (*e.g.* Dessart et al., 2009; Perego et al., 2014; Fujibayashi et al., 2020b), ν-driven winds in our simulations saturate shortly after merger. Notably, steady state ν-driven winds are generally referred to outflows that emerge on a timescale, hundreds of milliseconds longer than ours. Additionally, it is plausible that the approximated neutrino reabsorption scheme used in our simulations is insufficient in this case. Long-term simulations employing more advanced neutrino transport schemes are required to assess the properties of ν-driven winds. Additionally, the effects of magnetization are important for polar outflows (Siegel et al., 2017; Metzger et al., 2018b; Fernández et al., 2019; Miller et al., 2019a; Mösta et al., 2020). Our simulations, however, do not include magnetic fields.

We assess the outcome of r-process nucleosynthesis in the ejected matter via the precomputed parameterized model, based on the NRN `SkyNet` (Lippuner et al., 2015). The r-process yields in DE depend strongly on the binary mass ratio, with large amounts of lanthanides and actinides produced in high-q cases. Models with the highest mass ratios, that undergo PC, show actinides abundances in their DE similar to solar. Binaries with $q \sim 1$ produce less neutron-rich DE and the final abundances show a significant fraction of lighter elements.

If the post-merger remnant is long-lived, the final r-process abundances in total ejecta (that include DE and SWW) show large amounts of both heavy and light elements. The abundance pattern in these ejecta is similar to solar, down to $A \simeq 100$.

This result further emphasizes the importance of BNS mergers in cosmic chemical evolution.

Considering the thermal emission from the decay of r-process elements in ejecta, kN, from our models, we find that, when spherically symmetric kN models are considered (Villar et al., 2017a), none of our models can explain the AT2017gfo bolometric light curves. However, when anisotranisotropic multi-components kN models are considered, that take into account properties and geometry of ejecta, certain key features of AT2017gfo are recovered. Specifically, we find that the early blue emission can be explained when both DE and SWW are considered, and when the post-merger remnant is long-lived.

High electron fraction material was also shown to be present in outflows from BH-torus systems and thus does not necessarily require a long-lived remnant (Fujibayashi et al., 2020a). The late time red kilonova component requires massive, ∼20% of the disk mass, low-Y_e outflows. Such outflows can be driven by viscous processes and nuclear recombination on a timescale of seconds (*e.g.* Metzger et al., 2008).

Considering the synchrotron afterglow from the interaction between ejecta and the ISM, we find that the recently observed change in the afterglow of GRB170817A 10^3 days after merger can be explained by the kN afterglow produced by ejecta in ab-initio NR BNS simulations targeted to GW170817. Specifically, models with moderately stiff EOSs and moderately large mass ratios, that produce a mild amount of fast ejecta, are favored. This provides a new avenue to constrain properties of GW170817.

Future work

In order to investigate post-merger dynamics in more detail, *e.g.*: (i) assess remnant lifetime and ultimate fate, (ii) verify the presence of SWW and ν-driven winds and their properties, high resolution long-term (several seconds) 3D neutrino-radiation GRMHD simulations, computed with advanced microphysical EOSs with finite temperature effects are required. This might become possible as new, more advanced NR codes become available (*e.g.* Daszuta et al., 2021). Special attention should be given to the neutrino treatment methods as they strongly affect the properties and composition of ejecta. Several methods that are now in development, such as gray or spectral M1 (Foucart et al., 2016a; Roberts et al., 2016), or Monte-Carlo methods, would allow one to further constrain ejecta properties and the relation between these properties and binary parameters. Current leakage-based schemes, such as the M0 scheme used in this thesis and the M1-leakage scheme of Sekiguchi et al. (2015) and Fujibayashi et al. (2018) cannot adequately treat the diffusion of neutrinos from the interior of the post-merger NS remnant. Additionally, the MHD effects need to be re-examined. While it is apparent that MHD is crucial for launching the relativistic jet, its effects on ejecta and nucleosynthesis is not yet clear (Siegel et al., 2018; Fernández et al., 2019).

On the other front, the growing number of observational facilities and their increasing sensitivity requires continuous advancements in methods used to model EM counterparts to mergers. For instance, EM follow-up of GW170817 started ∼11 hours after the GW trigger, and thus the very early emission was not observed. If such emission is detected in future events it would provide very important information on ejecta properties and merger dynamics. Specifically, prompt γ-ray emission from a SGRB allows one to gauge the energetics of the event and properties of the system. The UV-precursor emission can hint at the presence of the very fast ejecta component that can be later verified with afterglow observations.

With respect to kN models the attention needs to be given to (i) the geometry of ejecta (ii) the dynamical evolution of ejecta (iii) the non-LTE effects. The latter are especially important as, with the launch of James Webb Space Telescope (JWST), the late kN emission in IR band would become observable for an event in the relative vicinity.

As GRB170817A has demonstrated, observations of SGRBs originating from BNS mergers can shed light on the properties of the BNS progenitor system and its astrophysical environment, as well as jet properties and jet physics (*e.g.* Hajela et al., 2019). Development of GRB models that can take advantage of multi-epoch observations, including observations of the motion of the flux centroid (*e.g.* Fernández et al., 2021), and models that allow for an arbitrary jet structure and complexity, are required. Additionally, as some SGRBs have shown to exhibit distinctive features in their X-ray LCs, such as plateau (Kumar et al., 2014), it is important to account for these features in GRB modeling as they can provide crucial information on the post-merger remnant (*e.g.* Gibson et al., 2017).

Several processes in the pre-merger and post-merger stages of the BNS system can produce EM signals that could be their respective "smoking guns". For instance, the EM emissions from inspiraling strongly magnetized NSs (*e.g.* Beloborodov, 2020), fallback accretion onto a BH (*e.g.* Desai et al., 2019) and NS (*e.g.* Gibson et al., 2017).

Finally, combining the aforementioned methods and models would result in a surrogate EM model of BNS mergers that, in tandem with already actively developing surrogate GW models, would allow for the most informed inference of binary properties. An example of such a model is the `NMMA` pipeline (Dietrich et al., 2020) that was recently used to obtain constraints on $R_{1.4}$, employing models of kN, GWs, and incorporating data from nuclear physics, pulsar observations and GW170817.

Growing samples of observed BNS mergers in GWs and EM spectrum in the next decade will provide an unprecedented amount of information that would require constant re-analysis with ever-advancing models, techniques and our understanding of the merger processes. This is a formidable challenge and interesting at that.

Appendix A

BNS ejecta and disk mass statistics

In the main text, in Ch. 3, Sec. 3.2, we discussed the statistics of ejecta properties, comparing different datasets with different physics inputs. Here we provide the details of the analysis.

As the errors for ejecta quantities are not available for most datasets, we uniformly employ the following assumptions. Following Radice et al. (2018a), for the DE mass we consider an uncertainty defined as

$$\Delta M_{\text{ej}} = 0.5 M_{\text{ej}} + 5 \times 10^{-5} \mathrm{M}_{\odot} \,. \tag{A.1}$$

For the ejecta velocity and for the electron fraction we consider $\Delta \upsilon_{\text{ej}} = 0.02\,c$ and $\Delta Y_e = 0.01$ as fiducial uncertainties, respectively. The latter value is justified by the robust behavior of the average electron fraction in simulations where multiple resolutions are available. Notably, it is possible that uncertainties are larger due to the approximate nature of current neutrino treatments (see *e.g.*, Foucart et al. (2016a, 2018). We leave a more accurate investigation to future works, when more simulations with advanced neutrino treatment become available, such as the M1 and Monte Carlo schemes. For the disk mass we assume

$$\Delta M_{\text{disk}} = 0.5 M_{\text{disk}} + (5 \times 10^{-4}) \mathrm{M}_{\odot} \,, \tag{A.2}$$

again following Radice et al. (2018a).

A.1 Method

We perform two types of analysis: (i) we assess the quality of different fitting formulae for a given dataset and determine the best performing one; (ii) we evaluate the differences between datasets that simulate microphysics and neutrinos in different ways (if at all). For (i) we consider the fitting formulae available in the literature, and new ones based on simple polynomials in key BNS parameters, *i.e.*, the tidal deformability parameter, $\tilde{\Lambda}$, and mass ratio, q. To assess their performance, we employ the basic fitting procedure with least square method, minimizing the χ^2_ν (discussed below) or the residuals. The χ^2_ν statistics reads

$$\chi^2_\nu = \frac{\chi^2}{N-C} = \frac{1}{N-C}\sum_{i=1}^{N}\left(\frac{o_i - e_i}{o_i^{\text{err}}}\right)^2, \tag{A.3}$$

where N is the number of points in the dataset, C is the number of coefficients in the fitting formula (thus $N-C$ defines the number of degrees of freedom), o_i are the dataset values and o_i^{err} are their errors, e_i are the values predicted by the fitting model, and $o_i - e_i$ are the residuals. The closer the value of χ^2_ν to 1, the better the fitting formula performs. Additionally, we compute the coefficient of determination, R^2, defined as

$$R^2 = 1 - \frac{\sum\limits_{i=1}^{N}(o_i - e_i)^2}{\sum\limits_{i=1}^{N}(o_i - \mu)^2}, \tag{A.4}$$

where μ is the mean value of $\{o_i\}_{i=1,N}$. Here, again, the closer R^2 is to 1, the better the fit.

The fitting procedure is conducted first for the `M0RefSet` to establish the baseline, and repeated each time as we add a new dataset until all models are included. Tables with coefficients for all fitting formulae are reported at the end of this Chapter, in Sec. A.4.

To evaluate the influence of different physics input in simulations on the statistical behavior of an ensemble of models we employ the following procedure. We begin with the dataset that is uniform in physics and code, the `M0RefSet`, all models in which have fixed chirp mass. Then we add models from the `M0/M1Set` that also include effects of neutrino heating and cooling, but which is not uniform in numerical setup and exact neutrino treatment. To assess how statistical properties changed, we consider the mean value and standard deviation. To investigate the effects of the absence of neutrino reabsorption we add the `LeakSet`, where only neutrino cooling is present, and repeat the analysis. Finally, to assess the effect of neutrinos and changes in the EOS treatment we repeat the analysis with all datasets, including models of the `NoNusSet`.

A.2 Analysis of dynamical ejecta

A.2.1 Dynamical ejecta mass

The mass of the DE averaged over all the models of `M0RefSet` is

$$\overline{M^{\rm d}_{\rm ej}} = (3.51 \pm 2.57) \times 10^{-3} {\rm M}_{\odot} \,, \tag{A.5}$$

where we also report the standard deviation computed over the relevant simulation sample. If we add other models with neutrino heating and cooling, *i.e.*, the `M0/M1Set` models, we observe that the mean value increases to $(4.17 \pm 3.65) \times 10^{-3} {\rm M}_{\odot}$. This is due to models with M1 neutrino scheme of Vincent et al. (2020) and Sekiguchi et al. (2016).

The inclusion of models with neutrino cooling only, `LeakSet`, leads to the decrease in $M^{\rm d}_{\rm ej}$ to $2.91 \times 10^{-3} {\rm M}_{\odot}$. Including the rest of the models (those without neutrinos, `NoNusSet`), we observe that the $M^{\rm d}_{\rm ej}$ rises to $5.56 \times 10^{-3} {\rm M}_{\odot}$. This is due to the addition of models computed with polytropic EOSs, specifically, models from Dietrich et al. (2017a), that display the largest ejecta masses among all the datasets.

Next, we perform the fitting procedure to the total ejecta mass. We consider the widely used fitting formulae first (Kawaguchi et al., 2016; Dietrich et al., 2017b; Radice et al., 2018a),

$$\begin{split}\left(\frac{M^{\rm d}_{\rm ej}}{10^{-3}{\rm M}_{\odot}}\right)_{\rm fit} = \Bigg[\alpha\left(\frac{M_B}{M_A}\right)^{1/3}\left(\frac{1-2C_A}{C_A}\right) + \beta\left(\frac{M_B}{M_A}\right)^{n} \\ +\gamma\left(1-\frac{M_A}{M_{b\,A}}\right)\Bigg] M_{b\,A} + (A \leftrightarrow B) + \delta,\end{split} \tag{A.6}$$

and the fitting formula presented in Krüger et al. (2020):

$$\left(\frac{M^{\rm d}_{\rm ej}}{10^{-3}{\rm M}_{\odot}}\right)_{\rm fit} = \left(\frac{\alpha}{C_A} + \beta\frac{M_B^n}{M_A^n} + \gamma C_A\right) M_A + (A \leftrightarrow B) \ \ . \tag{A.7}$$

We also employ simple second-order polynomials: the one-parameter formula $(\tilde{\Lambda})$ and the two-parameter formula in $(q, \tilde{\Lambda})$,

$$P^1_2(\tilde{\Lambda}) = b_0 + b_1\tilde{\Lambda} + b_2\tilde{\Lambda}^2, \tag{A.8}$$

$$P^2_2(q,\tilde{\Lambda}) = b_0 + b_1 q + b_2\tilde{\Lambda} + b_3 q^2 + b_4 q\tilde{\Lambda} + b_5\tilde{\Lambda}^2 \,. \tag{A.9}$$

The fitting procedure is performed considering the $\log_{10}(M^{\rm d}_{\rm ej})$ instead of $M^{\rm d}_{\rm ej}$ for

TABLE A.1: Performance of different fitting formulae (in columns) for various ejecta properties and sets of data (in rows). The mean is the average value across a sample of simulations. The values are the χ-squared χ^2_ν obtained via least-square method and error measured discussed in the text. The best fitting formula for a given dataset is characterized by the lowest value of χ^2_ν.

$\log_{10}(M^{\rm d}_{\rm ej})$	Datasets	Mean	Eq. (A.6)	Eq. (A.7)	$P^1_2(\tilde\Lambda)$	$P^2_2(q,\tilde\Lambda)$
	`MORefSet`	3.84	2.23	1.58	3.03	1.55
	& `MO/M1Set`	26.66	16.85	10.60	37.29	56.45
	& `LeakSet`	99.11	30.12	11.91	45.59	24.40
	& `NoNusSet`	196.52	84.81	39.88	123.56	44.36
$\langle v_{\rm ej}\rangle$	Datasets	Mean	Eq. (A.11)		$P^1_2(\tilde\Lambda)$	$P^2_2(q,\tilde\Lambda)$
	`MORefSet`	3.76	1.51		3.24	1.05
	& `MO/M1Set`	4.03	2.42		3.35	1.67
	& `LeakSet`	7.10	6.07		6.34	5.09
	& `NoNusSet`	7.95	6.79		7.64	6.83
$\langle Y_{\rm e}\rangle$	datasets	Mean			$P^1_2(\tilde\Lambda)$	$P^2_2(q,\tilde\Lambda)$
	`MORefSet`	42.49			43.69	9.07
	& `MO/M1Set`	37.78			38.62	9.68
	& `LeakSet`	35.80			36.27	24.96
$\langle\theta_{\rm RMS}\rangle$	datasets	Mean			$P^1_2(\tilde\Lambda)$	$P^2_2(q,\tilde\Lambda)$
	`MORefSet`	20.68			21.66	4.55
	& `MO/M1Set`	18.18			18.69	4.17
	& `LeakSet`	15.56			14.34	8.73

numerical reasons. This is motivated by the fact that even within the `MORefSet`, values of the $M^{\rm d}_{\rm ej}$ change by an order of magnitude for very similar values of q and $\tilde\Lambda$ (Fig. 3.9). Additionally, the error measure we consider for $M^{\rm d}_{\rm ej}$, Eq. (A.1), is biased towards the data with smaller values of $M^{\rm d}_{\rm ej}$ (the lower error bar for the lower $M^{\rm d}_{\rm ej}$). A possible alternative approach is to consider the residuals instead of χ^2_ν for the minimization. In the case of $M^{\rm d}_{\rm ej}$, however, we find that the two approaches lead to similar qualitative fit within the domain of calibration.

Considering the fitting formulae from the literature, Eq. (A.6) and Eq. (A.7), we find that the outcome of the fitting procedure depends strongly on the non-linear fitting algorithm and on initial guesses. This makes the fitting ill-constrained. Moreover, in Eq. (A.7) the compactness enters twice with opposite trends. The physical motivation of this choice is not clear. We report all the fit calibrations in Sec. A.4 with the calibration for the polynomials reported in Tab. A.3; and for the Eqs.(A.6)-(A.7) in Tab. A.4.

The performance of different fitting formulae is reported in Tab. A.1 in terms of the χ^2_ν. Starting with the `MORefSet` we observe that the best fitting formula that

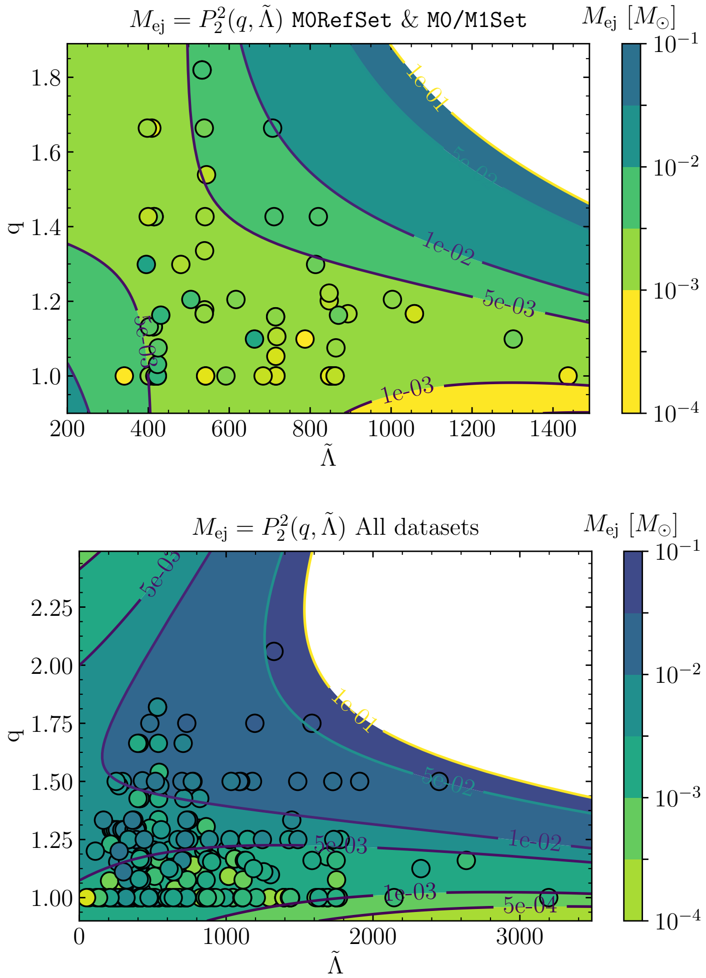

FIGURE A.1: Ejecta masses inferred from $P_2^2(q, \tilde{\Lambda})$ fitting formula (colored contours) and ejecta masses from NR simulations (colored markers). If fit predicts the value correctly, the colors match. The *top panel* shows the fit calibrated with `M0RefSet` and `M0/M1Set` only. The *bottom panel* shows the fit calibrated with all datasets available. (Adapted from Nedora et al. (2020))

gives the lowest $\chi^2_\nu = 1.55$, is the second order two-parameter polynomial $P_2^2(q, \tilde{\Lambda})$. Notably, Eq. (A.7) gives a very similar $\chi^2_\nu = 1.58$. Adding models of `M0/M1Set` we find a rise in χ^2_ν across all fitting formulae. This can be attributed to the models of `M0/M1Set` spanning a significantly broader range in terms of $\tilde{\Lambda}$. Additionally, with the inclusion of models from `M0/M1Set`, systematic and methodological uncertainties enter the picture, and as we shall see from the analysis, they dominate the overall statistics.

When all datasets are included, the $P_2^2(q, \tilde{\Lambda})$ and Eq. (A.7), remain the best fitting formulae albeit with large χ^2_ν of 44 and 40 respectively. The similar performance of these fitting formulae can be attributed to the fact that in both, mass ratio enters

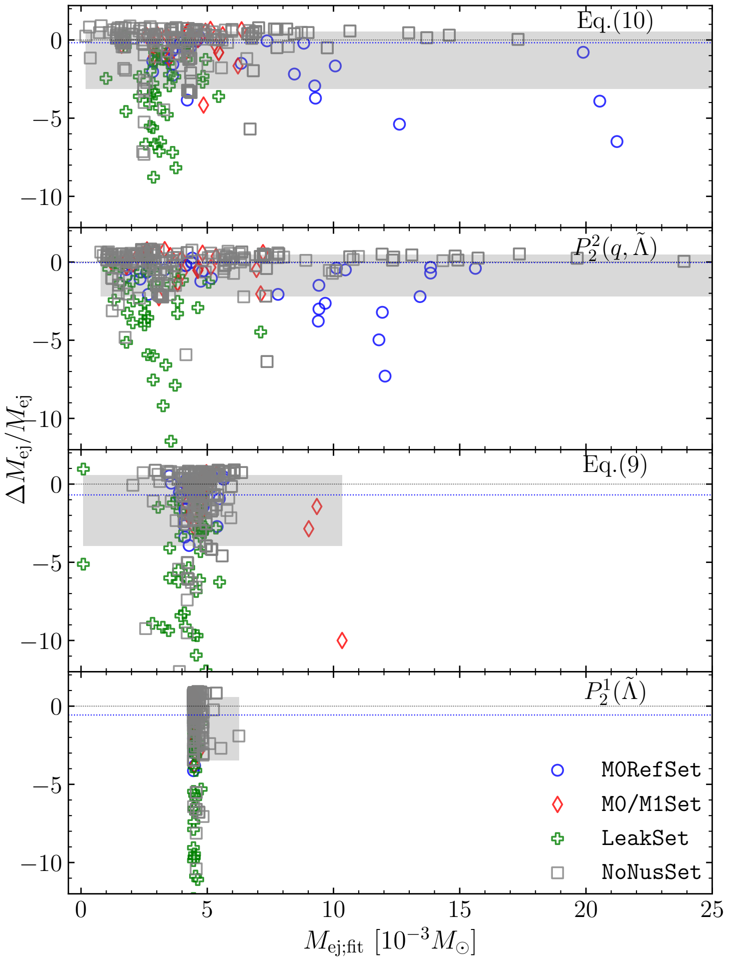

FIGURE A.2: Normalized residuals as a function of predicted ejecta mass for four fitting formulae (one per subpanel) and for four different calibration sets (different markers) that correspond to four entries in Tab. A.1. Here $\Delta M_{\rm ej} = M_{\rm ej} - M_{\rm ej}^{\rm fit}$. From top to bottom the fitting formulae are arranged based on their χ_ν^2: from lowest to highest, *i.e.*, the top subpanel shows the best fit. (Adapted from Nedora et al. (2020)).

explicitly, allowing the fit to capture the leading trends in data. Meanwhile, regarding Eq. (A.6), it was pointed out in Radice et al. (2018a) that this formula does not reproduce well the systematic trends in the set of models with the leakage neutrino scheme.

Notably, the second order polynomial in only one quantity, $\tilde{\Lambda}$, is failing to capture the main trends in data with $\chi_\nu^2 = 123$ when all models from all datasets are considered. Similarly, a fit with no free parameters, the mean value, does not perform well, and results in very large $\chi_\nu^2 = 196$. Thus, we conclude that dependency on the mass ratio ought to be included into a fitting formula in order to capture the leading trends in statistical behaviour of $M_{\rm ej}^{\rm d}$.

We show how the $P_2^2(q,\tilde{\Lambda})$ performs when only the `M0RefSet` & `M0/M1Set` or all available models are considered in Fig. A.1. We observe that the smooth polynomial fit cannot capture oscillations in data. Overall, while for the `M0RefSet` & `M0/M1Set` leading trends seems to be captured to some extent, for all datasets the fit's predictive power reduces significantly.

We display the relative differences between the model data and data obtained from fitting formulae in Fig. A.2. The plot shows that none of the fitting formulae can reproduce the $M_{\rm ej}^{\rm d}$ of `LeakSet` models. Notably, while Eq. (A.7) and $P_2^2(q,\tilde{\Lambda})$ showed similar χ_ν^2, the plot shows that the latter reproduces the high ejecta masses better. The poor performance of the single parameter polynomial, $P_2^1(\tilde{\Lambda})$, is clear, as the fit gives an almost flat distribution around the mean value of $M_{\rm ej}^{\rm d}$. Similarly, Eq. (A.6) cannot reproduce the large masses of a subset of models.

Overall we conclude that the intrinsic scatter in data hinders the performance of any smooth fitting formula. The inclusion of mass ratio is required to capture certain leading trends in data and the simple polynomial $P_2^2(q,\tilde{\Lambda})$ shows a reasonably good statistical performance. The statistical analysis for considered datasets suggests that the $M_{\rm ej}^{\rm d}$ depends strongly on the physics inputs of simulations: the neutrino scheme and EOS treatment. The magnitude of systematic uncertainties reduces the ability of any fitting formula to identify and capture leading trends.

A.2.2 Mass-averaged velocity

The average of the mass-averaged ejecta velocity, $\langle v_\infty^{\rm d}\rangle$, of all models of `M0RefSet` is

$$\overline{\langle v_\infty^{\rm d}\rangle} = (0.17 \pm 0.04)\,c. \tag{A.10}$$

The average $\langle v_\infty^{\rm d}\rangle$ does not significantly change when models of the `M0/M1Set` are added, and remain at $(0.18 \pm 0.04)\,c$. Hence, we note that the ejecta velocity is recovered robustly by simulations with similar physics inputs but different numerical setups (unlike the ejecta mass). Adding models with neutrino leakage scheme only, from the `LeakSet`, we find that the mean value of the ejecta velocity increases to $0.19\,c$, while if all models from all datasets are considered, the increase is more significant, to $0.23\,c$. The latter can be attributed to models with polytropic EOSs of Bauswein et al. (2013b) that show the highest $\langle v_\infty^{\rm d}\rangle$.

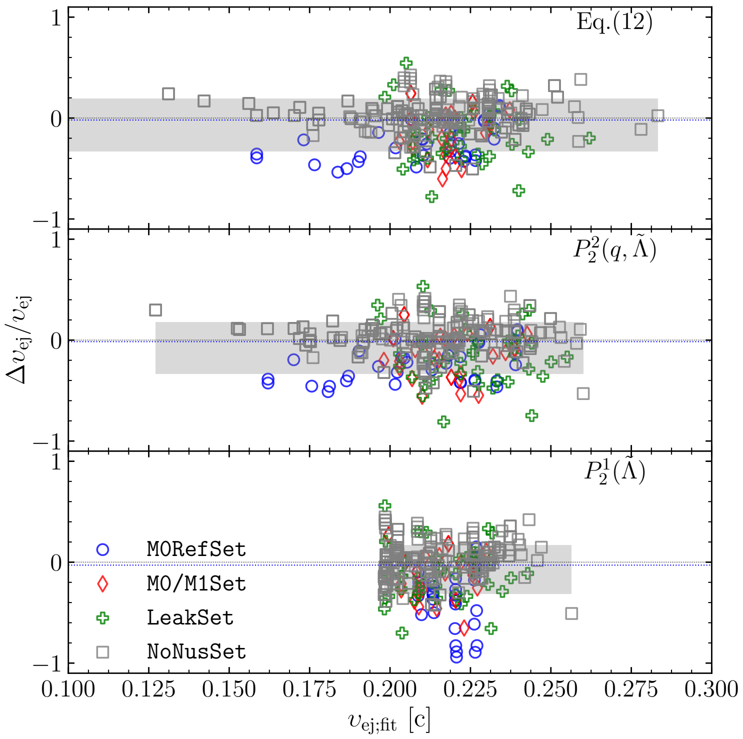

FIGURE A.3: Same as Fig. A.2, but for ejecta mass-averaged velocity. Here $\Delta\upsilon_{\rm ej} = \upsilon_{\rm ej} - \upsilon_{\rm ej}^{\rm fit}$. (Adapted from Nedora et al. (2020)).

We consider the fitting formula to the ejecta velocity as a function of binary parameters presented in Dietrich et al. (2017a) and Radice et al. (2018a) as

$$\langle v_{\infty}^{\rm d}\rangle_{\rm fit} = \left[\alpha\left(\frac{M_A}{M_B}\right)(1+\gamma C_A)\right] + (A \leftrightarrow B) + \beta\,, \tag{A.11}$$

and one and two- parameter second order polynomials in q and $\tilde{\Lambda}$, Eq. (A.8)-(A.9). Notably, the former equation, Eq. (A.11), gives a fit that is not well constrained and was found to depend on the choice of the initial guesses for the fitting procedure. We report the fits' calibration in Tab. A.3 for the polynomials and in Tab. A.4 for the Eq. (A.11).

The performance of different fitting formulae is reported in Tab. A.1 in terms of χ_ν^2. For the models of `M0RefSet`, the best fitting model is $P_2^2(q,\tilde{\Lambda})$ giving the lowest $\chi_\nu^2 = 1.1$. The second best is the Eq. (A.11) with $\chi_\nu^2 = 1.5$. The hierarchy does not change when all the datasets are considered with the exception of the set of models with no neutrinos and mostly polytropic EOSs from Bauswein et al. (2013b). When all available models are considered, the two fitting formulae give comparable results

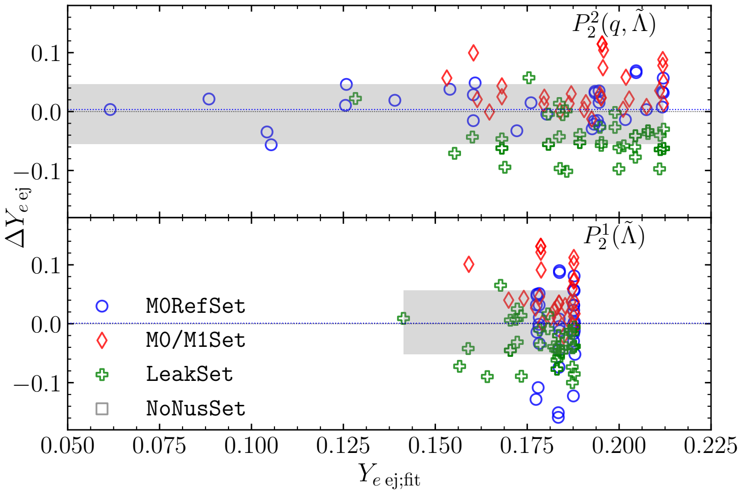

FIGURE A.4: Same as Fig. A.2, but for mass-averaged electron fraction. Here $\Delta Y_{e\,\mathrm{ej}} = Y_{e\,\mathrm{ej}} - Y_{e\,\mathrm{ej}}^{\mathrm{fit}}$. (Adapted from Nedora et al. (2020)).

in terms of χ^2_ν.

In Fig. A.3, values of $\langle v_\infty^{\mathrm{d}}\rangle$ from all datasets are compared to those inferred from fitting formulae. Notably, $P_2^2(q,\tilde\Lambda)$ and Eq. (A.11) are able to reproduce simulation data within a ∼50% error margin. However, models from `NoNusSet` are not well reproduced by any fitting formula considered. The single parameter polynomial, $P_2^1(\tilde\Lambda)$, does not reproduce well models with low $\langle v_\infty^{\mathrm{d}}\rangle$ and in general shows worse performance in predicting the $\langle v_\infty^{\mathrm{d}}\rangle$.

A.2.3 Electron fraction

Considering the average value of the mass-averaged electron fraction, $\langle Y_e^{\mathrm{d}}\rangle$, we find that when only models of the `M0RefSet` are considered, it varies from 0.03, found in very high mass ratio binaries that produce cold, low-Y_e, tidal ejecta, to 0.27 in $q\sim 1$ binaries. The mean value is

$$\overline{\langle Y_e^{\mathrm{d}}\rangle} = 0.18 \pm 0.07. \tag{A.12}$$

Adding the rest of the models with neutrino heating and cooling, from the `M0/M1Set`, we observe an increase in the mean $\langle Y_e^{\mathrm{d}}\rangle$, to 0.20 ± 0.06. This can be attributed to the overall high $\langle Y_e^{\mathrm{d}}\rangle$ found in models with leakage+M1 neutrino scheme of Sekiguchi et al. (2015, 2016). Additionally, most of the models of `M0/M1Set` are low mass ratio models (*e.g.* Vincent et al., 2020). Models with leakage neutrino scheme of the `LeakSet`, naturally, have on average lower $\langle Y_e^{\mathrm{d}}\rangle$ of 0.14 ± 0.04. If models of the `M0/M1Set` and

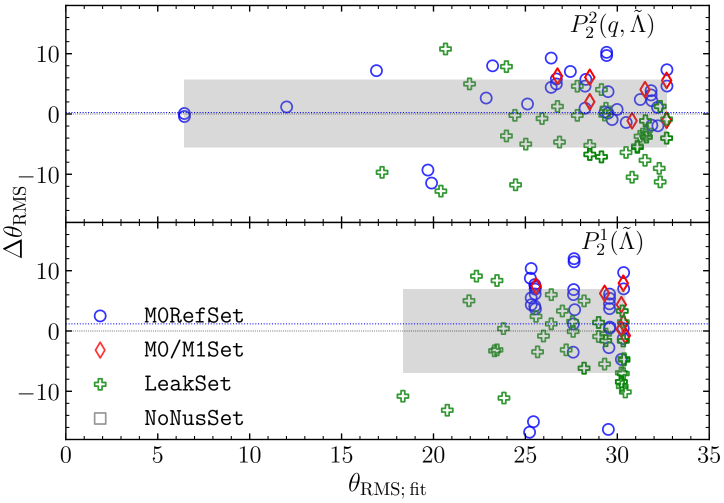

FIGURE A.5: Same as Fig. A.2, but for the ejecta RMS half-opening angle. Here $\Delta\theta_{\rm RMS} = \theta_{\rm RMS} - \theta_{\rm RMS}^{\rm fit}$. (Adapted from Nedora et al. (2020)).

`M0RefSet` are added, the overall average electron fraction decreases back to 0.18 with a standard deviation of 0.06.

As fitting formulae we consider only the polynomials, Eq. (A.8)-(A.9). We report the resulted calibration in Tab. A.3. When only models of `M0RefSet` are considered, fitted with $P_2^2(q,\tilde\Lambda)$, the result is $\chi_\nu^2 = 9.1$. This value increases only slightly to 9.7 when other models with neutrino cooling and heating (from the `M0/M1Set`) are added. This suggests that $P_2^2(q,\tilde\Lambda)$ is able to capture the leading trends in data (if the physical setup is similar). If we add models of the `LeakSet`, where the data is statistically different, the χ_ν^2 increases to 24.9.

We compare the values of $\langle Y_e^{\rm d}\rangle$ from datasets and predicted by fitting formulae in Fig. A.4. Notably, for all datasets, the $P_2^2(q,\tilde\Lambda)$ is able to reproduce both, low-Y_e and high-Y_e models of `M0/M1Set` and `M0RefSet`, and is the best fitting formula among those considered.

A.2.4 Root mean square half-opening angle

The average value of RMS half-opening angle, $\langle\theta_{\rm RMS}\rangle$, of the `M0RefSet` is

$$\overline{\langle\theta_{\rm RMS}\rangle} = (28.9 \pm 9.2)\,\text{deg}\,, \tag{A.13}$$

The inclusion of models with neutrino reabsorption from Radice et al. (2018a) decreases the mean value only slightly to $\overline{\langle\theta_{\rm RMS}\rangle} = (27.6 \pm 7.9)\,\text{deg}$.

Having a rather small sample of models we limit the statistical analysis, and consider only polynomial fitting formulae, Eqs. (A.8)-(A.9), whose calibration is reported in Tab. A.3. For the fitting procedure we adopted a uniform error of 2 deg in accordance with Radice et al. (2018a).

We find that $P_2^2(q,\tilde{\Lambda})$ performs significantly better than one-parameter $P_2^1(\tilde{\Lambda})$, and gives $\chi_\nu^2 = 4.6$. The value decreases to 4.2 when all models with neutrino absorption are considered (including those of Radice et al. (2018a)). The inclusion of models with leakage scheme from the same work raises the χ_ν^2 by almost a factor of 2. We present the comparison of fitting formulae performances in terms of χ_ν^2 in Tab. A.1.

The comparison between the values of $\langle\theta_{\rm RMS}\rangle$ from datasets, and inferred by fitting formulae, is presented in Fig. A.5. The plot shows that the $P_2^2(q,\tilde{\Lambda})$ reproduces the low-$\langle\theta_{\rm RMS}\rangle$ models considerably better than the one-parameter $P_2^1(\tilde{\Lambda})$. Both fitting formulae are able to reproduce the simulation data within the ∼10 deg error margin.

A.3 Remnant disk

Considering disk masses of models of the `M0RefSet` (see Ch. 3, Sec. 3.1) we find that $M_{\rm disk}$ varies between $0.01\,{\rm M}_\odot$ in models with short-lived remnants, and $0.3\,{\rm M}_\odot$ in models with long-lived remnants. The mean value is

$$\overline{M_{\rm disk}} = (0.156 \pm 0.084)\,{\rm M}_\odot. \tag{A.14}$$

The value decreases slightly to $(0.147 \pm 0.075)\,{\rm M}_\odot$ if all models with advanced physics are added (*i.e.*, models of the `M0/M1Set`). The addition of models of the `LeakSet` decreases the mean value further to $0.125\,{\rm M}_\odot$ with a standard deviation of $0.081\,{\rm M}_\odot$. This is because the largest set of models of `LeakSet` – models from Radice et al. (2018a) – includes binaries with very high total mass that at merger form a BH with no disk left. If we add models of the `NoNusSet`, the mean value does not seem to be affected as models of this dataset show properties that are in general in agreement with previous datasets.

It is important to emphasize that there are large uncertainties that enter the statistical analysis of disk masses, in addition to fundamental differences between disks around BH and NS remnants. Specifically, we emphasize that in the source material (see Chapter 3, Tab. 3.1) the disk mass is computed with different methods. In Dietrich et al. (2015, 2017a) only disks around BH remnants are considered, and their masses are evaluated ≈1 ms after the BH formation as a baryonic mass outside the apparent

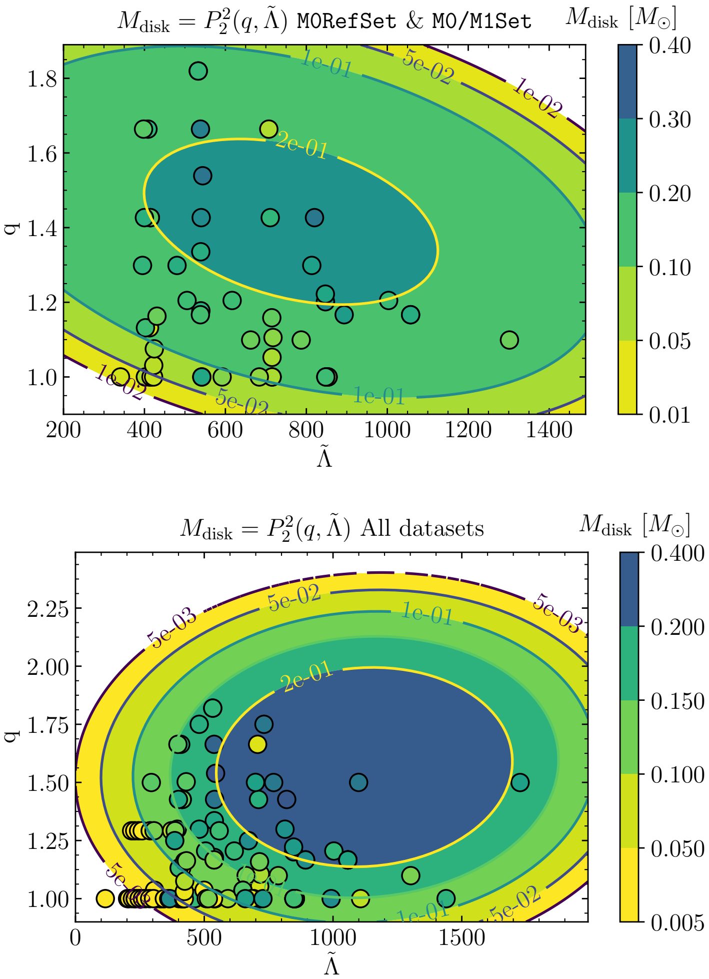

FIGURE A.6: Same as Fig. A.2, but for the disk mass. (Adapted from Nedora et al. (2020)).

horizon, while in Sekiguchi et al. (2016) the disk masses are evaluated ≈30 ms after the collapse. In Radice et al. (2018a), disks around both BH and NS remnants are considered. In the case of a BH, the $M_{\rm disk}$ is evaluated as a mass outside the apparent horizon. In the case of a NS, the same density criterion for the disk is adopted as in our analysis (see Ch. 2, Sec. 2.6), *i.e.*, the baryonic mass with rest mass density $\rho \leq 10^{13}$ g cm^{-3}. In Kiuchi et al. (2019) this density criterion is used regardless of the remnant: BH or NS, with the $M_{\rm disk}$ evaluated at an unspecified time. In Vincent et al. (2020) the density criterion is used, and only disks around NS remnants are evaluated at fixed ∼7.5 ms after merger. This is, however, significantly shorter than the end time of our simulations, when we evaluated the disk mass. The method differences can introduce systematic factor of an order of $\sim 2-5$.

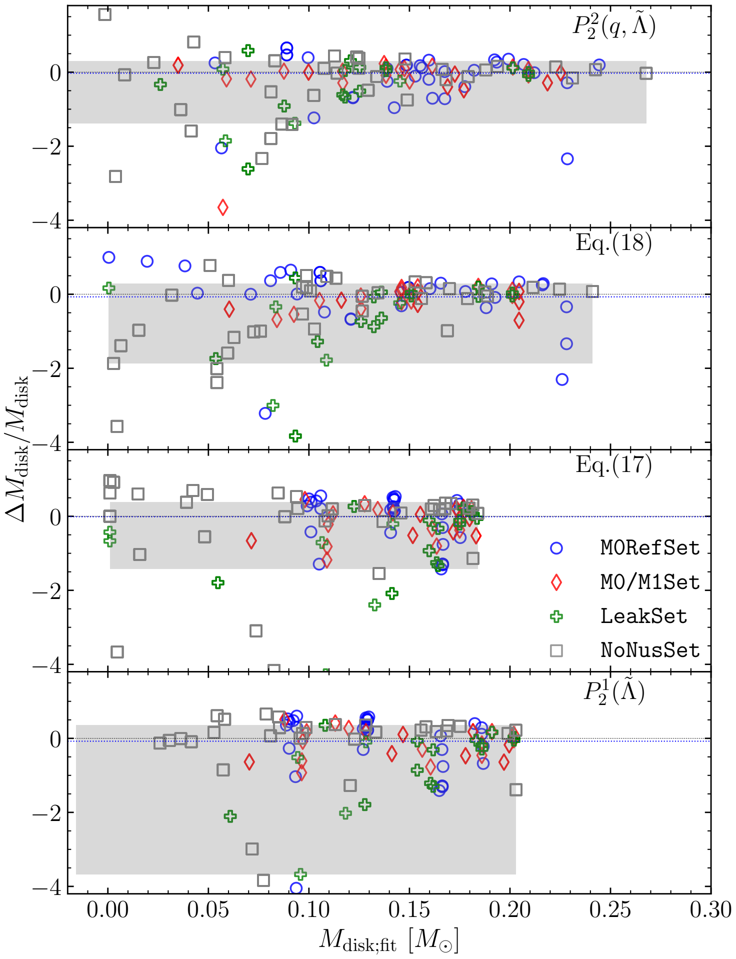

FIGURE A.7: Normalized residuals as a function of predicted disk mass for four fitting formulae (one per subpanel) and for four different calibration sets (different markers), corresponding to four entries in Tab. A.2. Here $\Delta M_{\rm ej} = M_{\rm ej} - M_{\rm ej}^{\rm fit}$. From top to bottom the fitting formulae are arranged based on their χ_ν^2: from lowest to highest, *i.e.*, the top subpanel shows the best fit. (Adapted from Nedora et al. (2020)).

We consider the fitting formulae to the $M_{\rm disk}$ as functions of binary parameters following Radice et al. (2018a),

$$\left(\frac{M_{\rm disk}}{M_\odot}\right)_{\rm fit} = \max\left\{10^{-3}, \alpha + \beta \tanh\left(\frac{\tilde{\Lambda} - \gamma}{\delta}\right)\right\}, \tag{A.15}$$

and following Krüger et al. (2020),

$$\left(\frac{M_{\rm disk}}{M_\odot}\right)_{\rm fit} = M_A \max\left\{5 \times 10^{-4}, (\alpha C_A + \beta)^\gamma\right)\right\} + (A \leftrightarrow B)\,, \tag{A.16}$$

TABLE A.2: Reduced χ-squared χ^2_ν for different fit models for the final disk mass.

datasets	Mean	Eq. (A.15)	Eq. (A.16)	$P^1_2(\tilde{\Lambda})$	$P^2_2(q,\tilde{\Lambda})$
`M0RefSet`	2956.22	1927.27	2198.85	2574.14	425.41
& `M0/M1Set`	1523.78	784.72	894.75	1074.14	174.82
& `LeakSet`	3064.62	543.20	629.95	757.43	202.23
& `NoNusSet`	2549.50	574.90	442.79	603.87	197.58

as well as the simple polynomials in q and $\tilde{\Lambda}$, Eqs. (A.8)-(A.9).

We find that the value of $M_{\rm disk}$ can change by up to an order of magnitude for similar values of q and $\tilde{\Lambda}$. Meanwhile, the error measure adapted for the $M_{\rm disk}$, Eq. (A.2), is biased towards the lower values. The solution that we resorted to in the case of $M^{\rm d}_{\rm ej}$, *i.e.*, to invoke the $\log_{10}$ of the quantity, is not applicable here due to special forms of fitting formulae, Eqs. (A.15)-(A.16), that lead to singularities in fitting. In addition, the fitting function Eq. (A.16) is not smooth and can return singular values. We thus resort to minimizing residuals instead of χ^2_ν. However, we still employ χ^2_ν for the comparison of different fitting formulae performances.

Calibrations of polynomial fitting formulae are reported in Tab. A.5, and for fitting formualae, Eqs. (A.8)-(A.9), in Tab. A.6. Fit performances in terms of χ^2_ν are presented in Tab. A.2 for all fitting formulae.

Upon visual inspection we find that the $M_{\rm disk}$ shows dependency on the mass ratio and on $\tilde{\Lambda}$. Indeed, considering models of the `M0RefSet` we find that the polynomial in q and $\tilde{\Lambda}$ displays the best performance with $\chi^2_\nu = 425$, with the second best being, Eq. (A.16) with $\chi^2_\nu = 443$. We recall that large values of χ^2_ν are expected, as the fitting procedure minimizes residuals and not χ^2_ν. The addition, models with advanced physics of the `M0/M1Set` reduces the χ^2_ν to 175 for the $P^2_2(q,\tilde{\Lambda})$. When the remaining models are added, the χ^2_ν rises only slightly to 197.6.

The values of $M_{\rm disk}$ from datasets alongside the values predicted by $P^2_2(q,\tilde{\Lambda})$ (colored contours) are shown in Fig. A.6. Similarly to the ejecta mass, smooth fitting formulae, such as $P^2_2(q,\tilde{\Lambda})$, cannot reproduce the data on the level of individual models. However, the polynomial appears to be able to capture leading trends in data when models of the `M0RefSet` & `M0/M1Set` are considered. When simulations from all datasets are combined for the calibration, the predictive ability of the fit reduces considerably.

The relative differences between the data and values given by various fitting formulae are shown in Fig. A.7. The plot shows that the Eq. (A.15) and $P^1_2(\tilde{\Lambda})$ fitting formulae fail to predict high disk masses found in simulations with high mass ratio. Eq. (A.16) reproduces better large M_{disk} values, but it fails to capture smaller disk masses of models of the `NoNusSet`. An overall better performance is seen for $P_2^2(q, \tilde{\Lambda})$, as it is able to reproduce large M_{disk} values and gives lower residuals. This indicates that both q and $\tilde{\Lambda}$ are important for capturing the leading trends in M_{disk}. However, we note that both residuals and χ_ν^2 for all fitting models are large. With the currently available data, fitting formulae are able to reproduce the simulation values within an order of magnitude only.

The statistical analysis of the M_{disk} highlights large systematic and method-of-computation uncertainties. The leading trends in data appears to be given by the q and $\tilde{\Lambda}$. However, a larger sample of models and separate analysis of disks around BH and NS remnants are required to improve the fitting formulae and investigate the statistics more thoroughly.

A.4 Tables with fitting coefficients

In this section we summarizes all fit coefficients. Dynamical ejecta coefficients can be found in Tab. A.3 and Tab. A.4 for the polynomials and fitting formulae respectively. Disk mass coefficients can be found in Tab A.5 and Tab. A.6 for the polynomials and fitting formulae respectively. The coefficients for the best (lowest χ_ν^2) fitting formulae are highlighted in the tables.

Table A.3: Dynamical ejecta properties: coefficients for polynomial regression of various quantities. Results for both first order and second order polynomials are reported $P_2^1(\tilde{\Lambda})$ and $P_2^2(q,\tilde{\Lambda})$ The recommended calibration for $P_2^2(q,\Lambda)$ is highlighted.

Quantity	Datasets	b_0	b_1	b_2	b_3	b_4	b_5	χ_ν^2	R^2
$\log_{10}(M_{\rm ej}^{\rm d})$	`M0RefSet`	-3.69	4.34×10^{-3}	-3.66×10^{-6}				3.0	0.035
	& `M0/M1Set`	-2.10	-5.84×10^{-4}	8.86×10^{-8}				37.3	0.056
	& `LeakSet`	-2.85	8.99×10^{-4}	-7.42×10^{-7}				45.6	0.017
	& `NoNusSet`	-2.35	-1.29×10^{-5}	1.82×10^{-8}				123.6	-0.020
$v_\infty^{\rm d}$ [c]	`M0RefSet`	4.63×10^{-1}	-9.58×10^{-4}	7.30×10^{-7}				3.2	0.213
	& `M0/M1Set`	3.43×10^{-1}	-4.84×10^{-4}	3.25×10^{-7}				3.3	0.211
	& `LeakSet`	2.77×10^{-1}	-2.38×10^{-4}	1.39×10^{-7}				6.3	0.133
	& `NoNusSet`	2.50×10^{-1}	-6.71×10^{-5}	2.16×10^{-8}				7.6	0.051
$Y_e^{\rm d}$	`M0RefSet`	3.17×10^{-1}	-5.82×10^{-4}	5.41×10^{-7}				43.7	0.062
	& `M0/M1Set`	1.99×10^{-1}	-3.08×10^{-5}	4.62×10^{-8}				38.6	0.026
	& `LeakSet`	1.45×10^{-1}	1.09×10^{-4}	-6.91×10^{-8}				36.3	0.017
$\langle\theta_{\rm RMS}\rangle$ [deg]	`M0RefSet`	$4.09\times10^{+1}$	-5.32×10^{-2}	5.20×10^{-5}				21.7	0.045
	& `M0/M1Set`	2.55×10^{1}	3.76×10^{-3}	4.33×10^{-6}				18.7	0.047
	& `LeakSet`	1.47×10^{1}	3.37×10^{-2}	-1.79×10^{-5}				14.3	0.115
$\log_{10}(M_{\rm ej}^{\rm d})$	`M0RefSet`	1.04	-3.31	-6.89×10^{-3}	4.19×10^{-1}	5.09×10^{-3}	5.83×10^{-7}	1.6	0.748
	& `M0/M1Set`	3.35×10^{-2}	-1.44	-6.24×10^{-3}	-1.36×10^{-1}	3.99×10^{-3}	9.03×10^{-7}	56.4	0.192
	& `LeakSet`	-5.75	3.84	1.19×10^{-3}	-1.02	-5.72×10^{-4}	-4.98×10^{-7}	24.4	0.122
	& `NoNusSet`	-4.87	3.63	-1.53×10^{-3}	-1.15	1.09×10^{-3}	7.34×10^{-8}	44.4	0.702
$v_\infty^{\rm d}$ [c]	`M0RefSet`	7.20×10^{-1}	-2.04×10^{-1}	-1.20×10^{-3}	-4.05×10^{-2}	3.92×10^{-4}	5.20×10^{-7}	1.1	0.769
	& `M0/M1Set`	6.39×10^{-1}	-1.98×10^{-1}	-8.98×10^{-4}	-3.63×10^{-2}	3.42×10^{-4}	3.26×10^{-7}	1.7	0.626
	& `LeakSet`	5.67×10^{-1}	-3.26×10^{-1}	-3.58×10^{-4}	5.35×10^{-2}	1.27×10^{-4}	1.25×10^{-7}	5.1	0.324
	& `NoNusSet`	4.31×10^{-1}	-2.13×10^{-1}	-6.80×10^{-5}	4.61×10^{-2}	3.06×10^{-6}	2.04×10^{-8}	6.8	0.162
$Y_e^{\rm d}$	`M0RefSet`	-3.13×10^{-2}	2.84×10^{-1}	5.89×10^{-4}	-1.48×10^{-1}	-2.02×10^{-4}	-2.78×10^{-7}	9.1	0.824
	& `M0/M1Set`	2.65×10^{-1}	2.52×10^{-2}	2.31×10^{-4}	-6.28×10^{-2}	-1.88×10^{-4}	-1.86×10^{-8}	9.7	0.768
	& `LeakSet`	-2.53×10^{-1}	6.26×10^{-1}	5.02×10^{-4}	-2.39×10^{-1}	-3.04×10^{-4}	-1.25×10^{-7}	25.0	0.345
$\langle\theta_{\rm RMS}\rangle$ [deg]	`M0RefSet`	-6.85×10^{1}	1.29×10^{2}	1.18×10^{-1}	$-5.31\times10^{+1}$	-2.78×10^{-2}	-6.97×10^{-5}	4.5	0.819
	& `M0/M1Set`	-4.80×10^{1}	1.21×10^{2}	5.92×10^{-2}	$-5.10\times10^{+1}$	-2.26×10^{-2}	-2.52×10^{-5}	4.2	0.804
	& `LeakSet`	-1.04×10^{2}	1.77×10^{2}	1.10×10^{-1}	$-6.04\times10^{+1}$	-6.50×10^{-2}	-2.47×10^{-5}	8.7	0.483

TABLE A.4: Dynamical ejecta properties: coefficients for the fitting formulae discussed in the text for various datasets.

Quantity	Fit	Datasets	α	β	γ	δ	n	χ^2_ν	R^2
$\log_{10}(M^{\rm d}_{\rm ej})$	Eq. (A.6)	`M0RefSet`	1.089×10^{-1}	4.900×10^{-1}	6.487	-7.187	3.110×10^{-1}	2.2	0.401
		& `M0/M1Set`	-1.172×10^{-1}	-4.157×10^{-1}	2.434×10^{-1}	2.363×10^{-1}	3.175×10^{-1}	16.9	0.079
		& `LeakSet`	-1.448×10^{-1}	-1.433	2.487	2.827	3.004×10^{-1}	30.1	0.112
		& `NoNusSet`	1.370×10^{-2}	-6.171×10^{-1}	2.202	-1.279	5.503×10^{-1}	84.8	0.016
$\log_{10}(M^{\rm d}_{\rm ej})$	Eq. (A.7)	`M0RefSet`	-1.914×10^{-3}	2.204×10^{-2}		-6.912×10^{-2}	1.288	1.6	0.527
		& `M0/M1Set`	-1.051×10^{-3}	1.160×10^{-2}		-3.717×10^{-2}	1.299	10.6	0.158
		& `LeakSet`	-1.212×10^{-3}	1.351×10^{-2}		-4.319×10^{-2}	1.318	11.9	0.241
		& `NoNusSet`	-3.667×10^{-4}	3.100×10^{-3}		-1.068×10^{-2}	1.628	39.9	-0.214
$v^{\rm d}_\infty$ [c]	Eq. (A.11)	`M0RefSet`	-7.591×10^{-1}	1.333	-1.541			1.5	0.635
		& `M0/M1Set`	-5.867×10^{-01}	1.145	-1.207			2.4	0.428
		& `LeakSet`	-4.089×10^{-1}	9.296×10^{-1}	-7.041×10^{-1}			6.1	0.170
		& `NoNusSet`	-3.650×10^{-1}	8.229×10^{-1}	-1.130			6.8	0.157

Table A.5: Disk mass: coefficients for polynomial regression of various quantities. Results for both first order and second order polynomials are reported $P_2^1(\tilde{\Lambda})$ and $P_2^2(q,\tilde{\Lambda})$ The recommended calibration for $P_2^2(q,\Lambda)$ is highlighted.

Datasets	b_0	b_1	b_2	b_3	b_4	b_5	χ_ν^2	R^2
`M0RefSet`	-2.40×10^{-2}	5.55×10^{-4}	-3.94×10^{-7}				2574.1	0.027
& `M0/M1Set`	-1.03×10^{-2}	4.07×10^{-4}	-2.23×10^{-7}				1074.1	0.092
& `LeakSet`	-7.46×10^{-2}	4.99×10^{-4}	-2.41×10^{-7}				757.4	0.299
& `NoNusSet`	-6.86×10^{-2}	4.80×10^{-4}	-2.12×10^{-7}				603.9	0.408
`M0RefSet`	-1.57	2.07	9.83×10^{-4}	-6.67×10^{-1}	-2.55×10^{-4}	-4.61×10^{-7}	425.4	0.415
& `M0/M1Set`	-1.51	2.04	7.71×10^{-4}	-6.45×10^{-1}	-2.74×10^{-4}	-2.52×10^{-7}	174.8	0.542
& `LeakSet`	-1.47	2.02	6.85×10^{-4}	-6.28×10^{-1}	-3.17×10^{-4}	-1.44×10^{-7}	202.2	0.671
& `NoNusSet`	-8.57×10^{-1}	1.13	4.22×10^{-4}	-3.74×10^{-1}	3.46×10^{-5}	-2.13×10^{-7}	197.6	0.659

TABLE A.6: Disk mass: coefficients for the fitting formulae discussed in the text for various datasets.

Fit	Datasets	α	β	γ	δ	$\chi^2_{\rm dof}$	R^2
Eq. (A.15)	`M0RefSet`	1.457×10^{-1}	2.833×10^{-2}	$4.755 \times 10^{+2}$	4.632	1927.3	0.103
	& `M0/M1Set`	1.349×10^{-1}	3.322×10^{-2}	$4.578 \times 10^{+2}$	1.945×10^{-1}	784.7	0.173
	& `LeakSet`	-9.829×10^{1}	9.845×10^{1}	$-3.158 \times 10^{+2}$	$1.790 \times 10^{+2}$	543.2	0.342
	& `NoNusSet`	-3.737×10^{1}	3.756×10^{1}	$-9.683 \times 10^{+2}$	$4.028 \times 10^{+2}$	574.9	0.436
Eq. (A.16)	`M0RefSet`	-1.017	1.006	1.307×10^{1}		2198.9	0.152
	& `M0/M1Set`	-1.789	1.045	8.457		894.8	0.233
	& `LeakSet`	-4.309	8.633×10^{-1}	1.439		629.9	0.400
	& `NoNusSet`	-4.247	8.384×10^{-1}	1.349		442.8	0.506

Bibliography

Burbidge, E. Margaret et al. (1957). “Synthesis of the Elements in Stars”. In: *Rev. Mod. Phys.* 29 (4), pp. 547–650. DOI: `10.1103/RevModPhys.29.547`. URL: `https://link.aps.org/doi/10.1103/RevModPhys.29.547`.

Clayton, Donald D. (1968). *Principles of stellar evolution and nucleosynthesis.*

Shakura, N. I. et al. (1973). “Black holes in binary systems. Observational appearance”. In: *Astron. Astrophys.* 24, pp. 337–355.

Blandford, R. D. et al. (1976). “Fluid dynamics of relativistic blast waves”. In: *Physics of Fluids* 19, pp. 1130–1138. DOI: `10.1063/1.861619`.

Weaver, T. A. et al. (1978). “Presupernova evolution of massive stars.” In: *The Astrophysical Journal* 225, pp. 1021–1029. DOI: `10.1086/156569`.

Dormand, J.R. et al. (1980). “A family of embedded Runge-Kutta formulae”. In: *Journal of Computational and Applied Mathematics* 6.1, pp. 19–26. ISSN: 0377-0427. DOI: `https://doi.org/10.1016/0771-050X(80)90013-3`. URL: `https://www.sciencedirect.com/science/article/pii/0771050X80900133`.

Riper, K.A. van et al. (1981). “Stellar core collapse. I - Infall epoch”. In: *Astrophys. J.* 249, p. 270. DOI: `10.1086/159285`.

Thorne, Kip S. (1981). “Relativistic radiative transfer - Moment formalisms”. In: *mnras* 194, pp. 439–473. DOI: `10.1093/mnras/194.2.439`. URL: `https://ui.adsabs.harvard.edu/abs/1981MNRAS.194..439T`.

Arnett, W. D. (1982). “Type I supernovae. I - Analytic solutions for the early part of the light curve”. In: *The Astrophysical Journal* 253, pp. 785–797. DOI: `10.1086/159681`. eprint: `ui.adsabs.harvard.edu/abs/1982ApJ...253..785A`.

Shapiro, S. L. et al. (1983). *Black holes, white dwarfs, and neutron stars: The physics of compact objects*. New York, USA: Wiley.

Bruenn, S. W. (1985). “Stellar core collapse - Numerical model and infall epoch”. In: *apjs* 58, pp. 771–841. DOI: `10.1086/191056`.

Mueller, E. (1986). “Nuclear-reaction networks and stellar evolution codes - The coupling of composition changes and energy release in explosive nuclear burning”. In: *Astronomy & Astrophysics* 162.1-2, pp. 103–108.

Rybicki, George B. et al. (1986). *Radiative Processes in Astrophysics.*

Service, A. T. (1986). “Fitting Formulae for the Equation of State of a Perfect, Semirelativistic Boltzmann Gas”. In: *The Astrophysical Journal* 307, p. 60. DOI: 10.1086/164392.

Rolfs, Claus E. et al. (1988). *Cauldrons in the cosmos : nuclear astrophysics*. Theoretical astrophysics. Chicago u.a.: University of Chicago Press, XVIII, 561 S. ISBN: 0-226-72456-5. URL: https://repository.gsi.de/record/66499.

Eichler, David et al. (1989). “Nucleosynthesis, Neutrino Bursts and Gamma-Rays from Coalescing Neutron Stars”. In: *Nature* 340, pp. 126–128. DOI: 10.1038/340126a0.

Mathews, G. J. et al. (1990). “New insights into the astrophysical r-process”. In: *Nature 345*, p. 491. DOI: 10.1038/345491a0.

Prantzos, N. et al. (1990). “The s-process in massive stars : yields as a function of stellar mass and metallicity.” In: *Astronomy & Astrophysics* 234, p. 211.

Lattimer, James M. et al. (1991). “A Generalized equation of state for hot, dense matter”. In: *Nucl. Phys.* A535, pp. 331–376. DOI: 10.1016/0375-9474(91)90452-C.

Mao, Shude et al. (1992). “On the Cosmological Origin of Gamma-Ray Bursts”. In: *The Astrophysical Journal Letters* 388, p. L45. DOI: 10.1086/186326.

Meegan, C. A. et al. (1992). “Spatial distribution of gamma-ray bursts observed by BATSE”. In: *Nature* 355, pp. 143–145. DOI: 10.1038/355143a0.

Piran, Tsvi (1992). “The Implications of the Compton (GRO) Observations for Cosmological Gamma-Ray Bursts”. In: *The Astrophysical Journal Letters* 389, p. L45. DOI: 10.1086/186345.

Rees, M. J. et al. (1992). “Relativistic fireballs - energy conversion and time - scales”. In: *Mon. Not. Roy. Astron. Soc.* 258, pp. 41–43.

Woosley, S. E. et al. (1992). “The alpha -Process and the r-Process”. In: *The Astrophysical Journal* 395, p. 202. DOI: 10.1086/171644.

Band, D. et al. (1993). “BATSE Observations of Gamma-Ray Burst Spectra. I. Spectral Diversity”. In: *The Astrophysical Journal* 413, p. 281. DOI: 10.1086/172995.

Fenimore, E. E. et al. (1993). “The intrinsic luminosity of γ-ray bursts and their host galaxies”. In: *Nature* 366.6450, pp. 40–42. DOI: 10.1038/366040a0.

Kouveliotou, Chryssa et al. (1993). “Identification of Two Classes of Gamma-Ray Bursts”. In: *The Astrophysical Journal Letters* 413, p. L101. DOI: 10.1086/186969.

Meszaros, P. et al. (1993). “Gamma-ray bursts: Multiwaveband spectral predictions for blast wave models”. In: *Astrophys. J. Lett.* 418, pp. L59–L62. DOI: `10.1086/187116`. arXiv: `astro-ph/9309011`.

Paczynski, Bohdan et al. (1993). “Radio transients from gamma-ray bursters”. In: *Astrophys. J. Lett.* 418, p. L5. DOI: `10.1086/187102`. arXiv: `astro-ph/9307024`.

Qian, Y.Z. et al. (1996). “Nucleosynthesis in neutrino driven winds: 1. The Physical conditions”. In: *Astrophys. J.* 471, pp. 331–351. DOI: `10.1086/177973`. arXiv: `astro-ph/9611094`.

Ruffert, M. H. et al. (1996). “Coalescing neutron stars: A step towards physical models. I: Hydrodynamic evolution and gravitational- wave emission”. In: *Astron. Astrophys.* 311, pp. 532–566. arXiv: `astro-ph/9509006`.

Banyuls, Francesc et al. (1997). “Numerical $\{3+1\}$ General Relativistic Hydrodynamics: A Local Characteristic Approach”. In: *apj* 476.1, pp. 221–231. DOI: `10.1086/303604`.

Costa, E. et al. (1997). “Discovery of an X-ray afterglow associated with the gamma-ray burst of 28 February 1997”. In: *Nature* 387, pp. 783–785. DOI: `10.1038/42885`. arXiv: `astro-ph/9706065`.

Meszaros, P. et al. (1997). “Optical and long wavelength afterglow from gamma-ray bursts”. In: *Astrophys. J.* 476, pp. 232–237. DOI: `10.1086/303625`. arXiv: `astro-ph/9606043`.

Paradijs, J. van et al. (1997). “Transient optical emission from the error box of the gamma-ray burst of 28 February 1997”. In: *Nature* 386, pp. 686–689. DOI: `10.1038/386686a0`.

Dermer, Charles D. et al. (1998). “Electron acceleration and synchrotron radiation in decelerating plasmoids”. In: *New Astron.* 3, p. 157. DOI: `10.1016/S1384-1076(98)00004-9`. arXiv: `astro-ph/9712052`.

Frontera, F. et al. (1998). “Spectral properties of the prompt x-ray emission and afterglow from the gamma-ray burst of 28 February 1997”. In: *Astrophys. J. Lett.* 493, p. L67. DOI: `10.1086/311132`. arXiv: `astro-ph/9711279`.

Li, Li-Xin et al. (1998). “Transient events from neutron star mergers”. In: *Astrophys. J. Lett.* 507, p. L59. DOI: `10.1086/311680`. arXiv: `astro-ph/9807272`.

Sari, Re’em et al. (1998). “Spectra and light curves of gamma-ray burst afterglows”. In: *Astrophys. J. Lett.* 497, p. L17. DOI: `10.1086/311269`. arXiv: `astro-ph/9712005`.

Hix, W.Raphael et al. (1999). “Computational methods for nucleosynthesis and nuclear energy generation”. In: *Journal of Computational and Applied Mathematics*

109.1, pp. 321 –351. ISSN: 0377-0427. DOI: https://doi.org/10.1016/S0377-0427(99)00163-6. URL: http://www.sciencedirect.com/science/article/pii/S0377042799001636.

Timmes, F. X. et al. (1999). "The Accuracy, Consistency, and Speed of Five Equations of State for Stellar Hydrodynamics". In: *The Astrophysical Journal Supplement Series* 125.1, pp. 277–294. DOI: 10.1086/313271. URL: https://doi.org/10.1086%2F313271.

Alcubierre, Miguel et al. (2000). "Towards an understanding of the stability properties of the (3+1) evolution equations in General Relativity". In: *Phys. Rev. D* 62, p. 124011. DOI: 10.1103/PhysRevD.62.124011. arXiv: gr-qc/9908079.

Baumgarte, Thomas W. et al. (2000). "On the Maximum Mass of Differentially Rotating Neutron Stars". In: *Astrophys. J.* 528, p. L29. arXiv: astro-ph/9910565.

Pinto, Philip A. et al. (2000). "The Physics of Type IA Supernova Light Curves. II. Opacity and Diffusion". In: *The Astrophysical Journal* 530.2, pp. 757–776. DOI: 10.1086/308380.

Wheeler, J. Craig et al. (2000). "Asymmetric Supernovae, Pulsars, Magnetars, and Gamma-Ray Bursts". In: *The Astrophysical Journal* 537.2, pp. 810–823. DOI: 10.1086/309055. URL: https://doi.org/10.1086%2F309055.

Woosley, S. E. et al. (2002). "The evolution and explosion of massive stars". In: *Rev. Mod. Phys.* 74 (4), pp. 1015–1071. DOI: 10.1103/RevModPhys.74.1015. URL: https://link.aps.org/doi/10.1103/RevModPhys.74.1015.

Alcubierre, Miguel et al. (2003). "Gauge conditions for long term numerical black hole evolutions without excision". In: *Phys. Rev. D* 67, p. 084023. DOI: 10.1103/PhysRevD.67.084023. arXiv: gr-qc/0206072.

Baumgarte, Thomas W. et al. (2003). "Numerical relativity and compact binaries". In: *Phys. Rept.* 376, pp. 41–131. DOI: 10.1016/S0370-1573(02)00537-9. arXiv: gr-qc/0211028.

Panaitescu, A. et al. (2003). "Properties of relativistic jets in gamma-ray burst afterglows". In: *AIP Conf. Proc.* 662.1. Ed. by G. R. Ricker et al., pp. 305–312. DOI: 10.1063/1.1579365. arXiv: astro-ph/0109124.

Rosswog, S. et al. (2003a). "High Resolution Calculations of Merging Neutron Stars I: Model Description and Hydrodynamic Evolution". In: *Mon. Not. Roy. Astron. Soc.* 345, p. 1077. DOI: 10.1046/j.1365-2966.2003.07032.x. arXiv: astro-ph/0110180.

Rosswog, Stephan et al. (2003b). “High resolution calculations of merging neutron stars. 2: Neutrino emission”. In: *Mon.Not.Roy.Astron.Soc.* 342, p. 673. DOI: `10.1046/j.1365-8711.2003.06579.x`. arXiv: `astro-ph/0302301 [astro-ph]`.

Shizuka, Akiyama et al. (2003). “The Magnetorotational Instability in Core-Collapse Supernova Explosions”. In: *The Astrophysical Journal* 584.2, pp. 954–970. DOI: `10.1086/344135`. URL: `https://doi.org/10.1086%2F344135`.

Argast, D. et al. (2004). “Neutron star mergers versus core-collapse supernovae as dominant r-process sites in the early galaxy”. In: *Astron. Astrophys.* 416, pp. 997–1011. DOI: `10.1051/0004-6361:20034265`. arXiv: `astro-ph/0309237`.

De Donder, Erwin et al. (2004). “The Influence of binaries on galactic chemical evolution”. In: *New Astron. Rev.* 48, pp. 861–975. DOI: `10.1016/j.newar.2004.07.001`. arXiv: `astro-ph/0410024`.

Gehrels, Neil et al. (2005). “A short gamma-ray burst apparently asssociated with an elliptical galaxy at redshift z=0.225”. In: *Nature* 437, pp. 851–854. DOI: `10.1038/nature04142`. arXiv: `astro-ph/0505630`.

Shibata, Masaru et al. (2005). “Merger of binary neutron stars with realistic equations of state in full general relativity”. In: *Phys. Rev.* D71, p. 084021. DOI: `10.1103/PhysRevD.71.084021`. arXiv: `gr-qc/0503119`.

Burrows, Adam et al. (2006). “Neutrino opacities in nuclear matter”. In: *Nucl. Phys.* A777, pp. 356–394. DOI: `10.1016/j.nuclphysa.2004.06.012`. arXiv: `astro-ph/0404432 [astro-ph]`.

Duez, Matthew D. et al. (2006). “Evolution of magnetized, differentially rotating neutron stars: Simulations in full general relativity”. In: *Phys. Rev.* D73, p. 104015. DOI: `10.1103/PhysRevD.73.104015`. arXiv: `astro-ph/0605331`.

Hix, Willaim Raphael et al. (2006). “Thermonuclear kinetics in astrophysics”. In: *Nucl. Phys. A* 777, pp. 188–207. DOI: `10.1016/j.nuclphysa.2004.10.009`. arXiv: `astro-ph/0509698`.

Johannesson, Gudlaugur et al. (2006). “Energy Injection in GRB Afterglow Models”. In: *Astrophys. J.* 647, pp. 1238–1249. DOI: `10.1086/505520`. arXiv: `astro-ph/0605299`.

Meter, James R. van et al. (2006). “How to move a black hole without excision: Gauge conditions for the numerical evolution of a moving puncture”. In: *Phys. Rev. D* 73, p. 124011. DOI: `10.1103/PhysRevD.73.124011`. arXiv: `gr-qc/0605030`.

Shibata, Masaru et al. (2006). “Merger of binary neutron stars to a black hole: disk mass, short gamma-ray bursts, and quasinormal mode ringing”. In: *Phys.Rev.* D73,

p. 064027. DOI: 10.1103/PhysRevD.73.064027. arXiv: astro-ph/0603145 [astro-ph].

Wanajo, Shinya (2006). “The r-Process in the Proto-Neutron-Star Winds with Anisotropic Neutrino Emission”. In: *Astrophys. J. Lett.* 650, pp. L79–L82. DOI: 10.1086/508568. arXiv: astro-ph/0608539.

Andersson, N. et al. (2007). “Relativistic fluid dynamics: Physics for many different scales”. In: *Living Rev. Rel.* 10, p. 1. DOI: 10.12942/lrr-2007-1. arXiv: gr-qc/0605010.

Arnould, M. et al. (2007). “The r-process of stellar nucleosynthesis: Astrophysics and nuclear physics achievements and mysteries”. In: *Phys. Rept.* 450, pp. 97–213. DOI: 10.1016/j.physrep.2007.06.002. arXiv: 0705.4512 [astro-ph].

Burrows, Adam et al. (2007). “Simulations of Magnetically-Driven Supernova and Hypernova Explosions in the Context of Rapid Rotation”. In: *Astrophys. J.* 664, pp. 416–434. DOI: 10.1086/519161. arXiv: astro-ph/0702539.

Gourgoulhon, Eric (Mar. 2007). “3+1 formalism and bases of numerical relativity”. In: arXiv: gr-qc/0703035.

Meyer, B. S. et al. (2007). “Libnucnet: A Tool for Understanding Nucleosynthesis”. In: *Meteoritics and Planetary Science Supplement* 42, p. 5215.

Nakar, Ehud (2007). “Short-Hard Gamma-Ray Bursts”. In: *Phys. Rept.* 442, pp. 166–236. DOI: 10.1016/j.physrep.2007.02.005. arXiv: astro-ph/0701748.

Alcubierre, M. (2008). *Introduction to 3+1 Numerical Relativity*. Ed. by M. Alcubierre. Oxford University Press.

Arnowitt, Richard L. et al. (2008). “The Dynamics of general relativity”. In: *Gen. Rel. Grav.* 40, pp. 1997–2027. DOI: 10.1007/s10714-008-0661-1. arXiv: gr-qc/0405109 [gr-qc].

Beloborodov, Andrei M. (2008). “Hyper-accreting black holes”. In: *AIP Conf. Proc.* 1054, p. 51. DOI: 10.1063/1.3002509. arXiv: 0810.2690 [astro-ph].

Dermer, Charles D. et al. (Sept. 2008). “Gamma Ray Bursts and the Fermi Gamma Ray Space Telescope: Notes to the La Plata Lectures”. In: arXiv: 0809.3959 [astro-ph].

Font, Jose A. (2008). “Numerical Hydrodynamics and Magnetohydrodynamics in General Relativity”. In: *Living Rev. Rel.* 11, p. 7. DOI: 10.12942/lrr-2008-7.

Metzger, B.D. et al. (2008). “Time-Dependent Models of Accretion Disks Formed from Compact Object Mergers”. In: *Mon.Not.Roy.Astron.Soc.* 390, p. 781. DOI: 10.1111/j.1365-2966.2008.13789.x. arXiv: 0805.4415 [astro-ph].

Binnington, Taylor et al. (2009). “Relativistic theory of tidal Love numbers”. In: *Phys. Rev. D* 80, p. 084018. DOI: `10.1103/PhysRevD.80.084018`. arXiv: `0906.1366 [gr-qc]`.

Damour, Thibault et al. (2009a). “Improved resummation of post-Newtonian multipolar waveforms from circularized compact binaries”. In: *Phys. Rev.* D79, p. 064004. DOI: `10.1103/PhysRevD.79.064004`. arXiv: `0811.2069 [gr-qc]`.

Damour, Thibault et al. (2009b). “Relativistic tidal properties of neutron stars”. In: *Phys. Rev.* D80, p. 084035. DOI: `10.1103/PhysRevD.80.084035`. arXiv: `0906.0096 [gr-qc]`.

Dessart, Luc et al. (2009). “Neutrino signatures and the neutrino-driven wind in Binary Neutron Star Mergers”. In: *Astrophys.J.* 690, p. 1681. DOI: `10.1088/0004-637X/690/2/1681`. arXiv: `0806.4380 [astro-ph]`.

Lee, William H. et al. (2009). “Phase transitions and He-synthesis driven winds in neutrino cooled accretion disks: prospects for late flares in short gamma-ray bursts”. In: *Astrophys.J.* 699, pp. L93–L96. DOI: `10.1088/0004-637X/699/2/L93`. arXiv: `0904.3752 [astro-ph.HE]`.

Arcones, A. et al. (2010). “Electron fraction constraints based on nuclear statistical equilibrium with beta equilibrium”. In: *Astronomy & Astrophysics* 522, A25, A25. DOI: `10.1051/0004-6361/201014276`. arXiv: `1002.3854 [astro-ph.SR]`.

Baumgarte, Thomas et al. (2010). *Numerical Relativity*. Cambridge: Cambridge University Press.

Bernuzzi, Sebastiano et al. (2010). “Constraint violation in free evolution schemes: comparing BSSNOK with a conformal decomposition of Z4”. In: *Phys. Rev.* D81, p. 084003. DOI: `10.1103/PhysRevD.81.084003`. arXiv: `0912.2920 [gr-qc]`.

Damour, Thibault et al. (2010). “Effective One Body description of tidal effects in inspiralling compact binaries”. In: *Phys. Rev.* D81, p. 084016. DOI: `10.1103/PhysRevD.81.084016`. arXiv: `0911.5041 [gr-qc]`.

Hempel, Matthias et al. (2010). “Statistical Model for a Complete Supernova Equation of State”. In: *Nucl. Phys.* A837, pp. 210–254. DOI: `10.1016/j.nuclphysa.2010.02.010`. arXiv: `0911.4073 [nucl-th]`.

Metzger, B. D. et al. (2010). “Electromagnetic counterparts of compact object mergers powered by the radioactive decay of r-process nuclei”. In: *Monthly Notices of the Royal Astronomical Society* 406.4, pp. 2650–2662. DOI: `10.1111/j.1365-2966.2010.16864.x`. arXiv: `1001.5029 [astro-ph.HE]`.

O'Connor, Evan et al. (2010). "A New Open-Source Code for Spherically-Symmetric Stellar Collapse to Neutron Stars and Black Holes". In: *Class. Quant. Grav.* 27. Ed. by Christian D. Ott et al., p. 114103. DOI: `10.1088/0264-9381/27/11/114103`. arXiv: `0912.2393 [astro-ph.HE]`.

Sekiguchi, Yuichiro (2010). "An implementation of the microphysics in full general relativity: A general relativistic neutrino leakage scheme". In: *Class.Quant.Grav.* 27, p. 114107. DOI: `10.1088/0264-9381/27/11/114107`.

Typel, S. et al. (2010). "Composition and thermodynamics of nuclear matter with light clusters". In: *Phys. Rev.* C81, p. 015803. DOI: `10.1103/PhysRevC.81.015803`. arXiv: `0908.2344 [nucl-th]`.

Goriely, Stephane et al. (2011). "R-Process Nucleosynthesis in Dynamically Ejected Matter of Neutron Star Mergers". In: *Astrophys. J. Lett.* 738, p. L32. DOI: `10.1088/2041-8205/738/2/L32`. arXiv: `1107.0899 [astro-ph.SR]`.

Hotokezaka, Kenta et al. (2011). "Binary Neutron Star Mergers: Dependence on the Nuclear Equation of State". In: *Phys.Rev.* D83, p. 124008. DOI: `10.1103/PhysRevD.83.124008`. arXiv: `1105.4370 [astro-ph.HE]`.

Käppeler, F. et al. (2011). "The s process: Nuclear physics, stellar models, and observations". In: *Reviews of Modern Physics* 83.1, pp. 157–194. DOI: `10.1103/RevModPhys.83.157`. arXiv: `1012.5218 [astro-ph.SR]`.

Nakar, Ehud et al. (2011). "Radio Remnants of Compact Binary Mergers - the Electromagnetic Signal that will follow the Gravitational Waves". In: *Nature* 478, pp. 82–84. DOI: `10.1038/nature10365`. arXiv: `1102.1020 [astro-ph.HE]`.

Rezzolla, Luciano et al. (2011). "The missing link: Merging neutron stars naturally produce jet-like structures and can power short Gamma-Ray Bursts". In: *Astrophys. J.* 732, p. L6. DOI: `10.1088/2041-8205/732/1/L6`. arXiv: `1101.4298 [astro-ph.HE]`.

Roberts, L. F. et al. (2011). "Electromagnetic Transients Powered by Nuclear Decay in the Tidal Tails of Coalescing Compact Binaries". In: *The Astrophysical Journal Letters* 736.1, L21, p. L21. DOI: `10.1088/2041-8205/736/1/L21`. arXiv: `1104.5504 [astro-ph.HE]`.

Ruiz, Milton et al. (2011). "Constraint preserving boundary conditions for the Z4c formulation of general relativity". In: *Phys. Rev.* D83, p. 024025. DOI: `10.1103/PhysRevD.83.024025`. arXiv: `1010.0523 [gr-qc]`.

Sekiguchi, Yuichiro et al. (2011). "Gravitational waves and neutrino emission from the merger of binary neutron stars". In: *Phys.Rev.Lett.* 107, p. 051102. DOI: `10.1103/PhysRevLett.107.051102`. arXiv: `1105.2125 [gr-qc]`.

Thielemann, F. K. et al. (2011). "What are the astrophysical sites for the r-process and the production of heavy elements?" In: *Progress in Particle and Nuclear Physics* 66.2. Particle and Nuclear Astrophysics, pp. 346 –353. ISSN: 0146-6410. DOI: `https://doi.org/10.1016/j.ppnp.2011.01.032`. URL: `http://www.sciencedirect.com/science/article/pii/S0146641011000330`.

Vidana, Isaac et al. (2011). "Estimation of the effect of hyperonic three-body forces on the maximum mass of neutron stars". In: *EPL* 94.1, p. 11002. DOI: `10.1209/0295-5075/94/11002`. arXiv: `1006.5660 [nucl-th]`.

Winkler, Christoph et al. (2011). "INTEGRAL: Science Highlights and Future Prospects". In: *Space Science Reviews* 161.1-4, pp. 149–177. DOI: `10.1007/s11214-011-9846-0`. arXiv: `1110.6279 [astro-ph.HE]`.

Bernuzzi, Sebastiano et al. (2012). "Tidal effects in binary neutron star coalescence". In: *Phys.Rev.* D86, p. 044030. DOI: `10.1103/PhysRevD.86.044030`. arXiv: `1205.3403 [gr-qc]`.

Bucciantini, N. et al. (2012). "Short GRBs with Extended Emission from Magnetar Birth: Jet Formation and Collimation". In: *Mon. Not. Roy. Astron. Soc.* 419, p. 1537. DOI: `10.1111/j.1365-2966.2011.19810.x`. arXiv: `1106.4668 [astro-ph.HE]`.

Cao, Zhoujian et al. (2012). "Numerical stability of the Z4c formulation of general relativity". In: *Phys.Rev.* D85, p. 124032. DOI: `10.1103/PhysRevD.85.124032`. arXiv: `1111.2177 [gr-qc]`.

Damour, Thibault et al. (2012). "Energy versus Angular Momentum in Black Hole Binaries". In: *Phys.Rev.Lett.* 108, p. 131101. DOI: `10.1103/PhysRevLett.108.131101`. arXiv: `1110.2938 [gr-qc]`.

Dominik, Michal et al. (2012). "Double Compact Objects I: The Significance of the Common Envelope on Merger Rates". In: *Astrophys. J.* 759, p. 52. DOI: `10.1088/0004-637X/759/1/52`. arXiv: `1202.4901 [astro-ph.HE]`.

Eerten, H.J. van et al. (2012). "Gamma-ray burst afterglow scaling relations for the full blast wave evolution". In: *Astrophys. J. Lett.* 747, p. L30. DOI: `10.1088/2041-8205/747/2/L30`. arXiv: `1111.3355 [astro-ph.HE]`.

Granot, Jonathan et al. (Mar. 2012). "On the lateral expansion of gamma-ray burst jets". In: *Monthly Notices of the Royal Astronomical Society* 421.1, pp. 570–587.

ISSN: 0035-8711. DOI: 10.1111/j.1365-2966.2011.20335.x. eprint: astro-ph/1109.6468. URL: https://doi.org/10.1111/j.1365-2966.2011.20335.x.

Korobkin, O. et al. (2012). “On the astrophysical robustness of neutron star merger r-process”. In: *Mon. Not. Roy. Astron. Soc.* 426, p. 1940. DOI: 10.1111/j.1365-2966.2012.21859.x. arXiv: 1206.2379 [astro-ph.SR].

Lattimer, James M. (2012). “The nuclear equation of state and neutron star masses”. In: *Ann. Rev. Nucl. Part. Sci.* 62, pp. 485–515. DOI: 10.1146/annurev-nucl-102711-095018. arXiv: 1305.3510 [nucl-th].

Martinez-Pinedo, G. et al. (2012). “Charged-current weak interaction processes in hot and dense matter and its impact on the spectra of neutrinos emitted from proto-neutron star cooling”. In: *Phys. Rev. Lett.* 109, p. 251104. DOI: 10.1103/PhysRevLett.109.251104. arXiv: 1205.2793 [astro-ph.HE].

Pe’er, Asaf (2012). “Dynamical Model of an Expanding Shell”. In: *The Astrophysical Journal Letters* 752.1, L8, p. L8. DOI: 10.1088/2041-8205/752/1/L8. arXiv: 1203.5797 [astro-ph.HE].

Radice, David et al. (2012). “THC: a new high-order finite-difference high-resolution shock-capturing code for special-relativistic hydrodynamics”. In: *Astron. Astrophys.* 547, A26. DOI: 10.1051/0004-6361/201219735. arXiv: 1206.6502 [astro-ph.IM].

Weyhausen, Andreas et al. (2012). “Constraint damping for the Z4c formulation of general relativity”. In: *Phys. Rev. D* 85, p. 024038. DOI: 10.1103/PhysRevD.85.024038. arXiv: 1107.5539 [gr-qc].

Winteler, C. et al. (2012). “Magnetorotationally Driven Supernovae as the Origin of Early Galaxy r-process Elements?” In: *Astrophysical Journal Letters* 750.1, L22, p. L22. DOI: 10.1088/2041-8205/750/1/L22. arXiv: 1203.0616 [astro-ph.SR].

Barnes, Jennifer et al. (2013). “Effect of a High Opacity on the Light Curves of Radioactively Powered Transients from Compact Object Mergers”. In: *Astrophys. J.* 775, p. 18. DOI: 10.1088/0004-637X/775/1/18. arXiv: 1303.5787 [astro-ph.HE].

Bauswein, A. et al. (2013a). “Prompt merger collapse and the maximum mass of neutron stars”. In: *Phys.Rev.Lett.* 111.13, p. 131101. DOI: 10.1103/PhysRevLett.111.131101. arXiv: 1307.5191 [astro-ph.SR].

Bauswein, A. et al. (2013b). “Systematics of dynamical mass ejection, nucleosynthesis, and radioactively powered electromagnetic signals from neutron-star mergers”. In: *Astrophys.J.* 773, p. 78. DOI: 10.1088/0004-637X/773/1/78. arXiv: 1302.6530 [astro-ph.SR].

Berger, E. et al. (2013). “An r-process Kilonova Associated with the Short-hard GRB 130603B”. In: *Astrophys. J. Lett.* 774, p. L23. DOI: `10.1088/2041-8205/774/2/L23`. arXiv: `1306.3960 [astro-ph.HE]`.

Fernández, Rodrigo et al. (2013). “Delayed outflows from black hole accretion tori following neutron star binary coalescence”. In: *Mon. Not. Roy. Astron. Soc.* 435, p. 502. DOI: `10.1093/mnras/stt1312`. arXiv: `1304.6720 [astro-ph.HE]`.

Galeazzi, Filippo et al. (2013). “Implementation of a simplified approach to radiative transfer in general relativity”. In: *Phys. Rev. D* 88, p. 064009. DOI: `10.1103/PhysRevD.88.064009`. arXiv: `1306.4953 [gr-qc]`.

Hilditch, David et al. (2013). “Compact binary evolutions with the Z4c formulation”. In: *Phys. Rev.* D88, p. 084057. DOI: `10.1103/PhysRevD.88.084057`. arXiv: `1212.2901 [gr-qc]`.

Hotokezaka, Kenta et al. (2013a). “Mass ejection from the merger of binary neutron stars”. In: *Physical Review D* 87.2, p. 024001. DOI: `10.1103/PhysRevD.87.024001`.

Hotokezaka, Kenta et al. (2013b). “The mass ejection from the merger of binary neutron stars”. In: *Phys.Rev.* D87, p. 024001. DOI: `10.1103/PhysRevD.87.024001`. arXiv: `1212.0905 [astro-ph.HE]`.

Kasen, Daniel et al. (2013). “Opacities and Spectra of the r-process Ejecta from Neutron Star Mergers”. In: *Astrophys. J.* 774, p. 25. DOI: `10.1088/0004-637X/774/1/25`. arXiv: `1303.5788 [astro-ph.HE]`.

Nava, L. et al. (2013). “Afterglow emission in gamma-ray bursts - I. Pair-enriched ambient medium and radiative blast waves”. In: *Monthly Notices of the Royal Astronomical Society* 433.3, pp. 2107–2121. DOI: `10.1093/mnras/stt872`. arXiv: `1211.2806 [astro-ph.HE]`.

Piran, Tsvi et al. (2013). “The Electromagnetic Signals of Compact Binary Mergers”. In: *Mon. Not. Roy. Astron. Soc.* 430.3, pp. 2121–2136. DOI: `10.1093/mnras/stt037`. arXiv: `1204.6242 [astro-ph.HE]`.

Radice, David (2013). “Advanced Numerical Approaches in the Dynamics of Relativistic Flows”. PhD thesis. Hannover U.

Rezzolla, L. et al. (2013). *Relativistic Hydrodynamics*. 1st ed. Mathematics. Oxford: Oxford University Press. ISBN: 9780198528906.

Siegel, Daniel M. et al. (2013). “Magnetorotational instability in relativistic hypermassive neutron stars”. In: *Phys. Rev. D* 87.12, p. 121302. DOI: `10.1103/PhysRevD.87.121302`. arXiv: `1302.4368 [gr-qc]`.

Steiner, Andrew W. et al. (2013). “Core-collapse supernova equations of state based on neutron star observations”. In: *Astrophys. J.* 774, p. 17. DOI: 10.1088/0004-637X/774/1/17. arXiv: 1207.2184 [astro-ph.SR].

Tanaka, Masaomi et al. (2013). “Radiative Transfer Simulations of Neutron Star Merger Ejecta”. In: *Astrophys.J.* 775, p. 113. DOI: 10.1088/0004-637X/775/2/113. arXiv: 1306.3742 [astro-ph.HE].

Tanvir, N.R. et al. (2013). “A "kilonova" associated with short-duration gamma-ray burst 130603B”. In: *Nature* 500, p. 547. DOI: 10.1038/nature12505. arXiv: 1306.4971 [astro-ph.HE].

Wanajo, Shinya (2013). “The r-process in Proto-neutron-star Wind Revisited”. In: *Astrophysical Journal Letters* 770.2, L22, p. L22. DOI: 10.1088/2041-8205/770/2/L22. arXiv: 1305.0371 [astro-ph.SR].

Bernuzzi, Sebastiano et al. (2014). “Mergers of binary neutron stars with realistic spin”. In: *Phys.Rev.* D89, p. 104021. DOI: 10.1103/PhysRevD.89.104021. arXiv: 1311.4443 [gr-qc].

Favata, Marc (2014). “Systematic parameter errors in inspiraling neutron star binaries”. In: *Phys.Rev.Lett.* 112, p. 101101. DOI: 10.1103/PhysRevLett.112.101101. arXiv: 1310.8288 [gr-qc].

Foucart, Francois et al. (2014). “Neutron star-black hole mergers with a nuclear equation of state and neutrino cooling: Dependence in the binary parameters”. In: *Phys. Rev.* D90, p. 024026. DOI: 10.1103/PhysRevD.90.024026. arXiv: 1405.1121 [astro-ph.HE].

Grossman, Doron et al. (2014). “The long-term evolution of neutron star merger remnants – II. Radioactively powered transients”. In: *Mon. Not. Roy. Astron. Soc.* 439.1, pp. 757–770. DOI: 10.1093/mnras/stt2503. arXiv: 1307.2943 [astro-ph.HE].

Kaplan, J.D. et al. (2014). “The Influence of Thermal Pressure on Equilibrium Models of Hypermassive Neutron Star Merger Remnants”. In: *Astrophys.J.* 790, p. 19. DOI: 10.1088/0004-637X/790/1/19. arXiv: 1306.4034 [astro-ph.HE].

Kiuchi, Kenta et al. (2014). “High resolution numerical-relativity simulations for the merger of binary magnetized neutron stars”. In: *Phys.Rev.* D90.4, p. 041502. DOI: 10.1103/PhysRevD.90.041502. arXiv: 1407.2660 [astro-ph.HE].

Kumar, Pawan et al. (2014). “The physics of gamma-ray bursts \& relativistic jets”. In: *Phys. Rept.* 561, pp. 1–109. DOI: 10.1016/j.physrep.2014.09.008. arXiv: 1410.0679 [astro-ph.HE].

Longland, R. et al. (2014). “Performance improvements for nuclear reaction network integration”. In: *Astronomy & Astrophysics* 563, A67, A67. DOI: 10.1051/0004-6361/201321958. arXiv: 1401.5762 [astro-ph.SR].

Metzger, Brian D. et al. (2014). “Red or blue? A potential kilonova imprint of the delay until black hole formation following a neutron star merger”. In: *Mon.Not.Roy.Astron.Soc.* 441, p. 3444. DOI: 10.1093/mnras/stu802. arXiv: 1402.4803 [astro-ph.HE].

Mösta, Philipp et al. (2014). “Magnetorotational Core-Collapse Supernovae in Three Dimensions”. In: *Astrophys. J. Lett.* 785, p. L29. DOI: 10.1088/2041-8205/785/2/L29. arXiv: 1403.1230 [astro-ph.HE].

Neilsen, David et al. (2014). “Magnetized Neutron Stars With Realistic Equations of State and Neutrino Cooling”. In: *Phys.Rev.* D89.10, p. 104029. DOI: 10.1103/PhysRevD.89.104029. arXiv: 1403.3680 [gr-qc].

Perego, Albino et al. (2014). “Neutrino-driven winds from neutron star merger remnants”. In: *Mon.Not.Roy.Astron.Soc.* 443, p. 3134. DOI: 10.1093/mnras/stu1352. arXiv: 1405.6730 [astro-ph.HE].

Wanajo, Shinya et al. (2014). “Production of all the r-process nuclides in the dynamical ejecta of neutron star mergers”. In: *Astrophys. J.* 789, p. L39. DOI: 10.1088/2041-8205/789/2/L39. arXiv: 1402.7317 [astro-ph.SR].

Bernuzzi, Sebastiano et al. (2015). “Modeling the complete gravitational wave spectrum of neutron star mergers”. In: *Phys. Rev. Lett.* 115, p. 091101. DOI: 10.1103/PhysRevLett.115.091101. arXiv: 1504.01764 [gr-qc].

Cescutti, G. et al. (2015). “The role of neutron star mergers in the chemical evolution of the Galactic halo”. In: *Astronomy and Astrophysics* 577, A139, A139. DOI: 10.1051/0004-6361/201525698. arXiv: 1503.02954 [astro-ph.GA].

Dietrich, Tim et al. (2015). “Numerical relativity simulations of neutron star merger remnants using conservative mesh refinement”. In: *Phys. Rev.* D91.12, p. 124041. DOI: 10.1103/PhysRevD.91.124041. arXiv: 1504.01266 [gr-qc].

Eichler, M. et al. (2015). “The Role of Fission in Neutron Star Mergers and its Impact on the r-Process Peaks”. In: *Astrophys. J.* 808.1, p. 30. DOI: 10.1088/0004-637X/808/1/30. arXiv: 1411.0974 [astro-ph.HE].

Fontes, C. J. et al. (2015). “Relativistic opacities for astrophysical applications”. In: *High Energy Density Physics* 16, pp. 53–59. ISSN: 1574-1818. DOI: https://doi.org/10.1016/j.hedp.2015.06.002. URL: https://www.sciencedirect.com/science/article/pii/S1574181815000555.

Foucart, Francois et al. (2015). "Post-merger evolution of a neutron star-black hole binary with neutrino transport". In: *Phys. Rev.* D91.12, p. 124021. DOI: `10.1103/PhysRevD.91.124021`. arXiv: `1502.04146 [astro-ph.HE]`.

Goriely, Stephane et al. (2015). "Impact of weak interactions of free nucleons on the r-process in dynamical ejecta from neutron-star mergers". In: *Mon. Not. Roy. Astron. Soc.* 452.4, pp. 3894–3904. DOI: `10.1093/mnras/stv1526`. arXiv: `1504.04377 [astro-ph.SR]`.

Hotokezaka, Kenta et al. (2015a). "Mass ejection from neutron star mergers: different components and expected radio signals". In: *Mon. Not. Roy. Astron. Soc.* 450, pp. 1430–1440. DOI: `10.1093/mnras/stv620`. arXiv: `1501.01986 [astro-ph.HE]`.

Hotokezaka, Kenta et al. (2015b). "Short-lived ^{244}Pu Points to Compact Binary Mergers as Sites for Heavy r-process Nucleosynthesis". In: *Nature Phys.* 11, p. 1042. DOI: `10.1038/nphys3574`. arXiv: `1510.00711 [astro-ph.HE]`.

Ishimaru, Yuhri et al. (2015). "Neutron Star Mergers as the Origin of r-process Elements in the Galactic Halo Based on the Sub-halo Clustering Scenario". In: *The Astrophysical Journal Letters* 804.2, L35, p. L35. DOI: `10.1088/2041-8205/804/2/L35`. arXiv: `1504.04559 [astro-ph.GA]`.

Jin, Zhi-Ping et al. (2015). "The Light Curve of the Macronova Associated With the Long–short Burst GRB 060614". In: *Astrophys. J. Lett.* 811.2, p. L22. DOI: `10.1088/2041-8205/811/2/L22`. arXiv: `1507.07206 [astro-ph.HE]`.

Just, Oliver et al. (2015). "Comprehensive nucleosynthesis analysis for ejecta of compact binary mergers". In: *Mon. Not. Roy. Astron. Soc.* 448.1, pp. 541–567. DOI: `10.1093/mnras/stv009`. arXiv: `1406.2687 [astro-ph.SR]`.

Kastaun, Wolfgang et al. (2015). "Properties of hypermassive neutron stars formed in mergers of spinning binaries". In: *Phys.Rev.* D91.6, p. 064027. DOI: `10.1103/PhysRevD.91.064027`. arXiv: `1411.7975 [gr-qc]`.

Lippuner, Jonas et al. (2015). "r-Process Lanthanide Production and Heating Rates in Kilonovae". In: *Astrophys. J.* 815.2, p. 82. DOI: `10.1088/0004-637X/815/2/82`. arXiv: `1508.03133 [astro-ph.HE]`.

Martin, Dirk et al. (2015). "Neutrino-driven winds in the aftermath of a neutron star merger: nucleosynthesis and electromagnetic transients". In: *Astrophys. J.* 813.1, p. 2. DOI: `10.1088/0004-637X/813/1/2`. arXiv: `1506.05048 [astro-ph.SR]`.

Metzger, Brian D. et al. (2015). "Neutron-powered precursors of kilonovae". In: *Mon. Not. Roy. Astron. Soc.* 446, pp. 1115–1120. DOI: `10.1093/mnras/stu2225`. arXiv: `1409.0544 [astro-ph.HE]`.

Mösta, Philipp et al. (2015). "A large scale dynamo and magnetoturbulence in rapidly rotating core-collapse supernovae". In: *Nature* 528, p. 376. DOI: `10.1038/nature15755`. arXiv: `1512.00838 [astro-ph.HE]`.

Nishimura, N. et al. (2015). "The r-process nucleosynthesis in the various jet-like explosions of magnetorotational core-collapse supernovae". In: *Astrophys. J.* 810.2, p. 109. DOI: `10.1088/0004-637X/810/2/109`. arXiv: `1501.06567 [astro-ph.SR]`.

Palenzuela, Carlos et al. (2015). "Effects of the microphysical Equation of State in the mergers of magnetized Neutron Stars With Neutrino Cooling". In: *Phys. Rev.* D92.4, p. 044045. DOI: `10.1103/PhysRevD.92.044045`. arXiv: `1505.01607 [gr-qc]`.

Paschalidis, Vasileios et al. (2015). "One-arm Spiral Instability in Hypermassive Neutron Stars Formed by Dynamical-Capture Binary Neutron Star Mergers". In: *Phys. Rev.* D92.12, p. 121502. DOI: `10.1103/PhysRevD.92.121502`. arXiv: `1510.03432 [astro-ph.HE]`.

Sekiguchi, Yuichiro et al. (2015). "Dynamical mass ejection from binary neutron star mergers: Radiation-hydrodynamics study in general relativity". In: *Phys.Rev.* D91.6, p. 064059. DOI: `10.1103/PhysRevD.91.064059`. arXiv: `1502.06660 [astro-ph.HE]`.

Voort, Freeke van de et al. (2015). "Galactic r-process enrichment by neutron star mergers in cosmological simulations of a Milky Way-mass galaxy". In: *Monthly Notices of the Royal Astronomical Society* 447.1, pp. 140–148. DOI: `10.1093/mnras/stu2404`. arXiv: `1407.7039 [astro-ph.GA]`.

Wallner, A. et al. (2015). "Abundance of live ^{244}Pu in deep-sea reservoirs on Earth points to rarity of actinide nucleosynthesis". In: *Nature Communications* 6, 5956, p. 5956. DOI: `10.1038/ncomms6956`. arXiv: `1509.08054 [astro-ph.SR]`.

Wehmeyer, B. et al. (2015). "Galactic evolution of rapid neutron capture process abundances: the inhomogeneous approach". In: *Monthly Notices of the Royal Astronomical Society* 452.2, pp. 1970–1981. DOI: `10.1093/mnras/stv1352`. arXiv: `1501.07749 [astro-ph.GA]`.

Yang, Bin et al. (2015). "A possible Macronova in the late afterglow of the 'long-short' burst GRB 060614". In: *Nature Commun.* 6, p. 7323. DOI: `10.1038/ncomms8323`. arXiv: `1503.07761 [astro-ph.HE]`.

Ajello, M. et al. (2016). "Fermi-LAT Observations of High-Energy γ-Ray Emission Toward the Galactic Center". In: *Astrophys. J.* 819.1, p. 44. DOI: `10.3847/0004-637X/819/1/44`. arXiv: `1511.02938 [astro-ph.HE]`.

Barnes, Jennifer et al. (2016). “Radioactivity and thermalization in the ejecta of compact object mergers and their impact on kilonova light curves”. In: *Astrophys. J.* 829.2, p. 110. DOI: `10.3847/0004-637X/829/2/110`. arXiv: `1605.07218 [astro-ph.HE]`.

Bernuzzi, Sebastiano et al. (2016). “How loud are neutron star mergers?” In: *Phys. Rev.* D94.2, p. 024023. DOI: `10.1103/PhysRevD.94.024023`. arXiv: `1512.06397 [gr-qc]`.

Dietrich, Tim (2016). “Binary neutron star merger simulations”. Dissertation, Friedrich-Schiller-Universität Jena, 2016. PhD thesis. Jena.

East, William E. et al. (2016a). “Equation of state effects and one-arm spiral instability in hypermassive neutron stars formed in eccentric neutron star mergers”. In: *Class. Quant. Grav.* 33.24, p. 244004. DOI: `10.1088/0264-9381/33/24/244004`. arXiv: `1609.00725 [astro-ph.HE]`.

East, William E. et al. (2016b). “Relativistic Simulations of Eccentric Binary Neutron Star Mergers: One-arm Spiral Instability and Effects of Neutron Star Spin”. In: *Phys. Rev.* D93.2, p. 024011. DOI: `10.1103/PhysRevD.93.024011`. arXiv: `1511.01093 [astro-ph.HE]`.

Fernández, Rodrigo et al. (2016). “Electromagnetic Signatures of Neutron Star Mergers in the Advanced LIGO Era”. In: *Ann. Rev. Nucl. Part. Sci.* 66, pp. 23–45. DOI: `10.1146/annurev-nucl-102115-044819`. arXiv: `1512.05435 [astro-ph.HE]`.

Foucart, Francois et al. (2016a). “Impact of an improved neutrino energy estimate on outflows in neutron star merger simulations”. In: *Phys. Rev.* D94.12, p. 123016. DOI: `10.1103/PhysRevD.94.123016`. arXiv: `1607.07450 [astro-ph.HE]`.

Foucart, Francois et al. (2016b). “Low mass binary neutron star mergers : gravitational waves and neutrino emission”. In: *Phys. Rev.* D93.4, p. 044019. DOI: `10.1103/PhysRevD.93.044019`. arXiv: `1510.06398 [astro-ph.HE]`.

Ji, Alexander P. et al. (2016). “R-process enrichment from a single event in an ancient dwarf galaxy”. In: *Nature* 531.7596, pp. 610–613. DOI: `10.1038/nature17425`. arXiv: `1512.01558 [astro-ph.GA]`.

Jin, Zhi-Ping et al. (2016). “The Macronova in GRB 050709 and the GRB/macronova connection”. In: *Nature Commun.* 7, p. 12898. DOI: `10.1038/ncomms12898`. arXiv: `1603.07869 [astro-ph.HE]`.

Kawaguchi, Kyohei et al. (2016). “Models of Kilonova/macronova Emission From Black Hole–neutron Star Mergers”. In: *Astrophys. J.* 825.1, p. 52. DOI: `10.3847/0004-637X/825/1/52`. arXiv: `1601.07711 [astro-ph.HE]`.

Lehner, Luis et al. (2016a). "m=1 instability and gravitational wave signal in binary neutron star mergers". In: *Phys. Rev.* D94.4, p. 043003. DOI: `10.1103/PhysRevD.94.043003`. arXiv: `1605.02369 [gr-qc]`.

Lehner, Luis et al. (2016b). "Unequal mass binary neutron star mergers and multi-messenger signals". In: *Class. Quant. Grav.* 33.18, p. 184002. DOI: `10.1088/0264-9381/33/18/184002`. arXiv: `1603.00501 [gr-qc]`.

Radice, David et al. (2016a). "Dynamical Mass Ejection from Binary Neutron Star Mergers". In: *Mon. Not. Roy. Astron. Soc.* 460.3, pp. 3255–3271. DOI: `10.1093/mnras/stw1227`. arXiv: `1601.02426 [astro-ph.HE]`.

Radice, David et al. (2016b). "One-armed spiral instability in neutron star mergers and its detectability in gravitational waves". In: *Phys. Rev.* D94.6, p. 064011. DOI: `10.1103/PhysRevD.94.064011`. arXiv: `1603.05726 [gr-qc]`.

Roberts, Luke F. et al. (2016). "General Relativistic Three-Dimensional Multi-Group Neutrino Radiation-Hydrodynamics Simulations of Core-Collapse Supernovae". In: DOI: `10.3847/0004-637X/831/1/98`. arXiv: `1604.07848 [astro-ph.HE]`.

Ruiz, Milton et al. (2016). "Binary Neutron Star Mergers: a jet Engine for Short Gamma-ray Bursts". In: *Astrophys. J.* 824.1, p. L6. DOI: `10.3847/2041-8205/824/1/L6`. arXiv: `1604.02455 [astro-ph.HE]`.

Sekiguchi, Yuichiro et al. (2016). "Dynamical mass ejection from the merger of asymmetric binary neutron stars: Radiation-hydrodynamics study in general relativity". In: *Phys. Rev.* D93.12, p. 124046. DOI: `10.1103/PhysRevD.93.124046`. arXiv: `1603.01918 [astro-ph.HE]`.

Shibata, Masaru (2016). *Numerical Relativity*. Singapore: World Scientific.

Wu, Meng-Ru et al. (2016). "Production of the entire range of r-process nuclides by black hole accretion disc outflows from neutron star mergers". In: *Mon. Not. Roy. Astron. Soc.* 463.3, pp. 2323–2334. DOI: `10.1093/mnras/stw2156`. arXiv: `1607.05290 [astro-ph.HE]`.

Abbott, B. P. et al. (2017a). "Multi-messenger Observations of a Binary Neutron Star Merger". In: *Astrophys. J. Lett.* 848.2, p. L12. DOI: `10.3847/2041-8213/aa91c9`. arXiv: `1710.05833 [astro-ph.HE]`.

— (2017b). "Multi-messenger Observations of a Binary Neutron Star Merger". In: *Astrophys. J. Lett.* 848.2, p. L12. DOI: `10.3847/2041-8213/aa91c9`. arXiv: `1710.05833 [astro-ph.HE]`.

Abbott, Benjamin P. et al. (2017c). “GW170817: Observation of Gravitational Waves from a Binary Neutron Star Inspiral”. In: *Phys. Rev. Lett.* 119.16, p. 161101. DOI: `10.1103/PhysRevLett.119.161101`. arXiv: `1710.05832 [gr-qc]`.

Alexander, K. D. et al. (2017). “The Electromagnetic Counterpart of the Binary Neutron Star Merger LIGO/VIRGO GW170817. VI. Radio Constraints on a Relativistic Jet and Predictions for Late-Time Emission from the Kilonova Ejecta”. In: *Astrophys. J.* 848, p. L21. DOI: `10.3847/2041-8213/aa905d`. arXiv: `1710.05457 [astro-ph.HE]`.

Bauswein, Andreas et al. (2017). “Neutron-star radius constraints from GW170817 and future detections”. In: *Astrophys. J.* 850.2, p. L34. DOI: `10.3847/2041-8213/aa9994`. arXiv: `1710.06843 [astro-ph.HE]`.

Dietrich, Tim et al. (2017a). “Gravitational waves and mass ejecta from binary neutron star mergers: Effect of the mass-ratio”. In: *Phys. Rev.* D95.2, p. 024029. DOI: `10.1103/PhysRevD.95.024029`. arXiv: `1607.06636 [gr-qc]`.

Dietrich, Tim et al. (2017b). “Modeling dynamical ejecta from binary neutron star mergers and implications for electromagnetic counterparts”. In: *Class. Quant. Grav.* 34.10, p. 105014. DOI: `10.1088/1361-6382/aa6bb0`. arXiv: `1612.03665 [gr-qc]`.

Fontes, Christopher J. et al. (Feb. 2017). “A line-smeared treatment of opacities for the spectra and light curves from macronovae”. In: arXiv: `1702.02990 [astro-ph.HE]`.

Gibson, Sarah et al. (2017). “Fallback accretion on to a newborn magnetar: short GRBs with extended emission”. In: *Mon. Not. Roy. Astron. Soc.* 470.4, pp. 4925–4940. DOI: `10.1093/mnras/stx1531`. arXiv: `1706.04802 [astro-ph.HE]`.

Guilet, Jerome et al. (2017). “Magnetorotational instability in neutron star mergers: impact of neutrinos”. In: *Mon. Not. Roy. Astron. Soc.* 471.2, pp. 1879–1887. DOI: `10.1093/mnras/stx1739`. arXiv: `1610.08532 [astro-ph.HE]`.

Hanauske, Matthias et al. (2017). “Rotational properties of hypermassive neutron stars from binary mergers”. In: *Phys. Rev. D* 96.4, p. 043004. DOI: `10.1103/PhysRevD.96.043004`. arXiv: `1611.07152 [gr-qc]`.

Hjorth, Jens et al. (2017). “The Distance to NGC 4993: The Host Galaxy of the Gravitational-wave Event GW170817”. In: *Astrophys. J. Lett.* 848.2, p. L31. DOI: `10.3847/2041-8213/aa9110`. arXiv: `1710.05856 [astro-ph.GA]`.

Hotokezaka, Kenta et al. (2017). “Analytic heating rate of neutron star merger ejecta derived from Fermi’s theory of beta decay”. In: *Mon. Not. Roy. Astron. Soc.* 468.1, pp. 91–96. DOI: `10.1093/mnras/stx411`. arXiv: `1701.02785 [astro-ph.HE]`.

Kasen, Daniel et al. (2017). "Origin of the heavy elements in binary neutron-star mergers from a gravitational wave event". In: *Nature.* [Nature551,80(2017)]. DOI: `10.1038/nature24453`. arXiv: `1710.05463 [astro-ph.HE]`.

Kastaun, Wolfgang et al. (2017). "Structure of Stable Binary Neutron Star Merger Remnants: Role of Initial Spin". In: *Phys. Rev.* D96.4, p. 043019. DOI: `10.1103/PhysRevD.96.043019`. arXiv: `1612.03671 [astro-ph.HE]`.

Lamb, Gavin P. et al. (2017). "Electromagnetic Counterparts to Structured Jets from Gravitational Wave Detected Mergers". In: *Mon. Not. Roy. Astron. Soc.* 472.4, pp. 4953–4964. DOI: `10.1093/mnras/stx2345`. arXiv: `1706.03000 [astro-ph.HE]`.

Lazzati, Davide et al. (2017). "Off-axis emission of short γ-ray bursts and the detectability of electromagnetic counterparts of gravitational-wave-detected binary mergers". In: *Mon. Not. Roy. Astron. Soc.* 471.2, pp. 1652–1661. DOI: `10.1093/mnras/stx1683`. arXiv: `1610.01157 [astro-ph.HE]`.

Lippuner, Jonas et al. (2017a). "Signatures of hypermassive neutron star lifetimes on r-process nucleosynthesis in the disc ejecta from neutron star mergers". In: *Mon. Not. Roy. Astron. Soc.* 472.1, pp. 904–918. DOI: `10.1093/mnras/stx1987`. arXiv: `1703.06216 [astro-ph.HE]`.

Lippuner, Jonas et al. (2017b). "SkyNet: A modular nuclear reaction network library". In: *Astrophys. J. Suppl.* 233.2, p. 18. DOI: `10.3847/1538-4365/aa94cb`. arXiv: `1706.06198 [astro-ph.HE]`.

Margalit, Ben et al. (2017). "Constraining the Maximum Mass of Neutron Stars From Multi-Messenger Observations of GW170817". In: *Astrophys. J.* 850.2, p. L19. DOI: `10.3847/2041-8213/aa991c`. arXiv: `1710.05938 [astro-ph.HE]`.

Nishimura, Nobuya et al. (2017). "Uncertainties in s-process nucleosynthesis in massive stars determined by Monte Carlo variations". In: *Mon. Not. Roy. Astron. Soc.* 469.2, pp. 1752–1767. DOI: `10.1093/mnras/stx696`. arXiv: `1701.00489 [astro-ph.SR]`.

Perego, Albino et al. (2017). "AT2017gfo: An Anisotropic and Three-component Kilonova Counterpart of GW170817". In: *Astrophys. J.* 850.2, p. L37. DOI: `10.3847/2041-8213/aa9ab9`. arXiv: `1711.03982 [astro-ph.HE]`.

Piro, Anthony L. et al. (2017). "Evidence for Cocoon Emission from the Early Light Curve of SSS17a". In: arXiv: `1710.05822 [astro-ph.HE]`.

Radice, David (2017). "General-Relativistic Large-Eddy Simulations of Binary Neutron Star Mergers". In: *Astrophys. J.* 838.1, p. L2. DOI: `10.3847/2041-8213/aa6483`. arXiv: `1703.02046 [astro-ph.HE]`.

Rosswog, S. et al. (2017). “Detectability of compact binary merger macronovae”. In: *Class. Quant. Grav.* 34.10, p. 104001. DOI: 10.1088/1361-6382/aa68a9. arXiv: 1611.09822 [astro-ph.HE].

Schneider, A. S. et al. (2017). “Open-source nuclear equation of state framework based on the liquid-drop model with Skyrme interaction”. In: *Phys. Rev.* C96.6, p. 065802. DOI: 10.1103/PhysRevC.96.065802. arXiv: 1707.01527 [astro-ph.HE].

Siegel, Daniel M. et al. (2017). “Three-Dimensional General-Relativistic Magnetohydrodynamic Simulations of Remnant Accretion Disks from Neutron Star Mergers: Outflows and r-Process Nucleosynthesis”. In: *Phys. Rev. Lett.* 119.23, p. 231102. DOI: 10.1103/PhysRevLett.119.231102. arXiv: 1705.05473 [astro-ph.HE].

Smartt, S. J. et al. (2017). “A kilonova as the electromagnetic counterpart to a gravitational-wave source”. In: *Nature*. DOI: 10.1038/nature24303. arXiv: 1710.05841 [astro-ph.HE].

Tanaka, Masaomi et al. (2017). “Kilonova from post-merger ejecta as an optical and near-infrared counterpart of GW170817”. In: *Publ. Astron. Soc. Jap.* DOI: 10.1093/pasj/psx121. arXiv: 1710.05850 [astro-ph.HE].

Troja, E. et al. (2017). “The X-ray counterpart to the gravitational wave event GW 170817”. In: *Nature*. DOI: 10.1038/nature24290. arXiv: 1710.05433 [astro-ph.HE].

Tsujimoto, Takuji et al. (2017). “Chemical evolution of ^{244}Pu in the solar vicinity and its implications for the properties of r-process production”. In: *The Astrophysical Journal Letters* 835.1, L3, p. L3. DOI: 10.3847/2041-8213/835/1/L3. arXiv: 1701.02323 [astro-ph.GA].

Villar, V. Ashley et al. (2017a). “The Combined Ultraviolet, Optical, and Near-Infrared Light Curves of the Kilonova Associated with the Binary Neutron Star Merger GW170817: Unified Data Set, Analytic Models, and Physical Implications”. In: *Astrophys. J.* 851.1, p. L21. DOI: 10.3847/2041-8213/aa9c84. arXiv: 1710.11576 [astro-ph.HE].

Villar, V. Ashley et al. (2017b). “Theoretical Models of Optical Transients. I. A Broad Exploration of the Duration-Luminosity Phase Space”. In: *Astrophys. J.* 849, p. 70. DOI: 10.3847/1538-4357/aa8fcb. arXiv: 1707.08132 [astro-ph.HE].

Abbott, B. P. et al. (2018). “GW170817: Measurements of neutron star radii and equation of state”. In: *Phys. Rev. Lett.* 121.16, p. 161101. DOI: 10.1103/PhysRevLett.121.161101. arXiv: 1805.11581 [gr-qc].

Ai, Shunke et al. (2018). "The allowed parameter space of a long-lived neutron star as the merger remnant of GW170817". In: *Astrophys. J.* 860.1, p. 57. DOI: `10.3847/1538-4357/aac2b7`. arXiv: `1802.00571 [astro-ph.HE]`.

Bombaci, Ignazio et al. (2018). "Equation of state of dense nuclear matter and neutron star structure from nuclear chiral interactions". In: *Astron. Astrophys.* 609, A128. DOI: `10.1051/0004-6361/201731604`. arXiv: `1805.11846 [astro-ph.HE]`.

Bromberg, O. et al. (2018). "The γ-rays that accompanied GW170817 and the observational signature of a magnetic jet breaking out of NS merger ejecta". In: *Mon. Not. Roy. Astron. Soc.* 475.3, pp. 2971–2977. DOI: `10.1093/mnras/stx3316`. arXiv: `1710.05897 [astro-ph.HE]`.

De, Soumi et al. (2018). "Tidal Deformabilities and Radii of Neutron Stars from the Observation of GW170817". In: *Phys. Rev. Lett.* 121.9. [Erratum: Phys. Rev. Lett.121,no.25,259902(2018)], p. 091102. DOI: `10.1103/PhysRevLett.121.259902, 10.1103/PhysRevLett.121.091102`. arXiv: `1804.08583 [astro-ph.HE]`.

Duffell, Paul C. et al. (2018). "Jet Dynamics in Compact Object Mergers: GW170817 Likely had a Successful Jet". In: *Astrophys. J.* 866.1, p. 3. DOI: `10.3847/1538-4357/aae084`. arXiv: `1806.10616 [astro-ph.HE]`.

Fahlman, Steven et al. (2018). "Hypermassive Neutron Star Disk Outflows and Blue Kilonovae". In: *Astrophys. J.* 869.1, p. L3. DOI: `10.3847/2041-8213/aaf1ab`. arXiv: `1811.08906 [astro-ph.HE]`.

Foucart, Francois et al. (2018). "Evaluating radiation transport errors in merger simulations using a Monte Carlo algorithm". In: *Phys. Rev.* D98.6, p. 063007. DOI: `10.1103/PhysRevD.98.063007`. arXiv: `1806.02349 [astro-ph.HE]`.

Fujibayashi, Sho et al. (2018). "Mass Ejection from the Remnant of a Binary Neutron Star Merger: Viscous-Radiation Hydrodynamics Study". In: *Astrophys. J.* 860.1, p. 64. DOI: `10.3847/1538-4357/aabafd`. arXiv: `1711.02093 [astro-ph.HE]`.

Hotokezaka, Kenta et al. (2018). "Synchrotron radiation from the fast tail of dynamical ejecta of neutron star mergers". In: *Astrophys. J.* 867.2, p. 95. DOI: `10.3847/1538-4357/aadf92`. arXiv: `1803.00599 [astro-ph.HE]`.

Kasen, Daniel et al. (2018). "Radioactive Heating and Late Time Kilonova Light Curves". In: arXiv: `1807.03319 [astro-ph.HE]`.

Kawaguchi, Kyohei et al. (2018). "Radiative transfer simulation for the optical and near-infrared electromagnetic counterparts to GW170817". In: *Astrophys. J.* 865.2, p. L21. DOI: `10.3847/2041-8213/aade02`. arXiv: `1806.04088 [astro-ph.HE]`.

Kiuchi, Kenta et al. (2018). “Global simulations of strongly magnetized remnant massive neutron stars formed in binary neutron star mergers”. In: *Phys. Rev.* D97.12, p. 124039. DOI: `10.1103/PhysRevD.97.124039`. arXiv: `1710.01311 [astro-ph.HE]`.

Lippuner, Jonas (2018). “r-Process Nucleosynthesis in Neutron Star Mergers with the New Nuclear Reaction Network SkyNet”. Dissertation, Caltech, 2018. PhD thesis. California Institute of Technology. DOI: `doi:10.7907/Z9V40SCS`. URL: `https://resolver.caltech.edu/CaltechTHESIS:06072017-212011532`.

Metzger, Brian D. et al. (2018a). “A magnetar origin for the kilonova ejecta in GW170817”. In: *Astrophys. J.* 856.2, p. 101. DOI: `10.3847/1538-4357/aab095`. arXiv: `1801.04286 [astro-ph.HE]`.

— (2018b). “A magnetar origin for the kilonova ejecta in GW170817”. In: *Astrophys. J.* 856.2, p. 101. DOI: `10.3847/1538-4357/aab095`. arXiv: `1801.04286 [astro-ph.HE]`.

Radice, David et al. (2018a). “Binary Neutron Star Mergers: Mass Ejection, Electromagnetic Counterparts and Nucleosynthesis”. In: *Astrophys. J.* 869.2, p. 130. DOI: `10.3847/1538-4357/aaf054`. arXiv: `1809.11161 [astro-ph.HE]`.

Radice, David et al. (2018b). “GW170817: Joint Constraint on the Neutron Star Equation of State from Multimessenger Observations”. In: *Astrophys. J.* 852.2, p. L29. DOI: `10.3847/2041-8213/aaa402`. arXiv: `1711.03647 [astro-ph.HE]`.

Radice, David et al. (2018c). “Long-lived Remnants from Binary Neutron Star Mergers”. In: *Mon. Not. Roy. Astron. Soc.* 481.3, pp. 3670–3682. DOI: `10.1093/mnras/sty2531`. arXiv: `1803.10865 [astro-ph.HE]`.

Radice, David et al. (2018d). “Viscous-Dynamical Ejecta from Binary Neutron Star Merger”. In: *Astrophys. J. Lett.* 869, p. L35. DOI: `10.3847/2041-8213/aaf053`. arXiv: `1809.11163 [astro-ph.HE]`.

Siegel, Daniel M. et al. (2018). “Three-dimensional GRMHD simulations of neutrino-cooled accretion disks from neutron star mergers”. In: *Astrophys. J.* 858.1, p. 52. DOI: `10.3847/1538-4357/aabaec`. arXiv: `1711.00868 [astro-ph.HE]`.

Abbott, B. P. et al. (2019a). “GWTC-1: A Gravitational-Wave Transient Catalog of Compact Binary Mergers Observed by LIGO and Virgo during the First and Second Observing Runs”. In: *Phys. Rev.* X9.3, p. 031040. DOI: `10.1103/PhysRevX.9.031040`. arXiv: `1811.12907 [astro-ph.HE]`.

— (2019b). “Properties of the binary neutron star merger GW170817”. In: *Phys. Rev.* X9.1, p. 011001. DOI: `10.1103/PhysRevX.9.011001`. arXiv: `1805.11579 [gr-qc]`.

Barbieri, C. et al. (2019). “Light-curve models of black hole – neutron star mergers: steps towards a multi-messenger parameter estimation”. In: *Astron. Astrophys.* 625, A152. DOI: `10.1051/0004-6361/201935443`. arXiv: `1903.04543 [astro-ph.HE]`.

Bulla, Mattia (2019). “POSSIS: predicting spectra, light curves and polarization for multi-dimensional models of supernovae and kilonovae”. In: *Mon. Not. Roy. Astron. Soc.* 489.4, pp. 5037–5045. DOI: `10.1093/mnras/stz2495`. arXiv: `1906.04205 [astro-ph.HE]`.

Cromartie, H. Thankful et al. (2019). “Relativistic Shapiro delay measurements of an extremely massive millisecond pulsar”. In: *Nat. Astron.* 4.1, pp. 72–76. DOI: `10.1038/s41550-019-0880-2`. arXiv: `1904.06759 [astro-ph.HE]`.

Desai, Dhruv et al. (2019). “Imprints of r-process heating on fall-back accretion: distinguishing black hole – neutron star from double neutron star mergers”. In: *Mon. Not. Roy. Astron. Soc.* 485.3, pp. 4404–4412. DOI: `10.1093/mnras/stz644`. arXiv: `1812.04641 [astro-ph.HE]`.

Fernández, Rodrigo et al. (2019). “Long-term GRMHD simulations of neutron star merger accretion discs: implications for electromagnetic counterparts”. In: *Mon. Not. Roy. Astron. Soc.* 482.3, pp. 3373–3393. DOI: `10.1093/mnras/sty2932`. arXiv: `1808.00461 [astro-ph.HE]`.

Gaigalas, Gediminas et al. (2019). “Extended calculations of energy levels and transition rates of Nd II-IV ions for application to neutron star mergers”. In: *Astrophys. J. Suppl.* 240.2, p. 29. DOI: `10.3847/1538-4365/aaf9b8`. arXiv: `1901.10671 [astro-ph.SR]`.

Ghirlanda, G. et al. (2019). “Compact radio emission indicates a structured jet was produced by a binary neutron star merger”. In: *Science* 363, p. 968. DOI: `10.1126/science.aau8815`. arXiv: `1808.00469 [astro-ph.HE]`.

Hajela, A. et al. (2019). “Two Years of Nonthermal Emission from the Binary Neutron Star Merger GW170817: Rapid Fading of the Jet Afterglow and First Constraints on the Kilonova Fastest Ejecta”. In: *Astrophys. J. Lett.* 886.1, p. L17. DOI: `10.3847/2041-8213/ab5226`. arXiv: `1909.06393 [astro-ph.HE]`.

Kathirgamaraju, Adithan et al. (2019). “EM counterparts of structured jets from 3D GRMHD simulations”. In: *Mon. Not. Roy. Astron. Soc.* 484.1, pp. L98–L103. DOI: `10.1093/mnrasl/slz012`. arXiv: `1809.05099 [astro-ph.HE]`.

Kiuchi, Kenta et al. (2019). “Revisiting the lower bound on tidal deformability derived by AT 2017gfo”. In: *Astrophys. J.* 876.2, p. L31. DOI: `10.3847/2041-8213/ab1e45`. arXiv: `1903.01466 [astro-ph.HE]`.

Miller, Jonah M. et al. (2019a). "Full Transport Model of GW170817-Like Disk Produces a Blue Kilonova". In: *Phys. Rev.* D100.2, p. 023008. DOI: `10.1103/PhysRevD.100.023008`. arXiv: `1905.07477 [astro-ph.HE]`.

Miller, M. C. et al. (2019b). "PSR J0030+0451 Mass and Radius from *NICER* Data and Implications for the Properties of Neutron Star Matter". In: *Astrophys. J.* 887.1, p. L24. DOI: `10.3847/2041-8213/ab50c5`. arXiv: `1912.05705 [astro-ph.HE]`.

Nedora, Vsevolod et al. (2019). "Spiral-wave wind for the blue kilonova". In: *Astrophys. J.* 886.2, p. L30. DOI: `10.3847/2041-8213/ab5794`. arXiv: `1907.04872 [astro-ph.HE]`.

Perego, Albino et al. (2019). "Thermodynamics conditions of matter in neutron star mergers". In: *Eur. Phys. J.* A55.8, p. 124. DOI: `10.1140/epja/i2019-12810-7`. arXiv: `1903.07898 [gr-qc]`.

Radice, David et al. (2019). "Multimessenger Parameter Estimation of GW170817". In: *Eur. Phys. J.* A55.4, p. 50. DOI: `10.1140/epja/i2019-12716-4`. arXiv: `1810.12917 [astro-ph.HE]`.

Riley, Thomas E. et al. (2019). "A *NICER* View of PSR J0030+0451: Millisecond Pulsar Parameter Estimation". In: *Astrophys. J.* 887.1, p. L21. DOI: `10.3847/2041-8213/ab481c`. arXiv: `1912.05702 [astro-ph.HE]`.

Shibata, Masaru et al. (2019). "Merger and Mass Ejection of Neutron-Star Binaries". In: *Ann. Rev. Nucl. Part. Sci.* 69, pp. 41–64. DOI: `10.1146/annurev-nucl-101918-023625`. arXiv: `1908.02350 [astro-ph.HE]`.

Siegel, Daniel M. (2019). "GW170817–the first observed neutron star merger and its kilonova: implications for the astrophysical site of the r-process". In: *Eur. Phys. J. A* 55.11, p. 203. DOI: `10.1140/epja/i2019-12888-9`. arXiv: `1901.09044 [astro-ph.HE]`.

Beloborodov, Andrei M. (Nov. 2020). "Emission of magnetar bursts and precursors of neutron star mergers". In: arXiv: `2011.07310 [astro-ph.HE]`.

Bernuzzi, Sebastiano (2020). "Neutron Star Merger Remnants". In: *Gen. Rel. Grav.* 52.11, p. 108. DOI: `10.1007/s10714-020-02752-5`. arXiv: `2004.06419 [astro-ph.HE]`.

Bernuzzi, Sebastiano et al. (June 2020). "Accretion-induced prompt black hole formation in asymmetric neutron star mergers, dynamical ejecta and kilonova signals". In: *Mon. Not. Roy. Astron. Soc.* DOI: `10.1093/mnras/staa1860`. arXiv: `2003.06015 [astro-ph.HE]`.

Dietrich, Tim et al. (2020). “Multimessenger constraints on the neutron-star equation of state and the Hubble constant”. In: *Science* 370.6523, pp. 1450–1453. DOI: `10.1126/science.abb4317`. arXiv: `2002.11355 [astro-ph.HE]`.

Endrizzi, Andrea et al. (2020). “Thermodynamics conditions of matter in the neutrino decoupling region during neutron star mergers”. In: *Eur. Phys. J. A* 56.1, p. 15. DOI: `10.1140/epja/s10050-019-00018-6`. arXiv: `1908.04952 [astro-ph.HE]`.

Fore, Bryce et al. (2020). “Pions in hot dense matter and their astrophysical implications”. In: *Phys. Rev. C* 101.3, p. 035809. DOI: `10.1103/PhysRevC.101.035809`. arXiv: `1911.02632 [astro-ph.HE]`.

Fujibayashi, Sho et al. (2020a). “Mass ejection from disks surrounding a low-mass black hole: Viscous neutrino-radiation hydrodynamics simulation in full general relativity”. In: *Phys. Rev. D* 101.8, p. 083029. DOI: `10.1103/PhysRevD.101.083029`. arXiv: `2001.04467 [astro-ph.HE]`.

Fujibayashi, Sho et al. (July 2020b). “Post-merger Mass Ejection of Low-mass Binary Neutron Stars”. In: arXiv: `2007.00474 [astro-ph.HE]`.

Krüger, Christian Jürgen et al. (2020). “Estimates for Disk and Ejecta Masses Produced in Compact Binary Mergers”. In: *Phys. Rev. D* 101.10, p. 103002. DOI: `10.1103/PhysRevD.101.103002`. arXiv: `2002.07728 [astro-ph.HE]`.

Metzger, Brian D. (2020). “Kilonovae”. In: *Living Rev. Rel.* 23.1, p. 1. DOI: `10.1007/s41114-019-0024-0`. arXiv: `1910.01617 [astro-ph.HE]`.

Mösta, Philipp et al. (2020). “A magnetar engine for short GRBs and kilonovae”. In: *Astrophys. J. Lett.* 901, p. L37. DOI: `10.3847/2041-8213/abb6ef`. arXiv: `2003.06043 [astro-ph.HE]`.

Nedora, Vsevolod et al. (Nov. 2020). “Mapping dynamical ejecta and disk masses from numerical relativity simulations of neutron star mergers”. In: arXiv: `2011.11110 [astro-ph.HE]`.

Prantzos, N. et al. (2020). “Chemical evolution with rotating massive star yields II. A new assessment of the solar s- and r-process components”. In: *mnras* 491.2, pp. 1832–1850. DOI: `10.1093/mnras/stz3154`. arXiv: `1911.02545 [astro-ph.GA]`.

Radice, David (2020). “Binary Neutron Star Merger Simulations with a Calibrated Turbulence Model”. In: *Symmetry* 12.8, p. 1249. DOI: `10.3390/sym12081249`. arXiv: `2005.09002 [astro-ph.HE]`.

Radice, David et al. (2020). “The Dynamics of Binary Neutron Star Mergers and GW170817”. In: *Ann. Rev. Nucl. Part. Sci.* 70, pp. 95–119. DOI: `10.1146/annurev-nucl-013120-114541`. arXiv: `2002.03863 [astro-ph.HE]`.

Tanaka, Masaomi et al. (2020). “Systematic Opacity Calculations for Kilonovae”. In: *Mon. Not. Roy. Astron. Soc.* 496.2, pp. 1369–1392. DOI: `10.1093/mnras/staa1576`. arXiv: `1906.08914 [astro-ph.HE]`.

Troja, E. et al. (2020). “A thousand days after the merger: continued X-ray emission from GW170817”. In: *Mon. Not. Roy. Astron. Soc.* 498.4, pp. 5643–5651. DOI: `10.1093/mnras/staa2626`. arXiv: `2006.01150 [astro-ph.HE]`.

Vincent, Trevor et al. (2020). “Unequal Mass Binary Neutron Star Simulations with Neutrino Transport: Ejecta and Neutrino Emission”. In: *Phys. Rev.* D101.4, p. 044053. DOI: `10.1103/PhysRevD.101.044053`. arXiv: `1908.00655 [gr-qc]`.

Ayache, Eliot H. et al. (Apr. 2021). “GAMMA: a new method for modeling relativistic hydrodynamics and non-thermal emission on a moving mesh”. In: arXiv: `2104.09397 [astro-ph.HE]`.

Balasubramanian, Arvind et al. (Mar. 2021). “Continued radio observations of GW170817 3.5 years post-merger”. In: arXiv: `2103.04821 [astro-ph.HE]`.

Breschi, Matteo et al. (Jan. 2021). “`bajes`: Bayesian inference of multimessenger astrophysical data, methods and application to gravitational-waves”. In: arXiv: `2102.00017 [gr-qc]`.

Daszuta, Boris et al. (Jan. 2021). “GRAthena++: puncture evolutions on vertex-centered oct-tree AMR”. In: arXiv: `2101.08289 [gr-qc]`.

Fernández, Joseph John et al. (Jan. 2021). “Determining the viewing angle of neutron star merger jets with VLBI radio images”. In: arXiv: `2101.05138 [astro-ph.HE]`.

Hajela, A. et al. (Apr. 2021). “The emergence of a new source of X-rays from the binary neutron star merger GW170817”. In: arXiv: `2104.02070 [astro-ph.HE]`.

Logoteta, Domenico et al. (2021). “Microscopic equation of state of hot nuclear matter for numerical relativity simulations”. In: *Astron. Astrophys.* 646, A55. DOI: `10.1051/0004-6361/202039457`. arXiv: `2012.03599 [nucl-th]`.

Nedora, Vsevolod et al. (Apr. 2021a). “Dynamical ejecta synchrotron emission as possible contributor to the rebrightening of GRB170817A”. In: arXiv: `2104.04537 [astro-ph.HE]`.

Nedora, Vsevolod et al. (2021b). “Numerical Relativity Simulations of the Neutron Star Merger GW170817: Long-Term Remnant Evolutions, Winds, Remnant Disks, and Nucleosynthesis”. In: *Astrophys. J.* 906.2, p. 98. DOI: `10.3847/1538-4357/abc9be`. arXiv: `2008.04333 [astro-ph.HE]`.

Troja, E. et al. (Apr. 2021). “Accurate flux calibration of GW170817: is the X-ray counterpart on the rise?” In: arXiv: `2104.13378 [astro-ph.HE]`.

Curriculum Vitae

Personal details

Name	Vsevolod
Surname	Nedora
Address	Humboldtring 41, 14473 Potsdam, Germany
Email	vsevolod.nedora@gmail.com
Birth date	13.03.1993
Nationality	Russian

Education

2018–2021 *PhD in Theoretical Physics*

Theoretisch-Physikalisches Institute, Jena Germany

SUPERVISOR	Prof. Sebastiano Bernuzzi, sebastiano.bernuzzi@uni-jena.de
THESIS TITLE	Simulations of Binary Neutron Star Mergers: Mass Ejection and Electromagnetic Counterparts
GRADUATION	Expected: October 2021
GRADE	–

2016–2018 *Master's degree in Astrophysics*

Argerlander Institute for Astronomy, Bonn Germany

SUPERVISOR	Prof. Norbert Langer, nlanger@astro.uni-bonn.de Dr. Luca Grassitelli, luca@astro.uni-bonn.de
THESIS TITLE	Investigating the physical conditions at the base of the stellar wind of the massive helium stars. Applications for the mass loss rate constrains
GRADUATION	September 2018
GRADE	2.0/1.0 good

2010–2015 *Bachelor's degree in Physics*

Far-Eastern Federal University, Vladivostok Russia

SUPERVISOR	Prof. Vadim S. Artyukh, art@prao.ru
THESIS TITLE	Research of synchrotron emission of a simple spherical radio source
GRADUATION	July 2015
GRADE	5/5 excellent

Talks and Seminars

1. *Binary neutron star mergers: ejecta, nucleosynthesis and electromagnetic counterparts*
   RTG conference, Online (Jena), Germany, September 2021
2. *BNS mergers: EM counterparts & nucleosynthesis* (poster)
   ISAPP PhD school Summer School on Gravitational Waves, *online*, June, 2021
3. *Spiral-wave wind for the blue kilonova*
   MICRA workshop at TPI, Jena, Germnay August 2019
4. *Neutron Star Mergers & Electromagnetic Counterparts*
   ECT* conference plenary talk at University of Trento, Trento, Italy June 2019
5. *Numerical Relativity Informed Kilonova Model*
   RTG conference, Munich, Germnay, March 2019

Teaching

- Tutor at Bonn University for subjects: *Stars and Stellar Evolution* and *Nucleosynthesis*, 2017-2018 (for M.Sc. students)
- Lecturer and tutot at FSU Jena for *Compytational Physics II* (for B.Sc students)
- Advisor and corrector for *Project Practicum: Numerical solutions to wave equation*, 2019-2021 (for M.Sc. students)

Ort, Datum

Unterschrift

Zusammenfassung

Das Ziel dieser Arbeit ist es, unser Verständnis von Fusionen binärer Neutronensterne (BNS) und ihrer fundamentalen Physik durch den Einsatz modernster Numerischer Relativitätssimulationen (NR) mit fortgeschrittener Physik und elektromagentischen Modellen in Verbindung mit Multimessenger Beobachtungen von GW170817 voranzustreiben.

Betrachtet man die Entwicklung des Postfusionsregimes eines BNS-Fusionsüberrestes, so stellt man eine insgesamt starke Abhängigkeit vom Massenverhältnis des Systems und der Neutronenster-Zustandsgleichung sowie von den endlichen Temperatureffekten in letzterer fest. Einer der wichtigsten betroffenen Parameter ist die Lebensdauer des Überrests. Wir stellen fest, dass Modelle mit weicher Zustandsgleichung und/oder großem Massenverhältnis kurzlebige Neutronensternüberreste erzeugen, die innerhalb von wenigen ∼10 ms nach der Verschmelzung kollabieren. Symmetrischere Modelle mit steiferer Zustandsgleichung erzeugen langlebige, möglicherweise stabile Überreste. Die Lebensdauer des Fusionsüberrestes scheint mit der Akkretionsscheibenmasse für die $q \sim 1$ Modelle zu korrelieren, was mit früheren Erkenntnissen übereinstimmt (Radice et al., 2018a,b). Binärsysteme mit größeren Massenverhältnisen haben tendenziell massereichere Scheiben und massivere Gezeitenkomponenten von dynamischen Auswürfen.

Die langfristige Entwicklung des Postfusionsregimes von Neutronensternüberresten wird durch die Akkretion bestimmt, die durch Neutrinokühlung und viskose Spannungen hervorgerufen wird, sowie durch Massenauswurf, der durch Gravitations- und hydrodynamische Drehmomente und Neutrino-Resorption (Erwärmung) angetrieben ist. Bemerkenswerterweise, kollabiert ein neu gebildeter Neutronensternüberrest, der die maximale Masse eines Hypermassiven Neutronensternes in gleichmäßig rotierender Konfiguration übersteigt, nicht unbedingt zu einem Schwarzen Loch. Stattdessen können massive Winde, wie Spiralwellenwinde, den Überschuss an Masse (zusammen mit dem Drehimpuls) effizient beseitigen und den Neutronensternüberrest in eine starr rotierende Konfiguration bringen.

Betrachtet man die Materie, die während und nach der Verschmelzung ausgestoßen wird, so findet man zwei verschiedene Typen: dynamnischen Auswurf und Spiralwellenwinde im Postfusionsregime. In Bezug auf die erste Art erweitern wir die Analyse unserer eigenen Modelle unter Berücksichtigung aller verfügbaren BNS-Fusionsmodelle in der Literatur mit verschiedenen physikalischen Inputs. Die statistische Analyse der Eigenschaften des dynamnischen Auswurfs zeigt eine starke Abhängigkeit von der

Neutrino-Resorption. Ihre Einbeziehung erhöht die Masse und die Geschwindigkeit des Auswurfs. Des Weiteren ähnelt die Zusammensetzung des dynamnischen Auswurfs aus unseren Modellen, die mit einem angenäherten M0-Neutrino-Schema berechnet wurde, derjenigen, die in Simulationen mit anspruchsvolleren Neutrino-Behandlungsmethoden gefunden wurde (Sekiguchi et al., 2016; Vincent et al., 2020). Mithilfe des bisher größten Satzes von BNS-Simulationen verknüpfen wir die Eigenschaften des dynamnischen Auswurfes mit den binären Systemparametern unter Berücksichtigung einer Vielzahl von Anpassungsformeln. Wir aktualisieren diese Beziehungen, die für die Multimessenger-Astronomie sehr wichtig sind. Wir finden auch, dass ein einfaches Zwei-Parameter-Polynom, $P_2^2(q,\tilde{\Lambda})$, eine vergleichbare oder bessere statistische Leistung zeigt als andere Anpassungsformeln.

In Fällen, in denen der Fusionsüberrest langlebig ist, identifizieren wir eine neue Auswurfskomponente, die Spiralwellenwinde. Diese Winde werden durch Energie und Drehimpuls angetrieben, die vom Überrest, der der Bar-Mode und einarmigen dynamischen Instabilitäten unterworfen ist, in die Scheibe injiziert werden. Wir stellen fest, dass die Spiralwellenwinde innerhalb der Simulationszeit, bis zu $\sim$100 ms, nicht sättigen, es sei denn, der Neutronensternüberrest kollabiert zu einem Schwarzen Loch. Spiralwellenwinde haben eine breite Verteilung des Elektronenanteils, der im Durchschnitt höher ist als in dynamnischen Auswürfen. Spiralwellenwinde haben eine enge Geschwindigkeitsverteilung und können innerhalb einer Sekunde $\sim$0.1-0.5 $\mathrm{M}_{\odot}$ aus dem System extrahieren.

Ein Teil von Spiralwellenwinden, der entlang der polaren Achse kanalisiert ist und den höchsten Elektronenanteil aufweist, identifizieren wir als Neutrino-getriebenen Wind. Im Gegensatz zu anderen Studien über Neutrino-getriebene Ausströmungen (*e.g.* Dessart et al., 2009; Perego et al., 2014; Fujibayashi et al., 2020b), sättigen Neutrino-getriebene Winde in unseren Simulationen kurz nach der Fusion. Insbesondere beziehen sich stationäre, Neutrino-getriebene Winde im Allgemeinen auf Abflüsse, die auf einer Zeitskala entstehen, die Hunderte von Millisekunden länger als unsere ist. Darüber hinaus ist es plausibel, dass das in unseren Simulationen verwendete approximierte Neutrino-Reabsorptions Schema, in diesem Fall unzureichend ist. Langfristige Simulationen mit fortschrittlicheren Neutrinotransportschemata sind erforderlich, um die Eigenschaften von Neutrino-getriebenen Winden zu beurteilen. Außerdem sind die Auswirkungen der Magnetisierung für polare Ausströmungen wichtig (Siegel et al., 2017; Metzger et al., 2018b; Fernández et al., 2019; Miller et al., 2019a; Mösta et al., 2020). Unsere Simulationen beinhalten jedoch keine Magnetfelder.

Wir bewerten das Ergebnis von der r-Prozess Nukleosynthese in der ausgeworfenen Materie anhand eines vorberechneten, parametrisierten Modells, das auf dem Nuclear Reaction Network `SkyNet` (Lippuner et al., 2015) basiert. Die r-Prozess-Ergebnisse in den dynamnischen Auswürfen hängen stark vom binären Massenverhältnis ab, wobei in Fällen mit hohem q große Mengen an Lanthaniden und Aktiniden produziert werden. Modelle mit den höchsten Massenverhältnissen, die einen unverzüglichen Kollaps durchlaufen, zeigen Aktinidenhäufigkeiten in ihren dynamnischen Auswürfen, die denen des Sonnensystems ähneln. Binärsysteme mit $q \sim 1$ erzeugen weniger neutronenreiche dynamnische Auswürfe und die Endhäufigkeiten weisen einen signifikanten Anteil leichterer Elemente auf.

Wenn der Fusionsüberrest langlebig ist, zeigen die endgültigen r-Prozess-Häufigkeiten im Gesamtauswurf (dynamische Auswürfe und Spiralwellenwinde eingeschlossen) große Mengen von schweren und leichten Elementen. Das Häufigkeitsmuster in diesen Auswürfen ist ähnlich wie das im Sonnensystem, bis hinunter zu $A \simeq 100$. Dieses Ergebnis unterstreicht die Bedeutung von BNS-Fusionen für die kosmische chemischen Entwicklung.

Betrachtet man die thermische Emission aus dem Zerfall von r-Prozess-Elementen im Auswurf, eine so genannte Kilonova (kN), aus unseren Modellen, stellen wir fest, dass, wenn sphärisch symmetrische kN-Modelle betrachtet werden (Villar et al., 2017a), keines unserer Modelle die bolometrischen Lichtkurven von AT2017gfo erklären kann. Wenn jedoch anisotrope Multikomponenten kN-Modelle berücksichtigt werden, die die Eigenschaften und die Geometrie der Auswürfe berücksichtigen, werden bestimmte Schlüsselmerkmale von AT2017gfo wiederhergestellt. Wir stellen insbesondere fest, dass die frühe blaue Emission erklärt werden kann, wenn sowohl dynamische Auswürfe als auch Spiralwellenwinde berücksichtigt werden und wenn der Fusionsüberrest langlebig ist.

Es wurde auch gezeigt, dass Material mit hohem Elektronenanteil in Ausströmungen von Schwarzes Loch-Torus-Systemen vorhanden ist und daher nicht unbedingt einen langlebigen Überrest erfordert (Fujibayashi et al., 2020a). Die spätzeitliche rote Kilonova-Komponente erfordert massive, ∼20% der Scheibenmasse, Ausströmungen mit niedrigem Y_e. Solche Ausströmungen können durch viskose Prozesse und nukleare Rekombination auf einer Zeitskala von Sekunden (*e.g.* Metzger et al., 2008) angetrieben werden.

Unter Berücksichtigung des Synchrotron-Nachleuchtens durch die Wechselwirkung des Auswurfs mit dem Interstellaren Medium stellen wir fest, dass die kürzlich beobachtete

Veränderung des Nachleuchtens von GRB170817A 1000 Tage nach der Verschmelzung durch das kN-Nachleuchten erklärt werden kann, das durch ab-initio NR BNS-Simulationen berechnet wurde, die auf GW170817 ausgerichtet sind. Insbesondere Modelle mit mäßig steifer Zustandsgleichung und mäßig großem Massenvehältnis, die eine geringe Menge an schnellem Auswurf produzieren, werden bevorzugt. Dies bietet eine neue Möglichkeit, die Eigenschaften von GW170817 einzuschränken.

Selbstständigkeitserklärung

Ich erkläre hiermit, dass ich die vorliegende Arbeit selbständig, ohne unzulässige Hilfe Dritter und ohne Benutzung anderer als der angegebenen Hilfsmittel und Literatur angefertigt habe. Die aus anderen Quellen direkt oder indirekt übernommenen Daten und Konzepte sind unter Angabe der Quelle gekennzeichnet.

Bei der Auswahl und Auswertung dieser Arbeit haben mir die nachstehend aufgeführten Personen in beratender Weise unentgeltlich geholfen:

- Prof. Sebastiano Bernuzzi
- Prof. David Radice
- Prof. Albino Perego

In Bereichen bei denen auf Arbeit anderer zurückgegriffen wurde, ist dies ausdrücklich in der Arbeit erwähnt. Weitere Personen waren an der inhaltlich-materiellen Erstellung der vorliegenden Arbeit nicht beteiligt. Insbesondere habe ich hierfür nicht die entgeltliche Hilfe von Vermittlungs- bzw. Beratungsdiensten (Promotionsberater oder andere Personen) in Anspruch genommen. Niemand hat von mir unmittelbar oder mittelbar geldwerte Leistungen für Arbeiten erhalten, die im Zusammenhang mit dem Inhalt der vorgelegten Dissertation stehen. Die Arbeit wurde bisher weder im In- noch im Ausland in gleicher oder ähnlicher Form einer anderen Prüfungsbehörde vorgelegt.

Ich versichere ehrenwörtlich, dass ich nach bestem Wissen die reine Wahrheit gesagt und nichts verschwiegen habe.

Ort, Datum

Unterschrift